Circular and dual-linear polarized continuous transverse stub arrays for SatCom applications

Michele del Mastro

UNIVERSITÉ DE RENNES 1

THÈSE DE DOCTORAT DE

L'UNIVERSITÉ DE RENNES 1

ÉCOLE DOCTORALE N° 601
Mathématiques et Sciences et Technologies de l'Information et de la Communication
Spécialité : *Electronique*

Par

Michele DEL MASTRO

Circular and Dual-Linear Polarized Continuous Transverse Stub Arrays for SatCom Applications

Thèse présentée et soutenue à Rennes, le 14 Décembre 2020
Unité de recherche : IETR – UMR CNRS 6164, Institut d'Électronique et des Technologies du numéRique, Université de Rennes 1.

Rapporteurs avant soutenance :

Marianna IVASHINA	Professeur des universités, Chalmers Université de Technologie, Göteborg, Suède.
A. Bart SMOLDERS	Professeur des universités, Université de Technologie d'Eindhoven, Eindhoven, Pays-Bas.

Composition du Jury :

Examinateurs :	Giovanni TOSO	Ingénieur de Recherche, Agence Spatiale Européenne, Noordwijk, Pays-Bas.
	José I. H. HERRUZO	Professeur des universités, Université Polytechnique de Valence, Espagne.
Dir. de thèse :	Mauro ETTORRE	Chercheur CNRS, HDR, IETR, Rennes, France.
Co-dir. de thèse :	Ronan SAULEAU	Professeur des universités, HDR, Université de Rennes 1, Rennes, France.

Invité(s) :

Philippe POULIGUEN	Ingénieur de Recherche, HDR, Direction générale de l'armement, Bruz, France.
Patrick POTIER	Ingénieur de Recherche, Direction générale de l'armement, Paris, France.
Gilles QUAGLIARO	Ingénieur de Recherche, Thales SIX, Gennevilliers, France.
David G. OVEJERO	Chercheur CNRS, IETR, Rennes, France.

"*If you have raced with men on foot and they have worn you out, how can you compete with horses? If you feel secure only in a peaceful land, how will you manage in the flooding of the Jordan?*"

(Jeremiah 12:5)

"*Si perde verso il bianco Meridione,*
azzurro, rosso, l'Appennino, assorto
sotto le chiuse palpebre, all'alone

del mare di Gaeta e di Sperlonga...

Dietro il Massico stende Sparanise
candelabri di ulivi, tra festoni
di piante rampicanti sulle elisie

radure, dove lucono i lampioni
a San Nicola... Si spalanca il golfo
africano di Napoli, nazione

nel ventre della nazione... "

(Pier Paolo Pasolini, Le Ceneri di Gramsci)

"*Those who crawl on the earth are not exposed to falling as easily as those who climb the mountain tops. Those who sit by the fireplace are not as easily exposed to being lost as those who venture into the world. "*

(Søren Kierkegaard, Aut-Aut)

Acknowledgments

"The supreme vice is the shallowness. Whatever is realised is right."

(Oscar Wilde, De profundis)

Over the past three years, I have come to realize how fortunate I have been to run into so many precious people. Without any rhetoric, I can affirm that each of them has enriched me and contributed to my vocational, as well as personal, growth. Therefore, it is a duty to acknowledge them all sincerely, even though it is unfair to dedicate so a few lines to this end.

To my supervisors, special thanks are reserved for always encouraging me and giving me numerous priceless opportunities. Many thanks to prof. Ronan Sauleau for his advice, guidance and support throughout this thesis. All my highest gratitude goes to dr. Mauro Ettorre for his help and friendship. Without his advice and competence, this research work would not have been possible. In addition, I am sincerely grateful to dr. Philippe Pouliguen for his professionalism and kindness, a rare combination nowadays.

I would like to dedicate a special thought to prof. Anthony Grbic, who accepted me in his research group at the University of Michigan as visiting scholar. Sometimes, it is truly surprising to discover that life has reserved for you such extraordinary encounters. Dear Tony, thank you for everything and I sincerely hope I did not misspell your surname this time.

I also wish to acknowledge the members of the Ph.D. committee for the effort dedicated to improve the consistency of this manuscript.

Moreover, a special thank goes to the people who made pleasant my stay in IETR. For the help in dealing with French bureaucracy, I would like to thank Martine, Noëlle, and Nathalie. I thank dr. Laurent Le Coq for the fruitful technical discussions, as well as all members of MARS^2 team without whom it would not have been possible to enhance my thesis work. Many thanks to Frédéric Boutet and Xavier Morvan.

I am especially thankful to my love Clémence for her lightning arrival in my life. As once said by Erasmus of Rotterdam in praise of folly, I have to thank you for reminding me that days are too short not to dance endlessly. I am looking forward to seeing what happens next.

My heartfelt thanks go to the people who have marked my life in Rennes. During these years, my life has been inextricably linked to people who are and will always be a fundamental part of my inner world. Among them, I particularly wish to thank Nicola Bartolomei with whom I had the privilege of spending two years under the same roof. Together, we shared fears, worries, successes and, always together, we got lost a thousand times in the sweet notes of Pink Floyd. I wished that time would never end. A special thought is dedicated to Petros Bantavis (alias Petran). There are no words to describe how attached I am to his uniqueness and sweetness. The only thing I can say is: $\mu\epsilon\ \tau\rho\epsilon\lambda\alpha\iota\nu\epsilon\iota\varsigma$. I want to thank Stefano Lenzini for being part of this life experience, albeit briefly. I jealously keep in my heart the memories of a week spent together in Beg Meil. Many thanks to Thomas Ströber (alias Sir Tommasino or Tommaso il Moro) for his priceless friendship. Bumping into a German guy with a genuine Neapolitan heart is more unique than a rare case. Special thanks also go to Álvaro Pascual-Gracia (alias Alveen, Jasmeen, Mesmereen, Pelvereen, etc.) for the creative talks and the original Hispano-American accent (always a pleasure to listen to). I would be lying, if I said I am sorry to have accidentally broken his radiator. In no particular order, I would like to thank Laura, Antoine, Riccardo, Gaetano, Rosa, Sđrjan, Mattia, Giulia, Luan, Nicolas, Denys, Nicolas, Guillaume, etc. Many thanks to the colleagues at the University of Michigan, particularly Brian, Zhanni, and Cody.

Heartily thanks go to my long-term friends, now spread all over Europe. In particular, a special thought goes to Roberta who helped me to settle down in Ann Arbor.

Last but not least, I express my deepest gratitude to my family, central pillar of my existence. I will be forever indebted to my parents, Giuseppina and Francesco, for the sacrifices they had to endure to get me here today. I love you infinitely. I thank my sister, Concetta, and brother, Mario, for being part of my existence. A sweet thought is reserved to my grandmother. This thesis is dedicated to her too.

"In ultimo, ma non per importanza, vorrei esprimere la mia più profonda gratitudine per la mia famiglia, pilastro centrale della mia esistenza. Sarò per sempre indebitato con i miei genitori, Giuseppina e Francesco, per i sacrifici che hanno sopportato perché io potessi raggiungere questo traguardo. Vi amo profondamente. Ringrazio mia sorella, Concetta, e mio fratello, Mario, per essere parte della mia esistenza. Un dolce pensiero va a mia nonna. Questa tesi è dedicata anche a lei."

Michele Del Mastro

Résumé

La demande croissante en systèmes de communication par satellite à large bande a conduit au déploiement de constellations de satellites en bande K/Ka et au développement de nouveaux terminaux pour les utilisateurs fixes et mobiles [1, 2]. Les bandes attribuées pour les applications militaires et civiles pour la réception (Rx) et l'émission (Tx) sont respectivement 17,7-21,2 GHz et 27,5-31 GHz. Dans ces deux bandes, des exigences strictes sont imposées à l'antenne. L'antenne doit présenter un gain élevé ($>$ 30 dB) et fonctionner en polarisation circulaire ou double polarisation sur un secteur angulaire couvrant tout le plan azimutal et un grand angle en élévation (jusqu'à 60°).

Plusieurs solutions ont été proposées au cours des années récentes, telles que les réseaux « Continuous Transverse Stub » (CTS) [3], les réseaux connectés (en anglais « connected arrays ») [4] ou les réseaux phasés [1]. Les réseaux connectés sont des réseaux 2-D alimentés périodiquement à intervalles de Nyquist. Ces antennes présentent des largeurs de bande extrêmement importantes, des capacités de balayage étendues et une pureté de polarisation remarquable. Cependant, l'utilisation de plusieurs alimentations et des modules Tx/Rx associés affecte la taille finale et le coût de l'antenne. Les réseaux phasés sont des solutions extrêmement agiles, mais leur coût et les pertes des éléments actifs sont encore des facteurs extrêmement limitants.

Les réseaux CTS se composent de longues fentes rayonnantes, de hauteur finie, reliés à un système d'alimentation en guide à plans parallèles, en anglais parallel-plate waveguide (PPW), et rayonnant dans l'espace libre [3, 5]. Les fentes rayonnantes peuvent être alimentées en parallèle ou en série par un formateur de faisceau en PPW. Ainsi, lorsque les fentes sont alimentées en parallèle, les réseaux CTS présentent une très large bande passante et une large capacité de balayage [5]. Un autre avantage clé des réseaux CTS par rapport aux réseaux connectés et aux réseaux phasés est la possibilité d'alimentation du réseau par des formateurs de faisceau quasi-optiques, comme les systèmes

pillbox [6]. Les systèmes d'alimentation avec des formateurs de faisceau quasi-optiques réduisent drastiquement la complexité globale du système antennaire avec des capacités de balayage améliorées. De plus, un système hybride (mécanique / électronique) peut être utilisé pour pointer le faisceau principal de l'antenne : des solutions mécaniques sont employées en azimut et un système de commutation de faisceaux (« beam switching ») en élévation.

Le principal inconvénient des réseaux CTS est leur fonctionnement en simple polarisation linéaire en raison de leur mécanisme de rayonnement. La polarisation circulaire peut être obtenue en utilisant des polariseurs classiques avec un inconvénient sur l'épaisseur et la masse finale de l'antenne [3]. Aujourd'hui il n'existe pas de solutions connues dans la littérature ouverte concernant des réseaux CTS à double polarisation.

L'Institut d'Électronique et des Technologies du numéRique (IETR) travaille sur les réseaux CTS depuis 2012 dans le cadre de deux projets R&T du Centre National d'Études Spatiales (CNES). Ces deux projets CNES ont permis à l'IETR de développer des outils numériques pour l'analyse de ces réseaux [5]. Les outils ont été intégrés dans le logiciel PROFILE utilisé par le CNES pour la conception d'antennes. De plus, l'outil développé par l'IETR a été utilisé pour concevoir un réseau à large bande couvrant toute la bande Ka avec un champ de vision jusqu'à 45° en élévation avec une efficacité supérieur à 80% [6]. Cette antenne a suscité un très fort intérêt de la part de l'Agence Spatiale Européenne (ESA) et de Thales Alenia Space, Toulouse. L'antenne décrite en [6] a été présentée lors de plusieurs manifestations par Thales Alenia Space. En outre, le concept développé a été mis en œuvre et validé pour des applications 5G dans la bande à 60 GHz en utilisant un processus de fabrication LTCC (en anglais « Low Temperature Co-fired Ceramics ») [7, 8] et dans la bande E en utilisant des processus de fraisage classiques [9] et en technologies multicouches PCB (en anglais « Printed-Circuit Board ») [10].

L'objectif principal de cette thèse est d'étudier l'analyse et la conception des réseaux CTS à double polarisation. Un réseau alimenté en parallèle sera considéré pour un fonctionnement large bande. L'idée à la base de la thèse est d'utiliser des réseaux CTS multimodaux. Les réseaux CTS classiques adoptent le mode principal TEM (« Transerve Electromagnetic ») du guide PPW d'alimentation. Ici, nous proposons d'utiliser le mode TEM et le mode TE (« Transverse Electric

»). Ces deux modes sont orthogonaux et, si correctement alimentés, peuvent générer une double polarisation.

Plan de la thèse

Dans ce qui suit, nous proposons un bref résumé du contenu de chaque chapitre.

Au **Chapitre 1** nous commençons par expliquer la nécessité d'antennes à grande couverture et large bande dans des domaines d'applications spatiales. Le chapitre se poursuit avec un état de l'art et l'introduction de la structure de référence des antennes CTS qui sont étudiées et développées par la suite.

Au **Chapitre 2** nous proposons un code de raccordement modal (« Mode Matching ») (MM) pour l'analyse et la conception des réseaux CTS multimodaux. L'outil prend en compte des guides PPW multimodaux et l'excitation des différents modes propageant dans les guides. L'impédance en balayage du réseau de fentes, éventuellement en présence d'un radôme diélectrique multicouche, est calculée, dans le cas d'un réseau infini. Nous présentons ainsi une approche pour évaluer les diagrammes de rayonnement qui repose sur l'évaluation de l'amplitude et de la phase du champ à la sortie du formateur de faisceaux. Enfin, à l'aide des outils développés, une conception d'antenne est présentée. La technologie envisagées pour la fabrication est l'impression 3D.

Au **Chapitre 3** nous présentons une étude analytique de la dispersion en PPW, dont les plaques parallèles ont été remplacées par des surfaces d'impédance. Le modèle numérique sert à comprendre non seulement comment résoudre les problèmes de dispersion intermodale entre les modes TEM et TE, mais aussi comment concevoir des structures pour inhiber la propagation du mode TM (« Transverse Magnetic »).

Le **Chapitre 4** propose la conception d'une antenne CTS multimodale qui génère une double polarisation. Le verrou principal à lever pour la structure proposée est l'excitation du premier mode TM du guide PPW. Le mode TM présente la même fréquence de coupure que le mode TE; il donc pourrait se propager dans le guide. De plus, il peut se coupler très facilement au mode TEM du guide. Une solution possible pour éviter le couplage du mode TEM et du mode TM est d'utiliser des guides PPW avec des corrugations. La structure comporte des corrugations le long de la direction de propagation des modes.

Une périodicité des corrugations, proche de la limite quasi-statique ($\lambda/10$, où λ est la longueur d'onde) assure une faible anisotropie et une faible dispersion spatiale. Le PPW avec corrugations permet aux modes TE et TEM de se propager et d'éviter le couplage entre le mode TEM et le mode TM d'un guide PPW classique. L'antenne a été fabriquée et mesurée dans la chambre anéchoïque de l'IETR.

Au **Chapitre 5** nous proposons des radomes polarisants à faible profil et double bande pour réaliser des réseaux CTS en polarisation circulaire sans modifier l'architecture de l'antenne. Nous présentons une procédure de conception systématique basée sur des circuits équivalents qui modélisent le polariseur par des ondes incidentes en polarisation verticale et horizontale. Le polariseur génère une conversion de polarisation linéaire à circulaire dans les canaux Tx et Rx des bandes K et Ka. Les polarisations circulaires générées entre ces deux bandes sont orthogonales l'une à l'autre. Nous présentons la conception d'un polariseur qui comprend trois surfaces d'impédance anisotropes et deux substrats. Les résultats mesurés montrent que le polariseur possède des bandes passantes relatives 21% et 6% pour une gamme d'incidence d'au moins $\pm 45°$.

Au **Chapitre 6** nous proposons la conception d'une antenne CTS classique, entièrement intégrés en technologies multicouches PCB. L'antenne génère une polarisation linéaire sur une large bande. La réalisation des antennes CTS en technologie planaire favorise la miniaturisation et leur intégration dans les plateformes mobiles pour les applications SOTM (en anglais « Satelite communication on-the-move »). Nous introduisons un guide d'onde vertical entièrement intégrée dans le substrat qui supporte un mode quasi-TEM, en se rapprochant donc du fonctionnement d'un guide d'onde a plans parallèles. Enfine, nous présentons l'intégration du polariseur avec cette antenne CTS.

Au **Chapitre 7** nous dressons un bilan global des principaux résultats de la thèse en soulignant aussi quelques questions ouvertes qui restent encore à résoudre et également de possibles développements futurs.

Abstract

The ever increasing demand for high-data-rate wireless services has boosted the need for advanced satellite communication (SatCom) technologies. New generation satellite spacecrafts are now deployed in constellations orbiting in low and medium Earth orbits, e.g., the SpaceX's Starlink satellite mega constellation [11]. To ensure a near-global coverage, the on-board antennas are growingly quested to provide a multi-beam radiation. As consequence, the ground terminals must provide high-gain radiation over a large field-of-view, to track the satellites while flying at important angular velocities. A wideband operation is also required to improve the throughput for high-speed data rates. As a matter of example, SpaceX's Starlink constellation will offer speeds of up to a gigabit per second at a latency ranging from 25 ms to 35 ms [11]. The circular (CP) or dual-linear polarization also represents a key asset to mitigate the polarization mismatch that may occur in long-range radio transmissions. Furthermore, the antenna miniaturization has become mandatory in view of the hardware integration in a large variety of moving platforms.

In light of the above, the work outlined in this thesis focus on a promising candidate as a modern terminal SatCom antenna: the continuous transverse stub (CTS) array fed by quasi-optical beamformers. The CTS arrays are planar arrays, made of long slots, that have stood out for their broadband and wide-angle scanning performances during the last decades. The antenna comprises open-ended stubs, parallel-fed by a corporate feed network in parallel-plate waveguide (PPW) technology. A two-layer embedded parabola is employed for the antenna feeding through a focal array of horns. The antenna offers a beam-steering along with one of the principal planes. A two-dimensional (2-D) scan range can be attained with an azimuth rotation of the antenna module. As a drawback, the classical CTS arrays are inherently linearly-polarized. In this manuscript, an original concept is proposed to overcome this limitation, namely the dual-mode CTS array. The radiating stubs are enlarged in such a way to

support the propagation of three modes: the transverse electromagnetic (TEM) mode and the first transverse electric (TE_1) and magnetic (TM_1) modes. The TEM and TE_1 modes exhibit orthogonally-polarized E-fields in the waveguide cross-section. If properly excited, they can thus guarantee CP radiation.

In the first part of the thesis, an efficient analysis tool is presented and used to explore the maximum achievable performance in terms of antenna matching and radiation properties. Afterward, design guidelines are carried out, through which a structure is retrieved for operation in Ka-band. The antenna exhibits a high-gain (around 35 dB) over the 27.5-31 GHz band. Also, the axial ratio (AR) is below 3 dB all over the same band for a scan range of up to 20°.

After that, an in-depth analytic study is conducted to acquire know-how for solving dispersion issues suffered by the dual-mode CTS arrays. The modal analysis reveals that an equi-dispersive, dual-ortho-mode propagation is supported by PPWs, whose bounding walls are replaced with surface impedance boundary conditions. In addition, the developed model has been used for design purposes related to the modal filtering of the TM_1 mode.

By virtue of the aforementioned analysis, a dual-linear-polarized CTS array, based on longitudinally-corrugated PPWs, is designed and fabricated using stereolithography technology. The measured results establish a proof-of-concept that dual-polarized radiation is attainable with the dual-mode CTS arrays. The antenna array is planar and exhibits a low profile. A high-gain, as well as a wideband operation, is observed for discretely large field-of-views. This prototype also demonstrates that dual-linear radiation can be obtained without relying on egg-crate configurations that, being based on a traveling-wave working principle, are usually very narrowband. The antenna array performs over a 11.6% relative bandwidth with a radiation efficiency higher than 80%. The antenna scans for polar angles as far as 24°.

A dual-band, linear-to-circular polarization (LP-to-CP) converter with versatile polarization conversion is, afterward, analyzed and synthesized. Firstly, a systematic model is developed for the design. Secondly, a metasurface-based screen is designed by means of full-wave simulations. Finally, a prototype is realized and measured using a quasi-optical test bench. The measurements are in excellent agreement with the simulations.

In conclusion, an extremely low-profile CTS array is designed. The antenna

is fully realized in printed-circuit board (PCB) technology and represents an advanced example of a low-profile antenna. The array is designed to fulfill the requirements of modern SatCom applications, i.e., full coverage of the K/Ka-band. Specifically, the antenna is impedance-matched from 19 to 31 GHz and efficiently performs over a $\pm 20^{\circ}$ scanning range along the H-plane. The radiation efficiency is found to be higher than 70%. Being so broadband and compact, the possibility to combine the antenna with a dual-band polarizing screen is also investigated and discussed.

Keywords: SatCom applications, CTS antennas, quasi-optical beamformer, wideband, wide-angle scanning antenna, metasurface, dual-band LP-to-CP converter, impedance boundary condition, antenna miniaturization.

Contents

Acknowledgments **iv**

Résumé **vii**

Abstract **xi**

1 Introduction **1**

1.1 Overview of SatCom applications and needs 1

1.2 State-of-the-art: SatCom terminal antennas 7

1.2.1 Reflector and lens antennas 7

1.2.2 Phased arrays 8

Vivaldi arrays 9

PUMA arrays 9

Connected arrays 10

TCDA arrays 11

1.2.3 Continuous transverse stub arrays 12

1.2.4 Summary 15

1.3 Novelty of the thesis 16

1.3.1 Dual-mode CTS arrays 17

1.3.2 CTS arrays combined with circular polarizers 18

1.4 Outline of the thesis 19

2 Circularly-Polarized CTS Arrays **23**

2.1 Numerical model of over-moded CTS arrays 24

2.1.1 Active admittance under TEM excitation 29

2.1.2 Active admittance under TE_1 excitation 30

2.2 Numerical validation 32

2.2.1 TEM operation 33

2.2.2 TE_1 operation 34

2.3 Radiation pattern 36
2.3.1 Embedded element pattern 36
2.3.2 Axial ratio 39
2.4 Design guidelines 41
2.4.1 Antenna matching 41
2.4.2 Circular polarization 43
2.5 Over-moded CTS array in Ka-band 44
2.5.1 Input power division for optimal operation 48
2.5.2 Swallow-tail feeder 50
2.5.3 Corporate feed network 54
2.5.4 Pillbox beam-former 56
2.5.5 Antenna performance 60
2.5.6 Fabrication feasibility 64
2.6 Conclusions 65

3 Equi-dispersive dual-mode CTS arrays 67
3.1 Modal analysis 68
3.1.1 PPW loaded with surface impedances: TE modes 70
3.1.2 PPW loaded with surface impedances: TM modes 71
3.2 Equi-dispersive ortho-mode PPWs 72
3.3 Quasi-equidispersive 90°-phase delayed line 75
3.4 Equi-dispersive open-ended radiating stubs 79
3.5 Possible ways to design ED PPWs 81
3.6 Conclusions 82

4 Dual-Polarized, Dual-Mode CTS Array in Ka-Band 84
4.1 Analysis of longitudinally-corrugated PPW 85
4.2 Design of the corporate feed network 95
4.2.1 Open-ended radiating slots 96
4.2.2 Stages of 1-to-2 way power dividers 97
4.2.3 Radiation performance 100
4.3 Antenna architecture 102
4.3.1 Pillbox systems for TEM and TE_1 excitation 103
4.3.2 Fabricated prototype 108
4.4 Experimental results 112

4.5 State-of-the-art dual-polarized antennas 116
4.6 Conclusions 118

5 Dual-band, Orthogonally-Polarized LP-to-CP Converter 120
5.1 Analytic model 123
5.1.1 Design procedure 125
5.1.2 Numerical results 129
5.1.3 Physical design and full-wave results 132
5.2 Prototype and experimental results 135
5.2.1 Measured results for normal incidence 137
5.2.2 Measured results for oblique incidence 141
5.3 State-of-the-art comparison 143
5.4 Advantages and limitations of the model 144
5.5 Conclusions 146

6 Ultra-low-profile CTS array at K/Ka-band 148
6.1 Design procedure and antenna performance 150
6.1.1 Quasi substrate integrated PPW 150
6.1.2 Radiating cell and corporate feed network 153
6.1.3 Pillbox beam-former in PCB technology 156
6.1.4 Coaxial-to-GCPW-to-SIW transition 159
6.1.5 Performance of the antenna module 161
6.2 Prototype and experimental results 164
6.3 CTS array with the dual-band polarizer 169
6.4 Conclusions 175

7 Conclusions 177
7.1 Summary and achievements 177
7.2 Future perspectives 179

A Additional Material on Chapter 2 182
A.1 Entries of the matrices in (2.22) 182
A.2 Spectral Green's function of multi-layer medium 183
A.2.1 Vector potentials for electric and magnetic sources 183
A.2.2 Equivalence with transmission line theory 184
A.2.3 Spectral Green's function for magnetic source 185

B Complements on the study outlined in Chapter 3 **188**

B.1 Characteristic equation of TE modes 188

B.2 Characteristic equation of TM modes 190

B.3 Properties of Helmholtz operator with IBCs 191

B.3.1 Surface-wave modes in PPWs with IBCs 195

TM modes 195

TE modes 197

C Additional Details about Chapter 5 **199**

C.0.1 Closed form of Y_{s1} 199

C.0.2 Closed form of Y_{s2} 201

Bibliography **202**

List of publications **218**

About the author **221**

List of Figures

1.1 Summary of the SatCom links over the years. A graphic illustration shows the needed antenna modules to guarantee the RF communication for the different satellite orbits. 2
1.2 (a) Schematic view of the Galileo constellation. (b) Bottom view of the Galileo satellite system. Images courtesy of the European Space Agency [15]. 3
1.3 Frequency allocation of modern SatCom links for both civil and military applications. 4
1.4 Polarization loss factor for three different cases of transmit antenna. The receive antenna is rotated from x-axis to a 45° orientation. 6
1.5 Overview of the reflector and lens antennas, (a) Photograph of a high-gain reflector antenna at Ka-band. (b) Illustration of the homogeneous lens providing circular polarization. Pictures courtesy of [26, 29]. 8
1.6 Overview of the PUMA arrays, (a) Schematic of the array unit cell. (b) Fabricated prototype. Pictures courtesy of [34, 35]. . . 9
1.7 Overview of the Connected arrays, (a) Schematic of the array unit cell. (b) Backside of a fabricated prototype. Pictures courtesy of [4]. 11
1.8 Continuous transverse stub architecture proposed by (a) Lindenblad [49] and (b) Milroy [50]. 13
1.9 CTS antenna arrays proposed by ThinKom. Pictures courtesy of [3]. 13
1.10 E-field distribution in the cross section of an over-moded PPW. From left to right: TEM, TE_1 and TM_1 modes. 17

1.11 Dual-band, orthogonally-polarized SatCom systems. (a) Two apertures are used to receiving/transmitting LHCP and RHCP radiations separately in two non-adjacent bands. (b) One only aperture covering the K-/Ka-band is used in combination of a dual-band circular polarizer. 18

2.1 Geometry of the problem under analysis. The array consists of open-ended stubs, parallel-fed by over-moded PPWs. The long slots radiate into a multi-layered medium. Only three dielectric slabs are shown for the sake of clarity. (a) Perspective view. (b) Cross section in the xz-plane. 24

2.2 Simulation setup of the unit cell of over-moded CTS arrays. The structure is periodic along x- and y-axes. One dielectric layer of relative permettivity ϵ_{r2} is placed on the top of the radiating slots. 33

2.3 Active impedance for TEM-mode excitation versus frequency along the plane at $\phi = 90°$ for $\theta_0 = 30°$. The parameters used in the simulation are $a = 0.5c/\left(f_{min}\sqrt{\epsilon_{r1}}\right)$, $d = 1.07a$, $h = 0.5c/\left(f_{min}\sqrt{\epsilon_{r2}}\right)$, and $Z_{TEM} = \zeta$. 34

2.4 Active impedance for TEM-mode excitation versus frequency along the plane at $\phi = 0°$ for $\theta_0 = 30°$. The parameters used in the simulation are $a = 0.5c/\left(f_{min}\sqrt{\epsilon_{r1}}\right)$, $d = 1.07a$, $h = 0.5c/\left(f_{min}\sqrt{\epsilon_{r2}}\right)$, and $Z_{TEM} = \zeta$. 34

2.5 Active impedance for TE_1-mode excitation versus frequency along the plane at $\phi = 0°$ for $\theta_0 = 30°$. The parameters used in the simulation are $a = 0.5c/\left(f_{min}\sqrt{\epsilon_{r1}}\right)$, $d = 1.07a$, $h = 0.5c/\left(f_{min}\sqrt{\epsilon_{r2}}\right)$, and $Z_{TE_1} = 1/Y_1^{TE}$. 35

2.6 Active impedance for TE_1-mode excitation versus scan angles θ_0 along the plane $\phi = 0°$ at $f_0 = (f_{min} + f_{max})/2$. The parameters used in the simulation are $a = 0.5c/\left(f_{min}\sqrt{\epsilon_{r1}}\right)$, $d = 1.07a$, $h = 0.5c/\left(f_{min}\sqrt{\epsilon_{r2}}\right)$, and $Z_{TE_1} = 1/Y_1^{TE}$. 35

2.7 Active S-parameters for TE_1-mode excitation versus frequency (a) and scan angles θ_0 (b) along the plane $\phi = 90°$ at $f_0 = (f_{min} + f_{max})/2$. The parameters used in the simulation are $a = 0.5c/\left(f_{min}\sqrt{\epsilon_{r1}}\right)$, $d = 1.07a$, and $h = 0.5c/\left(f_{min}\sqrt{\epsilon_{r2}}\right)$. 36

2.8 Polar components of the embedded radiation pattern at the frequency $f_0 = (f_{min} + f_{max})/2$. The parameters used in the simulation are $a = 0.5c/\left(f_{min}\sqrt{\epsilon_{r1}}\right)$, and $d = 1.07a$. 37
2.9 (a), (b) Cartesian components of the radiation pattern and (c) their phase difference at the frequency $f_0 = (f_{min} + f_{max}/2)$. An array of eight radiating slots has been considered. 38
2.10 Axial ratio versus angles θ along the plane at $\phi = 0°$ at $f_0 = (f_{min} + f_{max}/2)$. The slots are air-filled and radiate in free space. The slot width is $a = 0.5\lambda_{max}$ and the array periodicity $d = 1.07a$. 40
2.11 (a) Axial ratio versus frequency along the main planes at $\theta_0 = 30°$ and (b) versus scan angles θ_0 at $f_0 = (f_{min} + f_{max})/2$. The parameters used in the simulation are $a = 0.5c/\left(f_{min}\sqrt{\epsilon_{r1}}\right)$, and $d = 1.07a$. 40
2.12 Maps of the active S-parameter as a function of frequency and the ratio d/a for (a), (c), (e) TEM and (b), (d), (f) TE_1 modes. The air-filled PPWs radiate in free space. Several scan angles in the planes $\phi_0 = 0°$ and $\phi_0 = 90°$ are considered. 42
2.13 Maps of the AR as a function of frequency and the ratio d/a. The air-filled PPWs radiate in free space. (a) Broadside array. (b) Array steering the beam at $\theta_0 = 30°$ along the plane $\phi_0 = 90°$. 44
2.14 3-D view of the finite-size over-moded CTS array. 45
2.15 Maps of the input reflection coefficient as a function of frequency and the scan angles θ_0. The air-filled PPWs radiate in free space. (a) TEM and (b) TE_1 mode operation. The array is steering the beam along the plane $\phi_0 = 90°$. 45
2.16 (a), (b) Polar components of the radiation pattern at the frequency $f_0 = 30$ GHz for different scan angles. (c) Axial ratio versus scan angle θ_0 at the frequency $f_0 = 30$ GHz. The array is steering the beam along the plane $\phi_0 = 90°$. 47
2.17 Axial ratio as a function of frequency and scan angle θ_0. The air-filled PPWs radiate in free space. The array is steering the beam along the plane $\phi_0 = 90°$. 48

2.18 Maps of the AR as function of the power ratio P_{TEM}/P_{TE_1} and (a) frequency for broadside radiation or (b) scan angle θ_0 at the central frequency $f_0 = 30$ GHz. The air-filled PPWs radiate in free space. The array is steering the beam along the plane $\phi_0 = 90°$. 49
2.19 3-D view of the finite-size over-moded CTS array comprising the structure used to feed the two modes. Geometrical parameters: $a = 7.2$ mm, $d = 1.1a$, $p = 2.3$ mm, $a_{in} = 2$ mm, and $d_y = 229.5$ mm. 50
2.20 (a) Geometry of the swallow-tail feeder. The plane-cut Σ_4 is 45°-oriented with respect to x-axis. All dimensions are in given in millimeters. (b) Simulation E-field into the feeder's unit cell. The E-fields lines are plotted at several sections along z-axis. . . 51
2.21 Unit cell of the over-moded CTS array. The structure is periodic along x- and y-axes. Period boundary conditions are placed on the lateral faces of the cell. Finally, a Floquet's port is placed on the top of the air box to account for the radiated fields in a periodic environment. Geometrical settings: $a = 7.2$ mm, $d = 1.1a$, $a_{in} = 2$ mm, and $a_{out} = 4.66$ mm. 52
2.22 Simulated active reflection coefficient of the CTS array's unit cell. The transmission coefficient is also reported in order to observe the input power's division between the TEM and TE_1 modes. The results refer to broadside radiation. 53
2.23 Simulated axial ratio of the CTS array's unit cell as a function of the frequency and scan angle θ_0. The antenna array is steering the beam along the yz-plane [see Fig. 2.21]. 54
2.24 Cross sectional view of the over-moded CTS array along the xz plane-cut. The antenna architecture comprises $N = 32$ radiating slots and a parallel feed network made of 1:2 power dividers in PPW technology. 54
2.25 Calculated directivity patterns of the over-moded CTS array at 29 GHz. (a) yz-plane. (b) xz-plane. 55
2.26 1-to-2 way, equal split power divider. All dimensions are given in millimeters. 55

2.27 E-field distribution along y-axis in the upper PPW of the pillbox system. The parabola is illuminated by the in-focus horn for boresight radiation. λ_0 is the free-space wavelength at 29 GHz. . 57
2.28 Computed radiation pattern at 29 GHz using an analytic calculation. The simulated E-field of the pillbox system has been used as windowing function. 57
2.29 E-field distribution along y-axis in the upper PPW of the pillbox system. The parabola is illuminated by a displaced horn with respect to the focus in order to steer the beam around $\theta_0 = 10°$. λ_0 is the free-space wavelength at 29 GHz. 58
2.30 Computed radiation pattern at 29 GHz using an analytic calculation. The pointing angle of the array is about 10°. The simulated E-field of the pillbox system has been used as windowing function. 59
2.31 3-D view of the antenna architecture. All dimensions are given in millimeters. 59
2.32 Simulated results of the over-moded CTS array in Ka-band. (a) Reflection coefficient. (b) Axial ratio. The antenna array scans along the yz-plane by displacing the input horn in the y-axis direction, as indicated in Fig. 2.31. 60
2.33 Simulated and computed radiation patterns of the over-moded CTS array at 29 GHz. (a) and (b) Broadside radiation. (c) and (d) Pointing angle θ_0. The antenna array performs beam scanning along the yz-plane by displacing the input horn in the y-axis direction, as indicated in Fig. 2.31. 61
2.34 Simulated gain at 29 GHz. The pointing angle of the array is about 10°. The antenna array performs beam scanning along the yz-plane by displacing the input horn in the y-axis direction, as indicated in Fig. 2.31. 62
2.35 Simulated RHCP patterns as function of the elevation angle θ and frequency. The patterns are taken in the yz-plane cut. (a) Broadside radiation. The array steers the main beam at the scanning angle θ_0 (b) 7.5°, (c) 13.8°, and (d) 20°. 63
2.36 Simulated half-power beam-width as a function of the elevation angle θ and frequency. The patterns are taken in the yz-plane cut. 64

2.37 Fabricated 4-slot CTS array using full-metal 3-D printing technology. (a) Perspective and (b) lateral view. 65

3.1 Geometry of the problem under analysis. The structure consists of two parallel plates, infinitely-extended along y-axis, modeled as surface reactance with respect to TE and TM modes. Modes propagate along the z-axis. 69

3.2 Impedance loci of TE and TM modes when the PPW's height is $h = \lambda/2$, where λ is the wavelength at 40 GHz. The characteristic equations are plotted at the operating frequency. The PPW is air-filled (i.e., $\epsilon_r = \mu_r = 1$). 73

3.3 Characteristic equation for (a),(b) TE and (c),(d) TM modes at the frequency f_{max}. The plot is shown in dB, thus the poles are illustrated with dark blue spots. The black circle indicate the visible range ($|k_x| = k$) and red dot markers represent the calculated poles using [87]. The PPW is air-filled. Parameter settings: $h = \lambda_{min}/2$ and $f_{max} = 3f_{co}^{TM}$. 74

3.4 Dispersion diagram of (a) TE and (b) TM modes for a ED PPW. Parameter settings: $h = \lambda_{min}/2$, $f_{max} = 3f_{co}^{TM}$ and $l = \lambda_{min}$. The PPW is air-filled. 75

3.5 Parametric plots of the eigenvalue k_x^{TE-} using equation (3.21) for increasing values of the PPW's lemgth l. The eigenvalue k_x^{TE-} starts being a slow-varying function with frequency when l is as big as a few wavelengths at the highest frequency. Simulation settings: $f_{max} = 2f_{co}^{TM}$ and $h = \lambda_{min}/2$. 77

3.6 Dispersion diagram for (a) $Z_{surf}^{TE} = i\omega L_{\Delta\phi}^{TE}$ and (b) $Z_{surf}^{TE} = i\omega\overline{L_{\Delta\phi}^{TE}}$. Parameter settings: $f_{co}^{TM} = 20$ GHz, $h = \lambda_{min}/2$, $f_{max} = 2f_{co}^{TM}$ and $l = 3\lambda_{min}$. The PPW is air-filled. 78

3.7 Plot of the surface impedance Z_{surf}^{TE} using the corresponding circuit elements as (3.22) and (3.24). 78

3.8 Unit cell of the ED CTS array for (a) TE and (b) TM modes. The width of the slots is $a = 4.28$ mm and the array periodicity is $d = 1.1a$. 79

3.9 Phases of TE and TM modes as a function of the variable z. at 29 GHz 80

3.10 Simulated AR as a function of frequency for ED open-ended stubs. The AR is computed both analytically and using the full-wave simulator [81], showing a very good agreement. 80
3.11 Simulation setup to synthetize the equi-dispersive dual-mode PPWs. 81

4.1 3-D view of a T-junction comprising over-moded PPWs. The height of each PPW is 7 mm. The structure is infinitely extended along y-axis. PEC/PMC boundary conditions are assumed along the xz-planes to take into account the periodicity of the structure along the y-axis. Studying TE_n and $\mathrm{TEM}/\mathrm{TM}_n$ mode excitation requires the use of PEC and PMC boundary conditions, respectively. 86
4.2 Simulated amplitude of the E-field at 30 GHz. The height of the T-junction is 7 mm. (a) TE_1 mode excitation. (b) TEM mode excitation. The simulations were carried out using [81]. 87
4.3 Cross sectional view of LCPPW along (a) xy- and (b) yz-plane. (c) 3-D view. 87
4.4 Characteristic equation of LCPPW for (a), (b) TE and (c), (d) TM modes at the frequency $f_{max} = 2f_{min}$. The plots are shown in dB, thus indicating the poles of characteristic equation with blue spots. The circle indicates the visible range ($|k_x| = k_0$) and red dot markers represent the calculated poles. These poles are found using a root-finding algorithm, e.g., Padé-based procedure [87]. 90
4.5 Calculated dispersion diagram. (a) standard PPW whose height is fixed to $\lambda_{max}/2$ where λ_{max} is the wavelength associated to the lowest operating frequency f_{min}. (b) Longitudinally-corrugated PPW whose dimensions are given by (4.12). 91
4.6 Parametric analysis of the quasi-TE_1 mode dispersion in LCPPW. Swept parameters: (a) p_c and (b) w_c. The LCPPW considers $h_{TEM} = 4$ mm and $h_{TE} = 7$ mm. 92
4.7 Parametric analysis of the quasi-TE_1 mode dispersion in LCPPW. Swept parameters: (a) h_{TE} and (b) h_c. The LCPPW considers $p_c = 0.15\lambda_0$ and $w_c = 0.05\lambda_0$. 92

4.8 3-D view of a T-junction comprising LCPPWs. The geometrical parameters of each LCPPW are $h_{TE} = 0.7\lambda_0$, $h_{TEM} = 0.4\lambda_0$, $p_c = 0.15\lambda_0$ and $w_c = 0.05\lambda_0$. The structure is infinitely extended along y-axis. 93
4.9 Simulated amplitude of the E-field at 30 GHz. The simulated structure is the one depicted in Fig. 4.8. Under quasi-TEM mode excitation: sections (a) Σ_1 and (b) Σ_2. Under quasi-TE_1 mode excitation: sections (a) Σ_1 and (b) Σ_2. The simulations were carried out using [81]. 93
4.10 Simulated transmission coefficient of the structure in Fig. 4.8 as a function of (a) h_{TE} and (b) h_c at 30 GHz. 94
4.11 Cross section of the proposed corporate feed network of the Ka-band dual-polarized, over-moded CTS array. The region occupied by corrugations is depicted in grey. Conversely, the metallic plates are shown in black. 95
4.12 Geometry of the open-ended radiating over-moded stubs. On the left, a cross-sectional view. On the right, a top view comprising E-field lines of the radiating modes. 96
4.13 Active S-parameters of the radiating elements under (a) TEM and (b) TE_1 mode operation for boresight radiation. 96
4.14 Input reflection coefficients at sections P1 to P8 (see Fig. 4.11) for TEM and TE_1 mode excitation for broadside radiation. For the sake of clarity, only port P1 to P4 are reported as the structure is symmetric. 97
4.15 Geometry of the three stages of balanced power dividers that realize the corporate feed network shown in Fig. 4.11. (a) Division stage T3. (b) Intermediate stage T2. (c) First division stage T1. 98
4.16 Simulated reflection coefficient at section T1_P1 of the finite- and infinite-size array. The simulated results accounts for both quasi-TEM and TE_1 mode operations. 99
4.17 Simulated E-field amplitude in the xz-plane for quasi- (a) TEM and (b) TE_1 excitation. 100

4.18 Simulated co-polar component of the radiation pattern at 30 GHz under quasi- (a) TEM and (b) TE_1 mode operation. The results are calculated along the yz-plane and refer to a boresight radiation. A numerical validation using the in-house tool presented in section 2.3 is also reported. 101
4.19 Simulated realized gain of the full-size dual-polarized CTS array when excited by quasi-TEM and TE_1 mode. A comparison with the long slot array stand-alone is also reported. 102
4.20 3-D and cross-sectional views of the designed dual-mode, dual-polarized CTS array. The radiating part of the antenna consists of that presented in Section 4.2, whereas two quasi-optical beamformers are used to excite the quasi- (a) TEM and (b) TE_1 modes, respectively. 103
4.21 Schematic drawing of the pillbox system from a top view. 104
4.22 Schematic illustrating the input feeding horn embedded in the pillbox system under quasi-TE_1 mode operation. (a) Top, (b) side and (c) 3-D view of the horn. (d) Fabricated prototype. . . 105
4.23 Amplitude of E-field in the bottom PPW of the pillbox beamformer for quasi-TE_1 mode. (a) Without and (b) with longitudinal corrugations. These plots refer to the xy-plane cut at $z = h_{TE}/2$. (c) Simulated far-field patterns of Horn 4 [see Fig. 4.21] at 30 GHz. The results are compared to those of quasi-TEM and non-corrugated quasi-TE_1 pillbox systems. 106
4.24 Schematic with main geometrical parameters of the cross section of the two pillbox systems: (a) TEM and (b) TE_1 mode. 107
4.25 Simulated radiation patterns of the open-ended pillbox systems at 30 GHz: (a) TEM and (b) TE_1 scenarios. The plots refer to the xy-plane. 108
4.26 (a) Exploded and (b) assembled view of the antenna architecture when fed by quasi-TE_1 pillbox beamformer. The various blocks are highlighted with different colors. 109

4.27 Detail of the LCPPW fabricated using SLA technology. (a) Building block's detail. (b) Before and (c) after copper plating. Also, photographs of all antenna building blocks of the overmoded CTS array: (a) before and (b) after the metal plating. . 110
4.28 Photographs of the assembled prototype. (a) Qausi TEM pillbox beamformer. (b) Radiating long slot array, (c) Prototype assembly. 111
4.29 Measured reflection coefficient of the designed dual-polarized CTS array: (a) TEM and (b) TE_1 excitation. The reflection coefficient are measured at the input of the seven feeding horns for different beam steering. 112
4.30 Measured radiation patterns (yz-pane cut) of the designed dual-polarized CTS array at 30 GHz when fed by quasi- (a) TEM and (b) TE_1 beamformers. Each beam is normalized to its maximum. 113
4.31 Measured gain patterns as function of frequency and elevation angle in yz-plane. The antenna is fed by the quasi-TEM pillbox beamformer. 114
4.32 Measured gain patterns as function of frequency and elevation angle in yz-plane. The antenna is fed by the quasi-TE_1 pillbox beamformer. 115
4.33 Measured realized gain of the dual-polarized CTS array when alternately-fed by two pillbox beamformers for a proper excitation of quasi- (a) TEM and (b) TE_1 modes. 116

5.1 Exploded view of the dual-band, orthogonally-polarized LP-to-CP converter. The incident waves are linearly polarized at 45° with respect to the orientation of the metal patterns. They are converted into right- and left-hand circularly-polarized waves in two separate bands. The polarizer is a symmetric structure consisting of three patterned metallic claddings (metasurfaces). . . 122
5.2 Geometry of the problem under analysis. Three anisotropic sheet admittances are cascaded along the z-axis. The external sheet admittances are equal. 123
5.3 Frequency response of Y_{s1}^{xx}. According to the sign of $B_{s1,01}^{xx}$, the frequency response of Y_{s1}^{xx} is assumed to be that of an inductor of a capacitor, refer to (5.11). (a) $B_{s1,01}^{xx} < 0$. (b) $B_{s1,01}^{xx} > 0$. . . 126

5.4 Frequency response of $Y_{sm}^{\psi\psi}$. According to the sign of $B_{sm,01}^{\psi\psi}$ and $B_{sm,02}^{\psi\psi}$, the frequency response of $Y_{sm}^{\psi\psi}$ is assumed to be that of a LC-series, refer to (5.16), (5.17) and (5.18). (a) $B_{sm,01}^{\psi\psi} > 0$ and $B_{sm,02}^{\psi\psi} < 0$. (b) $0 < B_{sm,01}^{\psi\psi} < B_{sm,02}^{\psi\psi}$. (c) $B_{sm,01}^{\psi\psi} < B_{sm,02}^{\psi\psi} < 0$. . . 128

5.5 Contour plots of the absolute value of (a) axial ratio and (b) transmission coefficient as a function of frequency and ϕ_{01}^{xx}. The dashed red line indicates the chosen operating point for the design. 130

5.6 Numerical results for the dual-band, orthogonally-polarized LP-to-CP converter with $\phi_{01}^{xx} = 82.5°$. Axial ratio and transmission coefficients for both RHCP and LHCP are plotted in two bands: (a) 17-21 GHz and (b) 27-31 GHz. 130

5.7 Equivalent circuit models of the structure. Networks for x- and y-polarized waves are analyzed separately. 131

5.8 Patterned metallic geometries of the metasurfaces' unit cell: (a) outer and (b) inner sheets. All dimensions are given in millimeters. The simulated susceptances for the patterned metallic geometries are shown in (c)-(e) for x- and (d)-(f) for y-polarized fields. The black and grey dot markers indicate the desired design values at the frequency f_{01} and f_{02}, respectively. 133

5.9 (a) Simulation setup of the polarizer's unit cell. A comparison between the circuit network and full-wave simulations [81] is reported. (b) Transmitted LHCP and RHCP. (c) Axial ratio. (d) Total transmission. The full-wave simulations considers a normal incidence onto the polarizer. Besides, the incident E-field is linearly-polarized in the direction $\hat{\alpha} = (\hat{x} \pm \hat{y})/\sqrt{2}$. 134

5.10 (a) PCB stack-up of the polarizer. (b) Fabricated prototype. The overall size of the board is $123.74 \times 123.74 \times 3.14$ mm^3. The outer metal pattern is highlighted by a zoomed-in photograph's detail. 136

5.11 Schematic drawing of the experimental setup used to measure the polarizer: quasi-optical test-bench [133]. 137

5.12 Comparison between measured and full-wave performance of the polarizer. (a) Transmitted LHCP and RHCP. (b) Axial ratio. (c) Total transmission of the polarization converter. The measurements refer to a normal illumination of the DUT. 138
5.13 (a) Phase difference $\Delta\phi = \phi^{yy} - \phi^{xx}$ comparison between measurements and simulations. Percentage error of measured data in the (a) downlink and (b) uplink of the K/Ka-band. 139
5.14 Tolerances effects of (a) d and (b) ϵ_r on AR using ECMs. The nominal values of d and ϵ_r are varied by fabrication tolerances provided by Rogers Corporation [134]. 140
5.15 Field orientation of the two scenarios considered in the measurements: (a) TE and (b) TM illumination. 141
5.16 Measured performance of the polarization converter under different incident angles in the βz-plane where $\hat{\beta} = \hat{\alpha} \times \hat{z}$, see Fig. 5.11. (a)-(c) Axial ratio. (b)-(d) Total transmission. Both vertical (TE) and horizontal (TM) E-field illuminations are considered. 142
5.17 (a) AR versus frequency for different substrate's thicknesses d. (b) Related circuit parameters. 145
5.18 (a) AR versus frequency for different substrate's dielectric constants ϵ_r. (b) Related circuit parameters. 146

6.1 Perspective view of the antenna architecture from the (a) lateral and bottom (b) views. The orange and grey colors indicate the copper and the substrates, respectively. Dimensions are given in millimeters. 149
6.2 Perspective view of a quasi substrate integrated parallel-plate waveguide. Geometrical parameters: $D = 0.3$ mm and $P = 0.6$ mm. 150
6.3 Dispersion diagram of the quasi-SI PPW shown in Fig. 6.2. The structure's geometrical parameters are: $D = 0.3$ mm, $P = 0.6$ mm, $a = 2.13$ mm, $\epsilon_r = 2.2$, and $d_z = 1.1$ mm. 151
6.4 (a) Cross-section of the quasi-SI PPW in the xz-plane cut. (b) Simulated insertion losses of the quasi-SI PPW. The vias' diameter is $D = 3$ mm. All other dimensions are given in millimeters. 152

6.5 Simulation setup of the radiating cell of the CTS array in PCB technology. The unit cell's performance has been studied using a full-wave simulator [72] in a periodic configuration. Geometrical parameters: $a = 2.13$ mm, $d = 2.73$ mm, $l = 1.544$ mm, $d_z = 0.558$ mm, $D = 0.3$ mm, $P = 0.6$ mm, and $\epsilon_r = 2.2$. 153
6.6 Simulated active reflection coefficient of the array's unit cell. The results are proposed for four beam directions along the yx-plane (H-plane). The simulation setup is depicted in Fig. 6.5. 154
6.7 Schematic drawing of the CFN made of 1-to-2 way power splitter network using quasi-SI PPW technology, as seen in the cross-section along the xz-axis. The dashed blue arrows depict the Poynting's vector of propagating waves in the structure. All dimensions are given in millimeters. 155
6.8 Simulated reflection coefficient of the CFN at section AA'. The array steers its main beam in the broadside direction. 156
6.9 Schematic of the quasi-optical system as seen from a top view. All the dimensions are given in millimeters. 156
6.10 Simulated magnitude of the field in the substrates (a) S1 and (b) S2. The parabola is illuminated by the Horn #1. The field is normalized to its maximum. 157
6.11 Simulated E-field in the substrates S2 as function of the variable y, when the parabola is illuminated by the horns (a) #1 and (b) #2. The radiating slots are centered at $y = 0$. λ_0 is the wavelength at 29 GHz. 158
6.12 Schematic drawing of the 3-D view of the coaxial-to-GCPW-to-SIW transition. The orange color is used to indicate the copper and the grey one stands for the connector's metal. Finally, the substrate is illustrated in green. 160
6.13 Schematic drawing of the top view of the coaxial-to-GCPW-to-SIW transition. The grey color is used to indicate the connector's metal. The orange and green colors illustrate the copper and the substrate, respectively. All dimensions are given in millimeters. . 160
6.14 Simulated S-parameters of the coaxial-to-GCPW-to-SIW transition. 161

6.15 Simulated input reflection coefficient of the antenna for horn #1 and #2 excitation. 162
6.16 Simulated radiation patterns using the numerical model presented in chapter 2.3.1 and the full-wave software [72] at 25 GHz. Each pattern is normalized to its maximum. (a) Horn #1. (b) Horn #2. 162
6.17 Simulated array directivity as function of the frequency and scan angle for horn (a) #1 and (b) #2 excitation. The patterns are simulated along the yz-plane. 163
6.18 Simulated radiation efficiency and realized gain of the antenna system. 163
6.19 Photographs of the fabricated prototype. (a) Perspective and (b) bottom views. (c) Antenna adjusted on a plastic support. 164
6.20 Measured reflection coefficients of the CTS array in PCB technology. 165
6.21 Measured normalized patterns at different frequencies. (a)-(f) Horn #1 excitation. (g)-(l) Horn #2 excitation. 166
6.22 Measured (a,c,e) co- and (b,d,f) cross-polarization patterns versus the frequency and the angle θ along the H-plane. 167
6.23 Measured (a) co- and (b) cross-polarization patterns versus the frequency and the angle θ along the E-plane. 168
6.24 Schematic of the simulation setup. The CFN of the array is simulated in a periodic environment and three electric sheet admittances are placed on the top of the radiating aperture, at a distance h. All the dimensions are given in millimeters. 169
6.25 Simulated axial ratio (AR) and reflection coefficient (at section AA') of the structure in Fig. 6.24. The gray areas indicate the achieved bands of operation. The latter are defined as the frequency ranges for which AR$<$ 3 dB and the reflection coefficient is below -10 dB. The array is pointing the main beam at broadside. 171
6.26 Photograph of the prototyped CTS array in PCB technology, used in combination with the dual-band polarizer shown in Fig. 5.10(b). 171

6.27 Measured axial ratio of the prototype shown in Fig. 6.26. The axial ratio is reported as function of the angle θ in the yz-plane and the frequency. Horn (a) #3, (b) #2 and (c) #1 excitation. . 172
6.28 Measured radiation patterns of the structure in Fig. 6.26. The radiation patterns are reported in the (ξ, ζ) space. Horn (a-b-c) #3, (d-e-f) #1 and (g-h-i) #2 excitation. The patterns are measured at 29 GHz. 174
6.29 Measured axial ratio as a function of the frequency. The axial ratio is computed in the pointing direction of the array and it is associated with the RHCP pattern. 175

A.1 Equivalent transmission line problem to obtain the normalized voltages (i.e., v_{TM} and v_{TE}) and currents (i.e., i_{TM} and i_{TE}). The unitary voltage generator is placed at the discontinuity $z = 0$. The height of each dielectric layer is indicated with h_n where $n \in \mathbb{N}^+$. 187

B.1 Generic waveguide cross-section. The waveguide contour is $\partial\Omega$. The structure has a cylindrical symmetry, i.e., the waveguide cross-section Ω is invariant along z-axis. Finally, $\hat{n}$ is the unitary vector normal to $\partial\Omega$, outwardly directed with respect to Ω. . . . 192
B.2 Impedance loci of TM modes when the PPW's height is $h = \lambda_{min}/2$, where λ_{min} is the wavelength at the highest frequency. The characteristic equations are plotted at the maximum frequency of $f_{max} = 40$ GHz. The PPW is air-filled (i.e., $\epsilon_r = \mu_r = 1$). The dot markers indicate the calculated eigenvalues using [87]. 196
B.3 Characteristic equation for TM modes at the frequency f_{max}. The plot is shown in dB, thus the poles are illustrated with dark blue spots. The black circle indicates the visible range ($|k_x| = k$) and red dot markers represent the calculated poles using [87]. The PPW is air-filled and its height is $h = \lambda_{min}/2$. 196

B.4 Impedance loci of TE modes when the PPW's height is $h = \lambda_{min}/2$, where λ_{min} is the wavelength at the highest frequency. The characteristic equations are plotted at the maximum frequency of $f_{max} = 40$ GHz. The PPW is air-filled (i.e., $\epsilon_r = \mu_r = 1$). The dot markers indicate the calculated eigenvalues using [87]. 197

B.5 Characteristic equation for TE modes at the frequency f_{max}. The plot is shown in dB, thus the poles are illustrated with dark blue spots. The black circle indicate the visible range ($|k_x| = k$) and red dot markers represent the calculated poles using [87]. The PPW is air-filled and its height is $h = \lambda_{min}/2$. 198

List of Tables

1.1 Summary of modern SatCom requirements. 6
1.2 State-of-the-art of SatCom terminals. 16

2.1 Performance of proposed CTS solution 41
2.2 Geometrical parameters of the 1:2 power dividers for each stage. All dimensions are given in millimeters 56

4.1 Main Parameters of the Power Dividers. 99
4.2 Main Parameters of the Pillbox Systems. 105
4.3 Measured XPD of the Dual-Polarized CTS Array in the Band 29-32 GHz. 115
4.4 State-of-the-art dual-polarized antennas. 117

5.1 Circuit elements obtained by using the analytic method proposed in Chapter 5.1 131
5.2 Measured fractional bandwidths of the proposed dual-band, orthogonally-polarized LP-to-CP converter under normal plane-wave incidence 141
5.3 Measured fractional bandwidths of the proposed dual-band, orthogonally-polarized LP-to-CP converter under oblique plane-wave incidence. 143
5.4 Comparison with state-of-the-art dual-band, orthogonally-polarized LP-to-CP converters. 143

List of Abbreviations

SatCom	**Sat**ellite **Com**munication
SOTM	**S**atellite communication **O**n-**T**he-**M**ove
CTS	**C**ontinuous **T**ransverse **S**tub
CP	**C**ircular **P**olarization
AR	**A**xial **R**atio
PPW	**P**arallel **P**late **W**aveguide
LCPPW	**L**ongitudinally-**C**orrugated **P**arallel **P**late **W**aveguide
Quasi-SI PPW	**Quasi**-**S**ubstrate-**I**ntegrated **P**arallel **P**late **W**aveguide
CFN	**C**orporate **F**eed **N**etwork
TEM	**T**ransverse **E**lectro**M**agnetic
TE	**T**ransverse **E**lectric
TM	**T**ransverse **M**agnetic
MMT	**M**ode **M**atching **T**echnique
GF	**G**reen's **F**unction
BC	**B**oundary **C**ondition
PEC	**P**erfect **E**lectric **C**onductor
PMC	**P**erfect **M**agnetic **C**onductor
ED	**E**qui-**D**dispersive
CE	**C**haracteristic **E**quation
ACBC	**A**symptotic **C**orrugation **B**oundary **C**ondition
LP-to-CP	**L**inear-**to**-**C**ircular **P**olarization
TL	**T**ransmission **L**ine
FSS	**F**requency **S**elective **S**urface
ECM	**E**quivalent **C**ircuit **M**odel
RHCP	**R**ight-**H**and **C**ircular **P**olarization
LHCP	**L**eft-**H**and **C**ircular **P**olarization
PCB	**P**rinted **C**ircuit **B**oard
DUT	**D**evice **U**nder **T**est

Physical Constants

Speed of Light	$c_0 = 2.99792458 \times 10^8$ ms^{-1}
Vacuum Permittivity	$\epsilon_0 = 8.854187817 \times 10^{-12}$ F/m
Vacuum Permeability	$\mu_0 = 4\pi \times 10^{-7}$ H/m
Free-Space Impedance	$\eta_0 = 120\pi\ \Omega$

List of Symbols

$\mathbf{E}$	Electric Field	V/m
$\mathbf{H}$	Magnetic Field	A/m
$\mathbf{M}$	Magnetic Current	V
P	Power	W ($\mathrm{J\,s^{-1}}$)
ω	Angular Frequency	rad
f	Frequency	Hz ($\mathrm{s^{-1}}$)
λ	Wavelength	$\mathrm{m^{-1}}$
β	Propagation Constant	rad/m
α	Attenuation Constant	rad/m
k	Angular Wavenumber	$\mathrm{m^{-1}}$
η	Characteristic Impedance	Ω
ϵ_r	Relative Permittivity	a-dimensional
μ_r	Relative Permeability	a-dimensional
i	Imaginary Unit	a-dimensional
∇	Laplace Operator	a-dimensional
$\nabla\cdot$	Divergence Operator	a-dimensional
$\nabla\times$	Curl Operator	a-dimensional
$\mathcal{H}\{\cdot\}$	Helmholtz Operator	a-dimensional
$\delta(\boldsymbol{r})$	Dirac Delta Function	a-dimensional
δ_{ij}	Kronecker Delta Function	a-dimensional

Dedicated to my family...

Alla mia famiglia...

Chapter 1

Introduction

1.1 Overview of SatCom applications and needs

Satellite communications (SatCom) consist of Earth-orbiting systems capable of receiving electromagnetic signals and relaying them back to the ground. They have been a significant part of domestic and global communications since the 1970s and have been rapidly evolving over the last decades. The first SatCom links have been allocated at C-band (4-8 GHz). As an example, the Anik A have been the world's first national domestic satellites, launched on November 9^{th}, 1972, and retired on July 15^{th}, 1982, for Canadian television broadcasting [12]. Each satellite, equipped with 12 C-band transponders, has been placed in geosynchronous or geostationary (GEO) orbits, about 36,000 km above the Earth [13]. Since the rotation period of GEO spacecrafts is the same as the Earth, they appear to be fixed in a stationary point with respect to the ground. As consequence, the on-board antennas required to these applications usually do not perform scanning [see Fig. 1.1] and a maximum of three satellites is enough for a full coverage of the Earth's surface. These satellites have been intensively used for a large variety of conventional services, such as direct-to-home television and/or broadcasts. Over the years, the quest for big data has become urgent and, consequently, the run-up to more efficient and complex technologies. The on-board antennas have been designed to cover narrower areas on the Earth, as depicted in Fig. 1.1. Specifically, the more directive the on-board antenna becomes and the bulkier it is, whereas the ground terminal device reduces its size accordingly, as illustrated in Fig. 1.1.

Nowadays, the huge demand for high-speed links continues growing at an ever-increasing rate and leads to investigating cutting-edge antenna solutions to

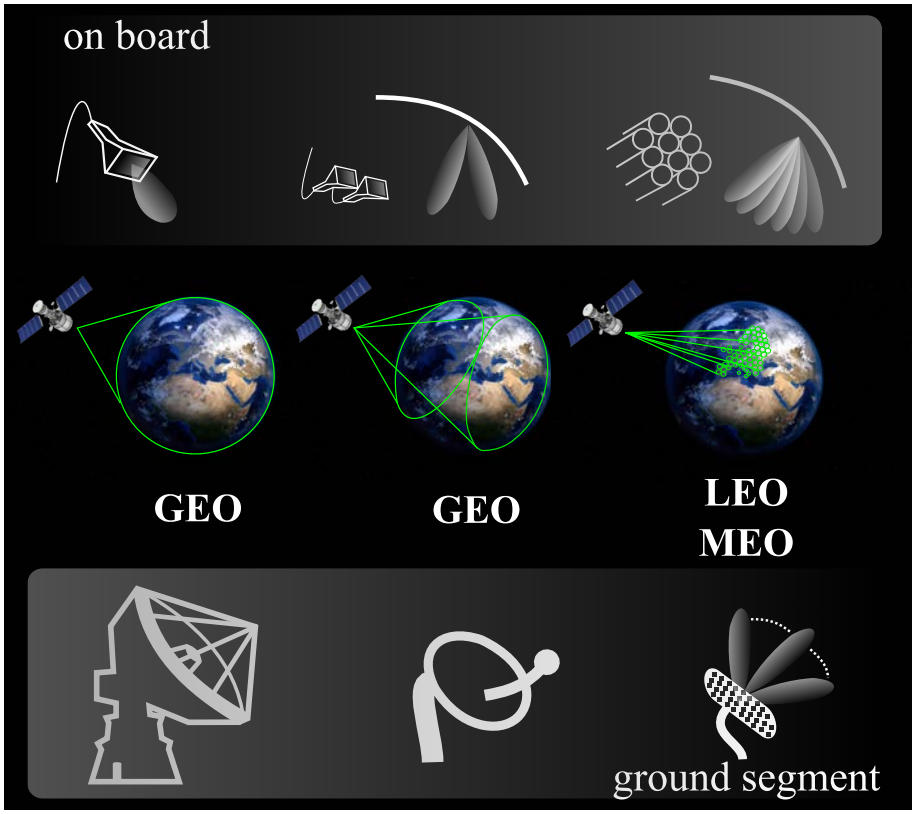

FIGURE 1.1: Summary of the SatCom links over the years. A graphic illustration shows the needed antenna modules to guarantee the RF communication for the different satellite orbits.

fulfill the modern SatCom requirements. As a matter of fact, GEO solutions are to be overcome by Low (LEO) and Medium (MEO) Earth Orbit communication systems, which are based on orbiting spacecrafts flying at a closer distance to the Earth (<1,500 km for LEO and 6,000-20,000 km for MEO). These SatCom links guarantee a reduced latency with respect to GEO ones, i.e., 1-4 ms instead of 125 ms. Note that the latency in SatComs has a negligible impact on standard services, such as TV broadcasting or satellite telephones, etc., whereas non-negligible effects are experienced for the new millennium applications, e.g., internet-of-things, real-time video rendering, navigation, etc. Furthermore, the LEO/MEO links should also support the frequency and polarization re-use over different beams. Being closer to the Earth's surface, LEO and MEO satellites also require less power as compared to GEO's and are generally deployed in satellite constellations. Each spacecraft, in fact, provides a limited coverage area on the Earth that moves as the satellite flies at a significant angular velocity, needed to maintain its orbit. For instance, the SpaceX's Starlink mega constellation of satellites consists of 12,000 internet satellites placed in 550 km

orbits at the zenith, flying at an angular velocity of 0.79 deg/s [11, 14]. A further representative example of satellite constellation is the European global navigation satellite system (GNSS), namely Galileo [15]. The Galileo constellation is a project created by the European GNSS Agency (GSA) and comprises 24 satellites along three MEO planes, plus two spare satellites per orbit [see Fig. 1.2(a)]. The Galileo space segment takes 14 hours to orbit the Earth and

(a) (b)

FIGURE 1.2: (a) Schematic view of the Galileo constellation. (b) Bottom view of the Galileo satellite system. Images courtesy of the European Space Agency [15].

8 active satellites are dedicated to each MEO orbit. Among a prominent RF hardware, each satellite includes also two phased arrays at L- and C-band, respectively. The antenna array at L-band transmits the navigation signal to the Earth in the 1.2-1.6 GHz frequency range by means of a multi-beam radiation. It is the main on-board antenna and it is placed at the bottom of each satellite, as it can be seen in Fig. 1.2(b). Two sensors are used to ensure that the satellite is pointing toward the Earth. The C-band antenna receives the navigation messages from the ground station (up-link), whereas a further L-band SAR antenna emits distress signals to the rescue coordination centre. This representative example is intended to show the complexity of a modern flying SatCom platform. In general, a LEO/MEO constellation's satellite must carry multi-beam antennas [see Fig. 1.1], such as phased arrays, lenses or quasi-optical systems [16–20]. This is to achieve a certain coverage of the Earth's surface by combining different beams together. A near-global coverage is usually obtained by placing these satellites in complementary orbital planes so that at least one satellite is visible at any time everywhere on the Earth.

From the ground segment standpoint, the new generation of SatCom terminal antennas must thus ensure a robust link by accurately tracking the satellite [see Fig. 1.1]. Large field-of-views are usually attained with mechanical solutions, e.g., two-axis positioners that adjust the pointing direction of a fixed-beam terminal antenna (typically a reflector) toward the satellite. The engine responsible for the beam steering might degrade the overall performance in terms of re-positioning velocity, as well as wear and tear. Furthermore, the bulkiness of such a solution is unappropriated to SatCom on-the-move (SOTM) applications, e.g., high-speed trains and aircrafts, where lightweight and low-profile antenna solutions are needed. For these reasons, antenna modules performing a wide-angle scan have been gaining interest during the last years [1]. Hybrid electro-mechanical antennas may also represent an alternative, as they achieve two-dimensional (2-D) scanning by combining a one-dimensional (1-D) wide-scanning antenna with a rotating platform.

For high-throughput satellite systems, modern SatCom terminal antennas are also required to achieve a wideband operation. A large range of SatCom links is currently allocated at Ku-band (12-18 GHz). Due to frequency channels saturation, modern communication links start targeting higher frequency

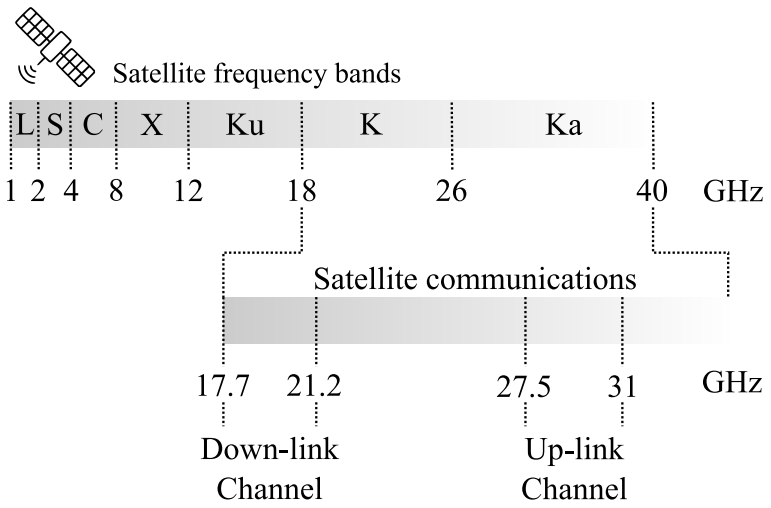

FIGURE 1.3: Frequency allocation of modern SatCom links for both civil and military applications.

bands, e.g., K- and Ka-band [21, 22]. As shown in Fig. 1.3, recent K/Ka-band SatCom applications use the 17.7-21.2 GHz band associated with the up-link channel, whereas the down-link one is approximately allocated at 27.5-31 GHz. Gain and directivity being equal, the K/Ka-band antennas exhibit reduced sizes

with respect to the ones at Ku-band. The drawback lies in the complexity of designing wideband antenna modules and, in addition, the atmospheric attenuation of electromagnetic waves is higher at those frequencies [23].

Last but not least, this generation of SatCom ground terminals is often requested to achieve circularly-polarized radiation. Circular polarization (CP) is, indeed, essential to increase the link reliability and robustness for long-range signal transmissions. Circularly-polarized radiation represents a key asset to suppressing the polarization mismatch, experienced by the signal while propagating in the atmosphere (e.g., Faraday rotation). To demonstrate this, it is worth defining the polarization loss factor (PLF) [24], as follows

$$PFL = |\hat{\rho}_{RX} \cdot \hat{\rho}_{TX}|^2 \tag{1.1}$$

where $\hat{\rho}_{RX}$ and $\hat{\rho}_{TX}$ are the polarization unit vectors of the receive (RX) and the transmit (TX) antennas, respectively. The PLF attains a value of 1, if there is no polarization mismatch between the RX and the TX antennas. A PLF equal to 0 indicates a complete polarization mismatch. As a matter of example, let us consider a linearly-polarized RX antenna, whose polarization unit vector rotates from x-axis to a 45°-oriented position with respect to x-axis. Its mathematical expression is given by the following parametric form:

$$\hat{\rho}_{RX} = \frac{\hat{x} + \rho_{RX,y}\hat{y}}{\sqrt{1 + \rho_{RX,y}^2}}, \qquad 0 \leq \rho_{RX,y} \leq 1 \tag{1.2}$$

The PLF is plotted in Fig. 1.4 for three cases of TX antennas with different polarization vectors: $\hat{\rho}_{TX} = \hat{x}$, $\hat{\rho}_{TX} = \hat{y}$, and $\hat{\rho}_{TX} = (\hat{x} \pm i\hat{y})/\sqrt{2}$. As shown in Fig. 1.4, the PLF ranges from 0 to 1 when the TX and RX antennas are both linearly-polarized. Specifically, a complete polarization mismatch is achieved for the orthogonal orientation of TX and RX antennas. On the other hand, if the TX antenna is circularly-polarized, at least half of the conveyed power is constantly received by the terminal. This simple example clearly shows that the CP enhances the reliability of the communication link. The mitigation of multipath fading and errors, resulting from misalignment between TX and RX antennas, represents a further reason to use CP [16]. Reversely, linear polarization is sometimes preferred to CP as it is less sensitive to atmospheric

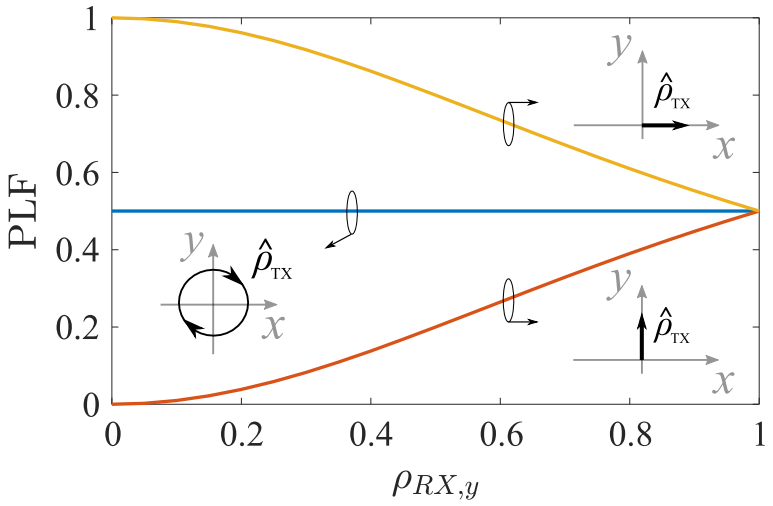

FIGURE 1.4: Polarization loss factor for three different cases of transmit antenna. The receive antenna is rotated from x-axis to a 45° orientation.

effects (rain attenuation), as reported by the International Telecommunication Union (ITU) recommendation BO.791 [25]. However, in the Annex 1 of ITU-R BO.791 [25] is also stated that this advantage of CP may not be significant if compared with linear polarization transmission on or near a 45° plane. Furthermore, it may be difficult to produce good cross-polar response with linear polarization (particularly for elliptical beams) and to transfer to a spare satellite at a different orbital position because of the need to realign the polarization plane [25]. All these reasons lead to the conclusion that circularly-polarized antennas are more suitable for the new generation of high-throughput SatCom terminals whose priority lies in guaranteeing the robustness and versatility of the long-range link.

A table summarizing the requirements of modern SatCom era is shown in Table 1.1. The design of high-efficiency antennas fulfilling the requirements

TABLE 1.1: SUMMARY OF MODERN SATCOM REQUIREMENTS.

	SPECIFICATION
Circular polarization	Axial ratio below 3 dB
Frequency range	Down-link: 17.7-21 GHz Up-link: 27.5-31 GHz
Field-of-view	Elevation from horizon: 20° to 90° Azimuth: 360°
Gain	30 dBi at 20° above the horizon
Low-profile	Body height below 15 cm

in Table 1.1 is non-trivial. Therefore, the work presented in this manuscript

aims at investigating novel antenna solutions performing highly-pure circular or dual-polarized radiation with a low-profile and wideband operation.

1.2 State-of-the-art: SatCom terminal antennas

The aim of this Section is to provide an overview of the state-of-the-art of antennas currently used in the ground segment. In the frame of the SatCom applications, a very large range of antenna solutions can be found in the literature. Given the aforementioned SatCom constraints, an assortment has been done among existing solutions and, particularly, the attention is paid on antennas attaining broadband operation, wide-angle scanning capabilities, and polarization diversity. Two families of antenna devices result to be appealing candidates for the ground segment of modern SatCom links. The first group comprises reflector and lens antennas, whereas the second one is constituted by phased arrays. Both antenna solutions show pros and cons, whose trade-off solution can be engineered accordingly to the specific applications and requirements. From this study, it emerges that the research of novel ground terminals still constitutes a hot topic nowadays; an intense research activity is thus necessary to further enrich the current state-of-the-art solutions.

1.2.1 Reflector and lens antennas

Reflectors constitute a well-known family of antenna systems. A horn antenna is usually employed as feeder, to obtain high directivity after a reflection from a parabolic mirror. They can ensure a broadband operation over a large field-of-view. Reflectors are also very versatile in terms of polarization agility, as they depend on the feeder's characteristics. Wide-angle scanning performance is achieved either with mechanical supports, used to adjust the pointing direction of a fixed beam [26, 27], or by employing feed-through lens combined to an array as feeder [28]. A fixed-beam reflector that attain scanning performances through a mechanical support [26] is shown in Fig. 1.5(a). As it can be seen in Fig. 1.5(a), reflector antennas are very bulky and, consequently, expensive to build. Their field of usage thus reduces, since their encumbrance makes them inappropriate to several SatCom applications, e.g., SOTM.

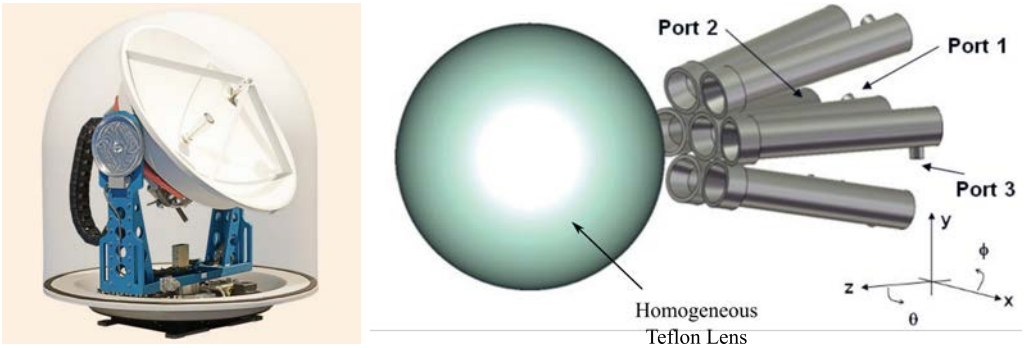

(a) (b)

FIGURE 1.5: Overview of the reflector and lens antennas, (a) Photograph of a high-gain reflector antenna at Ka-band. (b) Illustration of the homogeneous lens providing circular polarization. Pictures courtesy of [26, 29].

Lens antennas may represent an alternative to reflectors in terms of compactness. They have recently arisen interest from the scientific community, owing to their ultra large field-of-view ($\pm 75°$) [18], simplicity to design with tools based on geometrical optics [17], or easy integration as beam-forming network [30]. However, their are mostly known to operate in linear polarization. This point represents a big limitation for modern SatCom applications. The CP can be achieved by designing a homogeneous lens fed by an array of septum polarizers [29], as shown in Fig. 1.5(b). The latter solution is very cumbersome and inappropriate to the ground segment purposes. As for reflectors, the fabrication costs of lens antennas are usually rather high.

1.2.2 Phased arrays

Phased arrays represent an agile solution as antennas for the ground segment. In general, antenna arrays are made of radiating elements, arranged in a planar periodic (or non-periodic) configuration. Each element is connected to a phase shifter, used to provide a certain phase distribution for achieving beam scanning. Generally, this type of antennas can achieve 2-D scanning, without relying on any mechanical beam steering support. On the other hand, the planar feed network usually increases the antenna complexity and degrades its efficiency. In the following, a sorting of phased arrays is investigated and discussed to highlight eventual potentialities and limitations.

Vivaldi arrays

Vivaldi arrays are well-know for their ultra-wideband properties (easily in the order of 120%). They can be also designed to attain dual-polarized radiation with a discrete scan coverage (around ±30°), as reported in [31]. As for most of the phased arrays, their main limitation lies in the feeding system complexity, which limits the ideal achievable bandwidth of the array stand-alone. In fact, slotline-to-microstrip transitions are usually needed in the feed network to lower the antenna profile. A solution to overcome these issues may be found in the balanced antipodal Vivaldi antennas (BAVA) [32]. These antennas are nonetheless too bulky and exhibit relatively high costs. In fact, each radiating element is associated with an active component within the feeding network. Vivaldi arrays usually exhibit also high cross-polarization.

PUMA arrays

The planar ultra-wideband modular antenna (PUMA) arrays represent a clever way to realize the concept of the Wheeler's current sheet [33]. They consist of planar dipoles printed on a ground-backed substrate [see Fig. 1.6(a)]. Each

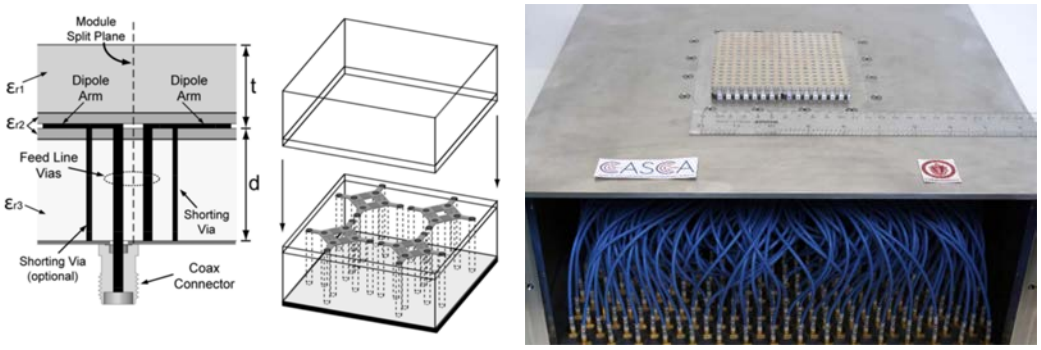

(a) (b)

FIGURE 1.6: Overview of the PUMA arrays, (a) Schematic of the array unit cell. (b) Fabricated prototype. Pictures courtesy of [34, 35].

dipole exhibits a strong capacitive reactance that is used to counteract the inductive one, resulting from the ground plane placed at $\lambda_0/4$ (λ_0 is a wavelength of reference) away from the dipoles. The egg-crate dipole array is fed by an unbalanced feeding mechanism through a pair of shorting vias [refer to Fig. 1.6(a)]. Unbalanced feed lines that feed the balanced dipole arms may result

in a "catastrophic" common-mode resonance, occurring in the middle band. Shorting vias connect the dipole arms to the ground, in such a way to enforce the vertical E-field component to zero. A strategical location for the vias is, hence, selected in order to shift this resonance out of the targeted band. In [35], the proposed PUMA array achieves an ultra-wideband performances, e.g., 7-21 GHz (100%). This antenna also offers a significant field-of-view (up to $\pm 45°$) and can be realized by employing only one printed-circuit board (PCB) layer [34]. The prototype in [35] attains also a dual-polarized radiation. The work in [36] presents an enhancement in PUMA architectures by adding a sub-array as a portion of the periodic original array. This solution reduces the costs and the overall profile of the antenna. Finally, a new class of PUMA arrays has been recently proposed in [37] for attaining a further enhanced bandwidth operation, i.e., 142%.

The drawback of these antennas lies in the feeding network that, in addition to being very costly (a phase shifter is required for each radiating element, as shown in Fig. 1.6(b)), requires also the use of baluns to suppress the common-mode resonance. Furthermore, the small thickness and the low permittivity of the substrate usually result in surface wave phenomena that lead to scan blindness at high frequencies. Finally, PUMA arrays usually suffer from high cross-polarization levels in the D-plane (45°-rotated with respect to the principal planes).

Connected arrays

Among recent phased array solutions, an interesting architecture is offered by connected arrays. They consist of electrically-small dipoles or slots, which are connected and parallel-fed by coaxial cables, arranged in a double mesh grid through a transition from vertical co-planar strip to vertical microstrip lines [see the array unit cell shown in Fig. 1.7(a)]. Connected arrays can efficiently operate over wide impedance-matched bands (around 30%) and can attain dual-polarized radiation [4]. The wideband performance derives from a strong mutual coupling between the connected radiating elements that results in a frequency-independent current, smoothly-distributed over the aperture [38, 39]. Connected arrays often offer good performances while scanning as far as 60° [4]. As shown in Fig. 1.7(a), their design is however non-straightforward, given that

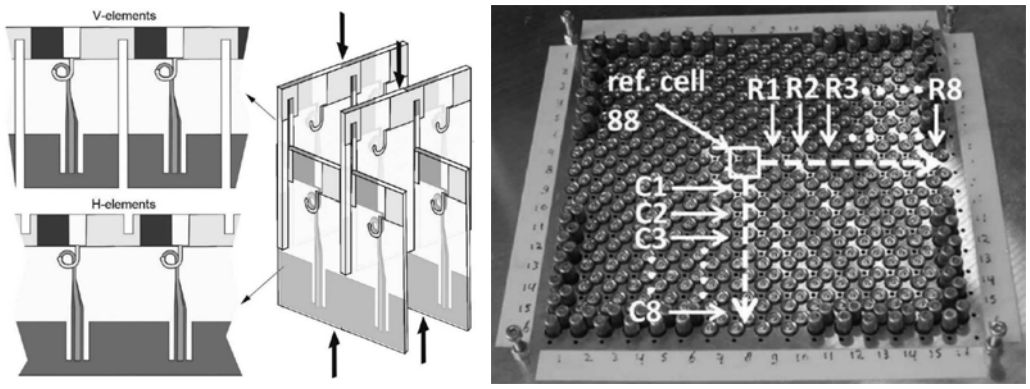

(a) (b)

FIGURE 1.7: Overview of the Connected arrays, (a) Schematic of the array unit cell. (b) Backside of a fabricated prototype. Pictures courtesy of [4].

various vertical cross-connected PCB boards are required for the fabrication. In addition, common-mode rejection loops are needed in combination with baluns for the feeding of each array cell. Radiation leakages may be present too, due to the propagation of undesired surface waves, and artificial dielectric layers (ADL) have been proposed as a solution in [40]. For the sake of completeness, these problems have been overcome by a low-cost planar structure, proposed in [41]. The array exhibits an impedance bandwidth in the 6-15 GHz band and offers a dual-linear polarization for scan angles up to 60° in the H-plane, as well as 80° in the E-plane.

As a drawback, several feeds (one for each radiating element) are required for the antenna supply [see Fig. 1.7(b)], which increase the costs considerably. A transmit/receive module is associated with each feed, thus increasing the number of active devices and related costs.

TCDA arrays

As for connected arrays, the tightly coupled dipole antenna (TCDA) arrays exploit the coupling between horizontal dipoles, placed above a conducting ground plane, and extends the bandwidth and scanning capability of the current sheet array (CSA), previously proposed by Munk [42]. These phased arrays exhibit ultra-wideband and very wide-angle scanning capabilities. Over the years, several architectures have been proposed to work both in single [43] or dual [44] linear polarization. For instance, the prototype in [44] covers the frequency

range from the upper-S to Ku bands (142%) and performs dual-polarized radiation up to 60°. Owing to their lightweight, TCDA arrays suit well as the replacement of multiple antennas. Also, spectral efficiency is possible by reusing intermediate frequencies for inter-satellite communications. As for all phased arrays, the main shortcoming lies in the complexity of the feeding system. Each set of cross-connected dipoles, in fact, requires the use of Marchand baluns, printed on vertical PCB boards, as well as a dedicated coaxial cable.

1.2.3 Continuous transverse stub arrays

From the study outlined in Section 1.2.2, it emerges that phased arrays offer an electronic 2-D scanning, which suits well to the real-time control of the beam direction of the antenna. However, their main shortcoming lies in the feeding system, deemed unsuitable as SatCom terminal due to costs and bulkiness. Attractive alternatives are broadband antennas, used in combination with beamformers or quasi-optical systems as feeding network. Specifically, a large variety of switched-beam devices are now available in the literature, such as beamforming networks (e.g., Butler or Nolen matrices [45, 46]) and/or quasi-optical systems (e.g., Rotman lenses [47] or pillbox couplers [19, 48]). This class of devices can provide a multi-beam radiation without requiring an elevate number of active elements. They can also be used to generate a continuous line source, which is employable to feed various types of antenna's radiating elements, e.g., long slots, metasurfaces, leaky-waves, etc. The following of this manuscript will focus on a class of antennas, the continuous transverse stub (CTS) arrays, that merges the simplicity of quasi-optical beamformers to the broadband and wide-angle scanning capabilities of phased arrays. Note that this antenna solution can offer the scanning along one plane only. The 2-D scanning capabilities are achieved by means of mechanical rotation of the overall module. The main focus of this thesis will be on the engineering of these structures in such a way to achieve circular or dual-linear polarization.

The parallel-fed CTS arrays have been receiving large attention for decades due to their inherent properties, suitable to fulfill the modern SatCom requirements. In 1948, the concept of multiple-slot antenna was patented by Lindenblad [49], whose antenna architecture is shown in Fig. 1.8(a). In 1993, Milroy

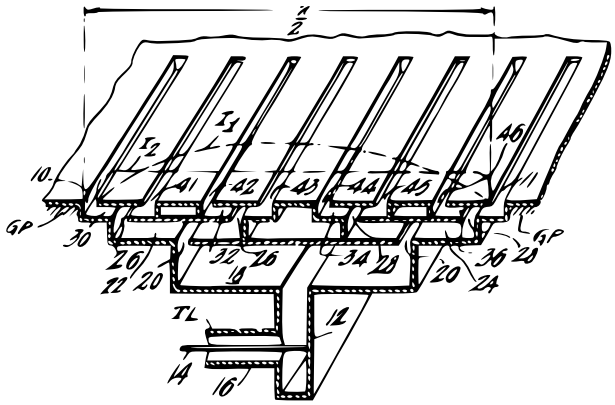

(a) Lindenblad's structure [49].

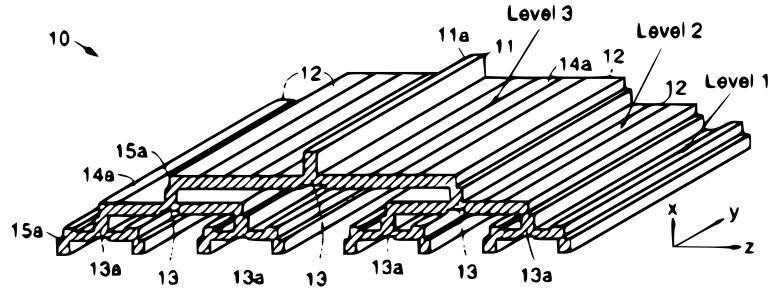

(b) Milroy's structure [50].

FIGURE 1.8: Continuous transverse stub architecture proposed by (a) Lindenblad [49] and (b) Milroy [50].

granted a patent on CTS devices [50], as shown in Fig. 1.8(b), and his structures demonstrated wideband capability with a contained overall profile [50–53]. Starting from the patents [50–53], the most evolved industrial products are today proposed by an American company founded in 2000, namely ThinKom [3]. The latter develops antenna solutions for the aeronautic and space market. In 2018, one of their product has been the first antenna able to track MEO satellites. In the same year, the module Ku3030, shown in Fig. 1.9(a), has been

(a) ThinKom Ku3030.

(b) ThinKom Ka2517.

FIGURE 1.9: CTS antenna arrays proposed by ThinKom. Pictures courtesy of [3].

proposed as an airborne antenna, able to track LEO/MEO satellites. In 2018, the product Ka2517 (shown in Fig. 1.9(b)) has been designed as a solution for LEO/MEO/GEO SatCom applications, attaining a 97.5° field-of-view with switchable circular polarization. The latter is achieved by means of a wideband circular polarizer placed in the very proximity of the radiating aperture. In the open literature, recent contributions [6, 9, 54] have proposed analytic tools to design CTS arrays, achieving wide-angle scanning performance by combining parallel-fed architectures with a continuous line source, i.e., a pillbox system [19, 20, 48]. The proposed antenna architecture consists of long radiating slots, parallel-fed by a corporate feed network (CFN) made of 1-to-2 way T-junctions in parallel plate waveguide (PPW) technology [refer to Fig. 1.8]. Unlike the structure in Fig. 1.8(a), the CFN in [6] is connected to a pillbox system, in such a way that each slot is illuminated by a uniform field distribution with a progressive phase. This feeding system enables the long slot array to steer the beam along the H-plane. Moreover, the architecture recently proposed in [55] has demonstrated a drastic reduction of the sidelobe levels (SLL) in the E-plane as well. Basically, this is achieved by employing a non-uniform CFN that provides a Gaussian-like field distribution along the periodic slots.

Standard CTS arrays exhibit wideband capabilities, due to the mono-modal property of the CFN. Indeed, the working principle of CTS arrays relies on the radiation of a transverse electromagnetic (TEM) mode, which is the only field distribution supported by the radiating slots. TEM modes do not exhibit cut-off frequency [56], thus the active impedance of the long slots remains fairly constant over a very large frequency range [5]. This is the consequence of the inherent ultra-wideband property of long slot arrays [57]. In fact, the active impedance of a generic long slot array is given by

$$Z_{act}^{long\ slot} = \frac{d_y}{d_x}\frac{k_0\eta_0}{2}\sum_{m_x=-\infty}^{+\infty}\frac{\mathrm{sinc}^2(k_{xm}t/2)}{k_0^2-k_{xm}^2\sum_{m_y=-\infty}^{+\infty}\frac{J_0(k_{ym}w/2)}{\sqrt{k_0^2-k_{xm}^2-k_{ym}^2}}} \tag{1.3}$$

where $J_0(k_y)$ is the Bessel function of first kind (order zero) and d_x and d_y are the double array periodicity. Also, k_0 and η_0 are the free-space wavenumber and impedance, respectively, t is the width of the line source and w that of the radiating slots. Finally, k_{xm} and k_{ym} are transverse eigenvalues associated to the corresponding Floquet modes. When the attention is restricted at low

frequencies, equation (1.3) can be simplified [57], thus yielding to

$$Z_{act}^{long\ slot} \xrightarrow{f\to 0} \frac{d_y}{d_x}\frac{\eta_0}{2}\frac{\cos\theta}{1-\sin^2\theta\sin^2\phi} \tag{1.4}$$

where θ and ϕ indicate the elevation and azimuth pointing angle of the array, respectively. Equation (1.4) shows that the active impedance of the radiating slots is constant in low frequency ranges, thus achieving "infinite" impedance bandwidth in theory [58]. It is possible to achieve the impedance matching condition, by playing with the array dimensions d_x and d_y. Given that $Z_{act}^{long\ slot}$ is frequency-independent at low frequencies, the impedance matching is thus valid over a large frequency range.

Although the mono-modal operation of CTS arrays broadens the impedance matching, it also represents a limitation in attaining CP. Standard CTS arrays are, indeed, inherently linearly-polarized. Existing solutions to provide CP typically rely on add-on linear-to-circular polarization (LP-to-CP) converters, placed in proximity of the radiating aperture [59]. This solution is straightforward but can degrade the overall performance of the CTS array, by increasing insertion losses and narrowing the field-of-view of the antenna. An alternative solution is proposed in [60]. This consists of two orthogonally-oriented, series-fed long slot structures. The array resembles egg-crate configurations that radiate dual-polarized fields using two separate apertures. The solution proposed in [60] represents a step forward in this field of study, yet it is extremely narrowband ($\sim$ 1 % of fractional bandwidth) and does not perform scanning.

1.2.4 Summary

The reported state-of-the-art has extensively detailed a limited range of SatCom terminal antennas among a large set of existing solutions. In particular, the main focus has concerned two types of solutions: phased arrays and long slot arrays fed by a quasi-optical beamformer. A comparison between the various solutions is summarized in Table 1.2. Phased array solutions show very good performances in terms of bandwidth and scanning range. Different types of wideband arrays are present in the literature [4, 31, 35, 37, 41, 44], but all of them are limited by the complexity of the feeding system. The latter, in fact,

TABLE 1.2: STATE-OF-THE-ART OF SATCOM TERMINALS.

REF.	ARCHITECTURE	POL.	BANDWIDTH	FEEDING SYSTEM	SCAN RANGE	POWER	COSTS	YEAR
[31]*	Vivaldi array	Dual LP	120%	Grid of connectors	±30° (2-D)	$\propto N^2$	High	2016
[35]*	PUMA array	Dual LP	100%	Grid of connectors	±45° (2-D)	$\propto N^2$	High	2012
[37]*	PUMA array	Dual LP	142%	Grid of connectors	±60° (2-D)	$\propto N^2$	Medium	2018
[4]*	Connected array	Dual LP	30%	Grid of connectors	±60° (2-D)	$\propto N^2$	High	2016
[41]*	Connected array	Dual LP	85.7%	Grid of connectors	±60° (2-D)	$\propto N^2$	Medium	2018
[44]*	TCDA array	Dual LP	142%	Grid of connectors	±60° (2-D)	$\propto N^2$	Medium	2015
Ku3030 [3]**	CTS array	Single LP	30%	n.a.	97.5° (H-plane)	$\propto N$	High	2018
Ka2517 [3]**	CTS array + polarizer	Switchable CP	54%	n.a.	97.5° (H-plane)	$\propto N$	High	2017
[6]**	CTS array	Single LP	40.6%	Pillbox system	±45° (H-plane)	$\propto N$	Medium	2015
[7]**	CTS array in LTCC	Single LP	27.5%	Pillbox system	Fixed beam	$\propto N$	Medium	2017
[9]**	CTS array	Single LP	19.1%	Pillbox system	Fixed beam	$\propto N$	Medium	2017
[60]**	Cross-connected slots	Dual CP	1.6%	Traveling wave	Fixed beam	$\propto N$	Low	2017

* A phased array made of $N \times N$ radiating elements is assumed.
** N indicates the number of coaxial connectors. A single coaxial connector is associated to a single beam.

usually consists of a double mesh grid of connectors. Each radiating element is fed by a dedicated connector, thus increasing the number of active elements considerably. Particularly, if we assume phased arrays having $N \times N$ elements, the associated power consumption is thus proportional to N^2. Owing to the use of a quasi-optical beamformer, a promising solution is offered by CTS arrays. Wideband performance are achieved, as well as a large field-of-view along one principal plane. A 2-D scanning can be also achieved by relying on an azimuth rotation of the antenna module. Commercial modules [3] are available on the market and they represent the most evolved CTS array solution as industrial product. In the open literature, several prototypes have been proposed [6, 7, 9] and demonstrated an excellent performance to fulfill modern SatCom requirements. The limitation of the CTS arrays is that they do not usually perform polarization agility. The CP is generally achieved by means of an add-on polarization controller, placed in front of the radiating aperture. So far as we know, the work in [60] is the only antenna solution, based on cross-connected long slots, that achieves the CP by relying on two separate apertures. As for all traveling-wave antennas, the solution in [60] is however very narrowband and scarcely efficient.

1.3 Novelty of the thesis

In this Section, the underlying idea of the thesis is outlined. In particular, two antenna solutions are proposed as terminal devices that fulfill modern SatCom requirements. The first idea is based on the novel concept of the dual-mode

CTS arrays, whereas the second relies on a dual-band polarizing screen, to be used in combination with an extremely low profile and wideband CTS array.

1.3.1 Dual-mode CTS arrays

A novel concept of CTS arrays, to achieve circular or dual-linear polarization, is proposed in this thesis. The underlying idea is based on the over-moded operation of the long slot arrays. The width of the slots is enlarged to propagate higher-order transverse electric (TE) and magnetic (TM) modes. Specifically, long slots of width $\lambda/2 < a < \lambda$ (where λ is the operating wavelength) can support three modes: TEM, TM_1 and TE_1. Fig. 1.10 depicts the E-field distri-

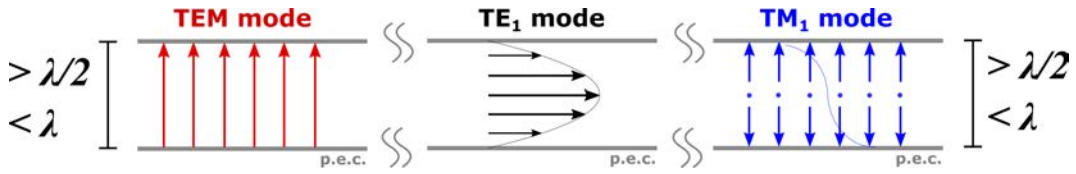

FIGURE 1.10: E-field distribution in the cross section of an over-moded PPW. From left to right: TEM, TE_1 and TM_1 modes.

bution over the cross-section of an over-moded PPW, whose height is comprised between a half and one wavelength. Fig. 1.10 shows that TEM and TE modes exhibit orthogonally-oriented E-fields in the waveguide's cross-section, able to radiate CP waves if properly excited. The novelty, introduced by this class of arrays, lies in providing CP radiation by resorting to a single radiating aperture that supports two orthogonally-polarized modes. Such a structure preserves all the advantages of parallel-fed CTS arrays, i.e., wideband, large field-of-view, low profile, line source, etc.

The main drawback of this class of CTS arrays is twofold. Firstly, the TEM and TE_1 modes exhibit different dispersive behaviors. Also, the TM_1 mode is undesired and, being degenerate with the TE_1 mode, can propagate in the structure. Throughout the manuscript, several paths will be explored to stem these issues. For instance, specific kinds of PPWs will be engineered and integrated into the antenna design, showing results of great interest to the scientific community.

1.3.2 CTS arrays combined with circular polarizers

As mentioned in Section 1.1, modern K/Ka-band SatCom terminals operate in two separate frequency bands: 17.7-21 GHz and 27.5-31 GHz, associated with the down-link and the up-link, respectively, as shown in Fig. 1.3. Orthogonal CPs are preferred in these two bands to further improve the isolation between the transmit and the receive signal. The design of antennas, providing orthogonal CPs in two non-adjacent bands, is thus becoming of increasing interest and represents a future challenge for the scientific community. However, the dual-mode CTS arrays cannot straightforwardly address this problem. As consequence, other solutions have to be investigated.

Nowadays, there are two main approaches to fulfill the above-mentioned SatCom requirements, as shown in Figs. 1.11(a) and (b). A first solution makes

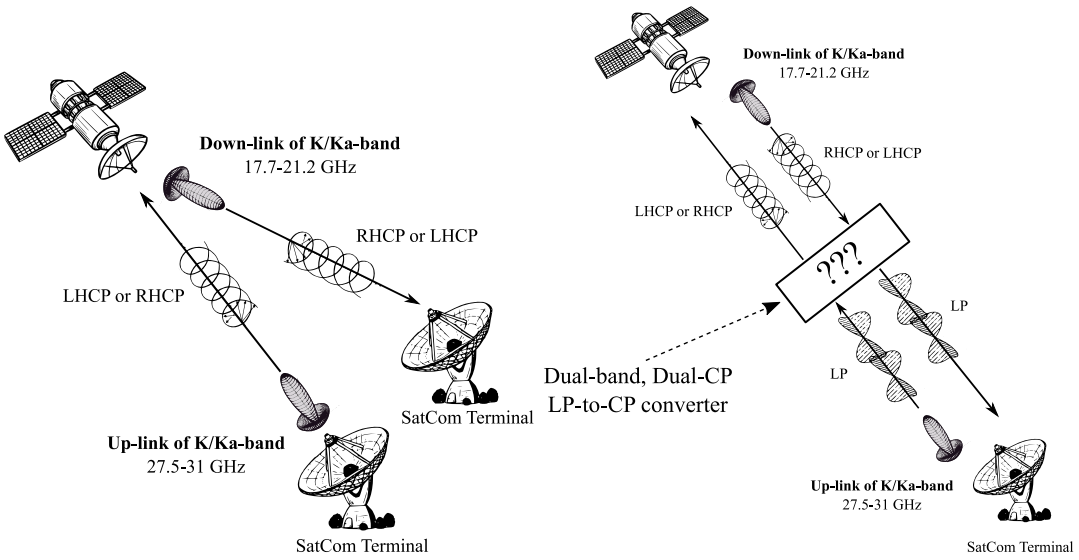

(a) Double apertures. (b) Single aperture.

FIGURE 1.11: Dual-band, orthogonally-polarized SatCom systems. (a) Two apertures are used to receiving/transmitting LHCP and RHCP radiations separately in two non-adjacent bands. (b) One only aperture covering the K-/Ka-band is used in combination of a dual-band circular polarizer.

use of two separate apertures that radiate CP waves in the up- and down-link channels of the K-/Ka-band [refer to Fig. 1.11(a)]. This solution is the one typically employed and it is based on two highly-efficient SatCom terminals, e.g., reflectors using dual-CP feeders [61, 62]. A recent solution is based on

continuous parallel-plate waveguide lenses and achieves multi-beam CP radiation [63]. Each beam is alternately right or left hand circularly-polarized and may represent a way to address the dual-band SatCom requirements. However, even though this antenna is very broadband, efficient, and reliable, it also exhibits high costs and fairly complex design. Also, the dual CP operation is only guaranteed at different pointing angles. On the other hand, an alternative solution is shown in Fig. 1.11(b). One only linearly-polarized SatCom aperture, that covers the K-/Ka-band, is used in combination with a dual-band linear-to-circular polarization (LP-to-CP) converter. This solution would help in strongly reducing the encumbrance of the overall SatCom system, as well as the costs. To date, the research activity on these applications is still at an early stage. Therefore, this thesis will focus on this solution and, particularly, on the design of dual-band planar polarizing screens. The combination of the polarizer with a very broadband CTS array (K and Ka bands) will be an additional subject of study.

1.4 Outline of the thesis

The aim of this thesis is to propose the study and the design of a novel antenna architecture, suitable to fulfill advanced SatCom requirements. As mentioned earlier, the antenna is based on the dual-mode operation of enlarged PPWs. It can attain wideband performance, as well as beam switching capability along one plane. A 2-D scan range is obtained by virtue of a hybrid electro-mechanical solution. Specifically, an azimuth rotation of the antenna allows a conical sector of scanning by means of an electrical one, resulting from the quasi-optical feed system. The work was funded by Direction Général de l'Armament (DGA) and Région Bretagne. Specifically, the thesis is structured into three major blocks.

The first research activity has focused on the development of an in-house tool and related analytic studies about the analysis of dual-mode CTS arrays, achieving circular or dual-linear polarization. A possible design is also proposed and is currently under fabrication using 3-D printing technology.

The second part is about the analysis and synthesis of a dual-band linear-to-circular (LP-to-CP) polarization converter that attains polarization diversity in the up-link and down-link channels of the K/Ka-band. This six-months work

has been carried out in collaboration with Prof. Anthony Grbic at the Radiation Laboratory, University of Michigan, Ann Arbor, USA. The dual-band polarized has been fabricated and measured using a quasi-optical test bench.

The third and last part concerns a research activity inserted in the context of a collaboration with Thales Communication and Security (TCS), in the framework of the R&D activity of the ANR-ASTRID-MATURATION project named RAFQO [64]. The goal of this collaboration is to develop a CTS array, that covers the K and Ka bands, with an extremely low-profile to target SOTM applications. A CTS array in PCB technology has been prototyped and tested to evaluate its performance. This antenna is also intended to be integrated with a dual-band LP-to-CP converter.

A more detailed explanation of the manuscript's organization is reported hereinafter.

Chapter 2 comprises two main parts: numerical modeling for the computation of the active impedance of over-moded, open-ended stubs and a possible design at Ka-band. An original numerical modeling, consisting of a mode-matching technique based on a spectral Green's function approach, is presented and intensively validated with full-wave simulations. The versatility of an in-house tool is fundamental to execute fast and accurate multi-parametric studies. The goal is to gain insights by exploring the antenna's potentialities and limitations. After being accurately validated, the code is used to retrieve design guidelines. A possible design of the dual-mode CTS array at the Ka-band is afterward proposed. The laser selective melting technology is selected for the fabrication and subjected to a feasibility test. To the moment of this manuscript's redaction, the antenna is under fabrication. Future works will focus on antenna testing.

Chapter 3 proposes an analytic study of PPWs with reactive walls. From this study, it emerges that the dispersion of reactive-loaded, open-ended stubs can be engineered in such a way to achieve an equi-dispersive, dual-mode propagation. This provides insights into solutions that overcome the issues of inter-modal dispersion (between TEM and TE_1 modes), experienced by the dual-mode CTS arrays introduced in Chapter 2. Also, the developed theory can be used to engineer structures that inhibit the propagation of the TM_1 mode, thus mitigating the undesired coupling that occurs between the TEM and TM_1

modes.

Chapter 4 introduces the design of a dual-linear-polarized CTS array. The antenna is made of over-moded stubs that support a dual-mode propagation, exhaustively studied in Chapter 2. The dispersion of each radiating stub is engineered *ad-hoc* by using the model developed in Chapter 3. A prototype has been fabricated in stereolithography technology and, afterward, tested in the anechoic chamber. The antenna array constitutes an important proof-of-concept that strengthens the usability of dual-mode CTS array for SatCom links. Specifically, the antenna array is designed at Ka-band and achieves an 11.6% fractional bandwidth of operation. It performs high-gain dual-polarized radiation while scanning up to $\pm 25^{\circ}$ with a radiation efficiency of 85%. This work is positioned as the first successful attempt to overcome the inherent linearly-polarized working principle of standard CTS arrays. Up to date, dual-polarized CTS arrays have indeed been proposed only in traveling-wave configurations, whose bandwidth of operation is very narrow. In addition, a quasi-optical beamformer has been used, for the first time, as a feed system to provide a dual-polarized multi-beam radiation.

Chapter 5 proposes an original design procedure to realize dual-band, orthogonally-polarized LP-to-CP converters. The model is based on equivalent circuit models and allows approaching the design without relying on any multi-parameter optimizations. A metasurface-based polarizer has been designed using two PCB boards and a prototype has been fabricated. Its performance has been intensively measured with a quasi-optical test bench, showing an excellent agreement with the predicted results. Among existing solutions, this polarizer constitutes the state-of-the-art, in terms of efficiency and purity of the polarization conversion. Also, the proposed model significantly eases in the design process that is carried out without massive optimization routines. The advantages and limitations of such a design procedure are also highlighted and exhaustively discussed in the last part of this Chapter.

Chapter 6 is about the design of a very broadband CTS array with an extreme low-profile. The antenna is fully realized in nine PCB layers and exploits a layer-to-layer capacitive coupling that enables the propagation in the vertical direction. The design has been carried out by means of full-wave simulations

and a prototype has been fabricated. The antenna demonstrates very broadband capabilities (50% of relative bandwidth) and achieves scanning agility. Also, an antenna efficiency higher than 70% is attained. The prompt for the antenna miniaturization is required to fulfill the demanding requirements of SOTM applications. The proposed solution proves that these specifications can be accomplished by a single device. The developed antenna architecture stands out not only for its compactness, but also for its simplicity to be integrated with add-on components. In fact, the combination with the dual-band polarized, introduced in Chapter 5, is seen to be feasible, so that a dual-band operation with high CP discrimination, between the two non-adjacent bands, can be performed by a single extremely-compact device.

Chapter 7 reviews the contributions of the thesis and discusses the to-do list and future developments.

Chapter 2

Circularly-Polarized CTS Arrays

An efficient numerical tool is crucial to explore the potentiality of the antenna described in Chapter 1.3.1. In this Chapter[1], a spectral mode-matching technique (MMT) is introduced to investigate the maximum achievable performance of the proposed structure. The numerical model builds on the work in [5], extending it to over-moded structures. Closed-form expressions are provided for the active admittance of an infinite, over-moded, long slot array. In particular, the active reflection coefficient of over-moded CTS arrays is calculated, when the open-ended stubs are parallel-fed by the TEM and TE_1 modes, respectively. The insight, given by dedicated numerical analyses, is of considerable importance to study the antenna's potentialities and limitations. The in-house tool, indeed, offers extreme versatility for the analysis of the array under various and precisely controlled excitations (e.g., single-mode, multi-mode), which is fundamental to perform fast and accurate parametric studies. The impact of the array parameters on the antenna's matching and radiation performance will be exhaustively displayed and discussed, thus easing a possible design of circularly-polarized SatCom terminal antenna at the Ka-band.

In the following, the impact on performances resulting from TM_1 mode propagation will be excluded. Except for broadside radiation, the TM_1 and TEM modes may generally occur in mutual coupling, while the array performs scanning. This unwanted effect is nonetheless negligible when considering that the E-field distribution of TM_1 mode exhibits null amplitude at the center of each radiating slot [see Fig. 1.10]. This means that the radiated power, associated with TM_1 mode, is small when compared to that of both TEM and TE_1 modes. Also, the dispersion of the radiating PPWs can be further

[1]This Chapter is an extended version of the article [J-1]. The list of the author's publications is included at the end of this Ph.D. dissertation.

engineered, in order to inhibit the TM_1 mode propagation within the operating frequency range. This point will be touched in Chapter 3.

2.1 Numerical model of over-moded CTS arrays

Fig. 2.1 shows the geometry of the problem under consideration. The planar array is infinitely extended in the xy-plane. The infinite array approximation turns out to be excellent while studying very large arrays [65]. The width of

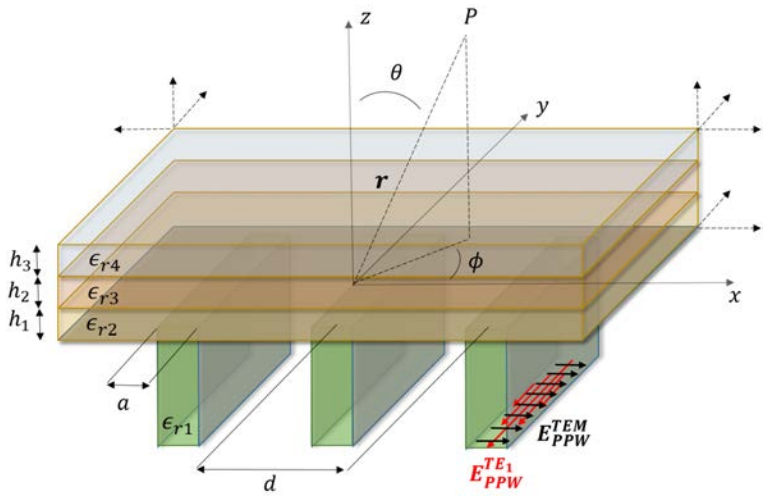

(a) 3-D view.

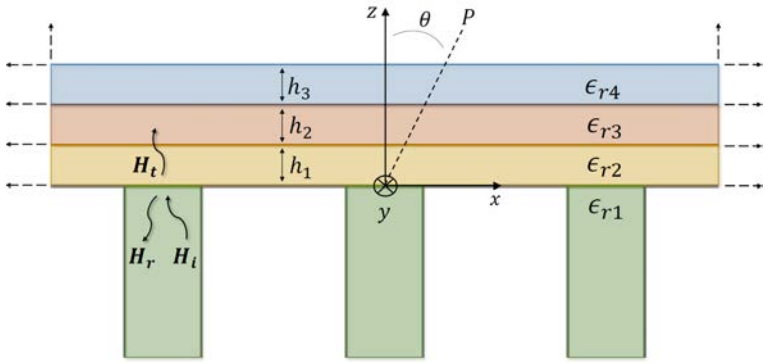

(b) Cross section along the xz-plane.

FIGURE 2.1: Geometry of the problem under analysis. The array consists of open-ended stubs, parallel-fed by over-moded PPWs. The long slots radiate into a multi-layered medium. Only three dielectric slabs are shown for the sake of clarity. (a) Perspective view. (b) Cross section in the xz-plane.

slots is a and the inter-element spacing is d. In order to maintain the propagation of only three modes (TEM, TE_1 and TM_1), the slots' height a is comprised between $\lambda/2$ and λ, where λ is the operating wavelength in the medium filling

the PPWs. This setting informs us that the maximum operating bandwidth of the antenna is 66.6% (i.e., $f_{max} = 2f_{min}$) theoretically. This result represents the first drawback when compared to mono-modal long slot arrays, which achieve "infinite" bandwidth in principle [58]. The proposed structure can however be classified as a broadband array. The PPWs are filled with material of relative dielectric constant ϵ_{r1}. The modes propagate in the direction of z-axis. The metallic part is considered lossless and, hence, modeled as a perfect electric conductor (PEC). The open-ended stubs radiate into a planar multi-layered medium. The number of dielectric layers can be arbitrarily chosen. Each dielectric layer has height h_q and dielectric permittivity $\epsilon_{r,q+1}$, where $q \in \mathbb{N}^+$.

The electromagnetic problem is studied by virtue of the equivalence theorem [24]. A magnetic field integral equation (MFIE) is derived by enforcing the continuity of tangential component of the magnetic field on the slots:

$$\hat{z} \times [\mathbf{H_i}(x,y,z) + \mathbf{H_r}(x,y,z) - \mathbf{H_t}(x,y,z)] \mid_{on\ \mathfrak{D}} = \mathbf{0} \tag{2.1}$$

where $\mathfrak{D} = \{(x,y,z) \in \mathbb{R}^3 : nd < x < a + nd \text{ with } n \in \mathbb{Z}, -\infty < y < +\infty, z = 0\}$. The entries $\mathbf{H_i}(x,y,z)$, $\mathbf{H_r}(x,y,z)$ and $\mathbf{H_t}(x,y,z)$ are,respectively, the incident, reflected, and transmitted magnetic fields at the discontinuity $z = 0$. A simple graphical representation of these fields is shown in Fig. 2.1(b). Given the structure is periodic, each field contribution in (2.1) is expressed exploiting the Floquet theory [66]. Specifically, the total field is rebuilt by expanding in Floquet's modes the field distribution over the central slot.

As it is well known, the general electromagnetic field in a hollow, lossless PPW can be expressed as a series of normal modes. The theory of waveguides is well established and is documented in various books [56, 67–70]. Given the absence of source, the problem reduces to solving Helmholtz equation and searching for the corresponding eigenvalues [71]. In formulae:

$$\mathcal{H}\left\{\phi_m^{\{TE,TM\}}\right\} = 0 \tag{2.2}$$

where $\mathcal{H}\{\cdot\} = \nabla_t^2 + \left(k_{t,m}^{\{TE,TM\}}\right)^2 = \frac{\partial^2}{\partial x^2} + \frac{\partial^2}{\partial y^2} + \left(k_{t,m}^{\{TE,TM\}}\right)^2$ is the Helmholtz operator and $m \in \mathbb{N}^+$. The eigenvalues $k_{t,m}^{\{TE,TM\}}$ are calculated enforcing the boundary conditions (BC) over the waveguide cross-section contour. Assuming

the contour C is PEC, TE and TM modes fulfill the following BCs, respectively

$$\begin{cases} \frac{\partial \phi_m^{TE}}{\partial n} = 0 & on\ C \\ \phi_m^{TM} = 0 & on\ C \end{cases} \tag{2.3}$$

where $C = \{(x, y, z) \in \mathbb{R}^3 : x = \{0, a\} \text{ with } n \in \mathbb{Z}, -\infty < y < +\infty, z = 0\}$ and $\frac{\partial}{\partial n} = \hat{n} \cdot \nabla$ is the directional derivative along the normal to the contour C. The modal vectors for TE and TM modes are obtained from the corresponding scalar potential, as follows

$$\begin{aligned} \mathbf{e_m^{TE}} &= \hat{z} \times \nabla_t \phi_m^{TE} \\ \mathbf{e_m^{TM}} &= -\nabla_t \phi_m^{TM} \end{aligned} \tag{2.4}$$

As mentioned earlier, the fields in a hollow waveguide can be thus expressed as a superimposition of TE and TM modes. Hereinafter, we will refer to the formulation proposed in [70]. After some algebraic manipulations, the formal expression of the transverse fields in PPWs can be arranged in the form:

$$\begin{aligned} \mathbf{E_{PPW}} = &\sum_{m=0}^{+\infty} \left(\frac{b_m^{TE}}{Y_m^{TE}} V_m^{TE} - \frac{b_m^{TM}}{Y_m^{TM}} V_m^{TM} \right) \cos\left(\frac{m\pi}{a} x\right) e^{-ik_{y0}y} \hat{x} \\ &+ \sum_{m=1}^{+\infty} \left(\frac{c_m^{TM}}{Y_m^{TM}} V_m^{TM} - \frac{c_m^{TE}}{Y_m^{TE}} V_m^{TE} \right) \sin\left(\frac{m\pi}{a} x\right) e^{-ik_{y0}y} \hat{y} \end{aligned} \tag{2.5}$$

$$\begin{aligned} \mathbf{H_{PPW}} = &\sum_{m=1}^{+\infty} \left(c_m^{TE} V_m^{TE} - c_m^{TM} V_m^{TM} \right) \sin\left(\frac{m\pi}{a} x\right) e^{-ik_{y0}y} \hat{x} \\ &+ \sum_{m=0}^{+\infty} \left(b_m^{TE} V_m^{TM} - b_m^{TM} V_m^{TM} \right) \cos\left(\frac{m\pi}{a} x\right) e^{-ik_{y0}y} \hat{y} \end{aligned} \tag{2.6}$$

where V_m^{TE} and V_m^{TM} are scalar modal functions of TE and TM modes, respectively. The entries b_m^{TE}, b_m^{TM}, c_m^{TE} and c_m^{TM} are calculated by enforcing the ortho-normalization property of waveguide modes [71], thus yielding to

$$\frac{b_m^{TE}}{Y_m^{TE}}, \frac{c_m^{TM}}{Y_m^{TM}} = \frac{ik_{y0}\sqrt{\nu_m/a}}{\sqrt{k_{y0}^2 + (m\pi/a)^2}}, \qquad \nu_m = \begin{cases} 1 & if \quad m = 0 \\ 2 & if \quad m \neq 0 \end{cases} \tag{2.7}$$

$$\frac{c_m^{TE}}{Y_m^{TE}}, \frac{b_m^{TM}}{Y_m^{TM}} = \frac{m\pi/a\sqrt{\nu_m/a}}{\sqrt{k_{y0}^2 + (m\pi/a)^2}}, \qquad \nu_m = \begin{cases} 1 & if \quad m = 0 \\ 2 & if \quad m \neq 0 \end{cases} \tag{2.8}$$

where $k_{y0} = k_0 \sin\theta_0 \sin\phi_0$ and (θ_0, ϕ_0) is the pointing direction of the array [see Fig. 2.1]. Furthermore, Y_m^{TE} and Y_m^{TM} represent the modal admittances of TE and TM modes, respectively. Since the structure is periodic, the Floquet's theory [66] can be applied to equations (2.5) and (2.6) to express the fields in (2.1).

Given the linearity of the problem, we will consider two separate modes to excite the stubs: TEM and TE_1. The incident magnetic field $\mathbf{H_i}(x, y, z)$ in (2.1) takes a different form according to the feeding mode, as follows

$$\mathbf{H_i^{TEM}} = \sum_{n=-\infty}^{+\infty} \mathbf{H_{PPW}^{TEM}}(x - nd, y) \prod_a \left(x - \tfrac{a}{2} - nd\right) e^{-ik_{x0}nd} \tag{2.9}$$

$$\mathbf{H_i^{TE_1}} = \sum_{n=-\infty}^{+\infty} \mathbf{H_{PPW}^{TE_1}}(x - nd, y) \prod_a \left(x - \tfrac{a}{2} - nd\right) e^{-ik_{x0}nd} \tag{2.10}$$

where $k_{x0} = k_0 \sin\theta_0 \cos\phi_0$ and

$$\mathbf{H_{PPW}^{TEM}} = \frac{iY_0^{TE} V_{inc}^{TE_0}}{\sqrt{a}} e^{-k_{y0}y} \hat{y} \tag{2.11}$$

$$\mathbf{H_{PPW}^{TE_1}} = \frac{Y_1^{TE} V_{inc}^{TE_1}}{k_1^{TE}} \sqrt{\frac{2}{a}} \left[\frac{\pi}{a} \sin\left(\frac{\pi}{a}x\right) \hat{x} + ik_{y0} \cos\left(\frac{\pi}{a}x\right) \hat{y}\right] \tag{2.12}$$

where $V_{inc}^{TE_0}$ and $V_{inc}^{TE_1}$ are the known scalar mode functions of the incident field under TEM and TE_1 mode operation, respectively. Moreover, k_1^{TE} is the eigenvalue associated to TE_1 mode and the rectangular function $\prod_a (x) = 1$ for $-a/2 < x < a/2$ and null elsewhere.

In turn, the expression for the reflected and transmitted magnetic fields in (2.1) are given by

$$\mathbf{H_r} = -\sum_{n=-\infty}^{+\infty} \mathbf{H_{PPW}}(x - nd, y) \prod_a \left(x - \tfrac{a}{2} - nd\right) e^{-ik_{x0}nd} \tag{2.13}$$

$$\mathbf{H_t} = \iint_{\mathbb{R}^2} \underline{\underline{G_t}}^{HM} (x - x', y - y') \, \mathbf{M_t}(x', y') \, dx'dy' \tag{2.14}$$

The reflected field $\mathbf{H_r}$ is found by inserting (2.6) into (2.13). The field transmitted over the slots $\mathbf{H_t}$ is calculated as convolution of the transverse dyadic Green's function $\underline{\underline{G_t}}^{HM}$ for a layered medium with the transverse magnetic current $\mathbf{M_t}(x, y)$ distribution on $\mathfrak{D}$. Guidelines to derive the transverse dyadic

Green's function $\underline{\underline{G_t}}^{HM}$ can be found in [70], whose approach is based on equivalent transmission line (TL) models. A systematic procedure to evaluate this class of Green's functions is outlined in Appendix A.2. The transverse magnetic current $\mathbf{M_t}(x, y)$ is given by

$$\mathbf{M_t}(x, y) = -\hat{z} \times \mathbf{E_{Floquet}}(x, y, z = 0) \tag{2.15}$$

where

$$\mathbf{E_{Floquet}} = \sum_{n=-\infty}^{+\infty} \mathbf{E_{PPW}}(x - nd, y) \prod_a \left(x - \tfrac{a}{2} - nd\right) e^{-ik_{x0}nd} \tag{2.16}$$

By inserting (2.5) into (2.16), the magnetic current in (2.15) is obtained. Note that $\mathbf{M_t}(x, y)$ is function of the scalar mode functions V_m^{TE} and V_m^{TM}. The Fourier transform is then performed to compute the convolution integral (2.14). For the sake of brevity, we directly report the extended form of $\mathbf{H_t}$, given by

$$\begin{aligned}\mathbf{H_t} \cdot \hat{x} = {} & \frac{e^{-ik_{y0}y}}{d} \sum_{m=1}^{+\infty} \left(\frac{c_m^{TM}}{Y_m^{TM}} V_m^{TM} - \frac{c_m^{TE}}{Y_m^{TE}} V_m^{TE} \right) \sum_{n=-\infty}^{+\infty} \Gamma_m(k_{xn}) \tilde{G}_{xx}^{HM}(k_{xn}, k_{y0}) e^{-ik_{xn}x} \\ & + \frac{e^{-ik_{y0}y}}{d} \sum_{m=0}^{+\infty} \left(\frac{b_m^{TM}}{Y_m^{TM}} V_m^{TM} - \frac{b_m^{TE}}{Y_m^{TE}} V_m^{TE} \right) \sum_{n=-\infty}^{+\infty} \Lambda(k_{xn}) \tilde{G}_{xy}^{HM}(k_{xn}, k_{y0}) e^{-ik_{xn}x}\end{aligned} \tag{2.17}$$

$$\begin{aligned}\mathbf{H_t} \cdot \hat{y} = {} & \frac{e^{-ik_{y0}y}}{d} \sum_{m=1}^{+\infty} \left(\frac{c_m^{TM}}{Y_m^{TM}} V_m^{TM} - \frac{c_m^{TE}}{Y_m^{TE}} V_m^{TE} \right) \sum_{n=-\infty}^{+\infty} \Gamma_m(k_{xn}) \tilde{G}_{yx}^{HM}(k_{xn}, k_{y0}) e^{-ik_{xn}x} \\ & + \frac{e^{-ik_{y0}y}}{d} \sum_{m=0}^{+\infty} \left(\frac{b_m^{TM}}{Y_m^{TM}} V_m^{TM} - \frac{b_m^{TE}}{Y_m^{TE}} V_m^{TE} \right) \sum_{n=-\infty}^{+\infty} \Lambda(k_{xn}) \tilde{G}_{yy}^{HM}(k_{xn}, k_{y0}) e^{-ik_{xn}x}\end{aligned} \tag{2.18}$$

where $k_{xn} = k_{x0} - 2n\pi/d$ and G_{ij}^{HM} is the Fourier transform of the (i, j)-th entry of the Green's dyad $\underline{\underline{G}}^{HM}$. The functions $\Gamma_m(k_x)$ and $\Lambda_m(k_x)$ are defined as

$$\Gamma_m(k_x) = \frac{a}{2} e^{i(k_x \frac{a}{2} + m\frac{\pi}{2})} \left[\operatorname{sinc}\left(k_x \frac{a}{2} + \frac{m\pi}{2}\right) - e^{-im\pi} \operatorname{sinc}\left(k_x \frac{a}{2} - \frac{m\pi}{2}\right) \right] \tag{2.19}$$

$$\Lambda(k_x) = \frac{a}{2i} e^{i(k_x \frac{a}{2} + m\frac{\pi}{2})} \left[\operatorname{sinc}\left(k_x \frac{a}{2} + \frac{m\pi}{2}\right) + e^{-im\pi} \operatorname{sinc}\left(k_x \frac{a}{2} - \frac{m\pi}{2}\right) \right] \tag{2.20}$$

where the unnormalized sinc(·) function is defined as

$$\mathrm{sinc}(x) = \begin{cases} \frac{\sin x}{x} & if \quad x \neq 0 \\ 1 & if \quad x = 0 \end{cases} \tag{2.21}$$

By inserting (2.17), (2.18) and (2.13) into (2.1), the MIFE is found as function of the unknown scalar mode functions V_m^{TE} and V_m^{TM}. This equation can be approximately solved by truncating the series to 2M-1 PPW modes and $2N_f+1$ Floquet modes, and applying the Galerkin projection to (2.1). Two different linear problems arise for the two selected modes. For each mode, the matrix-based form yields

$$\begin{bmatrix} \underline{\underline{Y}}^{TE,TE} & \underline{\underline{Y}}^{TE,TM} \\ \underline{\underline{Y}}^{TM,TE} & \underline{\underline{Y}}^{TM,TM} \end{bmatrix} \begin{bmatrix} \mathbf{V^{TE}} \\ \mathbf{V^{TM}} \end{bmatrix} = \begin{bmatrix} \mathbf{I_{01}} \\ \mathbf{I_{02}} \end{bmatrix} \tag{2.22}$$

where $\mathbf{V^{TE}} = \left[V_0^{TE}, V_1^{TE}, \ldots, V_{M-1}^{TE}\right]$ and $\mathbf{V^{TM}} = \left[V_1^{TM}, \ldots, V_{M-1}^{TM}\right]$ are the scalar mode functions of TE and TM modes in the PPWs, respectively. Depending on the type of impinging field we consider, i.e., TEM (2.9) or TE_1 (2.10), the known terms $\mathbf{I_{01}}$ and $\mathbf{I_{02}}$ take different forms. The mathematical expressions of the admittance matrix in (2.22) can be found in the Appendix A.1.

2.1.1 Active admittance under TEM excitation

The constant term in (2.22) is given by

$$\mathbf{I_{01}} = \begin{bmatrix} iV_{inc}^{TEM}\sqrt{a}Y_0^{TE} \\ 0 \\ \vdots \\ 0 \end{bmatrix}, \quad \mathbf{I_{02}} = \begin{bmatrix} 0 \\ \vdots \\ 0 \end{bmatrix} \tag{2.23}$$

where $V_{inc}^{TEM} = 1\,(V/\sqrt{m})$ and $Y_0^{TE} = 1/\zeta$ with ζ the intrinsic impedance of the medium inside the PPWs. By inverting (2.22), the scalar mode functions $V_{m=0,\ldots,M-1}^{TE}$ and $V_{m=1,\ldots,M-1}^{TM}$ can be calculated and the fields on the aperture expressed in a closed-form. The active admittance of the radiating slots can be then derived considering the power of TEM mode flowing through the slots. The

mathematical expression of the normalized active admittance $\bar{Y}_{act}^{TEM}$ is given by

$$\bar{Y}_{act}^{TEM} = -\frac{1}{|V_0^{TE}\sqrt{a}|^2}\int_{\mathfrak{D}} \mathbf{H_t}\cdot\mathbf{M}^{*}_{\mathbf{t,\ TEM}}\,dxdy \tag{2.24}$$

$$\mathbf{M_{t,\ TEM}} = -\frac{iV_0^{TE}}{\sqrt{a}}\prod_a\left(x-\tfrac{a}{2}\right)e^{-k_{y0}y}\hat{y} \tag{2.25}$$

In (2.24), $\mathbf{H_t}$ takes into account the contribution of higher order modes in the PPWs and the mutual coupling between the feeding waveguides [see (2.14)]. In (2.25), $\mathbf{M_{t,\ TEM}}$ considers only the effect of the fundamental mode within the PPWs. After computing the integral in (2.24), $\bar{Y}_{act}^{TEM}$ can be arranged in the form

$$\bar{Y}_{act}^{TEM} = -\frac{1}{|V_0^{TE}\sqrt{a}|^2}\left[\Psi_{1y}^{TEM}+\Psi_{2y}^{TEM}\right] \tag{2.26}$$

where

$$\begin{aligned}\Psi_{1y}^{TEM} = {} & \frac{i\left(V_0^{TE}\right)^*}{d\sqrt{a}}\sum_{m=1}^{M-1}\left(\frac{c_m^{TM}}{Y_m^{TM}}V_m^{TM}-\frac{c_m^{TE}}{Y_m^{TE}}V_m^{TE}\right)\\ & \times\sum_{n=-N_f}^{N_f}\Gamma_m(k_{xn})\tilde{G}_{yx}^{HM}(k_{xn},k_{y0})\Lambda_0(-k_{xn})\end{aligned} \tag{2.27}$$

$$\begin{aligned}\Psi_{2y}^{TEM} = {} & \frac{i\left(V_0^{TE}\right)^*}{d\sqrt{a}}\sum_{m=0}^{M-1}\left(\frac{b_m^{TM}}{Y_m^{TM}}V_m^{TM}-\frac{b_m^{TE}}{Y_m^{TE}}V_m^{TE}\right)\\ & \times\sum_{n=-N_f}^{N_f}\Lambda_m(k_{xn})\tilde{G}_{yy}^{HM}(k_{xn},k_{y0})\Lambda_0(-k_{xn})\end{aligned} \tag{2.28}$$

2.1.2 Active admittance under TE_1 excitation

When the array is excited by the TE_1 mode, the incident field is (2.10). In this case, the known term of the linear system (2.22) is given by

$$\mathbf{I_{01}} = \begin{bmatrix} 0 \\ \frac{iV_{inc}Y_1^{TE}}{k_1^{TE}}\sqrt{\frac{a}{2}}k_{y0} \\ 0 \\ \vdots \\ 0 \end{bmatrix}, \quad \mathbf{I_{02}} = \begin{bmatrix} \frac{V_{inc}^{TE_1}Y_1^{TE}}{k_1^{TE}}\frac{\pi}{\sqrt{2a}} \\ 0 \\ \vdots \\ 0 \end{bmatrix} \tag{2.29}$$

where $V_{inc}^{TE_1}=1\,(V/\sqrt{m})$, $Y_1^{TE}=\sqrt{k^2-\left(k_1^{TE}\right)^2}/(\zeta k)$, and $k_1^{TE}=\sqrt{(\pi/a)^2+k_{y0}^2}$. In (2.29), the non-null entry of $\mathbf{I_{02}}$ takes into account the coupling between TE

and TM modes which occurs when the antenna beam is steered in the planes $\phi \neq \{0°, 180°\}$.

As for TEM mode, by solving (2.22) the scalar mode functions $V^{TE}_{m=0,\ldots,M-1}$ and $V^{TM}_{m=1,\ldots,M-1}$ are found. The electromagnetic field on the plane of the slots is therefore completely-determined. The active admittance $\bar{Y}^{TE_1}_{act}$ can be then expressed as

$$\bar{Y}^{TE_1}_{act} = -\frac{1}{|V^{TE}_1\sqrt{a}|^2}\int_{\mathfrak{D}} \mathbf{H_t}\cdot\mathbf{M^*_{t,\ TE1}}\,dxdy \tag{2.30}$$

where

$$\mathbf{M_{t,\ TE1}} = M^x_{t,TE_1}\hat{x} + M^y_{t,TE_1}\hat{y} \tag{2.31}$$

with

$$\begin{aligned} M^x_{t,TE_1} = &-\sqrt{\frac{2}{a}}\frac{\frac{\pi}{a}V^{TE}_1 e^{-ik_{y0}y}}{\sqrt{k^2_{y0}+(\pi/a)^2}}\sum_{n=-\infty}^{+\infty}\sin\left(\frac{\pi}{a}(x-nd)\right) \\ &\times\prod\nolimits_a\left(x-\tfrac{a}{2}-nd\right)e^{-ik_{x0}nd} \end{aligned} \tag{2.32}$$

$$\begin{aligned} M^y_{t,TE_1} = &-\sqrt{\frac{2}{a}}\frac{ik_{y0}V^{TE}_1 e^{-ik_{y0}y}}{\sqrt{k^2_{y0}+(\pi/a)^2}}\sum_{n=-\infty}^{+\infty}\cos\left(\frac{\pi}{a}(x-nd)\right) \\ &\times\prod\nolimits_a\left(x-\tfrac{a}{2}-nd\right)e^{-ik_{x0}nd} \end{aligned} \tag{2.33}$$

The normalized active admittance $\bar{Y}^{TE_1}_{act}$ is calculated from (2.30) and can be arranged in the following mathematical form:

$$\bar{Y}^{TE_1}_{act} = -\frac{1}{|V^{TE}_1\sqrt{a}|^2}\left[\Psi^{TE_1}_{1x}+\Psi^{TE_1}_{2x}+\Psi^{TE_1}_{1y}+\Psi^{TE_1}_{2y}\right] \tag{2.34}$$

where

$$\begin{aligned} \Psi^{TE_1}_{1x} = &-\frac{\sqrt{\frac{2}{a}}\frac{\pi}{a}\left(V^{TE}_1\right)^*}{d\sqrt{k^2_{y0}+(\pi/a)^2}}\sum_{m=1}^{M-1}\left(\frac{c^{TM}_m}{Y^{TM}_m}V^{TM}_m - \frac{c^{TE}_m}{Y^{TE}_m}V^{TE}_m\right) \\ &\times\sum_{n=-N_f}^{N_f}\Gamma_m(k_{xn})\tilde{G}^{HM}_{xx}\Gamma_1(-k_{xn}) \end{aligned} \tag{2.35}$$

$$\Psi_{2x}^{TE_1} = -\frac{\sqrt{\frac{2}{a}}\frac{\pi}{a}\left(V_1^{TE}\right)^*}{d\sqrt{k_{y0}^2+(\pi/a)^2}}\sum_{m=0}^{M-1}\left(\frac{b_m^{TM}}{Y_m^{TM}}V_m^{TM}-\frac{b_m^{TE}}{Y_m^{TE}}V_m^{TE}\right) \times \sum_{n=-N_f}^{N_f}\Lambda_m(k_{xn})\tilde{G}_{xy}^{HM}\Gamma_1(-k_{xn}) \tag{2.36}$$

$$\Psi_{1y}^{TE_1} = \frac{\sqrt{\frac{2}{a}}ik_{y0}\left(V_1^{TE}\right)^*}{d\sqrt{k_{y0}^2+(\pi/a)^2}}\sum_{m=1}^{M-1}\left(\frac{c_m^{TM}}{Y_m^{TM}}V_m^{TM}-\frac{c_m^{TE}}{Y_m^{TE}}V_m^{TE}\right) \times \sum_{n=-N_f}^{N_f}\Gamma_m(k_{xn})\tilde{G}_{yx}^{HM}\Lambda_1(-k_{xn}) \tag{2.37}$$

$$\Psi_{2y}^{TE_1} = \frac{\sqrt{\frac{2}{a}}ik_{y0}\left(V_1^{TE}\right)^*}{d\sqrt{k_{y0}^2+(\pi/a)^2}}\sum_{m=0}^{M-1}\left(\frac{b_m^{TM}}{Y_m^{TM}}V_m^{TM}-\frac{b_m^{TE}}{Y_m^{TE}}V_m^{TE}\right) \times \sum_{n=-N_f}^{N_f}\Lambda_m(k_{xn})\tilde{G}_{yy}^{HM}\Lambda_1(-k_{xn}) \tag{2.38}$$

2.2 Numerical validation

The numerical model presented in Section 2.1 reports closed formulae to compute the active input impedance $Z_{act} = 1/\bar{Y}_{act}$ per unit length of open-ended stubs. The width of the slots is comprised between $\lambda/2$ and λ, thus the propagation of higher-order modes is supported. Particularly, two scenarios will be considered: over-moded long slot array parallel-fed by TEM mode and by TE_1 mode. The model has been extensively validated using the commercial full-wave simulator CST STUDIO SUITE® [72]. The setup of the simulation is depicted in Fig. 2.2. An open-ended stub radiates into free space. A dielectric layer of relative permittivity ϵ_{r2} and height $h_1 = 0.5c/(f_{min}\sqrt{\epsilon_{r2}})$ is placed on the top of the radiating slot. A waveguide port is used to launch the TEM and TE_1 modes into the feeding PPW. Unit cell boundary conditions are enforced on the lateral faces of the model. The reference plane of the derived active parameters is located over the slot. The main parameters of the structure are set as $f_{min} = f_{cut-off}^{TE_1}$, $f_{max} = 2f_{min}$, and $a = 0.5c/(f_{min}\sqrt{\epsilon_{r1}})$. These settings guarantee that only the fundamental (i.e., TEM) and the first two higher order modes (i.e., TE_1 and TM_1) can propagate into the PPWs. Finally, the spatial periodicity of the array is $d = 1.07a$ and the length of the slot is $d_y = \lambda_{max}/30$.

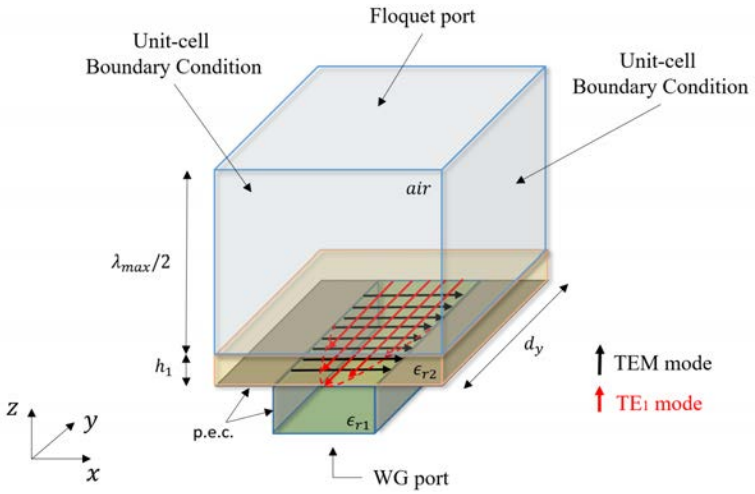

FIGURE 2.2: Simulation setup of the unit cell of over-moded CTS arrays. The structure is periodic along x- and y-axes. One dielectric layer of relative permettivity ϵ_{r2} is placed on the top of the radiating slots.

Note that CTS arrays are one-dimensional periodic structures based on long slots. In this case, such a very small periodicity along the slot is only used to validate the proposed tool numerically and avoid possible artifacts due to periodicity along the slot using [72]. Several combinations of ϵ_{r1} and ϵ_{r2} have been considered in order to exhaustively validate the numerical tool and provide some design guidelines in various scenarios.

2.2.1 TEM operation

The number of Floquet's modes required to get a stable convergence is $N_f = 10$, whereas the number of PPW modes is $M \geq 5$ both for the E-plane (i.e., $\phi = 0°$) and the H-plane (i.e., $\phi = 90°$). The real and the imaginary parts of the normalized active impedance versus frequency are shown in Fig. 2.3 along the H-plane. Likewise, the real and the imaginary parts of the normalized active impedance versus frequency are shown in Fig. 2.4 along the E-plane. An excellent agreement is observed between the proposed tool and the full-wave simulations. From this initial analysis, we start observing the wideband capability of the proposed radiating structure. As shown in Fig. 2.3, a broad impedance bandwidth is observed when the array is scanning along the H-plane. Particularly, the active S-parameter, corresponding to the case $\epsilon_{r1} = \epsilon_{r2} = 1$, is found to be below -10 dB over a 66.6% band (which is the maximum

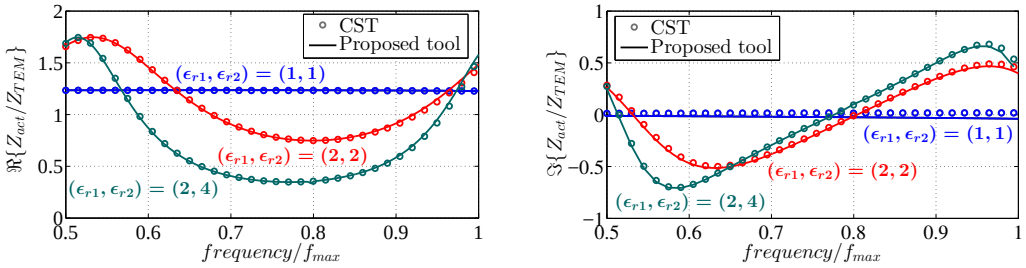

(a) Real part. (b) Imaginary part.

FIGURE 2.3: Active impedance for TEM-mode excitation versus frequency along the plane at $\phi = 90°$ for $\theta_0 = 30°$. The parameters used in the simulation are $a = 0.5c/\left(f_{min}\sqrt{\epsilon_{r1}}\right)$, $d = 1.07a$, $h = 0.5c/\left(f_{min}\sqrt{\epsilon_{r2}}\right)$, and $Z_{TEM} = \zeta$.

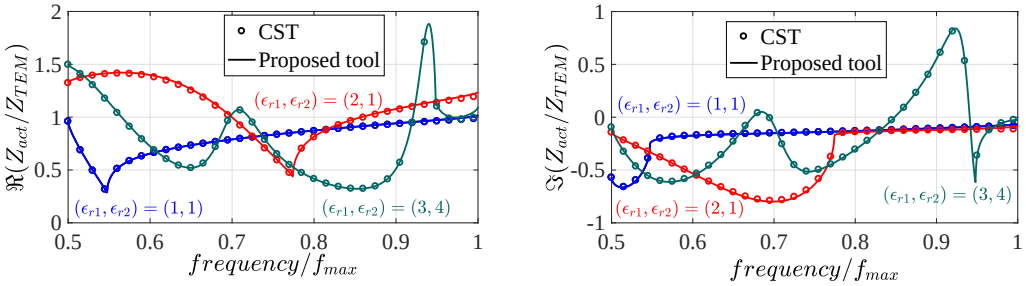

(a) Real part. (b) Imaginary part.

FIGURE 2.4: Active impedance for TEM-mode excitation versus frequency along the plane at $\phi = 0°$ for $\theta_0 = 30°$. The parameters used in the simulation are $a = 0.5c/\left(f_{min}\sqrt{\epsilon_{r1}}\right)$, $d = 1.07a$, $h = 0.5c/\left(f_{min}\sqrt{\epsilon_{r2}}\right)$, and $Z_{TEM} = \zeta$.

achievable), when the array is pointing at $\theta_0 = 30°$. We can thus conclude that the impedance bandwidth, resulting from TEM excitation, is infinitely-extended at lower frequencies in the case of over-moded long slots yet.

2.2.2 TE_1 operation

In this section, we validate the active impedance calculation for the TE_1 mode excitation. Fig. 2.5 depicts the real and imaginary parts of the normalized active impedance versus frequency along the plane $\phi = 0°$. A stable convergence is obtained considering $M \geq 8$ and $N_f \geq 10$. This method has been validated for several combinations of ϵ_{r1} and ϵ_{r2}, showing always an excellent agreement in comparison to full-wave simulations. For the sake of completeness, Fig. 2.6 plots real and imaginary parts of the active impedance, normalized to the wave

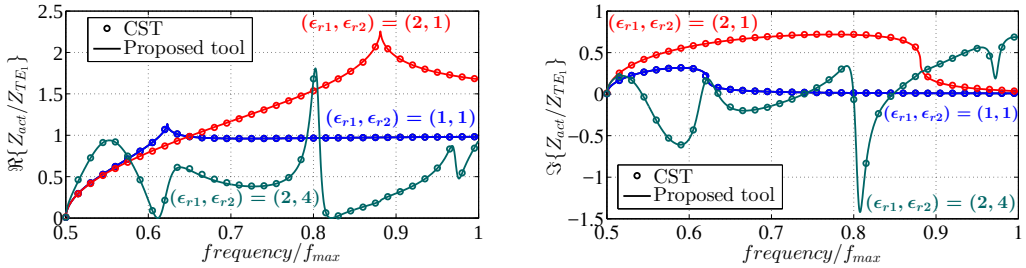

(a) Real part. (b) Imaginary part.

FIGURE 2.5: Active impedance for TE_1-mode excitation versus frequency along the plane at $\phi = 0°$ for $\theta_0 = 30°$. The parameters used in the simulation are $a = 0.5c/\left(f_{min}\sqrt{\epsilon_{r1}}\right)$, $d = 1.07a$, $h = 0.5c/\left(f_{min}\sqrt{\epsilon_{r2}}\right)$, and $Z_{TE_1} = 1/Y_1^{TE}$.

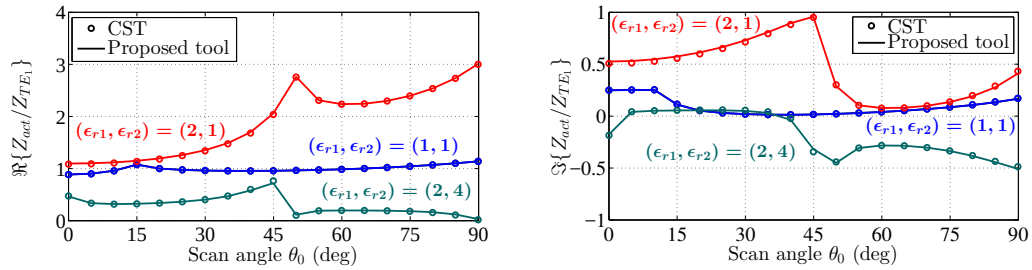

(a) Real part. (b) Imaginary part.

FIGURE 2.6: Active impedance for TE_1-mode excitation versus scan angles θ_0 along the plane $\phi = 0°$ at $f_0 = (f_{min} + f_{max})/2$. The parameters used in the simulation are $a = 0.5c/\left(f_{min}\sqrt{\epsilon_{r1}}\right)$, $d = 1.07a$, $h = 0.5c/\left(f_{min}\sqrt{\epsilon_{r2}}\right)$, and $Z_{TE_1} = 1/Y_1^{TE}$.

impedance $Z_{TE_1} = 1/Y_{TE_1}$ of the TE_1 mode versus the scan angles along the plane $\phi = 0°$ at $f_0 = (f_{min} + f_{max})/2$.

Finally, we also report the active S-parameter $S_{act} = (Z_{act} - aZ_{TE_1})/(Z_{act} + aZ_{TE_1})$ along the E-plane (i.e., $\phi = 90°$) versus frequency (Fig. 2.7(a)) and scan angles θ_0 (Fig. 2.7(b)). A stable convergence is achieved by considering $M \geq 10$ PPW modes and $N_f = 10$ Floquet modes. As shown in Fig. 2.7, a very wideband performance is obtained for the TE_1 mode in both E- and H-plane. To give an example, for the case $\epsilon_{r1} = \epsilon_{r2} = 1$, the active S-parameter is less than -10 dB over a 48.8% band [refer to Fig. 2.7(a)] along the E-plane, i.e., at $\phi = 90°$, when the array is pointing at $\theta_0 = 30°$. On the other hand, Fig. 2.7(b) shows that the proposed radiating structure attains a stable impedance matching over the $\pm 52°$ field-of-view.

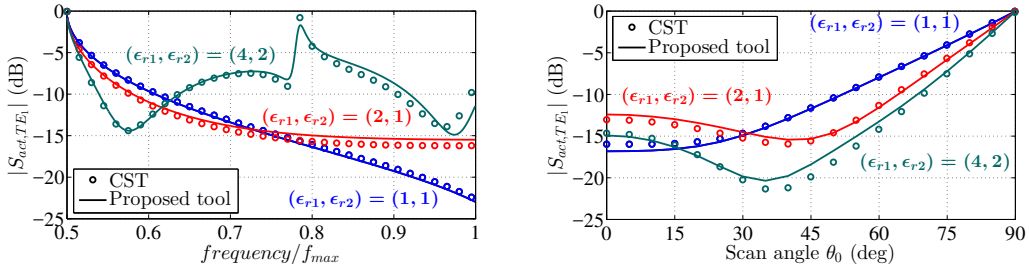

(a) $\theta_0 = 30°$. (b) $f_0 = (f_{min} + f_{max})/2$.

FIGURE 2.7: Active S-parameters for TE_1-mode excitation versus frequency (a) and scan angles θ_0 (b) along the plane $\phi = 90°$ at $f_0 = (f_{min} + f_{max})/2$. The parameters used in the simulation are $a = 0.5c/\left(f_{min}\sqrt{\epsilon_{r1}}\right)$, $d = 1.07a$, and $h = 0.5c/\left(f_{min}\sqrt{\epsilon_{r2}}\right)$.

2.3 Radiation pattern

The computation of the radiation pattern has been carried out by considering the embedded element pattern of the array [73]. The goal of this section is to analyze the advantages and limitations of the proposed CTS array for the CP generation. It is worth mentioning that no pure CP can be achieved by employing the TEM and the TE_1 modes in the PPWs. In fact, as detailed in [74], the transverse E-field profile of the TE_1 mode exhibits a cosine-like distribution with respect to the x-component, whereas the E-field profile of the TEM mode is uniform all over the slot. This means that only at the center of each radiating slot the TEM and TE_1 modes can have equal amplitude. Conversely, the two modes are in quadrature by default [74].

2.3.1 Embedded element pattern

The far-field polar components of the electric field are given by

$$\begin{aligned} E_r(r,\theta,\phi) &= 0 \\ E_\theta(r,\theta,\phi) &= \frac{ike^{-ikr}}{2\pi r}\left[f_x(\theta,\phi)\cos\phi + f_y(\theta,\phi)\sin\phi\right] \\ E_\phi(r,\theta,\phi) &= \frac{ike^{-ikr}}{2\pi r}\cos\theta\left[-f_x(\theta,\phi)\sin\phi + f_y(\theta,\phi)\cos\phi\right] \end{aligned} \tag{2.39}$$

where r is the radial distance [refer to Fig. 2.1(a)] and $\mathbf{f}(k_x, k_y)$ is given by

$$\mathbf{f}(k_x,k_y) = f_x\hat{x} + f_y\hat{y} = e^{ik_z z}\underline{\underline{\tilde{G}}}^{EM}(k_x,k_y,z)\tilde{\mathbf{M}}_{\mathbf{w}}(k_x,k_y) \tag{2.40}$$

that can be asymptotically evaluated in the stationary point $(k_{xs}, k_{ys}, k_{zs}) = (k_0 \sin\theta\cos\phi, k_0 \sin\theta \sin\phi, k_0 \cos\theta)$ [24] at the interface between the uppermost dielectric layer of the cover and the free-space. The calculation of the Fourier transform of the dyadic Green's function $\tilde{\underline{\underline{G}}}^{EM}$ in presence of a multi-layered structure is detailed in Appendix A.2. Finally, $\tilde{\mathbf{M}}_{\mathbf{w}}(k_x, k_y)$ stands for the Fourier transform of the windowed form of the magnetic current on the slots:

$$\tilde{\mathbf{M}}_{\mathbf{w}}(k_x, k_y) = \mathfrak{F}\left\{\mathbf{M}_{\mathbf{t}}(x, y)\prod_{d_y}(y)\prod_{N_{slots}a}(x - a/2)\right\} \tag{2.41}$$

where d_y is the dimension of the unit cell along y-axis, N_{slots} is the number of radiating slots and $\mathbf{M}_{\mathbf{t}}(x, y)$ is the magnetic current on the infinitely-extended slots. This approach is generally used for finite periodic structure applied to large arrays [75]. Given the presence of Floquet's modes, the windowing technique accounts for mutual coupling between array's cells [76].

Fig. 2.8 shows the embedded element pattern obtained by setting $f_{max} =$

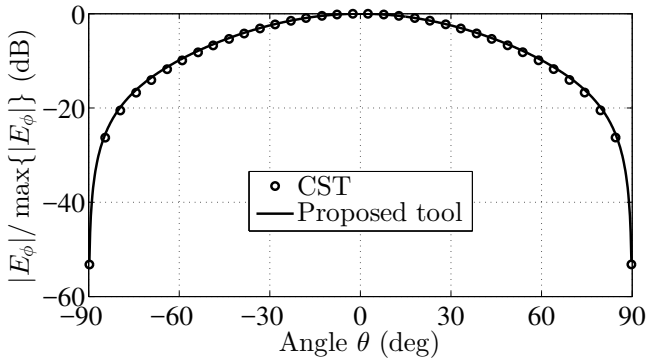

(a) E_ϕ-component in far-field region.

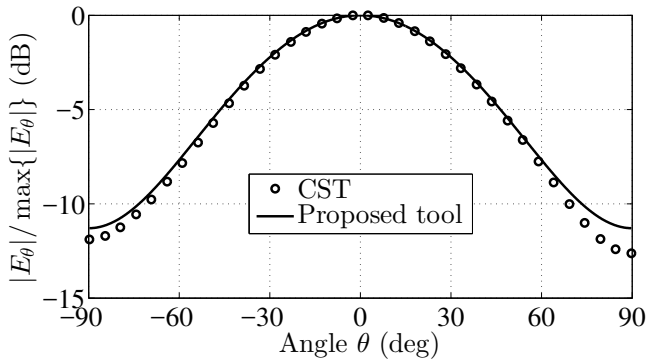

(b) E_θ-component in far-field region.

FIGURE 2.8: Polar components of the embedded radiation pattern at the frequency $f_0 = (f_{min} + f_{max})/2$. The parameters used in the simulation are $a = 0.5c/\left(f_{min}\sqrt{\epsilon_{r1}}\right)$, and $d = 1.07a$.

$2f_{min}$, $a = 0.5c/(f_{min}\sqrt{\epsilon_1})$, $d_y = c/(30f_{min})$, $d = 1.07a$, and $\epsilon_{r1} = 1$ and considering no dielectric layer covering the slots. The array is steering the beam at broadside at the frequency $f_0 = (f_{min} + f_{max})/2$. The full-wave results were obtained computing the transverse field distribution of the two modes on the plane of the aperture and making them radiate in the upper half-space. The simulation setup adopted in the commercial software is shown in Fig. 2.2. As shown in Fig. 2.8, an excellent agreement appears between full-wave simulations and the in-house tool.

The embedded element pattern can be used to reconstruct the radiation pattern of more realistic structures. Considering eight slots of length $d_y = 5\lambda_{max}$ and the results are plotted in Fig. 2.9. The radiation patterns are calculated

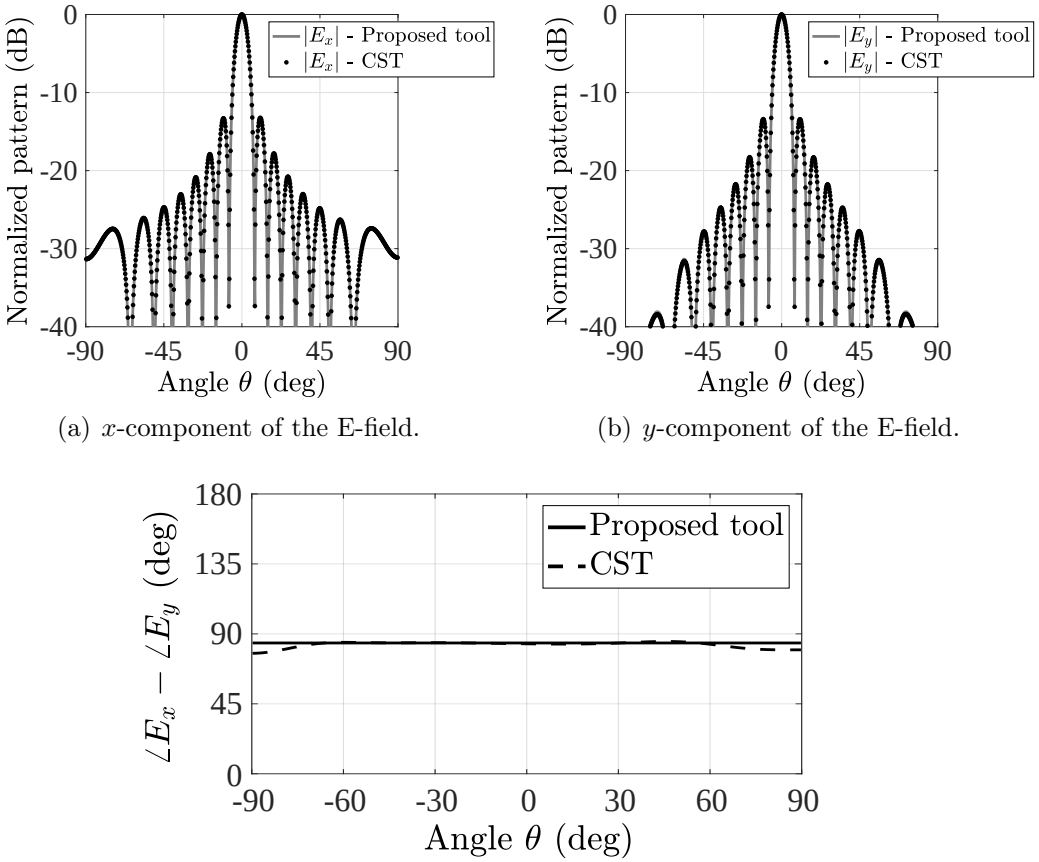

(a) x-component of the E-field.

(b) y-component of the E-field.

(c) Phase difference between E_x and E_y.

FIGURE 2.9: (a), (b) Cartesian components of the radiation pattern and (c) their phase difference at the frequency $f_0 = (f_{min} + f_{max}/2)$. An array of eight radiating slots has been considered.

along the plane $\phi = 90°$, which is the plane typically used for scanning [6].

As shown in Fig. 2.9(a) and (b), the amplitudes of the components along x- and y-axes are in very good agreement with full-wave simulations. The phase difference is reported in Fig. 2.9(c). The TEM and TE_1 modes radiate two orthogonal components 90°-phased with respect to each other.

2.3.2 Axial ratio

An important parameter to evaluate the purity of the CP generation is the axial ratio (AR) [24]

$$AR = \frac{|E_x|^2 + |E_y|^2 + \sqrt{\gamma}}{|E_x|^2 + |E_y|^2 - \sqrt{\gamma}}, \qquad 1 \leq AR \leq +\infty \tag{2.42}$$

where

$$\gamma = |E_x|^4 + |E_y|^4 + 2|E_x|^2|E_y|^2 \cos\left[2\left(\angle E_x - \angle E_y\right)\right] \tag{2.43}$$

This preliminary study considers that the input power (i.e., $P_{tot} = 1$ W) is equally splitted into each feeding mode (TEM and TE_1). The scalar modal functions V_{inc}^{TEM} and $V_{inc}^{TE_1}$ in (2.23) and (2.29) are chosen accordingly, yielding

$$V_{inc}^{TEm} = \sqrt{\frac{1}{Y_m^{TE} d_y}}, \qquad m = \{0, 1\} \tag{2.44}$$

where $V_{inc}^{TE_0} = V_{inc}^{TEM}$. It is worth noting that the power ratio between the two modes can be optimized to improve the polarization purity of the antenna This study will be presented in the Section 2.5.1. The results in Fig. 2.10 are obtained for different scan angles along the plane $\phi = 0°$. The agreement with full-wave simulations is very good. The CP performance of the array is stable over a large field-of-view. For example, the AR remains below 3 dB over a ±45° angular range, while steering the beam at broadside.

The AR has been also validated when calculated versus frequency and scan angles, as shown in Fig. 2.11. The AR is lower than 1.5 dB over a 39.5% fractional band [refer to Fig. 2.11(a)] and ±60° scanning range [refer to Fig. 2.11(b)] along the plane $\phi = 90°$ at the central frequency. Table 2.1 presents a summary of the performance associated to the geometry considered in this example. The parameters of the array are $\epsilon_{r1} = \epsilon_{r2} = 1$, $a = 0.5c/\left(f_{min}\sqrt{\epsilon_{r1}}\right)$, and $d = 1.07a$. The script BW_f stands for the impedance bandwidth of the

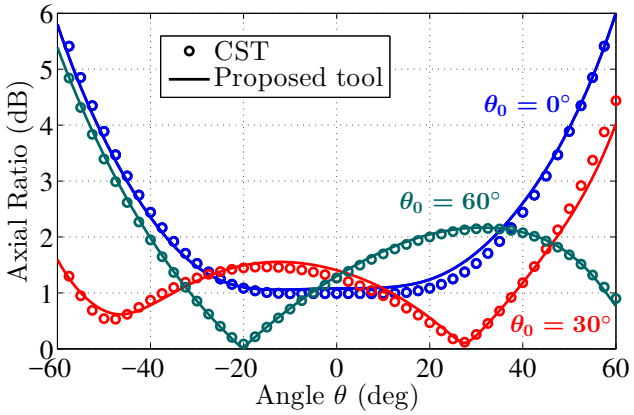

FIGURE 2.10: Axial ratio versus angles θ along the plane at $\phi = 0°$ at $f_0 = (f_{min} + f_{max}/2)$. The slots are air-filled and radiate in free space. The slot width is $a = 0.5\lambda_{max}$ and the array periodicity $d = 1.07a$.

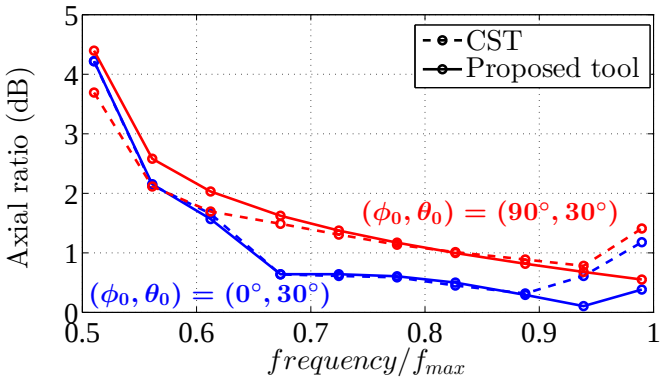

(a) AR versus frequency along the main planes at $\theta_0 = 30°$.

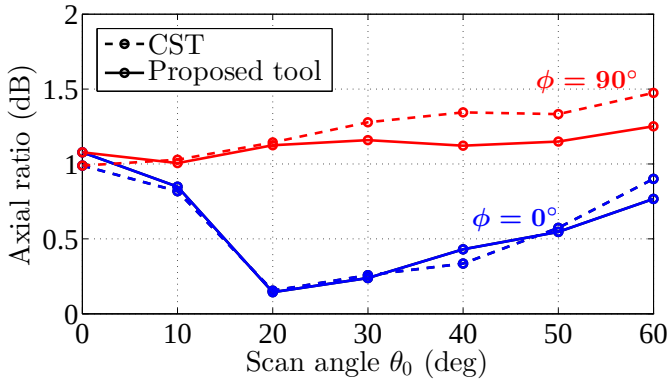

(b) AR versus scan angles θ_0 at $f_0 = (f_{min} + f_{max})/2$.

FIGURE 2.11: (a) Axial ratio versus frequency along the main planes at $\theta_0 = 30°$ and (b) versus scan angles θ_0 at $f_0 = (f_{min} + f_{max})/2$. The parameters used in the simulation are $a = 0.5c/\left(f_{min}\sqrt{\epsilon_{r1}}\right)$, and $d = 1.07a$.

infinite array and BW_θ for the scanning range at $f_0 = (f_{min} + f_{max})/2$. This summary relates to the beam-steering in the plane $\phi = 90°$, which is the one constantly devoid of grating lobes.

TABLE 2.1: PERFORMANCE OF PROPOSED CTS SOLUTION

	$\mathbf{BW}_f$ (%)	$\mathbf{BW}_\theta$
$S_{act} < -10$ (dB)	48.8 *	$\pm 51.9°$ **
$AR < 3$ (dB)	58.1 *	$\pm 90°$ **
$AR < 1.5$ (dB)	39.5 *	$\pm 60°$ **

* Elevation direction: $\theta_0 = 30°$;
** At $f_0 = (f_{min} + f_{max})/2$.

2.4 Design guidelines

This section discusses the choice of key design parameters and investigates the maximum achievable performance of over-moded CTS arrays in terms of bandwidth, scanning range, and AR. This study relies on extensive parametric analyses performed using the fast in-house tool presented and validated.

2.4.1 Antenna matching

The impact of the geometry on the antenna matching is the subject of this section. Over-moded CTS arrays exhibit an active reflection coefficient highly dependent on the width of the slots and their spatial periodicity. In the following, we will focus on the ratio d/a between the array periodicity and the width of the slots. A parametric study is performed by sweeping the value of d/a and observing its impact on the active reflection coefficients under TEM and TE_1 operation, respectively. We take as a representative example a structure comprising air-filled PPWs radiating in free space, i.e., $\epsilon_{r1} = \epsilon_{r2} = 1$. The performance of the array is evaluated for different scan angles in the planes $\phi = 0°$ and $\phi = 90°$. This study is carried out using the numerical tool presented earlier in this Chapter, which provides fast and accurate results for the active S-parameters. Assuming the array is fed by either a TEM or a TE_1 mode, the active reflection coefficients are plotted in Fig. 2.12. Let us remind

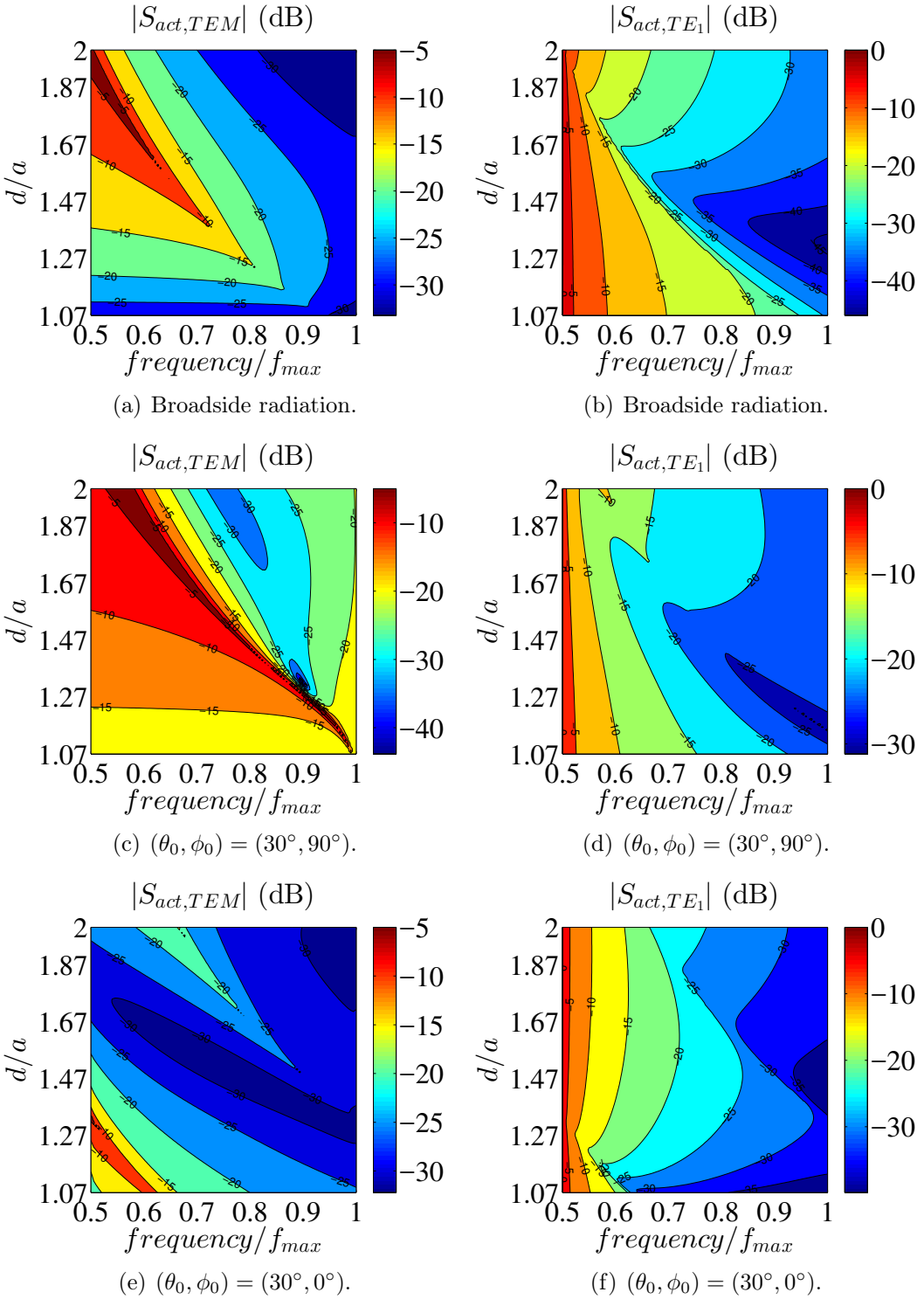

(a) Broadside radiation.

(b) Broadside radiation.

(c) $(\theta_0, \phi_0) = (30°, 90°)$.

(d) $(\theta_0, \phi_0) = (30°, 90°)$.

(e) $(\theta_0, \phi_0) = (30°, 0°)$.

(f) $(\theta_0, \phi_0) = (30°, 0°)$.

FIGURE 2.12: Maps of the active S-parameter as a function of frequency and the ratio d/a for (a), (c), (e) TEM and (b), (d), (f) TE_1 modes. The air-filled PPWs radiate in free space. Several scan angles in the planes $\phi_0 = 0°$ and $\phi_0 = 90°$ are considered.

that the width of the slots a of the proposed CTS array must be such that $\lambda/2 < a < \lambda$. This fact indicates that the active S-parameters may no longer

be frequency-independent in the plane $\phi = 90°$, as for the case studied in [5]. In fact, the maps in Fig. 2.12 indicate that the best value of the ratio d/a is strongly dependent on the scanning range and the bandwidth one would like to achieve.

At broadside, the best matching for the TEM mode is obtained by choosing $d/a \to 1$, as shown in Fig. 2.12(a), whereas for TE_1 mode by value of d/a as large as possible [refer to Fig. 2.12(b)]. In particular, the active reflection coefficient remains below -10 dB by choosing d/a such that $1 < d/a \leq 1.4$, in case of TEM mode excitation. When the array is fed by TE_1 modes, the best input matching is conversely reached out for $d/a \approx 1.92$. Thus, the stricter constraint is imposed by the TEM mode configuration and a good trade-off sizing is found by choosing $d/a \approx 1.4$.

In scanning, let us focus on the $\phi = 90°$ plane where no grating lobes occur. As shown in Figs. 2.12(c) and (d), the trend is the same as for broadside radiation. In this case, $|S_{act}| < -10$ dB is given by $d/a \approx 1.1$ for TEM mode and $d/a \approx 1.96$ for TE_1 mode. This means that the ratio d/a, for which achieving the largest bandwidth operation, is here given by $d/a \approx 1.1$. For the sake of completeness, we report also the maps along the plane $\phi = 0°$ in Figs. 2.12(e) and (f).

2.4.2 Circular polarization

The behavior of the AR, as a function of frequency and d/a ratio, is finally investigated to outline design guidelines for highly-pure CP radiation. The slots are still considered as being air-filled and radiating in free space, i.e., $\epsilon_{r1} = \epsilon_{r2} = 1$. Fig. 2.13(a) reports the parametric study when the array is steering the beam at broadside, whereas Fig.2.13(b) shows the results for the pointing angle $(\phi_0, \theta_0) = (90°, 30°)$. We can first notice that the AR worsens as the scan angle θ_0 is different than zero. The AR also decreases when $f/f_{max} \to 1$, given that the TE_1 cut-off frequency is enforced at the lowest frequency. It is also worth noting that this condition mitigates issues due to the dispersion between the TEM and TE_1 modes within the PPWs.

The results above imply that the AR performance improves as the ratio d/a is such that $d/a \to 1$. This intuitive trend is because a smaller array periodicity implies lower sidelobe levels in the far-field zone. However, as discussed in

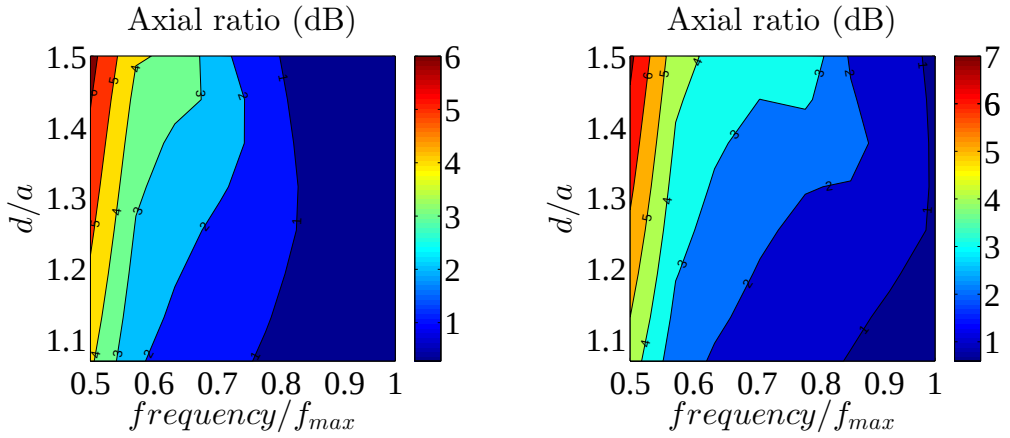

(a) Broadside radiation.

(b) $(\theta_0, \phi_0) = (30°, 90°)$.

FIGURE 2.13: Maps of the AR as a function of frequency and the ratio d/a. The air-filled PPWs radiate in free space. (a) Broadside array. (b) Array steering the beam at $\theta_0 = 30°$ along the plane $\phi_0 = 90°$.

Section 2.4.1, low values of d/a penalize the input matching when the array is excited by the TE_1 mode, especially at low frequencies. Thus, the optimal sizing relies on specific design goals and a trade-off occurs. A practical case-of-study is discussed in Section 2.5.

2.5 Over-moded CTS array in Ka-band

The goal of this section is to propose a possible design in Ka-band using the guidelines provided in Section 2.4. The antenna performance is observed in the frequency range 20-40 GHz. As a case-of-study, the dual-mode CTS array consists of four air-filled radiating slots that radiate in free space at first. The length of the slots along y-axis is $d_y = 5\lambda_{max} \sim 74.9$ mm, whereas their width is $a = 0.5c/f_{min} \sim 7.49$ mm. About the choice of the array periodicity d, a trade-off occurs between the input matching and AR performance, as detailed in the previous Section 2.4. Recalling the argumentation in Section 2.4.1, the best geometrical sizing in terms of matching is given by $1.1 < d/a < 1.4$, while scanning along the plane $\phi = 90°$. On the contrary, the largest AR bandwidth operation is given by $d/a \to 1$ [refer to Section 2.4.2]. Thus, the best choice for the array periodicity is $d = 1.1a \sim 8.20$ mm. A schematic drawing of the structure is depicted in Fig. 2.14.

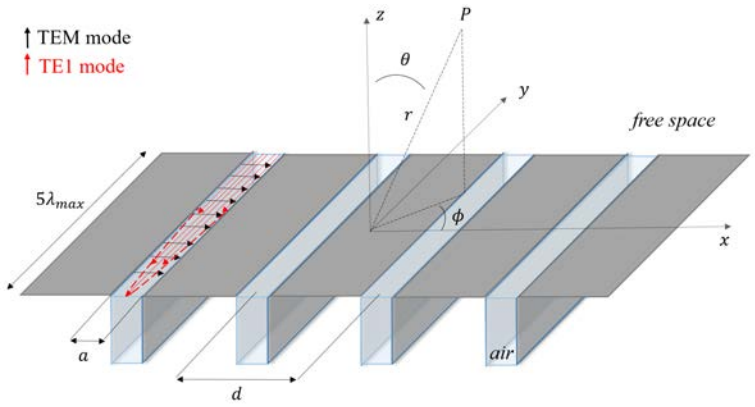

FIGURE 2.14: 3-D view of the finite-size over-moded CTS array.

The active reflection coefficient of the slots is displayed in Figs. 2.15(a) and (b) as function of both frequency and scan angles under TEM and TE_1 mode operation, respectively. Note that the active reflection coefficient is computed in

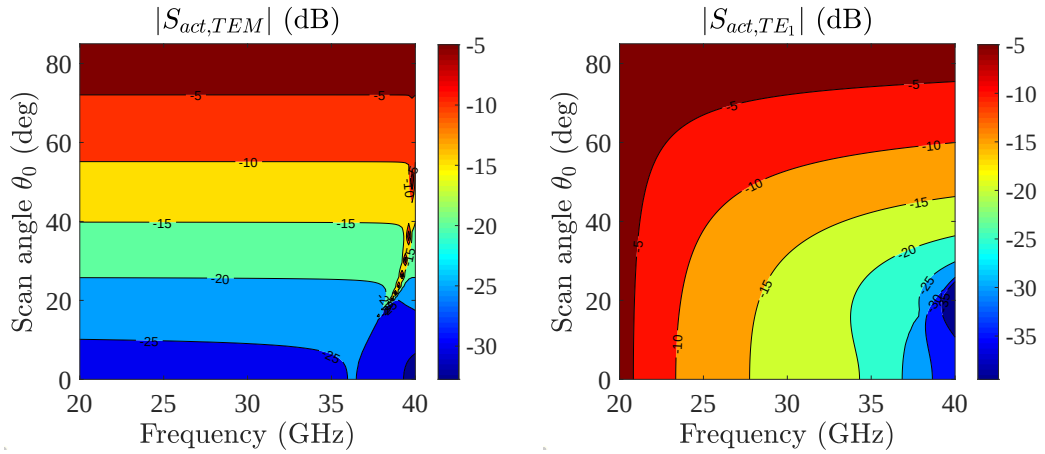

(a) TEM mode. (b) TE_1 mode.

FIGURE 2.15: Maps of the input reflection coefficient as a function of frequency and the scan angles θ_0. The air-filled PPWs radiate in free space. (a) TEM and (b) TE_1 mode operation. The array is steering the beam along the plane $\phi_0 = 90°$.

an infinite periodic environment. This is nonetheless a very good approximation because the large-array condition is considered [65]. Fig. 2.15(a) confirms the flat behaviour of the active reflection coefficient under TEM mode operation. This result is also valid in a monomodal enviroment, as detailed in [5]. As shown in Fig. 2.15(b), the TE_1 mode operation limits the antenna performance, as its frequency response worsens at lower frequencies due to the location of the TE_1 cut-off frequency at $f_{min} = 20$ GHz. Furthermore, the input reflection coefficient worsens in scanning for both modes. It consequently follows that the largest

bandwidth operation is reached out at broadside, where the relative bandwidth is about 52.9%. Besides, a wide scanning range is observed as well. Indeed, the active reflection coefficient $|S_{act}|$ is below -10 dB over a 40.8% relative bandwidth when the array steers its main beam at $\theta_0 = 45°$ in the plane $\phi = 90°$ [see Fig. 2.15].

The E-field polar components are calculated using the windowed approach, as detailed in Section 2.3.1, and are plotted at the central frequency $f_0 = 30$ GHz for different scan angles in Figs. 2.16(a) and (b). The far-field pattern is calculated at the radial distance $r = 2\lambda_{max}$ [refer to Fig. 2.1]. The AR is also plotted as function of the scan angle θ_0 in Fig. 2.16(c). About ~ 3 dB scan losses are observed while pointing at 45° in the plane $\phi = 90°$, as shown in Figs. 2.16(a) and (b). The proposed dual-mode CTS array is then classifiable as wide-scanning antenna [77]. It is also clearly shown in Figs. 2.16(a) and (b) that the two modes radiate two far-field orthogonal components. This is straightforward when looking at the end-fire radiation: the E_ϕ exhibits a null in the radiation pattern at the end-fire direction, given that the TE_1 mode has a cosine-like profile over the x-axis direction of the slots, i.e., null at the edges; the E_θ is conversely non-null at the end-fire direction, since the TEM mode has an uniform distribution along the radiating slots. Note also that the scanning range for which AR$<$ 3 dB is up to $\pm 76°$ at 30 GHz in the plane $\phi = 90°$, as plotted in Fig. 2.16(c).

Besides, the AR is plotted as a function of frequency and scan angle θ_0 in Fig. 2.17. By varying the scan angle along the plane $\phi = 90°$, the AR is computed in the pointing direction of the array. The results show that the AR frequency bandwidth is stable almost all over the entire scanning range of investigation. In other words, the AR does not significantly deteriorate while scanning. This is clearly visible from Fig. 2.16(a) and (b): the maximum amplitude of the two far-field orthogonal components is reduced simultaneously in scanning. As shown in Fig. 2.16(c), the AR is generally below 3 dB around the pointing angle of the array. Finally, dual-mode CTS arrays typically radiate highly-pure CP waves and its performance is mainly curtailed by the matching due to TE_1 mode operation.

In conclusion, it is worth noting that the antenna matching might be improved by placing dielectric layers on the top of the slots. This technique is

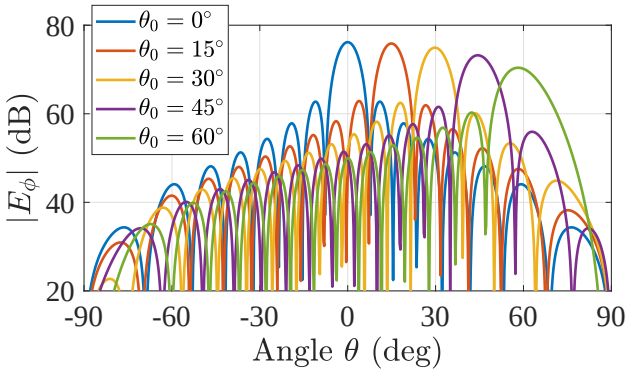

(a) $\phi-$component.

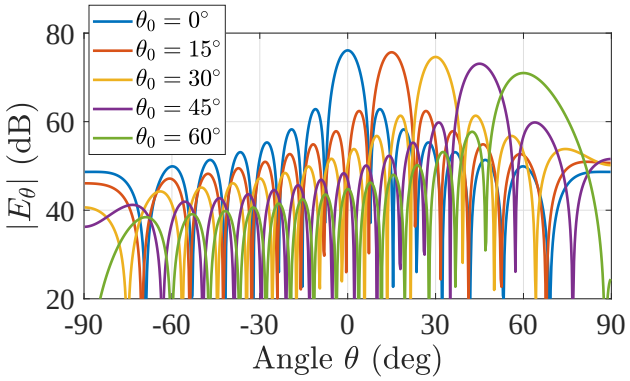

(b) $\theta-$component.

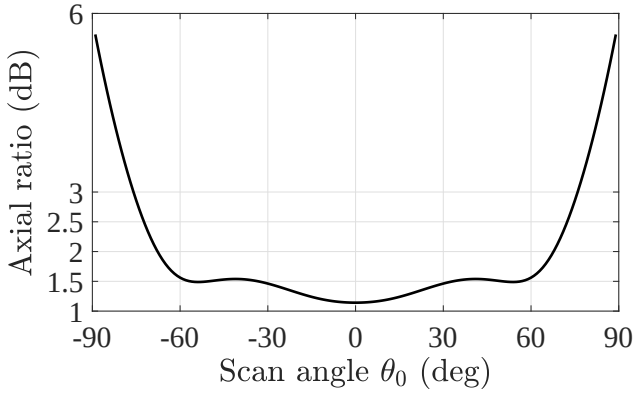

(c) Axial ratio.

FIGURE 2.16: (a), (b) Polar components of the radiation pattern at the frequency $f_0 = 30$ GHz for different scan angles. (c) Axial ratio versus scan angle θ_0 at the frequency $f_0 = 30$ GHz. The array is steering the beam along the plane $\phi_0 = 90°$.

referred to as wide-angle impedance matching (WAIM) and is well established in the literature [78]. For instance, Fig. 2.7(a) shows that the placement of a dielectric layer with $\epsilon_{r2} = 2$ slightly enlarges the antenna matching, when the slots are parallel-fed by TE_1 mode.

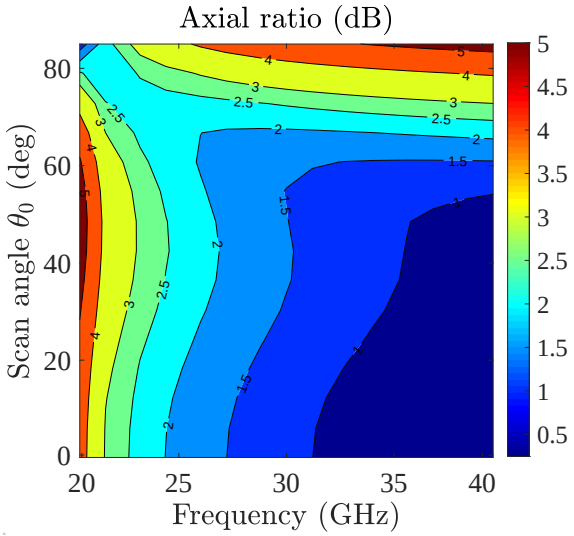

FIGURE 2.17: Axial ratio as a function of frequency and scan angle θ_0. The air-filled PPWs radiate in free space. The array is steering the beam along the plane $\phi_0 = 90°$.

2.5.1 Input power division for optimal operation

Hitherto, we have analyzed the radiation properties of over-moded CTS arrays considering the input power as equally-launched into the feeding TEM and TE_1 mode. In this scenario, the voltages used for the excitation are given by (2.44), corresponding to a unitary overall input power, i.e., $P_{tot} = 1$ W. It is worth investigating other scenarios considering a non-balanced distribution of the input power between the feeding modes. Indeed, the equal power division might not be the optimum split, achieving the largest impedance bandwidth and the highest CP purity. To this purpose, the amplitudes of the impinging modes can be optimized in order to further improve the AR performance of the antenna. The amplitudes of the voltage waves of the input modes are related to their power ratio as follows

$$V_{inc}^{TE_1} = V_{inc}^{TEM} \sqrt{\frac{Z_1^{TE}}{\eta_0}} \sqrt{\frac{P_{TE_1}}{P_{TEM}}} \tag{2.45}$$

where η_0 and Z_1^{TE} are the free space and TE_1 mode characteristic impedances, respectively, whereas P_{TEM} and P_{TE_1} are the input power of TEM and TE_1 modes, respectively. By enforcing the amplitude of TEM mode V_{inc}^{TEM} such that the maximum input power is $P_{tot} = P_{TEM} + P_{TE_1} = 1$ W, the ratio P_{TE_1}/P_{TEM} is varied and the AR monitored. In Fig. 2.18(a), the frequency behaviour of the

dual-mode CTS array is studied, when the beam is steered at broadside. In Fig.

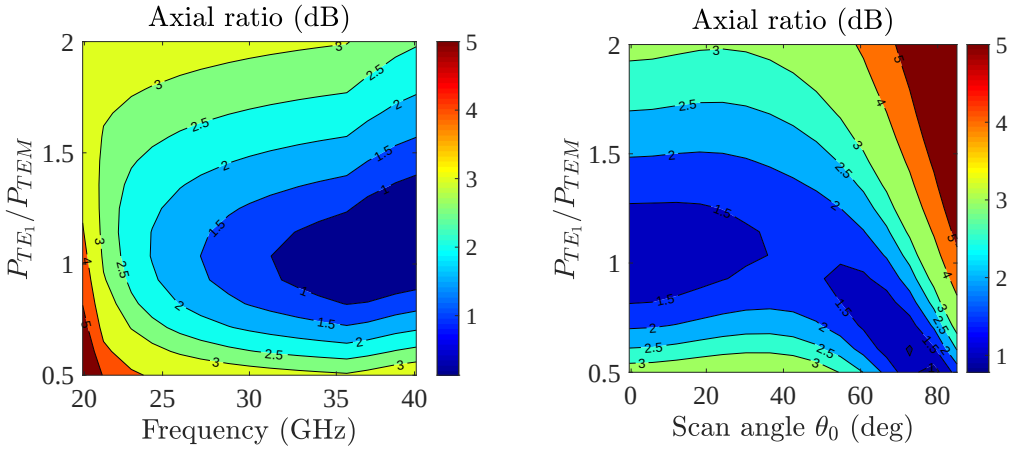

(a) Broadside radiation.

(b) $f_0 = 30$ GHz.

FIGURE 2.18: Maps of the AR as function of the power ratio P_{TEM}/P_{TE_1} and (a) frequency for broadside radiation or (b) scan angle θ_0 at the central frequency $f_0 = 30$ GHz. The air-filled PPWs radiate in free space. The array is steering the beam along the plane $\phi_0 = 90°$.

2.18(b) the AR is plotted versus the scan angle θ_0 at the central frequency $f_0 = 30$ GHz. From Fig. 2.18(a), it turns out that the best power split is achieved for $P_{TE_1}/P_{TEM} \sim 1.1$, which is rather close to the case analyzed previously (i.e., equal power division between the two feeding modes). While scanning at a defined frequency of operation, e.g., 30 GHz, it conversely emerges that the optimum power split for maximizing the antenna field-of-view is given by $P_{TE_1}/P_{TEM} \sim 0.82$, as shown in Fig. 2.18(b). However, the input matching of the antenna is satisfactory up to $\pm 45°$ in the plane $\phi = 90°$, as explained in Section 2.5. Such a scanning range is easily achieved for equal power division between the TEM and TE_1 modes. Specifically, the proposed dual-mode CTS array exhibits an AR lower than 3 dB up to $\pm 75.8°$ at the central frequency $f_0 = 30$ GHz when $P_{TE_1}/P_{TEM} = 1$. The setting of the ratio P_{TE_1}/P_{TEM} depends thus on the antenna requirements. From the physical design standpoint, an equal division of the input power represents the easiest solution. This is the reason why we will focus on the condition $P_{TE_1}/P_{TEM} = 1$ hereinafter.

2.5.2 Swallow-tail feeder

Throughout the analysis up to here reported, the two desired modes are excited on the aperture and no attention is paid to the design of a dedicated feeder. Hence, it follows a discussion about structures that realize the feeding of the over-moded stubs. A three dimensional (3-D) view of the long slot array is shown in Fig. 2.19. The structure comprises open-ended stubs of width $a = 7.2$

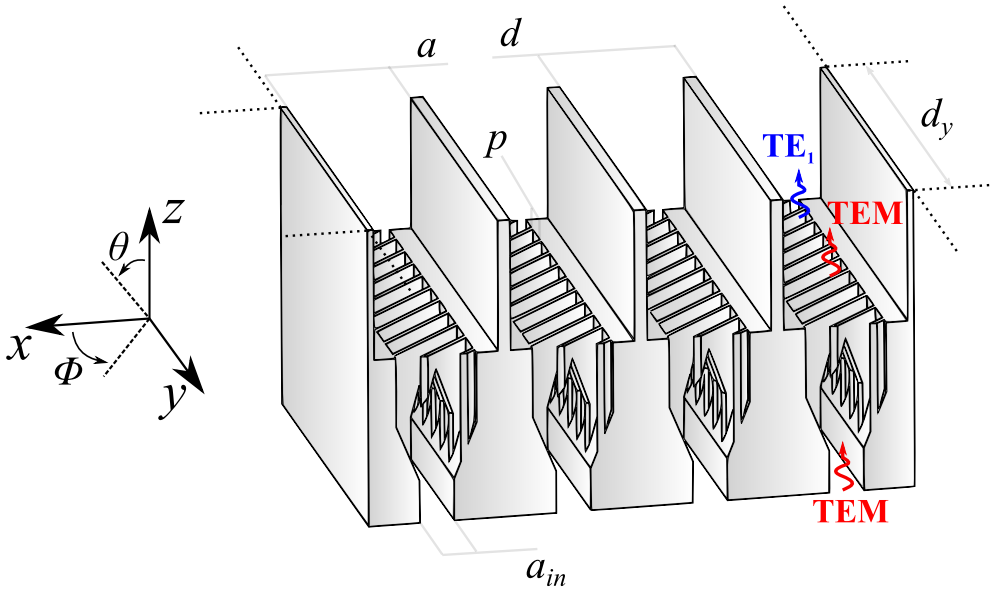

FIGURE 2.19: 3-D view of the finite-size over-moded CTS array comprising the structure used to feed the two modes. Geometrical parameters: $a = 7.2$ mm, $d = 1.1a$, $p = 2.3$ mm, $a_{in} = 2$ mm, and $d_y = 229.5$ mm.

mm. The stubs are over-moded and support the propagation of the TEM and TE_1 modes. The width of the long slots is slightly different with respect to that considered at the beginning of this section. This is due to guarantee an optimal operation of the structure in Ka-band in presence of the proposed feeder. The slots' length along y-axis is assumed to be $dy = 22\lambda_0$, with λ_0 being the wavelength at 29 GHz. This setting is to ensure a high-gain operation of the antenna which is mandatory to SatCom applications [1, 16]. Also, the radiating stubs are arranged in a periodic configuration of period $d = 1.1a$.

The feeding structure consists of a periodic grid of period $p = 2.3$ mm that is 45°-oriented with respect to x- and y-axes [see Fig. 2.19]. As shown in the plane-cut Σ_4 in Fig. 2.20(a), the shape of each grid's element along z-axis resembles a swallow's tail. We will thus employ this label to refer to it hereinafter. The geometry of the swallow-tail transition was obtained through an optimization

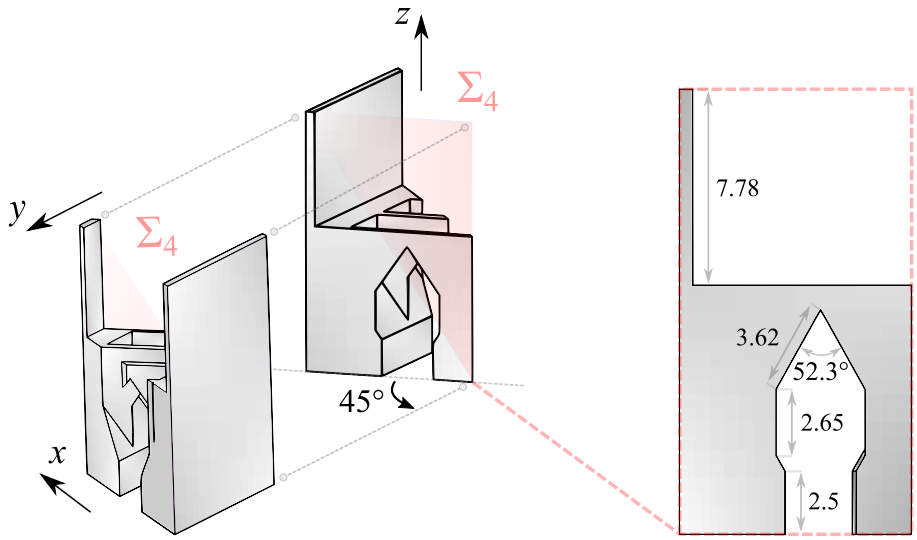

(a) Geometry of the swallow-tail feeder.

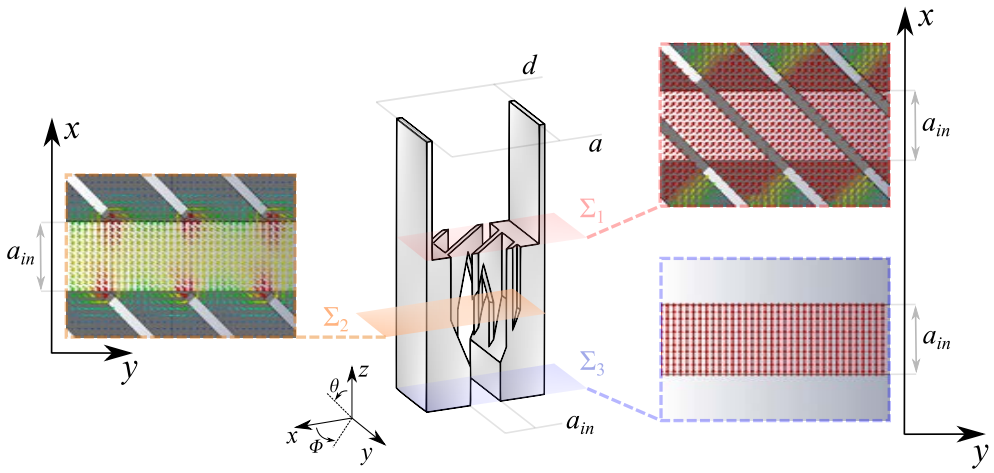

(b) Full-wave simulations of the swallow-tail feeder.

FIGURE 2.20: (a) Geometry of the swallow-tail feeder. The plane-cut Σ_4 is 45°-oriented with respect to x-axis. All dimensions are in given in millimeters. (b) Simulation E-field into the feeder's unit cell. The E-fields lines are plotted at several sections along z-axis.

procedure using [72]. All the details are reported in Fig. 2.20(a). The working principle of the swallow-tail feeder is shown in Fig. 2.20(b), by simulating the array's unit cell using the full-wave commercial software [72]. The bottom-most PPW is mono-modal (a_{in} = 2 mm) and supports the propagation of a TEM mode that is polarized along x-axis. The E-field distribution is plotted on the plane-cut Σ_3 in Fig. 2.20(a). While propagating along z-axis, the E-field lines are gradually rotated (plane-cut Σ_2 in Fig. 2.20(b)) to achieve a 45°-oriented polarization at the section where the grid meets the open-ended stub [see section

Σ_1 in Fig. 2.20(b)]. Given the E-field is 45°-polarized with respect to x- and y-axes, the input power will be approximately equally-launched into the TEM and TE_1 modes.

The set-up simulation of the array's unit cell is shown in Fig. 2.21. A waveguide port is used to launch a TEM mode into the input PPW of height a_{in}. The structure is simulated using the commercial software [72] in a periodic

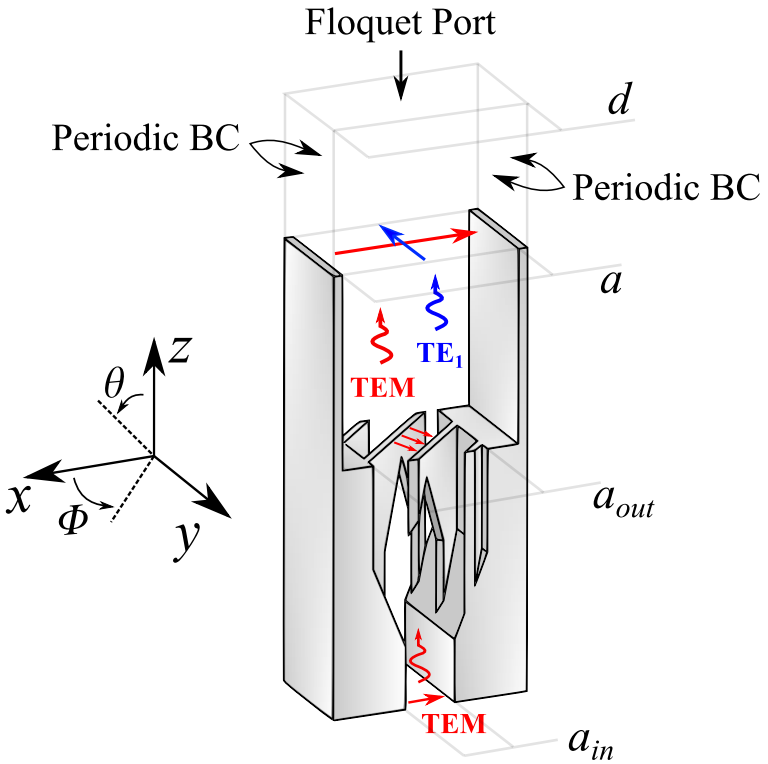

FIGURE 2.21: Unit cell of the over-moded CTS array. The structure is periodic along x- and y-axes. Period boundary conditions are placed on the lateral faces of the cell. Finally, a Floquet's port is placed on the top of the air box to account for the radiated fields in a periodic environment. Geometrical settings: $a = 7.2$ mm, $d = 1.1a$, $a_{in} = 2$ mm, and $a_{out} = 4.66$ mm.

environment. Periodic boundary conditions are, hence, enforced on the lateral faces of the unit cell. A Floquet's port was placed on the top of the radiating box. The radiated fields are then computed considering the radiation of a single cell and employing a superimposition of Floquet's harmonics. A graphical illustration of the E-field line orientation is also reported in Fig. 2.21. The TEM and TE_1 modes are polarized along x- and y-axes, respectively, and thus can be excited using the feeding grid that exhibits E-fields 45°-polarized with respect to them. The simulated active input reflection coefficient is shown in Fig. 2.22 for broadside radiation. The reflection coefficient is below -16 dB all over the

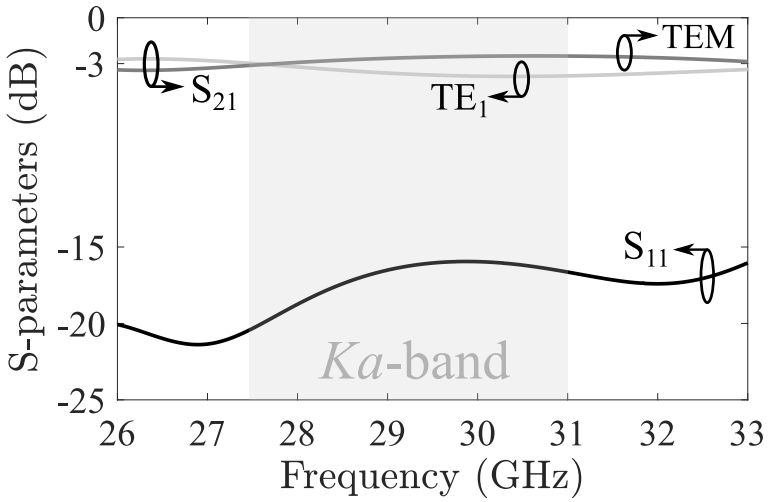

FIGURE 2.22: Simulated active reflection coefficient of the CTS array's unit cell. The transmission coefficient is also reported in order to observe the input power's division between the TEM and TE_1 modes. The results refer to broadside radiation.

Ka-band. The transmission coefficient was also computed with respect to TEM and TE_1 modes, by using an S-parameters analysis linking the feeding TEM mode and the two fundamental Floquet's harmonics. It can be observed that the transmission coefficient settles around -3 dB, meaning the input power is equally distributed between the two orthogonally-polarized modes. By post-processing the radiated fields, the CP purity is estimated in terms of AR. This analysis was carried out for different scan angles θ_0 over the frequency band of interest. The simulated results are reported as a contour plot in Fig. 2.23. A very high CP purity (i.e., AR $>$ 3 dB) is observed in the Ka-band over a scanning range up to $\pm 20°$. Note that the scanning range is found to be very much reduced with respect to the theoretical one observed in Fig. 2.17. This is due to the presence of the swallow-tail feeder and of a finite-size height of the open-ended radiating stubs. As mentioned earlier, dual-mode CTS arrays suffer from the dispersion behavior of the radiating modes. This effect degrades the antenna performance in scanning, due to the different electrical path lengths traveled by the two orthogonal modes. This problem can be solved by a properly engineered dispersion of this class of arrays. This analysis is reported in Chapter 3.

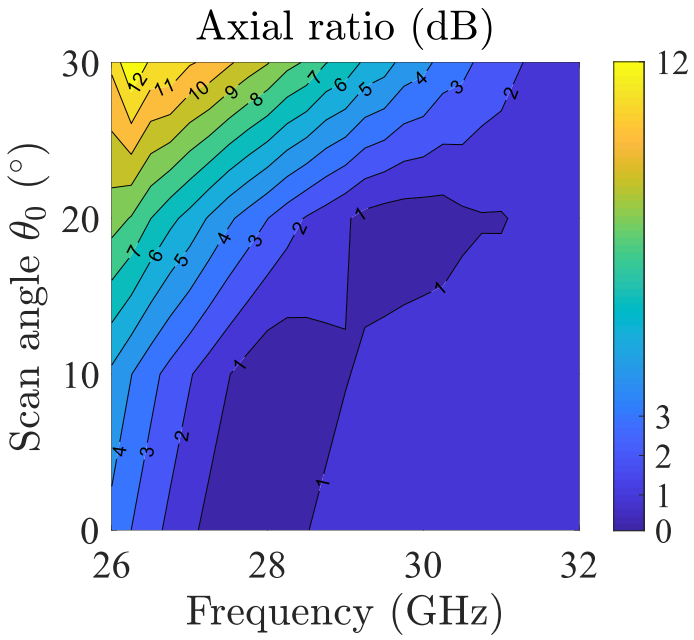

FIGURE 2.23: Simulated axial ratio of the CTS array's unit cell as a function of the frequency and scan angle θ_0. The antenna array is steering the beam along the yz-plane [see Fig. 2.21].

2.5.3 Corporate feed network

The radiating open-ended stubs are parallel-fed by a corporate feed network (CFN) made of mono-modal PPWs. Specifically, each pair of PPWs is excited by a 1-to-2 way, equal split power divider. Assuming N slots (N must be a power of two), the number of power dividers N_{T-jun} is given by

$$N_{T-jun} = \sum_{n=0}^{\log_2(N)-1} 2^n \tag{2.46}$$

The antenna architecture recalls that proposed in [6]. Its cross-section along

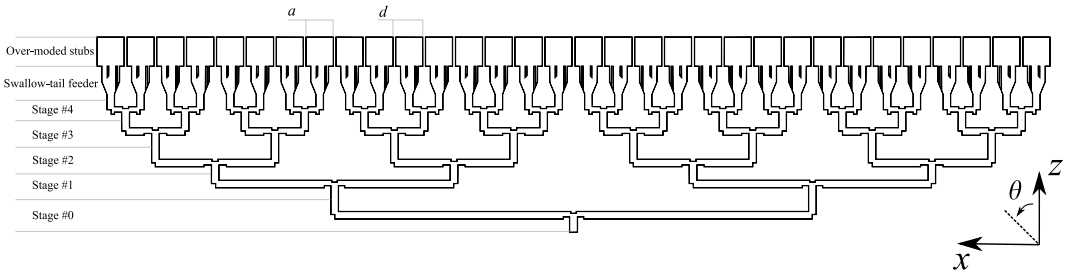

FIGURE 2.24: Cross sectional view of the over-moded CTS array along the xz plane-cut. The antenna architecture comprises $N = 32$ radiating slots and a parallel feed network made of 1:2 power dividers in PPW technology.

the xz-plane is shown in Fig. 2.24. Specifically, the number of radiating slots is $N = 32$, in order to achieve a very high directivity around the pointing direction of the array. In Fig. 2.25, the antenna directivity is calculated using the in-house tool and the full-wave simulator [72]. Specifically, the patterns

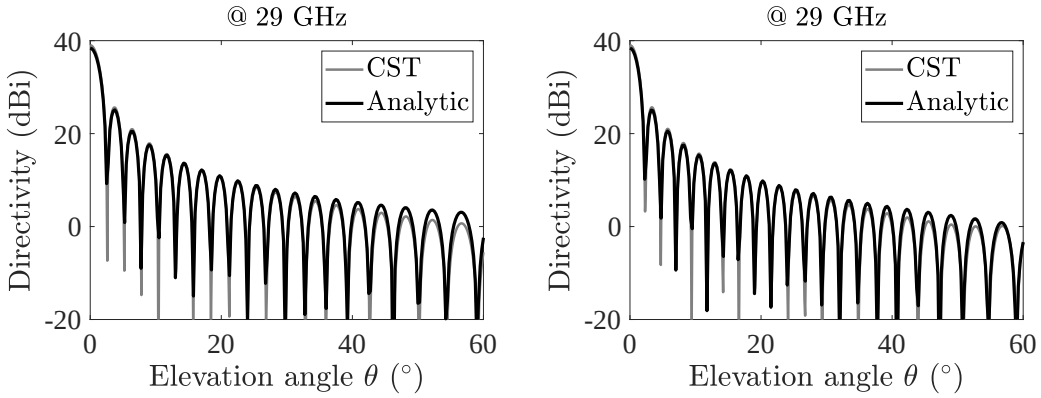

(a) yz-plane. (b) xz-plane.

FIGURE 2.25: Calculated directivity patterns of the over-moded CTS array at 29 GHz. (a) yz-plane. (b) xz-plane.

refer to the cuts along the yz- and xz-planes at 29 GHz in Figs.2.25 (a) and (b), respectively. The array is steering the beam from the broadside direction. The analytic computation accounts for the model introduced in Section 2.3 and makes use of a rectangular widowing function to truncate the magnetic current along y-axis. The agreement is excellent. The directivity peak is found to be about 39 dBi in the pointing direction of the array.

The number of 1-to-2 way power dividers is calculated using (2.46), thus yielding to $N_{T-jun} = 31$. Each power divider exhibits the same topological structure, whose schematic along the xz-plane is depicted in Fig. 2.26. The

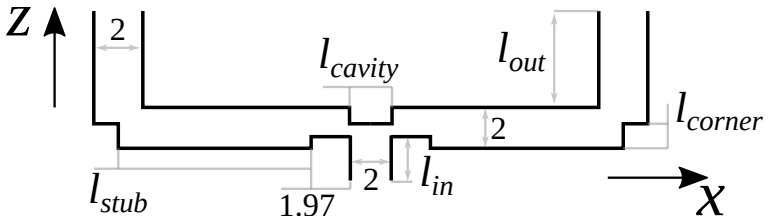

FIGURE 2.26: 1-to-2 way, equal split power divider. All dimensions are given in millimeters.

geometrical parameters associated to each stage are listed in Table 2.2. The design of the 1:2 power dividers is very straightforward. The initial dimensions are obtained following the approach proposed in [6]. Afterwards, they have been

tuned to improve the input matching offered by the CFN. The simulations were carried out in a periodic environment using the commercial software [72].

TABLE 2.2: GEOMETRICAL PARAMETERS OF THE 1:2 POWER DIVIDERS FOR EACH STAGE. ALL DIMENSIONS ARE GIVEN IN MILLIMETERS

Stage	l_{stub}	l_{cavity}	l_{in}	l_{out}	l_{corner}
# **0**	60.5	1.39	4.00	3.42	1.17
# **1**	28.8	1.39	3.42	2.05	1.17
# **2**	12.8	1.59	2.05	3.43	1.07
# **3**	4.88	1.59	3.43	2.07	1.14
# **4**	0.88	1.59	2.07	n.a.	1.18

2.5.4 Pillbox beam-former

The antenna array is fed by a quasi-optical system and, specifically, a pillbox coupler [6, 20, 30]. This is connected to the open-ended PPW of Stage #0 [see Fig. 2.24]. The structure consists of two stacked PPWs. A parabolic reflector is embedded in the bottom PPW. Cylindrical waves are launched onto the parabola using H-plane horns, yet integrated into the bottom PPW. After being reflected, the field is coupled to the upper-most PPW via etched slots. The cylindrical waves are so converted into plane ones. This type of feeding system is very interesting because it allows generating a continuous line source, with a gradually-phased distribution along the y-axis. The latter is achieved by displacing the feeding horns in the y-axis direction along the focal line of the parabola. The structure is not here reported as it is identical to that used in [6]. From the E-field distribution provided by the pillbox along the y-axis, one can predict the radiation of the CTS array. For instance, the in-focus horn illuminates the parabola resulting in a boresight radiation. The E-field distribution along y-axis in the upper PPW of the pillbox system has been carried out through full-wave simulations and it is reported in Fig. 2.27. The -10-dB-tapered area indicates the illuminated area on the long slots that contributes to the radiation. The maximum fluctuation of the E-field phase is found to be about 25° within the -10-dB-tapered area. The array's radiation can be predicted using the model proposed in Section 2.3. Hence, the pillbox's E-field

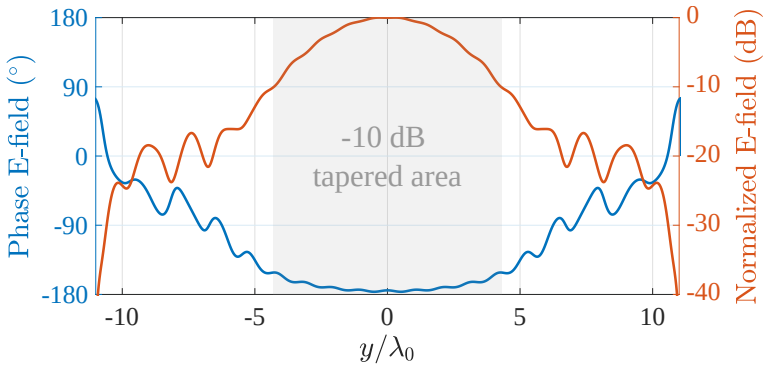

FIGURE 2.27: E-field distribution along y-axis in the upper PPW of the pillbox system. The parabola is illuminated by the in-focus horn for boresight radiation. λ_0 is the free-space wavelength at 29 GHz.

distribution must be considered as windowing function to obtain more realistic results. In formulae, equation (2.41) is to be replaced by

$$\tilde{\mathbf{M}}_{\mathbf{w}}(k_x, k_y) = \mathfrak{F}\left\{\mathbf{M_t}(x, y)|E_{taper}\,(y)\,|\textstyle\prod_{N_{slots}a}(x - a/2)\right\} \tag{2.47}$$

that extends the truncation of the magnetic current to more general scenarios. By using the E-field distribution in Fig. 2.27 as $E_{taper}(y)$ in (2.47), the analytic prediction of the patterns radiated by the long slot array is reported in Fig. 2.28. The patterns are calculated at 29 GHz for broadside radiation. The co-

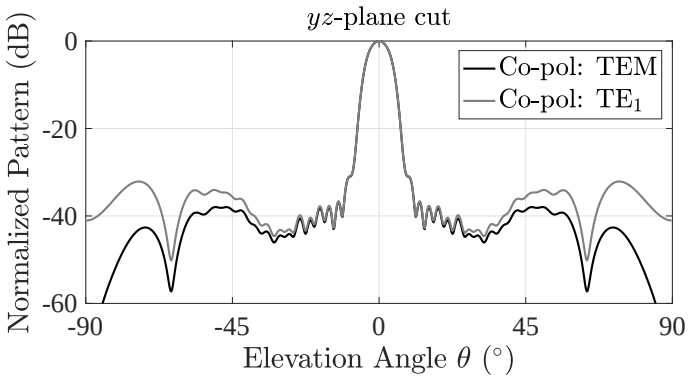

FIGURE 2.28: Computed radiation pattern at 29 GHz using an analytic calculation. The simulated E-field of the pillbox system has been used as windowing function.

polar components were computed according to the Ludwig's third definition [79,

80], yielding

$$\begin{matrix}\mathbf{E}^{\mathbf{TEM}}_{\mathbf{co\text{-}pol}}(r,\theta,\phi)\\ \mathbf{E}^{\mathbf{TE_1}}_{\mathbf{co\text{-}pol}}(r,\theta,\phi)\end{matrix} = E_\theta(r,\theta,\phi)\sin(\xi)\hat{\theta} + E_\phi(r,\theta,\phi)\cos(\xi)\hat{\phi} \tag{2.48}$$

where

$$\xi = \arctan\left(\left(\cos\theta\tan(\phi'-\phi)\right)^{-1}\right) \qquad \begin{cases} \phi' = 0 \quad if \quad TEM \\ \phi' = \pi/2 \quad if \quad TE_1 \end{cases} \tag{2.49}$$

In Fig. 2.28, the first side lobe levels (SLL) appears to be lower than -30 dB. The co-polar patterns also exhibit the same beam shape over a field-of-view up to $\pm 40°$ for both TEM and TE_1 modes.

For the sake of completeness, we report the same analysis when the antenna array performs scanning. In Fig. 2.29 the simulated E-field distribution of the pillbox system is shown. Note that the E-field phase distribution recalls a

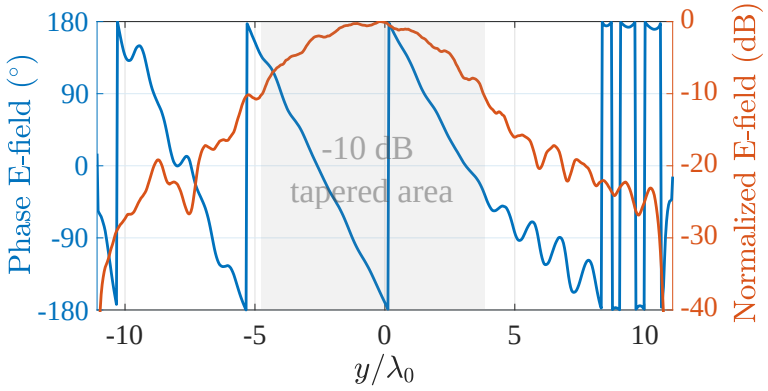

FIGURE 2.29: E-field distribution along y-axis in the upper PPW of the pillbox system. The parabola is illuminated by a displaced horn with respect to the focus in order to steer the beam around $\theta_0 = 10°$. λ_0 is the free-space wavelength at 29 GHz.

saw-tooth shape within the -10-dB-tapered area. This means that the slots are progressively phased to achieve beam scanning. The pillbox system is so able to generate a continuous excitation line by displacing the horn with respect to the focal point of the parabola. The pointing angle of the array can be computed as the derivative of the phase distribution in Fig. 2.29, thus yielding to a beam direction of about $\theta_0 = 10°$. The computed radiation patterns are reported in Fig. 2.30. The beams associated to TEM and TE_1 operations are very clear and directive. The first SLL is lower than -25.5 dB.

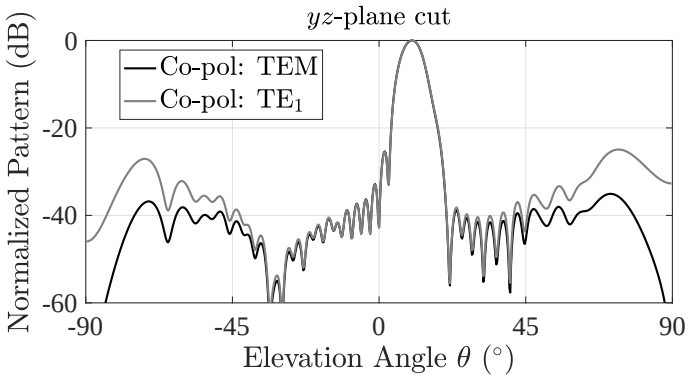

FIGURE 2.30: Computed radiation pattern at 29 GHz using an analytic calculation. The pointing angle of the array is about 10°. The simulated E-field of the pillbox system has been used as windowing function.

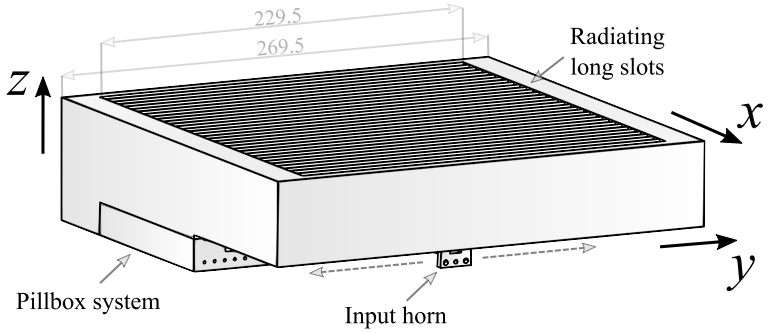

(a)

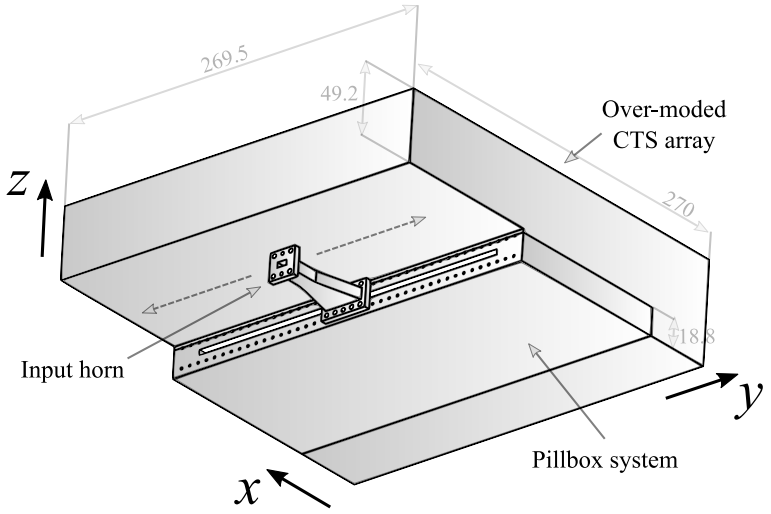

(b)

FIGURE 2.31: 3-D view of the antenna architecture. All dimensions are given in millimeters.

2.5.5 Antenna performance

The 3-D view of the final antenna architecture is depicted in Fig. 2.31. The CFN is connected to the pillbox system, whose parabola is illuminated by an H-plane horn. The horn is fed using a coaxial-to-WR28 connector, whose flange is shown in Fig. 2.31(b). The scanning performance is achieved by displacing the feeding horn along the y-axis, as schematically shown in Figs. 2.31(a) and (b).

The antenna system has been simulated using the full-wave simulator [81]. The reflection coefficient and the axial ratio are plotted in Figs. 2.32(a) and

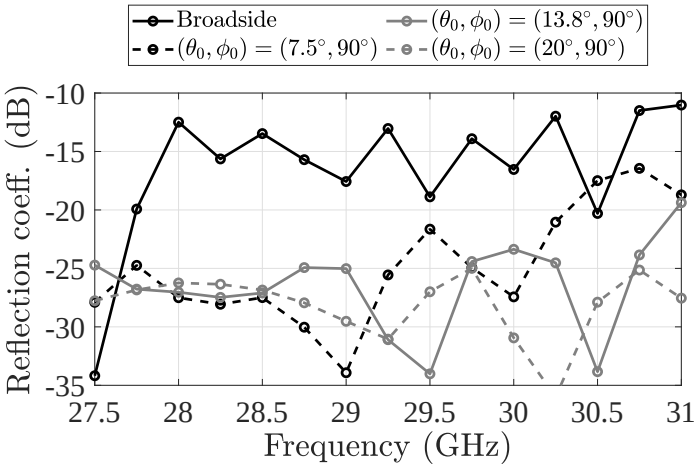

(a)

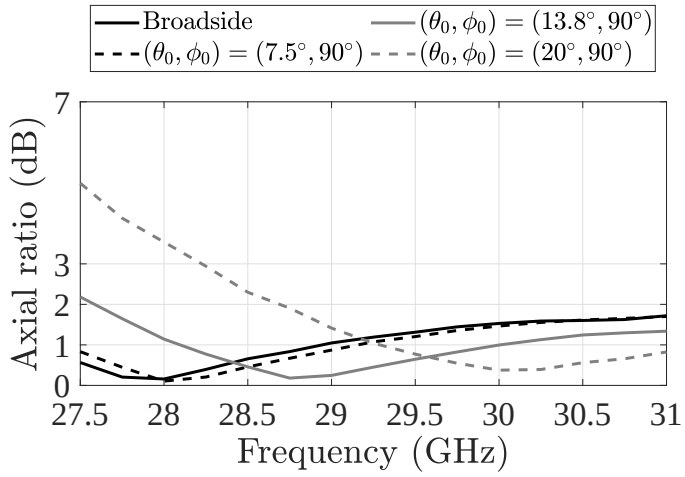

(b)

FIGURE 2.32: Simulated results of the over-moded CTS array in Ka-band. (a) Reflection coefficient. (b) Axial ratio. The antenna array scans along the yz-plane by displacing the input horn in the y-axis direction, as indicated in Fig. 2.31.

(b), respectively. The input reflection coefficient is below -10 dB, everywhere in the Ka-band. The worst scenario is obtained for the in-focus horn illumination, due to internal reflections of the quasi-optical system [6]. The pillbox design can be easily modified to enhance performances. A very high CP purity (AR below 3 dB) is observed all over the Ka-band. Fig. 2.32(b) specifically shows that a full coverage of the Ka-band is achieved for a scanning range up to $\pm 15°$. When the array steers the beam around 20°, the AR is less than 3 dB starting from 28.2 GHz. This effect has been exhaustively discussed earlier. It is thus a

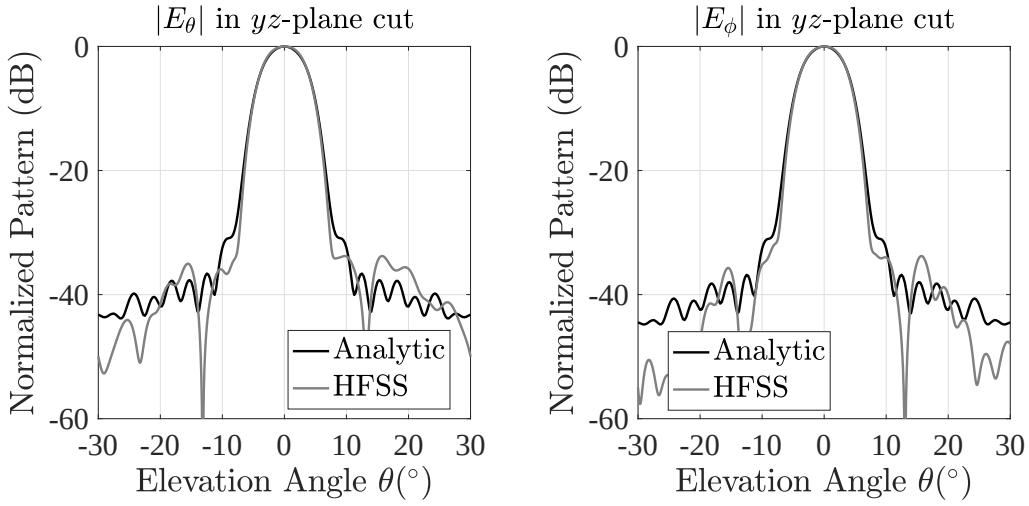

(a) Broadside.

(b) Broadside.

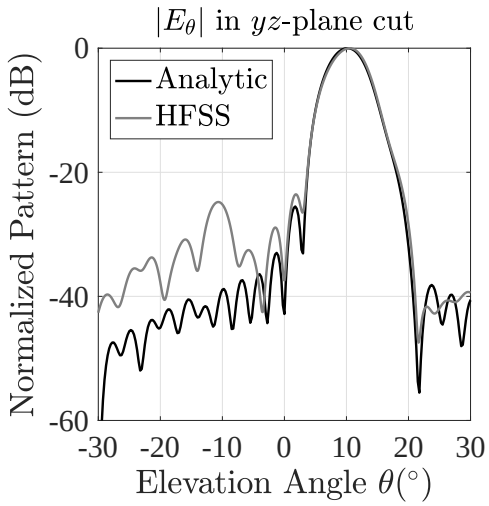

(c) $\theta_0 = 10°$.

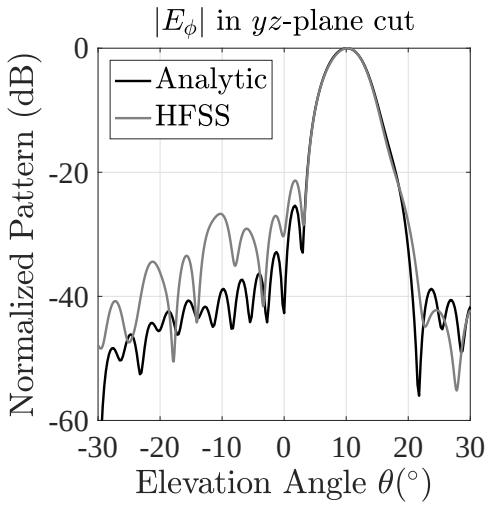

(d) $\theta_0 = 10°$.

FIGURE 2.33: Simulated and computed radiation patterns of the over-moded CTS array at 29 GHz. (a) and (b) Broadside radiation. (c) and (d) Pointing angle θ_0. The antenna array performs beam scanning along the yz-plane by displacing the input horn in the y-axis direction, as indicated in Fig. 2.31.

direct consequence of the variation due to dispersive behaviors of the two modes in propagation.

The radiation patterns of the antenna were calculated using the analytic model in Section 2.3 and validated by full-wave simulations. The E-field distribution of the pillbox system was used as windowing function (E_{taper} in (2.47)). The polar components are plotted in Figs. 2.33(a) and (b) for broadside radiation and in Figs. 2.33(c) and (d) for beam steering at $\theta_0 = 10°$ in the yz-plane. The computed main lobe is in excellent agreement with HFSS [81]. Eventual discrepancies are due to the fact that the analytic calculation does not consider edge effects deriving from the finiteness of the real structure. These results show that the developed numerical model represents a fast and accurate tool to predict the antenna performance. Also, these results show that very clear patterns are obtained in the yz-plane. The proposed antenna is, thus, able to radiate orthogonal components, without relying on any add-on device for polarization conversion. Furthermore, two orthogonal components are radiated having roughly the same amplitude, as shown in Fig. 2.34. These results

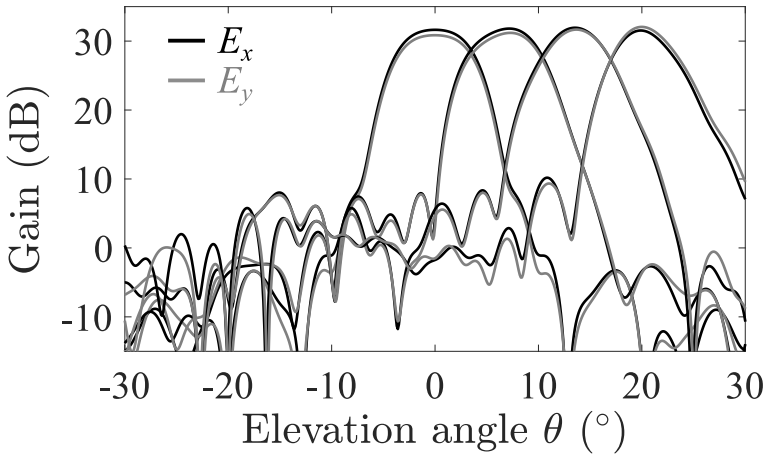

FIGURE 2.34: Simulated gain at 29 GHz. The pointing angle of the array is about 10°. The antenna array performs beam scanning along the yz-plane by displacing the input horn in the y-axis direction, as indicated in Fig. 2.31.

demonstrate that the proposed antenna can achieve dual-polarized radiation, by exploiting the electric properties of over-moded PPWs.

The pointing angle of the antenna array is very stable in frequency. Fig. 2.35 report the right-hand circularly-polarized (RHCP) patterns along the yz-plane as function of the elevation angle θ and the frequency for four radiated beam. Each pattern is normalized to its maximum. The simulations refer to

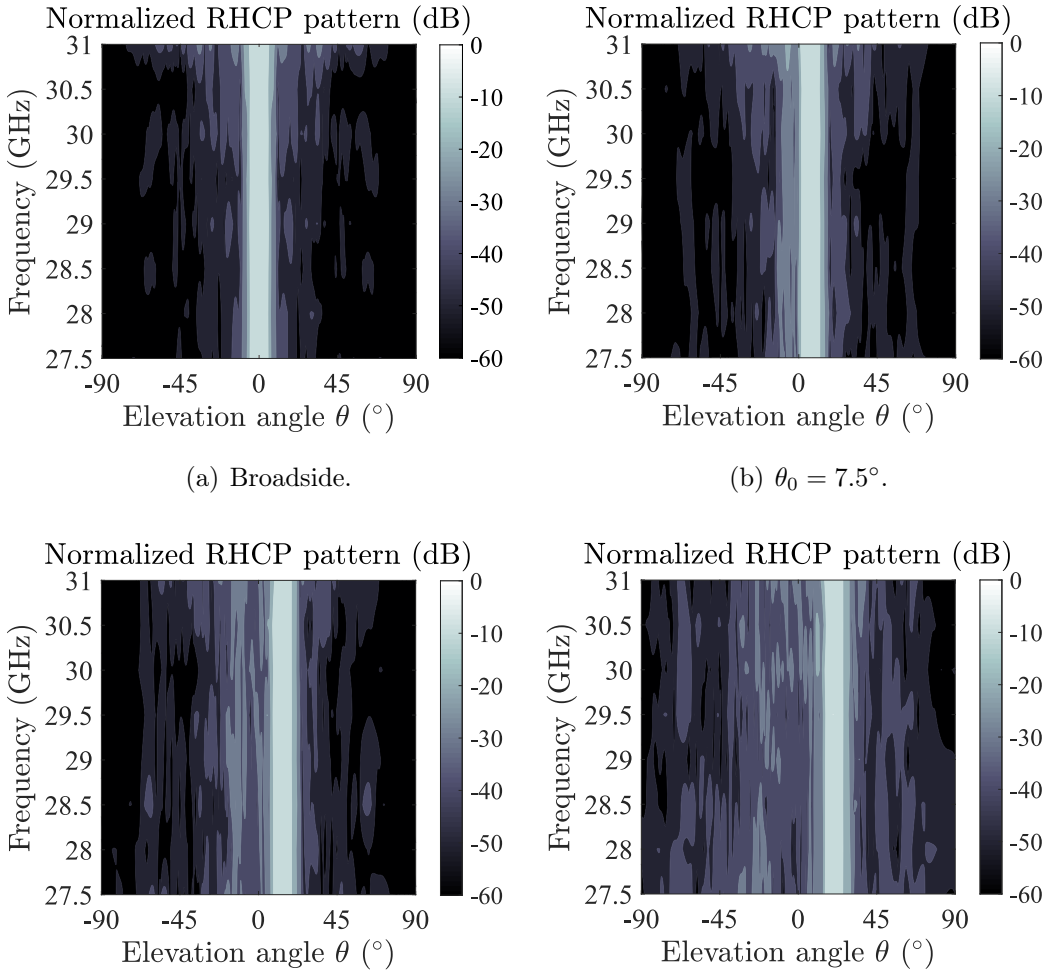

(a) Broadside.

(b) $\theta_0 = 7.5°$.

(c) $\theta_0 = 13.8°$.

(d) $\theta_0 = 20°$.

FIGURE 2.35: Simulated RHCP patterns as function of the elevation angle θ and frequency. The patterns are taken in the yz-plane cut. (a) Broadside radiation. The array steers the main beam at the scanning angle θ_0 (b) 7.5°, (c) 13.8°, and (d) 20°.

the entire antenna architecture [see Fig. 2.31] and are obtained with the full-wave commercial software [81]. These plots show that the pointing angle of the array is preserved within the overall Ka-band. The beamwidths remain, indeed, roughly unvaried in space and frequency. The worst scenario, in terms of SLLs, appear when the array is pointing at $\theta_0 = 20°$, as shown in Fig. 2.35(d). In this case, the first SLL is in average lower than -20 dB everywhere in the frequency band 27.5-31 GHz. The patterns of the cross polarization (i.e, left-hand circularly-polarized patterns) are not here reported for the sake of brevity. Their are found to be very much attenuated with respect to the RHCP patterns. The simulated results show values about -20 dB with respect to the

RHCP peaks for the outer-most beam.

Finally, it is worth discussing the half-power beam-width (HPBW) of the array. The -3 dB contour plot of the co-polar radiation patterns is reported in Fig. 2.36 as a function of the elevation angle θ and the frequency. The multi-

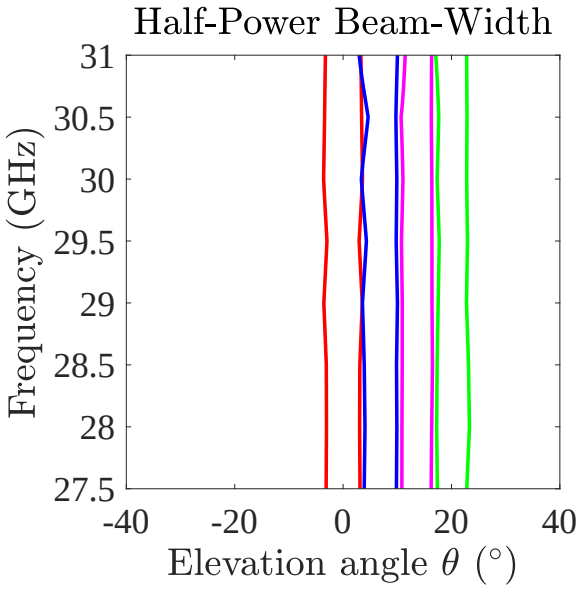

FIGURE 2.36: Simulated half-power beam-width as a function of the elevation angle θ and frequency. The patterns are taken in the yz-plane cut.

beam antenna array was designed in order to have adjacent beams intersecting each other at -3 dB from their peak level. This condition is to ensure that the surface, illuminated by the antenna array, will receive constantly at least half of the maximum radiated power. Fig. 2.36 shows that this requirement is well fulfilled along the scanning capability offered by the proposed circularly-polarized CTS array.

2.5.6 Fabrication feasibility

A few words are here spent about the fabrication process to realize the antenna module. Since the swallow-tail feeder is the most challenging part of the antenna in terms of geometry complexity, only the radiating part of the antenna has been selected for studying the fabrication feasibility. The full-metal 3-D printing technology is selected to test fabrication reliability. Specifically, a laser melting of $AlSi_{10}Mg$ is employed to shape the radiating part of the over-moded CTS

array [82]. As a representative example, the tests have been executed on a 4-slot CTS array and the fabricated pieces are shown in Fig. 2.37. The geometry

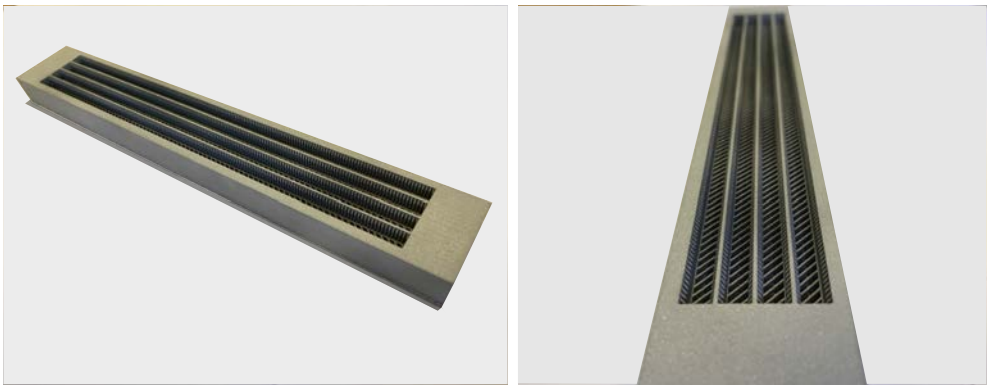

(a) Perspective view. (b) Lateral view.

FIGURE 2.37: Fabricated 4-slot CTS array using full-metal 3-D printing technology. (a) Perspective and (b) lateral view.

of the structure appears to be realized with satisfactory accuracy. Furthermore, the fabricated piece is very solid and robust. The surface roughness oscillates between 50 and 80 μm, which is an acceptable range of values for Ka-band applications.

This type of fabrication process has been thus selected for fabricating the 32-slot CTS array. At the time of the redaction of this manuscript, the fabrication of the circularly-polarized long slot array described above is ongoing. Once fabricated, the prototype will be experimentally tested in the facilities of the Institut d'Électronique et Technologies du numéRique (IETR).

2.6 Conclusions

In this Chapter, a novel concept of parallel-fed CTS array has been proposed and studied. This type of antenna array is made of long slots that support the propagation of the fundamental TEM mode and the first higher-order TE mode of PPW. Along the waveguide cross-section, these modes exhibit orthogonally-polarized E-fields, thus able to radiate circularly-polarized waves if properly excited. First, a numerical modeling of open-ended, over-moded stubs has been proposed in a periodic environment to investigate the potentialities and limitations of the antenna concept. The model makes use of a spectral mode-matching

approach that retrieves the active input impedance of the array, as well as calculates the radiated patterns for each mode excitation. This numerical tool is crucial to get physical in-sights about the antenna's working principle. It also allows obtaining efficient design guidelines. Secondly, a design has been proposed at the Ka-band. The feeding system of the radiating modes is realized using a twisted grid, embedded in the dual-mode PPWs. The antenna performance has been validated via full-wave simulations, showing an excellent agreement with the results predicted by the in-house tool. Specifically, the antenna array exhibits AR below 3 dB all over the Ka-band with scanning performance up to $\pm 25°$. Also, the 3-D printing technology has been considered to testing fabrication feasibility. The antenna module is currently under fabrication and will be measured in the IETR's facilities.

This type of CTS antennas is very innovative and ensure great performance in the framework of modern SatCom applications. In addition to being able to achieve CP radiation, this class of long slot array retains, indeed, all the valuable properties of standard parallel-fed CTS arrays, i.e., wide-band performance, wide scanning, low-profile, etc. For these reasons, they may represent a valid solution for the next generation SatCom ground terminals.

Chapter 3

Equi-dispersive dual-mode CTS arrays

This chapter introduces the modal analysis of parallel-plate waveguides (PPW) attaining the propagation of two equi-dispersive (ED), orthogonally-polarized modes. As discussed in Chapter 2, a circularly-polarized radiation can be obtained exploiting the electrical properties of over-moded PPWs. Over-sized PPWs support, indeed, the propagation of transverse electromagnetic (TEM) and electric (TE) modes, whose corresponding E-fields are orthogonally-polarized to each other in the waveguide cross-section [see Fig. 1.10]. If properly parallel excited, an array of over-moded long slots can thus provide radiated waves with orthogonal components. This property helps in overcoming the limitation of standard parallel-fed continuous transverse stub (CTS) arrays as inherently linearly-polarized antennas. However, the main drawback of the over-moded long-slot arrays lies in the different dispersive behavior of TEM and TE modes, which makes their design complex. Moreover, this issue limits the scanning performance of the antenna because the modes' electrical paths respond to different group velocities [see Fig. 2.1]. The physical insights provided by a complete study of non-standard PPWs are crucial to grasp the limitations and potentialities of guiding structures whose closed domain consists of parallel plates.

The main idea derives from observing that some guiding structures exhibit ED (same group velocity) propagation of two modes, having E-field lines orthogonally-oriented with respect to each other in the waveguide cross-section. Microwave components supporting such a modal propagation are largely used as millimeter-wave antenna feeds or radiating elements to generate circular (CP)

or dual-linear polarization. Square waveguides are, indeed, used as linear-to-circular polarizer feeds (e.g., septum polarizers [83, 84]) or unit cell for phased-array, attaining circular polarization (CP) [63, 85].

Guiding structures, supporting ED propagation of different modes, own this property to rotational/reflection symmetries along the transversal section of the waveguide. The contour geometry of a generic waveguide may, indeed, induce to the existence of degenerate modal branches, appropriate to supporting a multi-modal propagation with the same dispersive behavior. Some representative examples are square or circular guiding structures. A different case-of-study is the parallel plate domain. Standard PPWs, with perfect electric conductive plates, exhibit degenerate transverse electric (TE) and magnetic (TM) modes. However, a transverse electromagnetic (TEM) propagation is also supported by these structures. The latter represents a further source of intermodal dispersion.

In this Chapter[1], an analytic study of PPWs with properly engineered purely reactive walls is proposed. The parallel plate domain is contoured by impedance boundary conditions (IBM). The modal analysis of the structure is outlined and analytic closed-form expressions are provided to engineer its dispersion, as a possible strategy to inhibit the TEM propagation and achieve the aimed ED ortho-mode propagation. Finally, these waveguides are arranged in a periodic configuration as open-ended radiating stubs. The latter study is to observe the radiating properties when exploiting the orthogonality of two ED modes. Very high CP purity is demonstrated within a broad frequency range.

3.1 Modal analysis

In this Section, the modal analysis of PPWs with purely reactive IBC is reported. The electromagnetic field in a hollow, lossless, sourceless waveguide can be expressed as a superimposition of orthogonal modes. The modal theory is well-established and documented in the open literature [56, 70, 74]. In the following, we will focus on a parallel plate domain, as shown in Fig. 3.1. The structure is infinitely-extended along the y-axis and the modes propagate along the z-axis. Moreover, ϵ_r and μ_r are the dielectric permittivity and permeability

[1]This Chapter is an extended version of the letter [J-2]. The list of the author's publications is included at the end of this Ph.D. dissertation.

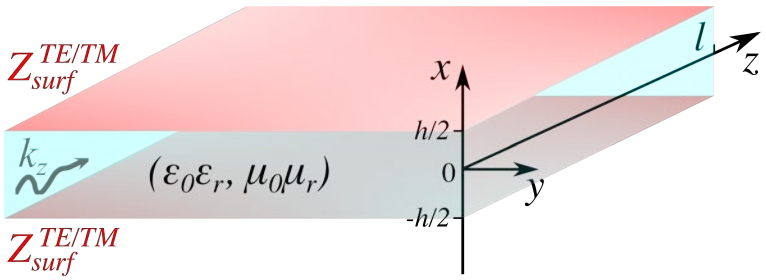

FIGURE 3.1: Geometry of the problem under analysis. The structure consists of two parallel plates, infinitely-extended along y-axis, modeled as surface reactance with respect to TE and TM modes. Modes propagate along the z-axis.

of the material filling the PPW, respectively. The bounding walls are modeled using IBCs. Studying TE and TM modes independently, the two plates have identical surface impedance. To streamline the maths, a scalar formulation will be considered hereinafter.

Since the structure is sourceless, the electromagnetic problem reduces to solving the Helmholtz's equation and searching for the corresponding eigenvalues. Given the quasi-electrostatic scenario, the fields are found as derivative of an arbitrary scalar potential. In formulae:

$$\mathcal{H}\left\{\phi^{TE/TM}\right\} = 0 \tag{3.1}$$

where $\phi^{TE/TM}$ is an arbitrarily chosen scalar potential and

$$\mathcal{H}\{\cdot\} = \nabla_t^2 + \left| k_t^{TE/TM} \right|^2 \tag{3.2}$$

is the Helmholtz operator with

$$\begin{aligned} \nabla_t^2 &= \partial_x^2 + \partial_y^2 \\ \left| k_t^{TE/TM} \right|^2 &= \left(k_x^{TE/TM}\right)^2 + \left(k_y^{TE/TM}\right)^2 \end{aligned} \tag{3.3}$$

Also, $k_x^{TE/TM}$ and $k_y^{TE/TM}$ are the transverse eigenvalues for both TE and TM modes, accordingly. Owing to the infinite extent of the structure in Fig. 3.1 along y-axis, it can be demonstrated that $k_y^{TE/TM} = 0$ as detailed in [70]. The eigenvalues $k_x^{TE/TM}$ are found by enforcing the IBC given by

$$\mathbf{E_t^{TE/TM}} = Z_{surf}^{TE/TM} \hat{n} \times \mathbf{H^{TE/TM}} \tag{3.4}$$

where $\mathbf{E_t} = E_y\hat{y} + E_z\hat{z}$ and $\hat{n}$ is the inward unit vector normal to the parallel plates ($\hat{n} = \pm\hat{x}$). Moreover, $Z_{surf}^{TE/TM}$ is the surface impedance delimiting the waveguide cross-section for TE and TM modes, accordingly. The latter is assumed to be purely reactive. Also, the same surface impedance is considered for the two plates for each mode category (TE or TM).

3.1.1 PPW loaded with surface impedances: TE modes

Equation (3.1) can be solved for TE modes, by arbitrarily assuming the scalar potential ϕ^{TE}. A convenient choice for ϕ^{TE} is inspired by [86] and takes the form

$$\phi^{TE} = A^{TE}\left[\xi^{TE+} + B^{TE}\xi^{TE-}\right] \tag{3.5}$$

where $\xi^{TE\pm} = e^{\pm ik_x^{TE}(x+h/2)}$ and h is the height of the PPW [see Fig. 3.1]. The parameters A^{TE} and B^{TE} are constants to be determined downstream from enforcing the IBC as (3.4). Considering the field components for TE modes are

$$\begin{aligned}\mathbf{E^{TE}} &= \left(0, E_y^{TE}, 0\right)\\ \mathbf{H^{TE}} &= \left(H_x^{TE}, 0, H_z^{TE}\right)\end{aligned} \tag{3.6}$$

the IBCs in (3.4) simplifies to the following form

$$\begin{aligned}Z_{surf}^{TE} &= +\frac{E_y^{TE}}{H_z^{TE}}\bigg|_{x=+h/2}\\ Z_{surf}^{TE} &= -\frac{E_y^{TE}}{H_z^{TE}}\bigg|_{x=-h/2}\end{aligned} \tag{3.7}$$

Using the modal theory [56], each field component is expressed as function of the arbitrary scalar potential ϕ^{TE}, thus yielding to $B^{TE\pm} = \pm e^{ik_x^{TE\pm}h}$. A two-form relation (superscripts $\pm$) is adopted to compact the mathematical content. The characteristic equation (CE) is found to be a function of Z_{surf}^{TE}, as follows

$$Z_{surf}^{TE\pm} = \frac{\omega\mu_0\mu_r}{k_x^{TE\pm}}\frac{1 - B^{TE\pm}}{1 + B^{TE\pm}} \tag{3.8}$$

where ω is the angular frequency. All the details on the derivation of (3.8) are reported in the Appendix B.1. The obtained CE is transcendental and, assuming Z_{surf}^{TE} as input entry, it is numerically solved for the eigenvalues $k_x^{TE\pm}$.

Given that we analyze a closed-domain problem, a discrete set of the eigenvalues $k_x^{TE\pm}$ is found, i.e., $k_{x,m=1,2,\ldots,+\infty}^{TE\pm}$. To this purpose, a Padé-approximant-based root-finding algorithm is used [87]. The field modal vectors are calculated using the scalar potential ϕ^{TE} and, after some algebraic manipulations, can be written as follows

$$\begin{aligned}
\boldsymbol{e_t^{TE\pm}} &= e_y^{TE\pm}\hat{y} = \begin{array}{c} iA^{TE+}\sin\left(k_x^{TE+}x\right) \\ A^{TE-}\cos\left(k_x^{TE-}x\right) \end{array} \hat{y} \\
\boldsymbol{h_z^{TE\pm}} &= h_z^{TE\pm}\hat{z} = i\partial_x e_y^{TE\pm}/(\omega\mu_0\mu_r)\hat{z} \\
\boldsymbol{h_t^{TE\pm}} &= h_x^{TE\pm}\hat{x} = \hat{z}\times\boldsymbol{e_t^{TE\pm}}
\end{aligned} \tag{3.9}$$

where

$$A^{TE\pm} = \sqrt{2/h}\left(\operatorname{sinc}\left(k_x^{TE\pm}h\right)\mp 1\right)^{-1/2} \tag{3.10}$$

which is found by enforcing the orthonormality property of waveguide modes [56]. Moreover, the $\operatorname{sinc}(\cdot)$ is the unnormalized sine function and the propagation constant is given by $k_z^{TE\pm} = \sqrt{k_0^2\epsilon_r\mu_r - \left(k_x^{TE\pm}\right)^2}$, where k_0 is the free space wavenumber.

3.1.2 PPW loaded with surface impedances: TM modes

The TM modes are calculated by assuming the following scalar potential

$$\phi^{TM} = A^{TM}\left[\xi^{TM+} + B^{TM}\xi^{TM-}\right] \tag{3.11}$$

where $\xi^{TM\pm} = e^{\pm ik_x^{TM}(x+h/2)}$. Note that the field components of TM modes are given by

$$\begin{aligned}
\mathbf{E^{TM}} &= \left(E_x^{TM}, 0, E_z^{TM}\right) \\
\mathbf{H^{TE}} &= \left(0, H_y^{TM}, 0\right)
\end{aligned} \tag{3.12}$$

thus yielding to the following IBC's simplified form [refer to (3.4)]:

$$\begin{aligned}
Z_{surf}^{TM} &= -\frac{E_z^{TM}}{H_y^{TM}}\bigg|_{x=+h/2} \\
Z_{surf}^{TM} &= +\frac{E_z^{TM}}{H_y^{TM}}\bigg|_{x=-h/2}
\end{aligned} \tag{3.13}$$

Considering each field component can be expressed as function of the scalar potential ϕ^{TM} [56], the CE is arranged in the form

$$Z_{surf}^{TM\pm} = \frac{k_x^{TM\pm}}{\omega\epsilon_0\epsilon_r}\frac{1+B^{TM\pm}}{1-B^{TM\pm}} \tag{3.14}$$

where $B^{TM\pm} = \pm e^{ik_x^{TM\pm}h}$. The mathematical derivation of (3.14) is reported in the Appendix B.2. Solving (3.14), a countable set of solutions is found, i.e., $k_{x,m=1,2,...,+\infty}^{TM\pm}$. The TM modal vectors are given by

$$\begin{aligned}
\boldsymbol{e_t^{TM\pm}} &= e_x^{TM\pm}\hat{x} = \begin{matrix} iA^{TM+}\sin\left(k_x^{TM+}x\right) \\ A^{TM-}\cos\left(k_x^{TM-}x\right) \end{matrix} \hat{x} \\
\boldsymbol{h_t^{TM\pm}} &= h_y^{TM\pm}\hat{y} = \hat{z}\times\boldsymbol{e_t^{TM\pm}} \\
\boldsymbol{e_z^{TM\pm}} &= e_z^{TM\pm}\hat{z} = -i\partial_x h_y^{TM\pm}/(\omega\epsilon_0\epsilon_r)\hat{z}
\end{aligned} \tag{3.15}$$

where

$$A^{TM\pm} = \sqrt{2/h}\left(\mathrm{sinc}\left(k_x^{TM\pm}h\right)\mp 1\right)^{-1/2} \tag{3.16}$$

Finally, the propagation constant can be written as $k_z^{TM\pm} = \sqrt{k_0^2\epsilon_r\mu_r - \left(k_x^{TM\pm}\right)^2}$.

3.2 Equi-dispersive ortho-mode PPWs

As discussed in Chapter 2, dual-mode CTS arrays exhibit important performances in terms of CP radiation and bandwidth. On the other hand, these arrays are also strongly dispersive, given that the two propagating modes respond to different group velocities. This issue can be solved by engineering dual-mode CTS arrays based on ED propagation. This valuable property is achieved considering PPWs bounded by reactive plates. The desired ED propagation can be linked to the surface impedances (3.8) and (3.14). As shown in Fig. 3.2, the sets of solutions for k_x^{TE} and k_x^{TM} have only two eigenvalues in the visible range ($|k_x^{TE/TM}| < k_0\sqrt{\epsilon_r\mu_r}$) when the surface impedance is inductive and capacitive for TE and TM modes, respectively. The two modes exhibit orthogonally-polarized E-fields along the waveguide cross-section. Note that this is only valid when the height of the PPW is smaller than half the operating wavelength ($h < \lambda/2$). Also, Z_{surf}^{TE} must be inductive, as well as Z_{surf}^{TM} capacitive. In more general scenarios, surface-wave modes ($k_x^{TE} = \Im\{k_x^{TE}\}$ and

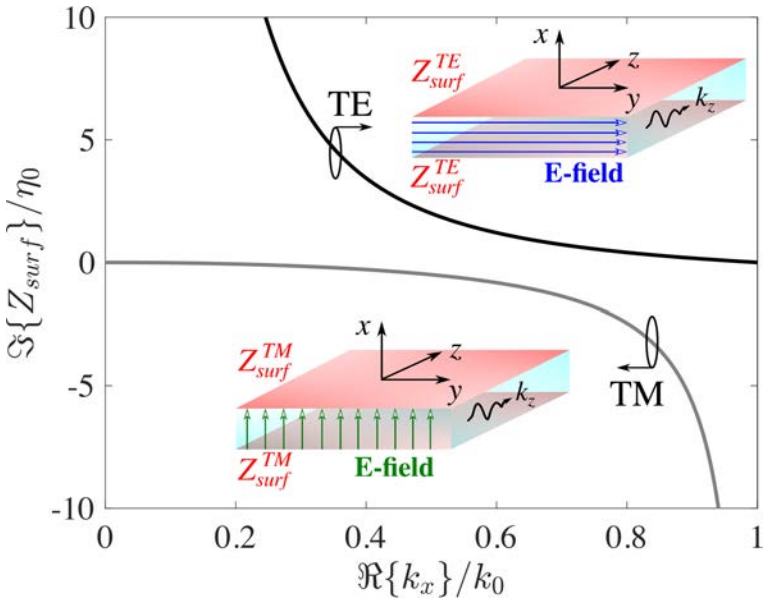

FIGURE 3.2: Impedance loci of TE and TM modes when the PPW's height is $h = \lambda/2$, where λ is the wavelength at 40 GHz. The characteristic equations are plotted at the operating frequency. The PPW is air-filled (i.e., $\epsilon_r = \mu_r = 1$).

$k_x^{TM} = \Im\{k_x^{TM}\}$) may be present too [88], although $h < \lambda/2$. The possible presence of purely imaginary eigenvalues $k_x^{TE/TM}$ is due to the fact that the Helmholtz operator is no longer Hermitian when it is subject to IBCs. This propriety is rigorously demonstrated in the Appendix B.3.

Being proved that two ortho-modes may be supported by the considered structure, the surface impedance $Z_{surf}^{TE/TM}$ can be then engineered to support ED propagation. Given that Z_{surf}^{TE} is required to be inductive and Z_{surf}^{TM} capacitive, their frequency behaviors are assumed to be as follows

$$Z_{surf}^{TE-} = i\omega L^{TE} \tag{3.17}$$

$$Z_{surf}^{TM-} = (i\omega C^{TM})^{-1} \tag{3.18}$$

The ED condition can be obtained by inserting (3.17) and (3.18) into (3.8) and (3.14), respectively, and enforcing $k_x^{TE-} = k_x^{TM-}$. After computing the product $Z_{surf}^{TE-} Z_{surf}^{TM-}$, the following ED condition is found

$$L^{TE} = C^{TM}\eta^2 \tag{3.19}$$

where $\eta = \eta_0\sqrt{\mu_r/\epsilon_r}$ and $\eta_0 = 120\pi\ \Omega$. To solve equation (3.19), a second

equation is needed to be solved for C^{TM}. The latter is then determined by arbitrarily setting the cut-off frequency of TM modes f_{co}^{TM}. In formulae:

$$C^{TM} = \left(\omega_{co}^{TM}\eta\right)^{-1} \cot\left(kh/2\right) \tag{3.20}$$

where $\omega_{co}^{TM} = 2\pi f_{co}^{TM}$ and $k = k_0\sqrt{\epsilon_r\mu_r}$.

As a representative example, ED PPWs are proposed to validate the analytic formuale reported above. The height of the PPW is chosen to be $h = \lambda_{min}/2$, where λ_{min} is the wavelength at the highest operating frequency (namely f_{max}). The cut-off frequency f_{co}^{TM} is arbitrarily selected between 0 GHz and f_{max}. Let us then assume $f_{max} = 3f_{co}^{TM}$. The capacitance C^{TM} is calculated using (3.20)

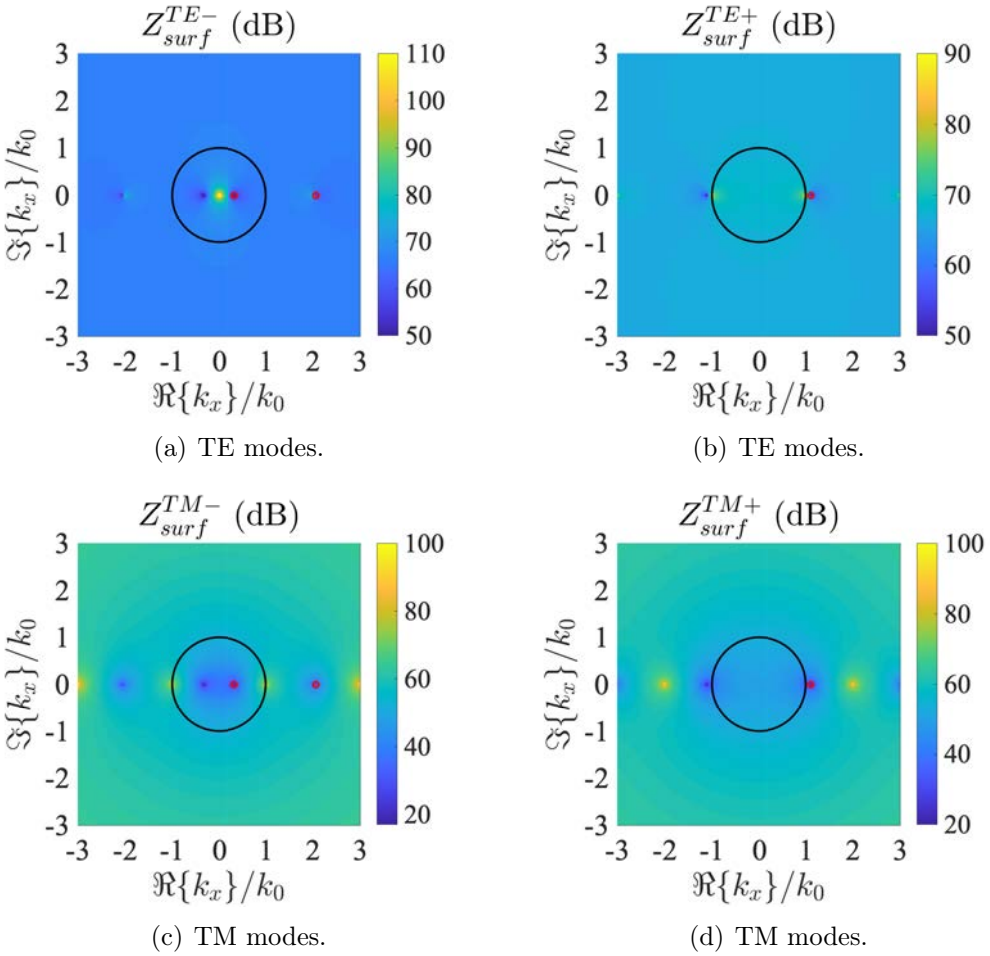

(a) TE modes. (b) TE modes.

(c) TM modes. (d) TM modes.

FIGURE 3.3: Characteristic equation for (a),(b) TE and (c),(d) TM modes at the frequency f_{max}. The plot is shown in dB, thus the poles are illustrated with dark blue spots. The black circle indicate the visible range ($|k_x| = k$) and red dot markers represent the calculated poles using [87]. The PPW is air-filled. Parameter settings: $h = \lambda_{min}/2$ and $f_{max} = 3f_{co}^{TM}$.

and L^{TE} using the ED condition (3.19), consequently. The CEs (3.8) and (3.14) are so numerically solved using (3.17) and (3.18) as surface impedances. They are plotted in Fig. 3.3 showing the CEs in dB. The eigenvalues correspond thus to very low values, i.e., blue spots in Fig. 3.3. It can be observed that the poles are equally located in the spectral domain for TE and TM modes, respectively. In other words, TE and TM modes form degenerate modal branches, as consequence of having enforced the ED condition (3.19). Moreover, Figs. 3.3(a) and (c) show that a dual-mode propagation is achieved, as two eigenvalues are located within the visible range ($|k_x| = k$). These two modes are orthogonally-oriented along the waveguide cross-section. For the sake of completeness, the dispersion diagrams of TE and TM modes are reported in Figs. 3.4(a) and (b), respectively. Fig. 3.4 shows that two ortho-modes are in propagation in the fre-

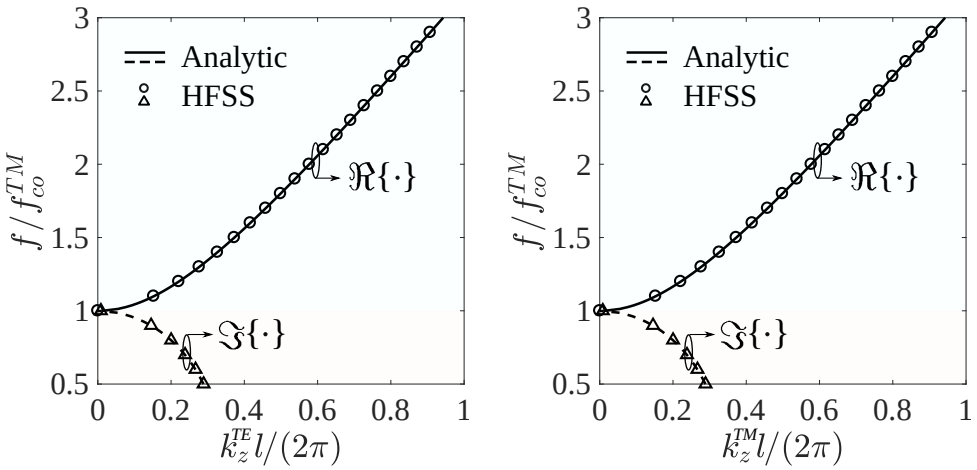

(a) TE modes. (b) TM modes.

FIGURE 3.4: Dispersion diagram of (a) TE and (b) TM modes for a ED PPW. Parameter settings: $h = \lambda_{min}/2$, $f_{max} = 3f_{co}^{TM}$ and $l = \lambda_{min}$. The PPW is air-filled.

quency range $[f_{co}^{TM}, f_{max}]$ and their dispersion curves are identical. The length of the considered PPW is $l = \lambda_{min}$. The analytic formulation is also validated with a full-wave commercial software [81], showing an excellent agreement.

3.3 Quasi-equidispersive 90°-phase delayed line

To attain a CP radiation, the ED PPWs must behave as an anisotropic crystal, meaning that two orthogonal components are 90°-phased with respect to

each other, while maintaining their amplitudes equal. This propagation characteristic is achieved from a suitable engineering of the dispersion. Let us begin observing that the eigenvalues k_x^{TM-} are frequency-independent, as consequence of having modeled Z_{surf}^{TM} as (3.18). By equaling equations (3.18) and (3.14), the angular frequency results, indeed, simplified to the left and right hand sides when solving for k_x^{TM-}. Once k_x^{TM-} is found, the eigenvalues of TE modes k_x^{TE-} are not automatically obtained, as they are dependent on the desired phase delay $\Delta\phi = \pi/2$. They are thus enforced to be as follows

$$k_x^{TE-} = \frac{1}{l}\sqrt{(k_x^{TM-}l)^2 + \Delta\phi\,(-\Delta\phi + 2lk_z^{TM-})} \tag{3.21}$$

where l is the length of the PPW [see Fig. 3.1]. The ED condition reduces then to a different form than (3.19), thus yielding to

$$L_{\Delta\phi}^{TE} = C^{TM}\frac{k_x^{TM-}}{k_x^{TE-}}\eta^2 \tan\left(\frac{k_x^{TM-}h}{2}\right)\cot\left(\frac{k_x^{TE-}h}{2}\right) \tag{3.22}$$

where C^{TM} is calculated as (3.20). The main drawback of (3.22) is that $L_{\Delta\phi}^{TE}$ might be strongly frequency-dependent. Since it has been demonstrated that k_x^{TM-} is constant, the term responsible for the frequency dependency of $L_{\Delta\phi}^{TE}$ is k_x^{TE-} as it can be seen in (3.21). This issue can be mitigated calculating the limit of (3.21), when the length of the PPW tends to infinity. In formulae:

$$\lim_{l\to+\infty} k_x^{TE-} = \lim_{l\to+\infty} \frac{\sqrt{(k_x^{TM-}l)^2 + \Delta\phi\,(-\Delta\phi + 2lk_z^{TM-})}}{l} = k_x^{TM-} = const \tag{3.23}$$

An estimation of the order of magnitude of the PPW's length l in terms of the smallest wavelength can be obtained by plotting (3.21) as a function of the frequency for increasing values of l. This study is reported in Fig. 3.5. The numerical results show that k_x^{TE-} starts being a slowly-varying function with frequency when l is as big as a few smallest wavelengths. In this scenario, the value of $L_{\Delta\phi}^{TE}$ as (3.22) can be approximated by its mean, thus yielding to

$$\overline{L_{\Delta\phi}^{TE}} = \frac{1}{meas\{\Delta f\}}\int_{\Delta f} L_{\Delta\phi}^{TE} df \tag{3.24}$$

where $\Delta f \equiv \left[f_{max}, f_{co}^{TM}\right]$.

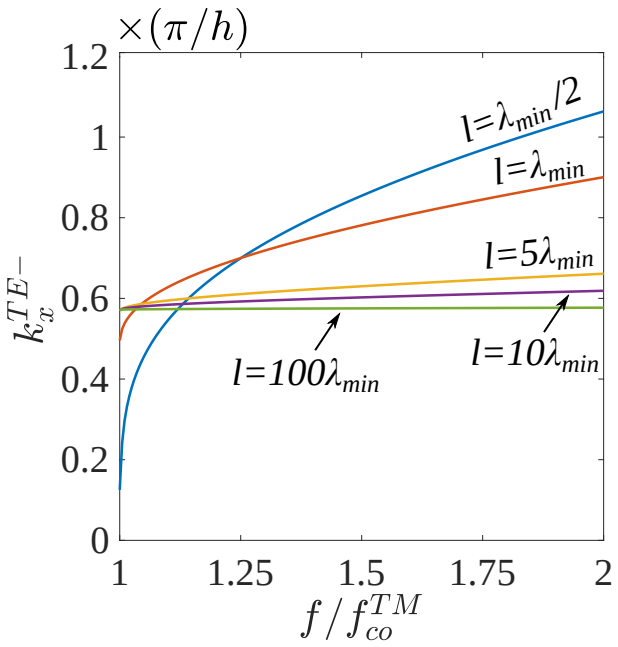

FIGURE 3.5: Parametric plots of the eigenvalue k_x^{TE-} using equation (3.21) for increasing values of the PPW's lemgth l. The eigenvalue k_x^{TE-} starts being a slow-varying function with frequency when l is as big as a few wavelengths at the highest frequency. Simulation settings: $f_{max} = 2f_{co}^{TM}$ and $h = \lambda_{min}/2$.

Finally, we can validate the dispersion engineering reported above by considering a representative example. The cut-off frequency of TM modes is set at 20 GHz. We consider a PPW having height $h = \lambda_{min}/2$. The capacitance C^{TM} can be thus calculated using (3.18). The maximum operating frequency is chosen to be twice the cut-off frequency f_{co}^{TM}. The length of the PPW is $l = 3\lambda_{min}$. The dispersion analysis of the structure is reported in Fig. 3.6. Specifically, the dispersion diagram using the non-approximated form of $L_{\Delta\phi}^{TE}$ [see equation (3.22)] is plotted in Fig. 3.6(a). It can be observed that the two modes are perfectly ED (same frequency dependency of their propagation constants) and 90°-phased one another all over the band $\left[f_{co}^{TM}, f_{max}\right]$. On the other hand, Fig. 3.6(b) reports the dispersion when the inductance $L_{\Delta\phi}^{TE}$ is approximated by (3.24). In this case, the two modes end up being no longer ED all over the frequency band $\left[f_{co}^{TM}, f_{max}\right]$. In fact, the use of (3.24) results in enabling the propagation of two quasi-ED ortho-modes. In other words, their phase difference equals 90° at only one frequency within the range $\left[f_{co}^{TM}, f_{max}\right]$. The analytic dispersion diagrams are also validated using the full-wave simulator [81], showing an excellent agreement. Finally, the surface impedance

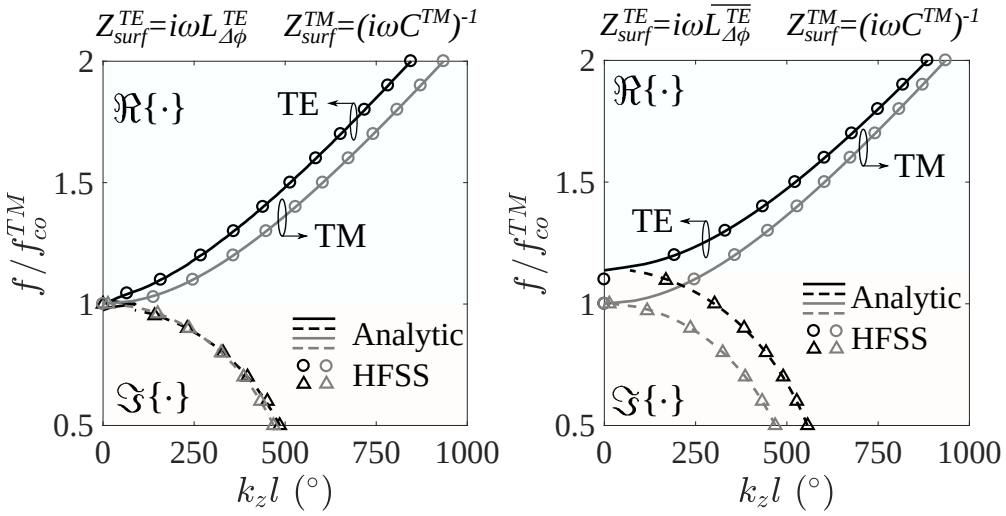

(a) TE modes. (b) TM modes.

FIGURE 3.6: Dispersion diagram for (a) $Z_{surf}^{TE} = i\omega L_{\Delta\phi}^{TE}$ and (b) $Z_{surf}^{TE} = i\omega \overline{L_{\Delta\phi}^{TE}}$. Parameter settings: $f_{co}^{TM} = 20$ GHz, $h = \lambda_{min}/2$, $f_{max} = 2f_{co}^{TM}$ and $l = 3\lambda_{min}$. The PPW is air-filled.

Z_{surf}^{TE} is plotted in Fig. 3.7 with the corresponding circuit elements. When the

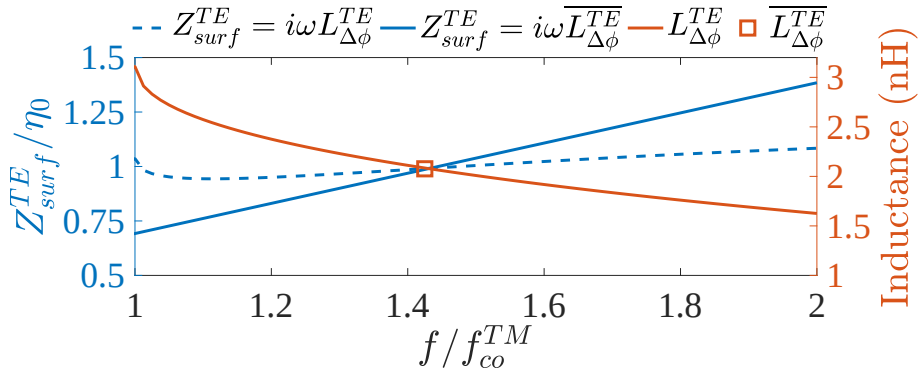

FIGURE 3.7: Plot of the surface impedance Z_{surf}^{TE} using the corresponding circuit elements as (3.22) and (3.24).

PPW's length is $l = 3\lambda_{min}$, the surface impedance Z_{surf}^{TE} given by (3.22) is a slowly-varying function of the frequency, as $L_{\Delta\phi}^{TE}$ is still frequency dependent [see orange solid line in Fig. 3.7]. When using the approximation (3.24), the surface impedance Z_{surf}^{TE} shows a linear behavior in frequency. In the latter scenario, the two modes will be perfectly ED at the frequency point for which the surface impedance Z_{surf}^{TE} equals its mean (square marker in Fig. 3.7).

3.4 Equi-dispersive open-ended radiating stubs

The aim of this Section is to show the achievable radiating performance of ED open-ended stubs. The dispersion of ED PPWs is analytically studied and radiating stubs are organized in a periodic environment, aiming to achieve CP radiation at the Ka-band. The unit cells of the ED CTS array are shown in Figs. 3.8(a) and (b) for TE and TM modes, respectively. A waveguide

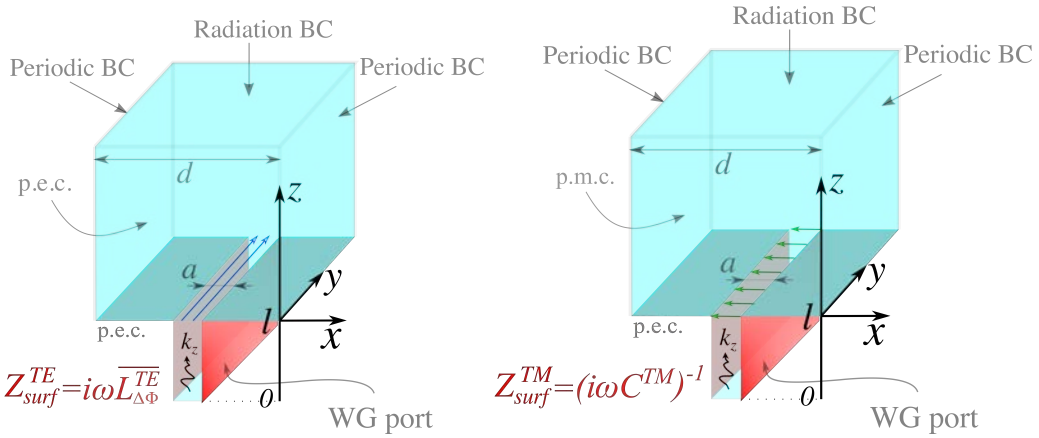

(a) TE modes. (b) TM modes.

FIGURE 3.8: Unit cell of the ED CTS array for (a) TE and (b) TM modes. The width of the slots is $a = 4.28$ mm and the array periodicity is $d = 1.1a$.

port is employed to launch the two modes into the feeding PPW. Periodic boundary conditions are enforced at the lateral faces of the unit cell along the x-axis for both TE and TM modes. Perfect electric and magnetic conductors are considered along the y-axis for optimal operation of TE and TM modes, alternately. Finally, radiation boundary conditions are enforced on the top of the radiating box. The width of the slots is set as $a = \lambda_{min}/2 = 4.28$ mm (λ_{min} is the wavelength at 35 GHz) for optimal operation at Ka-band. Also, the array inter-element spacing is $d = 1.1a$ to broaden the bandwidth [refer to Section 2.4]. The considered IBCs are considered using the circuit elements as (3.20) and (3.24). The cut-off frequency of the TM mode is set at 20 GHz. The PPW's length is $l = 5\lambda_{min}$ [see Figs. 3.8(a) and (b)].

The phases of the two modes are plotted in Fig. 3.9 as a function of the spatial variable z at 29 GHz. The two modes are equally phased at the input of the radiating stubs ($z = 0$). While propagating in the positive direction of z-axis, the TE and TM modes start phasing out each other. At the aperture level

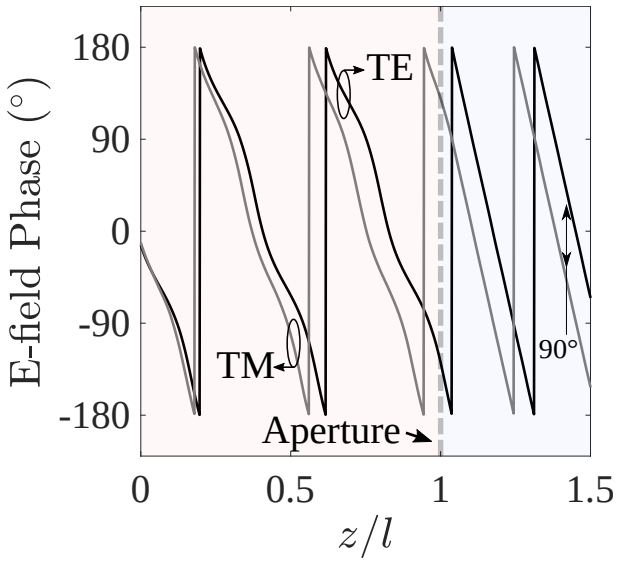

FIGURE 3.9: Phases of TE and TM modes as a function of the variable z. at 29 GHz

($z = l$), the two modes are 90° out-of-phase with respect to each other. The radiating field exhibits thus two orthogonal components, whose phase difference is 90°. The CP purity can be estimated in terms of the axial ratio (AR). A very high CP purity (AR below 3 dB) is achieved over the band 26.8-32.2 GHz (22.3% fractional bandwidth), as shown in Fig. 3.10. The simulated AR in Fig.

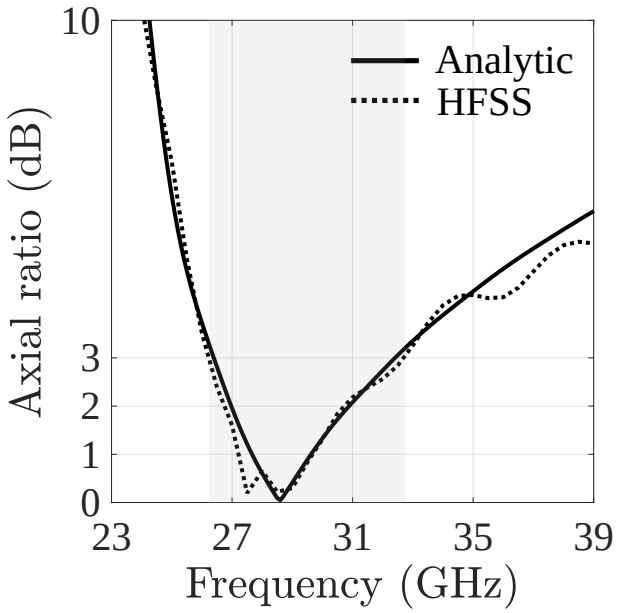

FIGURE 3.10: Simulated AR as a function of frequency for ED open-ended stubs. The AR is computed both analytically and using the full-wave simulator [81], showing a very good agreement.

3.10 is computed both analytically and by post-processing the radiated fields

using [81]. The analytic computation is obtained by means of the windowing approach outlined in Section 2.3.1. The magnetic current over the slots has been calculated considering the amplitude and phase E-field distribution provided by the two modes propagating within the ED PPWs. For the sake of simplicity, the employed windowing function is the rectangular one. The numerical results are found to be in excellent agreement with the full-wave simulator [81] up to 35 GHz. Beyond that frequency, higher-order modes start propagating as well for a total of four modes. The corresponding transverse eigenvalues of the two higher-order modes are exactly twice those of the fundamental ones.

3.5 Possible ways to design ED PPWs

This Section aims to shortly argue about possible ways to synthesize ED PPWs. Physical structures, that may realize reactive sheets, rely on metallic patterns printed on grounded dielectric slabs, as done in [89, 90]. These structures resemble anisotropic meta-waveguides and can be designed by following the approach outlined in Chapter 5 for frequency selective surfaces (FSS). Basically, equivalent circuit models can be employed to design the surface impedance for each field's component separately. Since the surface impedances are demanded to be inductive and capacitive for y- and x-polarized E-fields, respectively, their physical realization can be approached separately. Owing to their geometrical shape, meandered Jerusalem crosses [refer to Chapter 5] may represent a valid candidate as meta-waveguide's unit cell.

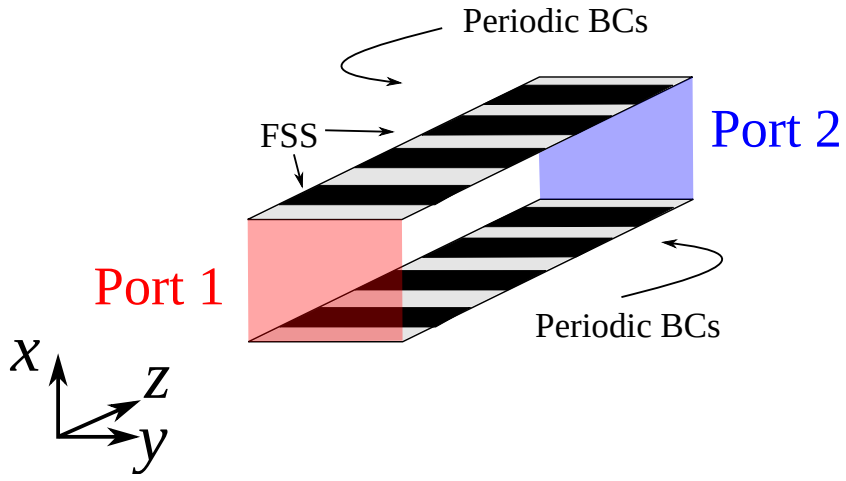

FIGURE 3.11: Simulation setup to synthetize the equi-dispersive dual-mode PPWs.

A successful synthesis method is the one employed in the work [91]. The simulation setup is shown in Fig. 3.11. Periodic boundary conditions are considered at the lateral faces of a parallel-plate structure, i.e., along the y-axis. Two waveguide ports are used to excite the two desired modes and the S-parameters are exported to reconstruct the desired propagation constant within the waveguide, by using the following formula [74]:

$$k_z^{TE/TM} = \sqrt{k^2\epsilon_r\mu_r - \left(k_x^{TE/TM}\right)^2} = \frac{1}{4D}\arccos(A) \tag{3.25}$$

where

$$\begin{aligned} A &= \frac{(1+S_{11})(1-S_{22})+S_{12}S_{21}}{2S_{21}} \\ D &= \frac{(1-S_{11})(1+S_{22})+S_{12}S_{21}}{2S_{21}} \end{aligned} \tag{3.26}$$

The geometrical parameters of the FSS's unit cell are to be tuned to obtain the desired propagation constant. As mentioned earlier, the design is carried out using two distinct circuit models. The E-field lines of the TE mode are y-oriented, whereas the TM ones are polarized along x-axis. Also, inductive reactive sheets are demanded to y-oriented fields and capacitive walls to x-oriented ones. Therefore, meandered Jerusalem crosses suit well as meta-waveguide's unit cell. The reactive impedances are not spatial-dependent, thus their design relies on the spatial homogenization, i.e., unit cell dimension electrically-small with respect to the operating wavelength. Two simulation setups [see Fig. 3.11] are then considered for the two field orientations. At the time of this manuscript's redaction, the design of this type of meta-waveguides has been not retrieved yet. Future research activities will focus on its design and integration within the antenna architecture of dual-mode ED CTS arrays.

3.6 Conclusions

In this Chapter, the modal analysis of PPWs with purely reactive walls has been reported. This type of waveguides can achieve an equi-dispersive, dual-mode propagation. The two modes are orthogonally-oriented along the waveguide cross-section and are employed to radiate circularly-polarized fields. Accurate analytic expressions are obtained for a proper dispersion engineering of these

structures. Specifically, the two modes are sought to exhibit the same dispersive behavior. The problem is studied by means of a dedicated eigenvalue analysis, leading to simple formulae to be employed in the model synthesis. An optimal operating point is thus easily attained. As a result, important physical insights are obtained and the analysis is extended to equi-dispersive, dual-mode PPWs that behave as an anisotropic crystal (i.e., 90° delayed anisotropic line). Afterward, these structures are arranged in a periodic environment as open-ended stubs, to investigate the radiating performance in terms of circular polarization. The numerical results demonstrate wideband capabilities (the axial ratio is below 3 dB over a fractional bandwidth of 22.3%). Given the arbitrariness of the cut-off frequencies, this bandwidth can be further enhanced. Equi-dispersive PPWs represent thus a valid solution to issues experienced by dual-mode CTS arrays (e.g., limited scanning range), due to a considerable inter-modal dispersion [refer to Chapter 2]. In conclusion, a short discussion about possible ways to address physical design is also reported.

Chapter 4

Dual-Polarized, Dual-Mode CTS Array in Ka-Band

As discussed in Chapter 2, dual-mode CTS arrays are able to provide the radiation of orthogonally-polarized fields by exploiting the electric properties of dual-mode parallel-plate waveguides (PPW). Specifically, arrays of long slots, whose width is comprised between a half and one operating wavelength, support the TEM and the first transverse electric (TE_1) modes. These two modes are orthogonally-polarized each other in the waveguide cross-section, as shown in Fig. 1.10, and can thus radiate dual-polarized fields. The main drawback is given by the presence of the first transverse magnetic (TM_1) mode, which is degenerate with the TE_1 mode. Since TM_1 and TEM modes exhibit E-fields polarized in the same direction, they may occur in strong mutual couplings along discontinuities. This problem is solved by employing anisotropic waveguides, whose dispersion behavior has been properly engineered. The basic idea lies in manipulating the boundary conditions (BC) of the feeding PPWs, in order to obtain *ad-hoc* engineered waveguide propagation [92]. The physical realization of the BCs relies on electrically-small periodic structures (e.g., corrugations, bed of nails, frequency-selective structures, etc.), employed as PPW's walls. By modeling these structures as equivalent surface impedance [88, 93], their dispersion can be tuned by playing with the geometrical parameters. This Chapter[1] proposes a solution relying on the use of longitudinally-corrugated PPWs (LCPPW). The work is the result of the research activity carried out at Institut d'Électronique et des Technologies du numéRique (IETR), in the frame of a collaboration with Centre National d'Etudes Spatiales (CNES). The antenna

[1]This Chapter is an extended version of the articles [J-4] and [J-5]. The list of the author's publications is included at the end of this Ph.D. dissertation.

performs dual-polarized radiation, attaining wideband and high-gain operation over a large field-of-view. A ten-fold bandwidth enhancement is demonstrated with respect to previous dual-polarized antennas based on cross-connected architectures. Two separate feeding systems (i.e., pillbox couplers) are used to illuminate the slots under TEM and TE_1 illuminations, respectively. The demonstration of a unique dual-mode line source is currently under investigation and is out the scope of this manuscript.

4.1 Analysis of longitudinally-corrugated PPW

An over-moded PPW of height comprised between a half and one wavelength supports the propagation of three modes (i.e., TEM, TE_1 and TM_1), whose transverse field profiles are shown in Fig. 1.10. The eigenvalues of metallic parallel-plate domain are found by solving (3.1) and enforcing (2.3), yielding to the following propagation constant [74]

$$\begin{aligned} k_{zn}^{TM} &= \sqrt{k^2 - \left(\frac{n\pi}{a}\right)^2}, \qquad n \in \mathbb{N} \\ k_{zn}^{TE} &= \sqrt{k^2 - \left(\frac{n\pi}{a}\right)^2}, \qquad n \in \mathbb{N}^+ \end{aligned} \tag{4.1}$$

where k is the wavenumber in the medium filling the PPW and a is the height of the PPW. Equation (4.1) tells us that the TE_n and TM_n modes are degenerate, thus they exhibit same cut-off frequency:

$$f_{cut-off}^{TE_n} = f_{cut-off}^{TM_n} = \frac{nc}{2a\sqrt{\epsilon_r}}, \qquad n \in \mathbb{N}^+ \tag{4.2}$$

where c is the speed of light and ϵ_r the relative permitivity of the material filling the PPW. The frequency range in which the PPW remains bimodal is given by

$$\begin{aligned} f_{min} = f_{cut-off}^{TE_1} &= \frac{c}{2a\sqrt{\epsilon_r}} \\ f_{max} &= 2f_{min} \end{aligned} \tag{4.3}$$

The height of the PPW is thus set as $a = \lambda_{max}/2$, where λ_{max} is the wavelength in guide associated with the minimum frequency. Using these settings, over-moded PPWs are fully characterized. This type of waveguides usually suffers

from strong mutual coupling between the TEM and TM_1 modes. Fig. 1.10 indeed shows that E-field lines are orthogonally-oriented for the TEM and TE_1 modes. Their mutual coupling is, therefore, roughly negligible and the corresponding analysis can be carried out independently for each mode. On the other hand, the TEM and TM_1 E-fields are polarized in the same direction, meaning they may occur in strong coupling with respect to one another. As a case-of-study, we consider a dual-mode T-junction, which is a basic component within the corporate feed network (CFN) in parallel-fed architectures of CTS arrays [6]. The considered T-junction geometry is shown in Fig. 4.1. When the

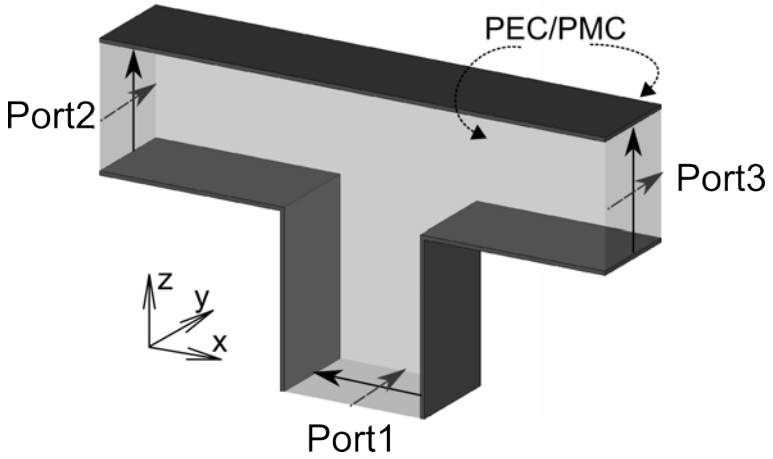

FIGURE 4.1: 3-D view of a T-junction comprising over-moded PPWs. The height of each PPW is 7 mm. The structure is infinitely extended along y-axis. PEC/PMC boundary conditions are assumed along the xz-planes to take into account the periodicity of the structure along the y-axis. Studying TE_n and TEM/TM_n mode excitation requires the use of PEC and PMC boundary conditions, respectively.

structure is excited by a pure TE_1 mode at Port 1, the output field at Port 2 and 3 is plotted in Fig. 4.2(a). It can be observed that the field profile remains almost unperturbed considering this type of T-junction. On the contrary, when Port 1 lunches a pure TEM mode, the field observed at Port 2 and 3 is a superimposition of the TEM and TM_1 modes, since non-negligible coupling effects occur at the section of the T-junction corners [see Fig. 4.2(b)]. As it is clearly visible in Fig. 4.2, the use of T-junctions made of over-moded PPWs is not suitable for our problem.

As mentioned earlier, a solution is to modify the BCs enforced on the parallel-plate domain, by placing electrically-small periodic structures on the

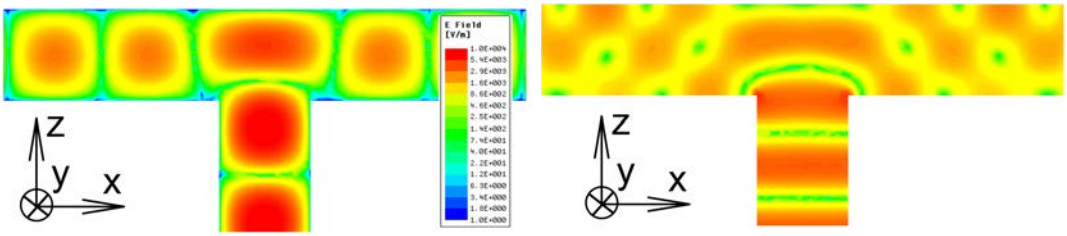

(a) TE_1 excitation. (b) TEM excitation.

FIGURE 4.2: Simulated amplitude of the E-field at 30 GHz. The height of the T-junction is 7 mm. (a) TE_1 mode excitation. (b) TEM mode excitation. The simulations were carried out using [81].

waveguide contour. In particular, we use longitudinal corrugations that aim to create a quasi hard-waveguide, as described in [93]. The perspective and cross sectional views of a LCPPWs are depicted in Fig. 4.3. The structure

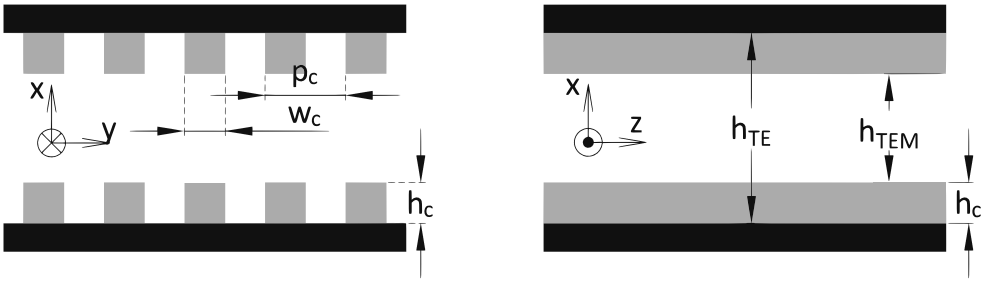

(a) Cross sectional view along xy-plane. (b) Cross sectional view along yz-plane.

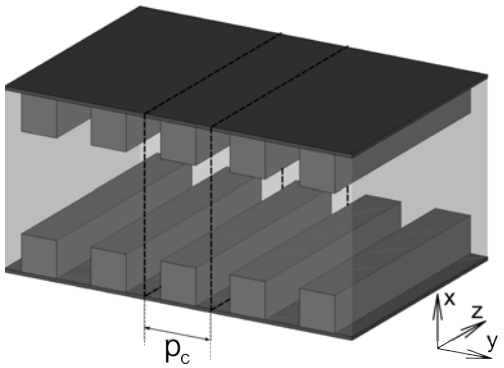

(c) Perspective view.

FIGURE 4.3: Cross sectional view of LCPPW along (a) xy- and (b) yz-plane. (c) 3-D view.

is infinite along y-axis and the modes propagate in the z-axis direction. The two metallic plates are spaced apart by h_{TE}, whereas the distance between the corrugations is h_{TEM} along the x-axis. The width of the corrugations is w_c and their linear spacing is p_c. Given p_c is electrically-small, the structure in Fig.

4.3 supports the propagation of two orthogonal modes (quasi-TE_1 and TEM), when the following settings are enforced

$$0 < h_{TEM} \leq \lambda_{min}/2 \tag{4.4}$$

$$h_{TEM} < h_{TE} \leq \lambda_{max}/2 \tag{4.5}$$

$$w_c < p_c \ll \lambda \tag{4.6}$$

$$f_{max} = 2f_{min} \tag{4.7}$$

Specifically, the propagation of the quasi-TEM mode is confined in the section $x \in [-h_{TEM}/2, h_{TEM}/2]$. On the contrary, the quasi-TE_1 mode E-field profile is extended to the whole waveguide cross-section $x \in [-h_{TE}/2, h_{TE}/2]$.

The proposed geometry of LCPPW can be easily understood by modeling the LCPPW as standard PPW, whose parallel plates are replaced with surface reactances. Basically, the corrugations are modeled as equivalent surface impedance accounting for TE and TM modes, respectively. The dispersion analysis of such structures follows the analytic model presented in Chapter 3. In particular, the surface impedance of longitudinal corrugations for TE modes is calculated using asymptotic corrugation boundary condition (ACBC) [94–97] and can be expressed in closed-form, thus yielding to

$$Z_{corr}^{TE} = i\omega\mu \frac{p_c - w_c}{p_c} \frac{\tan\left(k_x^{corr} h_c\right)}{k_x^{corr}} \tag{4.8}$$

where

$$k_x^{corr} = \sqrt{k_0^2(\epsilon_r^{corr} - 1) + k_x^2} \tag{4.9}$$

where k_0 is the free-space wavenumber and ϵ_r^{corr} is the dielectric constant of the material filling the corrugations. Moreover, the surface impedance of longitudinal corrugations for TM modes is calculated by considering a plane-wave equivalence of the PPW modes [74] and by studying the reflection properties of artificially hard-surfaces [98]. In formulae

$$Z_{corr}^{TM} = \frac{Z_x}{\eta_0} \sec\left(\theta_i^{TM}\right) \tag{4.10}$$

where

$$Z_x = -i\frac{p_c}{p_c - w_c}\eta_0\sqrt{\epsilon_r^{corr} - \sin^2\left(\theta_i^{TM}\right)}\cot\left(k_0 h_c\sqrt{\epsilon_r^{corr} - \sin^2\left(\theta_i^{TM}\right)}\right) \quad (4.11)$$

where η_0 is the free space impedance and θ_i^{TM} is the incident angle of TM modes in PPW by equivalence with the plane wave theory [74]. It can be seen that Z_{surf}^{TM} is nearly zero for a parallel plate problem. As representative example, the incident angle of TEM mode is $\theta_i^{TM} = 0°$ that corresponds to $Z_{surf}^{TM} = 0\ \Omega$, when inserted into (4.10). In general, $Z_{surf}^{TM} \to 0$ for higher order TM modes. When the corrugation are placed at distances given by (4.4), the propagation of quasi-TM_1 mode is cut off, whereas that of the TEM mode remains supported.

The dispersion of TE modes in LCPPW is obtained by equaling the right hand sides of equations (4.8) and (3.8). The characteristic equation (CE) of LCPPWs is so retrieved. The latter is transcendental and can be numerically solved using a Padé-approximant-based root-finding procedure [87]. Likewise, by equaling (4.10) and (3.14), the CE for TM modes in LCPPWs is found too. Fig. 4.4 plots the CE of TE and TM modes in LCPPWs at frequency f_{max} in dB. The following geometric parameters were considered throughout the analysis:

$$\begin{aligned} h_{TE} &= \lambda_{max}/2 \\ h_{TEM} &= \lambda_{min}/2 \\ w_c &= \lambda_{max}/20 \\ p_c &= \lambda_{max}/10 \\ f_{max} &= 2f_{min} \end{aligned} \quad (4.12)$$

The solid line circle represents the visible range, i.e., $\Re\{k_x\}^2 + \Im\{k_x\}^2 = k_0^2$, meaning that all the poles (blue spots in Fig. 4.4) located within such a circumference correspond to propagating modes. Also, the calculated roots are plotted in Fig. 4.4 using red dot markers. As shown in Figs. 4.4(a) and (b), one TE mode is in propagation at the highest frequency f_{max}. In the following, we will refer to this mode as quasi-TE_1 mode. Likewise, Figs. 4.4(c) and (d) show that a quasi-TEM mode ($k_x \sim 0$) propagates, whereas a quasi-TM_1 mode appears on the border of the visible range at f_{max}. It is worth plotting the dispersion diagram of such a structure. The propagation constant can be calculated as

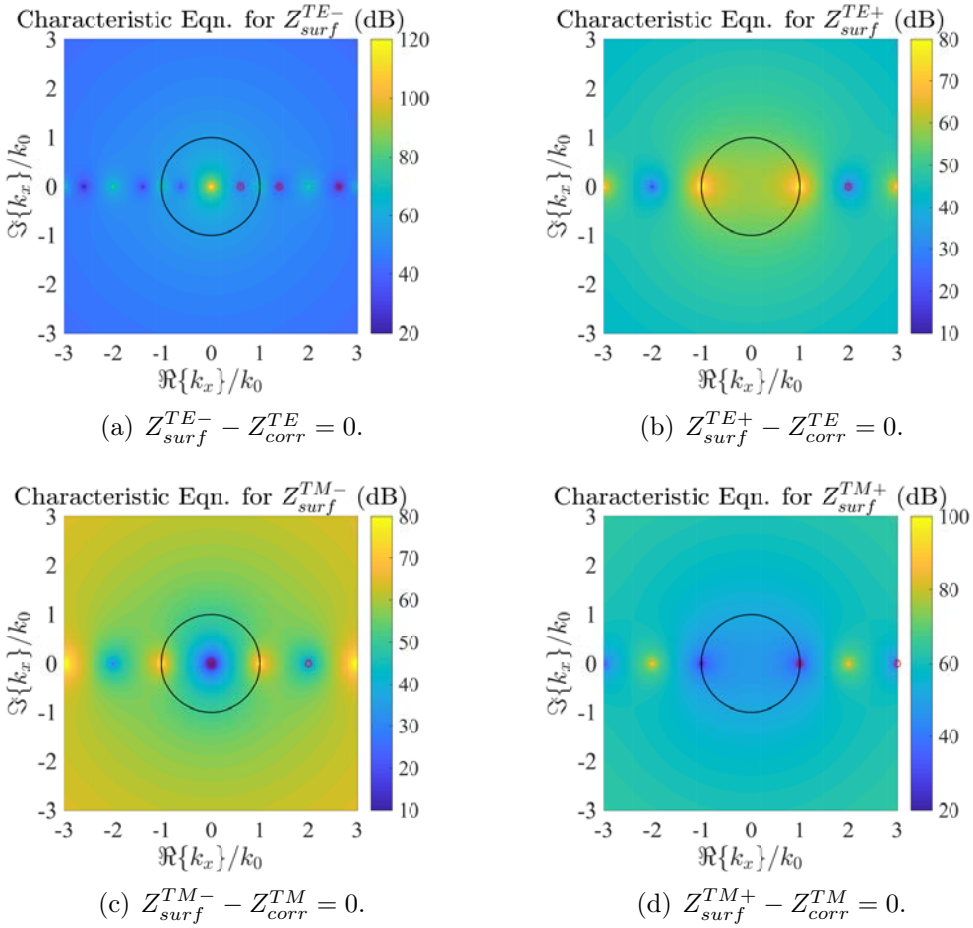

(a) $Z_{surf}^{TE-} - Z_{corr}^{TE} = 0$. (b) $Z_{surf}^{TE+} - Z_{corr}^{TE} = 0$.

(c) $Z_{surf}^{TM-} - Z_{corr}^{TM} = 0$. (d) $Z_{surf}^{TM+} - Z_{corr}^{TM} = 0$.

FIGURE 4.4: Characteristic equation of LCPPW for (a), (b) TE and (c), (d) TM modes at the frequency $f_{max} = 2f_{min}$. The plots are shown in dB, thus indicating the poles of characteristic equation with blue spots. The circle indicates the visible range ($|k_x| = k_0$) and red dot markers represent the calculated poles. These poles are found using a root-finding algorithm, e.g., Padé-based procedure [87].

follows

$$k_{zn}^{TM} = \sqrt{k^2 - \left(k_x^{TM}\right)^2}$$
$$k_{zn}^{TE} = \sqrt{k^2 - \left(k_x^{TE}\right)^2} \tag{4.13}$$

where k_x^{TM} and k_x^{TE} are the eigenvalues, being calculated by solving the corresponding CE numerically, as shown in Fig. 4.4. The calculated dispersion diagram is shown in Fig. 4.5, showing that LCPPWs support a quasi-TEM mode whose dispersion is roughly identical to that of the TEM mode in standard PPW. On the other hand, the quasi-TE_1 mode supported by LCPPW is slightly different than the TE_1 mode in PPW. Specifically, its cut-off frequency

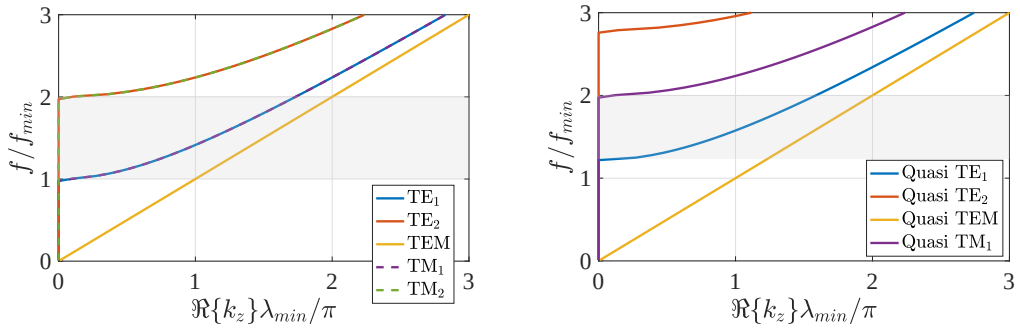

(a) Standard PPW. (b) Longitudinally-corrugated PPW.

FIGURE 4.5: Calculated dispersion diagram. (a) standard PPW whose height is fixed to $\lambda_{max}/2$ where λ_{max} is the wavelength associated to the lowest operating frequency f_{min}. (b) Longitudinally-corrugated PPW whose dimensions are given by (4.12).

is shifted at higher frequencies. It can be so concluded that longitudinal corrugations influence the dispersion of TE modes only. This valuable property can be thus used to engineer the dispersion of TE modes, while maintaining unperturbed that of the TEM mode. In conclusion, note that the proposed guide operates in bimodal regime within the frequency band $[\sim f_{min}, 2f_{min}]$, as indicated by the grey area in Fig. 4.5(b).

Now, let us focus on designing a LCPPW to operate in the frequency band 27-32 GHz. Based on the theoretical study as above, the parameters of the simulated LCPPW are: $h_{TE} = 0.7\lambda_0$, $h_{TEM} = 0.4\lambda_0$, and $d_z = 2\lambda_0$, where λ_0 is the wavelength in guide at 30 GHz. Multi-parameter studies have been carried out using the full-wave simulator [81], so that we can observe the impact of the corrugation geometry on the quasi-TE$_1$ mode dispersion. This analysis is shown in Figs. 4.6 and 4.7. The simulations have been carried out considering perfect electric conductor (PEC) as boundary condition on the lateral faces (xz-plane) of the LCPPW [see Fig. 4.3]. Fig. 4.6(a) shows that the cut-off frequency of the quasi-TE$_1$ mode decreases with frequency as the period of the corrugations p_c increases. Likewise, the same behavior is observed as the width of the corrugations w_c decreases. This effect is easy to understand: the onset of the quasi-TE$_1$ mode occurs when the electrical distance among adjacent corrugations is large enough to allow the y-oriented TE field to penetrate among them. Furthermore, Figs. 4.7(a) and (b) show that the height h_{TE} highly impacts on shifting the

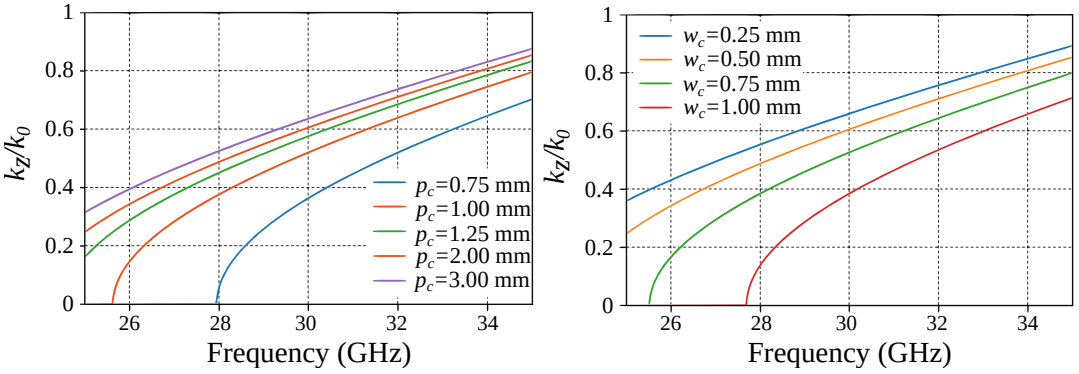

(a) Sweeping p_c. (b) Sweeping w_c.

FIGURE 4.6: Parametric analysis of the quasi-TE_1 mode dispersion in LCPPW. Swept parameters: (a) p_c and (b) w_c. The LCPPW considers $h_{TEM} = 4$ mm and $h_{TE} = 7$ mm.

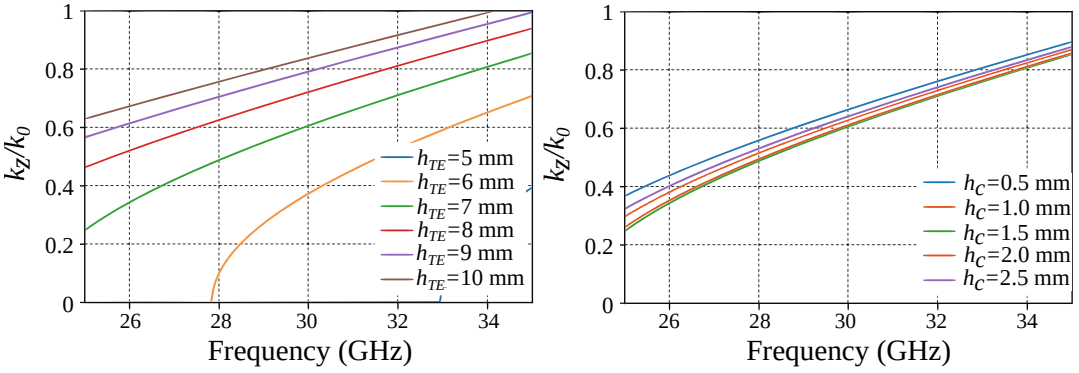

(a) Sweeping h_{TE}. (b) Sweeping h_c.

FIGURE 4.7: Parametric analysis of the quasi-TE_1 mode dispersion in LCPPW. Swept parameters: (a) h_{TE} and (b) h_c. The LCPPW considers $p_c = 0.15\lambda_0$ and $w_c = 0.05\lambda_0$.

cut-off frequency of the quasi-TE_1 mode. On the contrary, this effect is negligible while considering the influence of the height of the corrugations h_c. The latter is obviously explained considering that the y-oriented E-field lines of TE modes are nor affected as h_c increases.

At this point, we will focus on reducing the coupling effects due to the presence of the quasi-TM_1 mode. As mentioned earlier, this effect appears along discontinuities such as T-junctions. In the following, we shortly show that using T-junctions, made of LCPPWs, helps in deleting the coupling between quasi-TM_1 and TEM modes. A perspective view of such a structure is shown in Fig. 4.8. The E-field amplitude has been simulated along the vertical cut-planes Σ_1 and Σ_2 [refer to Fig. 4.8]. The simulated results are shown in Figs. 4.9(a)

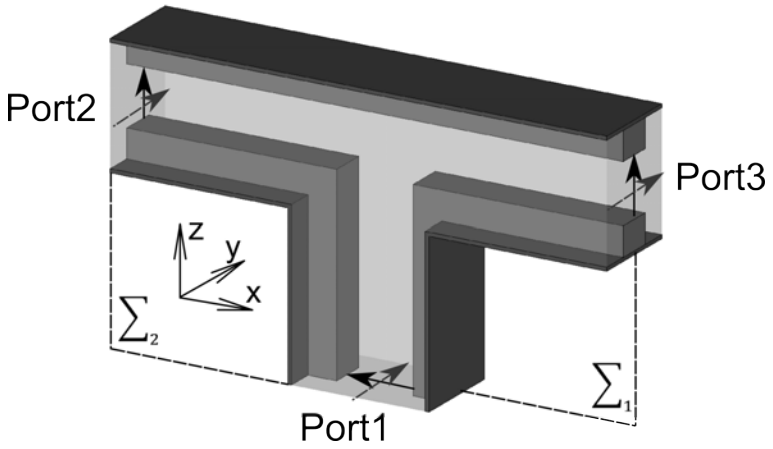

FIGURE 4.8: 3-D view of a T-junction comprising LCPPWs. The geometrical parameters of each LCPPW are $h_{TE} = 0.7\lambda_0$, $h_{TEM} = 0.4\lambda_0$, $p_c = 0.15\lambda_0$ and $w_c = 0.05\lambda_0$. The structure is infinitely extended along y-axis.

and (b), when Port 1 launches a quasi-TEM mode into the T-junction depicted

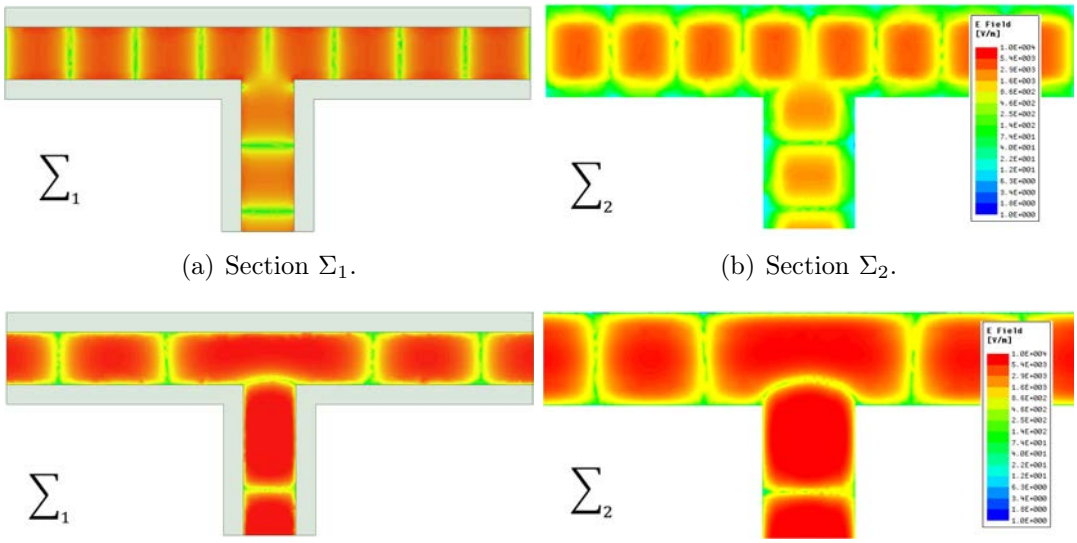

(a) Section Σ_1. (b) Section Σ_2.

(c) Section Σ_1. (d) Section Σ_2.

FIGURE 4.9: Simulated amplitude of the E-field at 30 GHz. The simulated structure is the one depicted in Fig. 4.8. Under quasi-TEM mode excitation: sections (a) Σ_1 and (b) Σ_2. Under quasi-TE_1 mode excitation: sections (a) Σ_1 and (b) Σ_2. The simulations were carried out using [81].

in Fig. 4.8. Likewise, Figs. 4.9(c) and (d) report the same simulation, but considering a quasi-TE_1 mode launched again from Port 1. The results reported in Fig. 4.9 demonstrate that T-junctions, made of LCPPWs, efficiently convey two orthogonally-polarized modes (quasi-TEM and TE_1), without occurring in strong mutual coupling with higher-order modes. It also emerges that, unlike

TEM mode, the quasi-TE_1 mode exhibits E-fields of significant amplitude, even within the grooves delimited by corrugations.

The transmission coefficient of the T-junction in Fig. 4.8 is plotted in Figs. 4.10(a) and (b) at 30 GHz as function of the LCPPW's height h_{TE} and the corrugation height h_c, respectively. This parametric analysis studies the impact

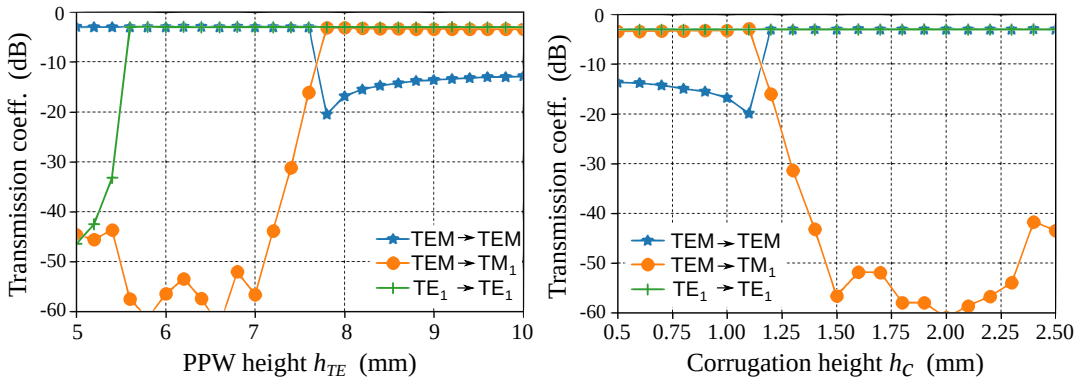

(a) $|S_{21}|$ versus h_{TE}. (b) $|S_{21}|$ versus h_c.

FIGURE 4.10: Simulated transmission coefficient of the structure in Fig. 4.8 as a function of (a) h_{TE} and (b) h_c at 30 GHz.

of the corrugation geometry to retrieve the best design goal. Specifically, in Fig. 4.10(a) the corrugation height is fixed as $h_c = 0.15\lambda_0$. Note that varying h_{TE} implies the height h_{TEM} is automatically calculated, by following the relation $h_{TEM} = h_{TE} - 2h_c$. Fig. 4.10(b) also shows the simulated transmission coefficient at 30 GHz as function of the corrugation height h_c, by having fixed the distance between the metallic plates as $h_{TE} = 0.7\lambda_0$. Ideal transmission is achieved when the T-junction equally splits the input power into the two output branches ($|S_{21}| = |S_{31}| = -3$ dB). From Fig. 4.10(a), it emerges that the transmission of the quasi-TE_1 mode occurs with negligible losses at frequencies slightly higher than its cut-off frequency (predicted by setting $h_{TE} = \lambda_0/2$). The transmission of the quasi-TEM mode appears devoid of strong coupling with the quasi-TM_1 mode, up to $h_{TE} > 0.7\lambda_0$. This is because the condition $h_{TE} > 0.7\lambda_0$ drives in having $h_{TEM} > \lambda_0/2$, thus enabling the propagation of the quasi-TM_1 mode. On the other hand, Fig. 4.10(b) shows that the transmission of the quasi-TE_1 mode is roughly constant with important variations of h_c. Conversely, the quasi-TEM mode does not couple with the quasi-TM_1 mode when $h_c > 0.12\lambda_0$. If $h_c < 0.12\lambda_0$, the inner region (bounded by corrugations) gets enlarged enough to enable the onset of the quasi-TM_1 mode.

4.2 Design of the corporate feed network

Section 4.1 provides physical insights to designing LCPPWs embedded in more complex structures, such as T-junctions. Following the guidelines presented in Section 4.1, we can now design a corporate feed network (CFN) to address the design of a dual-polarized over-moded CTS array in the Ka-band. The proposed CFN consists of 1-to-2 way T-junctions in LCPPW technology. The CFN is used to distribute the input power uniformly over eight radiating slots that support the propagation of two orthogonally-oriented modes (i.e., quasi-TEM and TE_1). The cross section of the proposed CFN is shown in Fig. 4.11. The inner region bounded by corrugation is drawn in white and it can be seen as

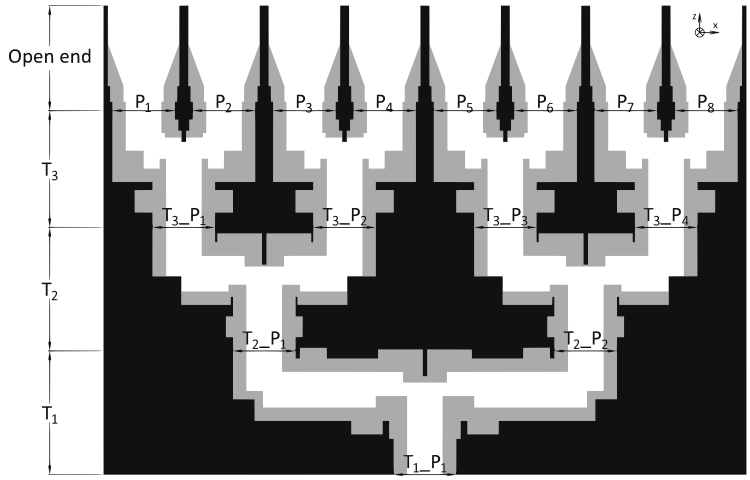

FIGURE 4.11: Cross section of the proposed corporate feed network of the Ka-band dual-polarized, over-moded CTS array. The region occupied by corrugations is depicted in grey. Conversely, the metallic plates are shown in black.

a hollow waveguide supporting the propagation of a quasi-TEM mode. The grey region is the one occupied by corrugations. Finally, the black part illustrates metal blocks. The geometry of the CFN is shaped by following the guidelines outlined in Section 4.2. In order to guarantee a pure dual-modal behavior in the frequency range 27-32 GHz, the following geometric parameters have been considered: $h_{TEM} = 0.4\lambda_0 = 4$ mm, $h_{TE} = 0.7\lambda_0 = 7$ mm, $h_c = 0.15\lambda_0 = 1.5$ mm, $p_c = 0.15\lambda_0 = 1.5$ mm and $w_c = 0.05\lambda_0 = 0.5$ mm.

4.2.1 Open-ended radiating slots

The radiating elements consist of long slots, supporting TEM and TE_1 modes. Their graphical representation is drawn in Fig. 4.12, along the antenna cross-section and from a top view. As shown in Fig. 4.12, a transition has been

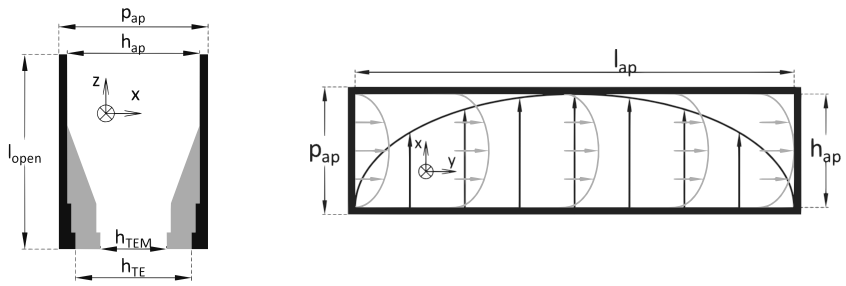

FIGURE 4.12: Geometry of the open-ended radiating over-moded stubs. On the left, a cross-sectional view. On the right, a top view comprising E-field lines of the radiating modes.

designed from LCPPW to over-moded PPW in the upper part of the radiating elements. This transition is necessary to attain equal directivity under TEM and TE_1 mode operations. As explained in Section 4.1, the quasi-TEM mode is indeed confined within the inner region delimited by the corrugations, whereas the quasi-TE_1 mode spreads all over the LCPPW cross-section. If we select open-ended LCPPWs as radiating elements, the efficient radiating area of the two modes will be different. To avoid this effect, an LCPPW-to-PPW transition is needed and the radiation efficiency maximized for the two modes. The width of the slots is set to $h_{ap} = 0.8\lambda_0 = 8$ mm, in order to maintain a pure dual-modal regime of the waveguide. Now, the periodicity of the slots p_{ap} has a strong

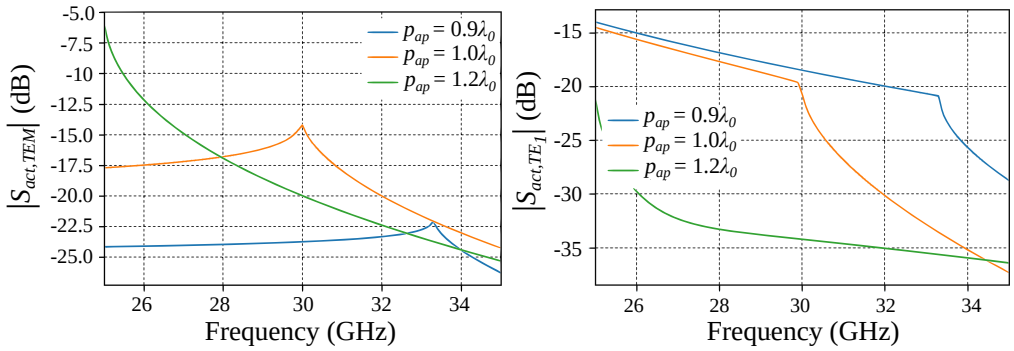

(a) TEM mode. (b) TE_1 mode.

FIGURE 4.13: Active S-parameters of the radiating elements under (a) TEM and (b) TE_1 mode operation for boresight radiation.

impact on the active reflection coefficient of the radiating slots. Using the in-house tool presented in Chapter 2.1, a parametric study has been carried out for different values of p_{ap}. This analysis is reported in Fig. 4.13. In Fig. 4.13(a), the reflection coefficient of TEM mode exhibits a peak for $p_{ap} = 10\lambda_0 = 10$ mm at the center of the band of interest. This peak moves out from the same band as $p_{ap} < 10\lambda_0$. The corresponding active reflection coefficient of TE_1 mode slowly varies with frequency for the same values of p_{ap}. For this reason, we select the operating point $p_{ap} = 9\lambda_0 = 9$ mm for the design. As mentioned earlier, an LCPPW-to-PPW transition is designed for the radiating elements. The input reflection coefficients at the sections P1 to P4 are plotted in Fig. 4.14. The

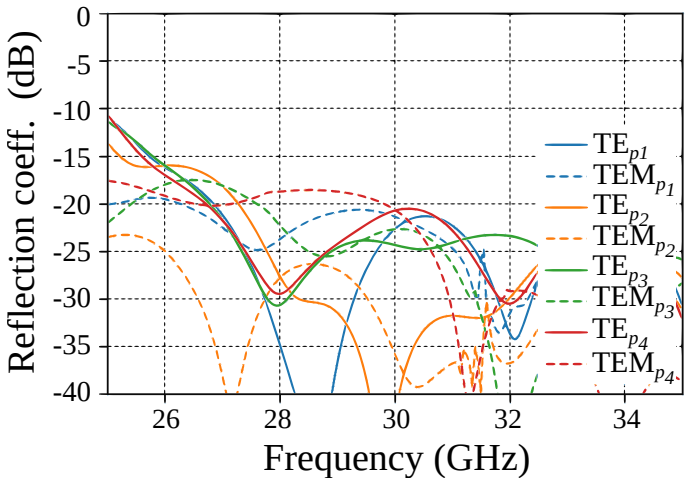

FIGURE 4.14: Input reflection coefficients at sections P1 to P8 (see Fig. 4.11) for TEM and TE_1 mode excitation for broadside radiation. For the sake of clarity, only port P1 to P4 are reported as the structure is symmetric.

reflection coefficients at sections P1 to P4 are below -15 dB all over the band 26-34 GHz when the array is pointing at broadside. in conclusion, the length of each radiating slot l_{ap} is set to 300 mm, in order to attain an array directivity higher than 33 dBi.

4.2.2 Stages of 1-to-2 way power dividers

The rest part of the CFN consists of three stages of balanced power dividers realized in LCPPW technology. Each division stage is depicted in Fig. 4.15 and has been designed by considering the inner region (bounded by corrugations) as an independent hollow waveguide that supports a quasi-TEM mode. In this case, design guidelines, based on transmission line models, have been employed

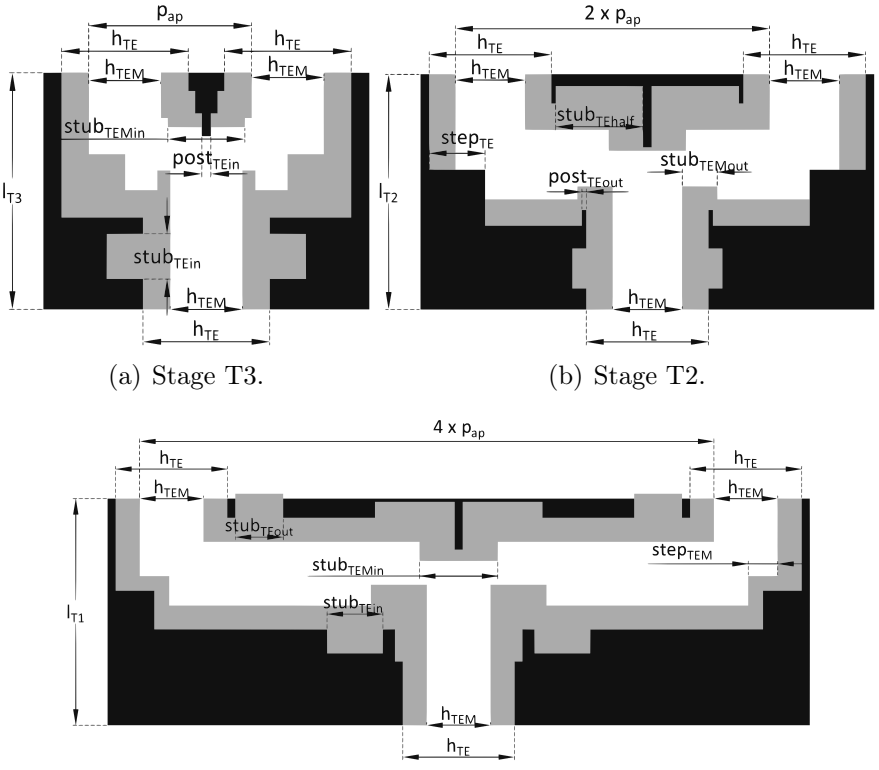

(a) Stage T3. (b) Stage T2.

(c) Stage T1.

FIGURE 4.15: Geometry of the three stages of balanced power dividers that realize the corporate feed network shown in Fig. 4.11. (a) Division stage T3. (b) Intermediate stage T2. (c) First division stage T1.

[6, 56]. The design of the corrugated region has been designed by means of full-wave simulations [81] and matching components (e.g., quarter wavelength stubs) have been introduced to improve the matching of the quasi-TE_1 mode. The geometric dimensions of the proposed structure are listed in Table. 4.1. The 1-to-2 way T-junction of stage T3 is shown in Fig. 4.15(a). This stage comprises four power dividers. The edge-to-edge distance of the output ports is $p_{ap} - h_{TE} = 2$ mm. The input reflection coefficient at Ports T3_P1 to T3_P4 [refer to Fig. 4.11] is below -15 dB all over the frequency band 27-32 GHz, under both TEM and TE_1 excitations. This simulation is not reported here for the sake of brevity. Fig. 4.15(b) depicts the intermediate stage of power dividers. This stage comprises two power dividers, as shown in Fig. 4.11. The impedance matching is improved using quarter wavelength stubs for the quasi-TE_1 excitation and employing cut edges for the quasi-TEM mode. Very narrow posts ($post_{TE_{out}} < \lambda_0/10$) have been inserted to further improve the matching of the quasi-TE_1 mode. The simulated reflection coefficient at sections T2_P1

TABLE 4.1: MAIN PARAMETERS OF THE POWER DIVIDERS.

	Stage T1	**Stage T2**	**Stage T3**
l_T	14.2	13.5	13.0
$step_{TE}$	2.42	3.20	n.a.
$step_{TEM}$	1.85	1.70	2.00
$stub_{TE_{in}}$	3.50	2.30	2.50
$stub_{TEM_{in}}$	4.90	4.40	4.25
$stub_{TE_{out}}$	3.00	n.a.	n.a.
$stub_{TEM_{out}}$	3.50	2.00	0.70
$stub_{TE_{half}}$	5.00	5.00	n.a.
$post_{TE_{in}}$	0.50	0.50	0.50
$post_{TE_{out}}$	n.a.	0.25	n.a.

* Dimensions are given in millimeters.

to T2_P2 shows a -20 dB impedance bandwidth all over the band 27-32 GHz. Finally, the power divider layout of stage T3 is depicted in Fig. 4.15(c). In this case, matching stubs have been inserted along the arms of the junction [refer to Fig. 4.11]. A very good matching is observed in this case for the two mode excitation as well. The simulated reflection coefficient at section T2_P1 is plotted in Fig. 4.16. Two scenarios have been considered: finite- and

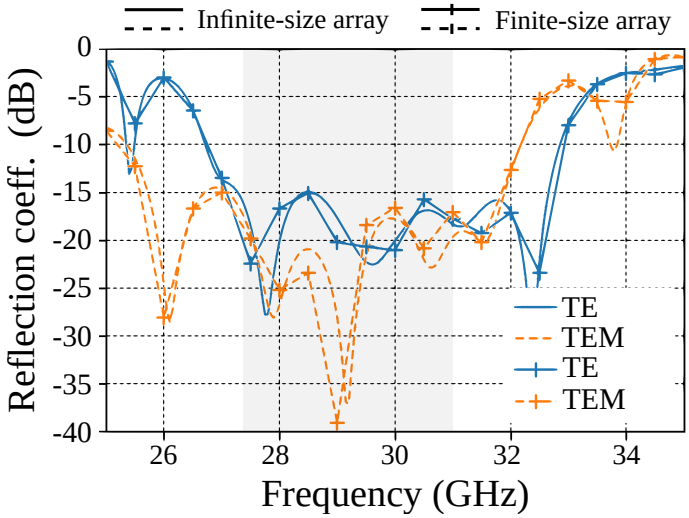

FIGURE 4.16: Simulated reflection coefficient at section T1_P1 of the finite- and infinite-size array. The simulated results accounts for both quasi-TEM and TE_1 mode operations.

infinite-size array. The simulation of the finite-size array has been carried out to observe the array's edge effects. As shown in Fig. 4.16, the designed array

exhibits negligible edge effects. A very good agreement is, indeed, achieved between the full-wave simulations of the finite and infinite array. This is likely due to the large electrical length of the array along y-axis (in the order of $30\lambda_0$). The antenna appears to be well-matched in the frequency band of interest, i.e., its input reflection coefficient is below -15 dB all over the Ka-band.

In conclusion, the simulated E-field amplitudes are shown in Figs. 4.17(a) and (b) for quasi-TEM and TE_1 excitations, respectively. The proposed CFN [see Fig. 4.11] efficiently supports a dual-mode propagation with negligible mutual coupling between the two modes. Figs. 4.17(a) shows that the quasi-TEM

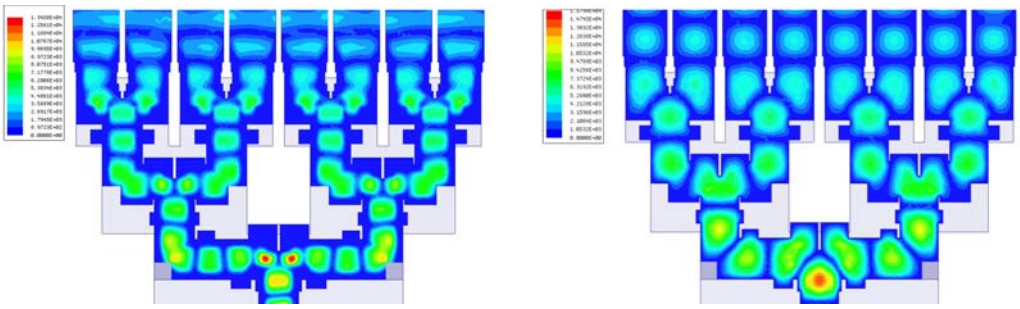

(a) Quasi-TEM excitation. (b) Quasi-TE_1 excitation.

FIGURE 4.17: Simulated E-field amplitude in the xz-plane for quasi- (a) TEM and (b) TE_1 excitation.

mode profile, along the propagation direction, is not altered by the presence of the other mode and the other way around. Specifically, the quasi-TEM mode propagation is mainly supported within the region bounded by the corrugation [refer to Fig. 4.17(a)], whereas the quasi-TE_1 spreads all over the whole LCPPW cross-section [see Fig. 4.17(b)].

4.2.3 Radiation performance

This Section aims at validating the radiation performance of the proposed dual-polarized over-moded CTS array. The antenna is able to radiate orthogonally-polarized fields, by exploiting the dual-modal behavior of over-moded PPWs. Specifically, the radiation of x- and y-polarized E-fields is attained by feeding the structure in Fig. 4.11 with the quasi-TEM and TE_1 modes, respectively. Normalized radiation patterns at 30 GHz are plotted in Figs. 4.18(a) and (b) along the yz-plane when the quasi-TEM and TE_1 modes are launched at section T1_P1, respectively. In Figs. 4.18(a) and (b), a comparison with

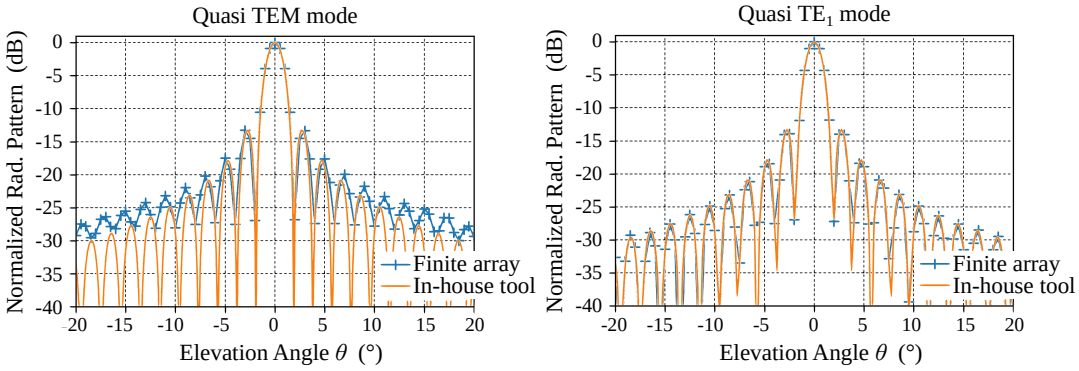

FIGURE 4.18: Simulated co-polar component of the radiation pattern at 30 GHz under quasi- (a) TEM and (b) TE_1 mode operation. The results are calculated along the yz-plane and refer to a boresight radiation. A numerical validation using the in-house tool presented in section 2.3 is also reported.

the numerical in-house tool, introduced in Chapter 2.3, is also reported. The radiation patterns are calculated using a rectangular function to window the magnetic current distribution over the radiating slots. The radiation pattern of the finite-size array is also computed considering copper as a conductive material for the metallic part. Despite this, an excellent agreement is observed between the full-wave simulation and the in-house tool. The side-lobe levels (SLL) are lower than -13 dB for both polarization. As demonstrated in [6], reduced SLLs can be further achieved by using a parabolic pillbox coupler beamformer [19, 20, 48], which creates a field tapering of the input source in the yz-plane.

Finally, the realized gain of the antenna is plotted for both polarization as a function of frequency in Fig. 4.19. The realized gain was simulated for the full-size array and compared with the gain of the long-slot array stand-alone. The computed gain for the slot array has been carried out using an in-house code, whose numerical model is presented in Chapter 2.3. Note that this tool does not account for ohmic losses, thus explaining the 0.2 and 0.6 dBi difference with the realized gain of the full antenna under quasi-TE_1 and TEM mode operations, respectively. The realized gains of the two radiated polarizations differ by only 0.4 dBi, resulting from the shared-aperture architecture and the input matching attained for both modes. To conclude, the designed antenna exhibits realized gains that vary from 33.1 to 34.6 dBi for both feeding modes all over the Ka-band.

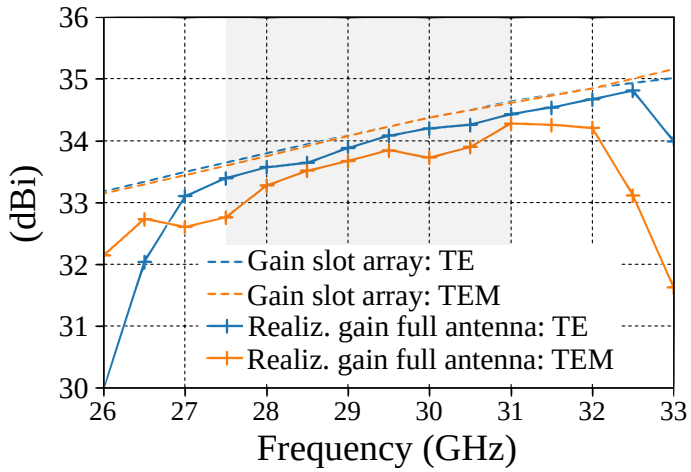

FIGURE 4.19: Simulated realized gain of the full-size dual-polarized CTS array when excited by quasi-TEM and TE_1 mode. A comparison with the long slot array stand-alone is also reported.

4.3 Antenna architecture

The aim of this Section is to present the experimental demonstration of the designed dual-mode CTS array. As aforementioned, this CTS array proposes a novel concept for achieving dual-polarized radiation, relying on feeding the radiating structure with two orthogonally-oriented modes. Polarization diversity is thus attained without using any mechanically-controlled rotation of the array, as done for example in [99]. Unlike [60, 99, 100], the antenna architecture that we propose requires two orthogonally-polarized line sources, applied at the bottom-most LCPPW of the CFN. Two separate pillbox couplers have been so designed to provide such a dual-polarized line source, as it is shown in Fig. 4.20. Each pillbox coupler is suitably designed to excite one mode at a time [6]. The realization of a dual-polarized line source, i.e., using a single quasi-optical system, is out of the scope of this work. The latter is indeed intended as a proof-of-concept of a novel CTS array, based on the dual-mode operation of over-sized PPWs [refer to Chapter 2]. A prototype has been fabricated. The stereolithography (SLA) technology has been selected to realize the radiating part [refer to 4.2] and used in combination with computer numerical control (CNC) milling for the fabrication of the beamformers.

We will refer to the two linearly-polarized radiated fields by discriminating between vertical (V) and horizontal (H) polarization hereinafter. The latter are given by the quasi-TEM and TE_1 mode operations, respectively. 1-D scanning

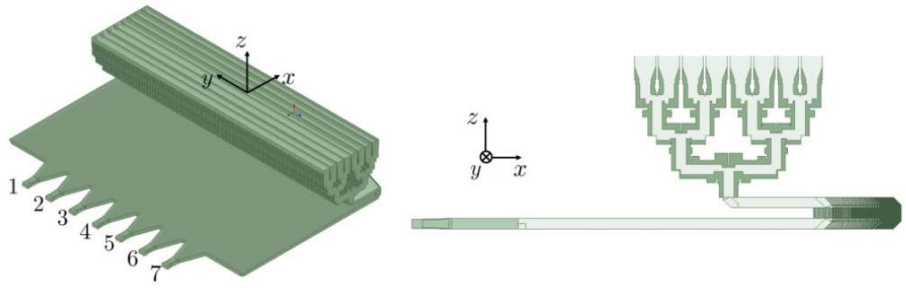

(a) Quasi-TEM pillbox beamformer.

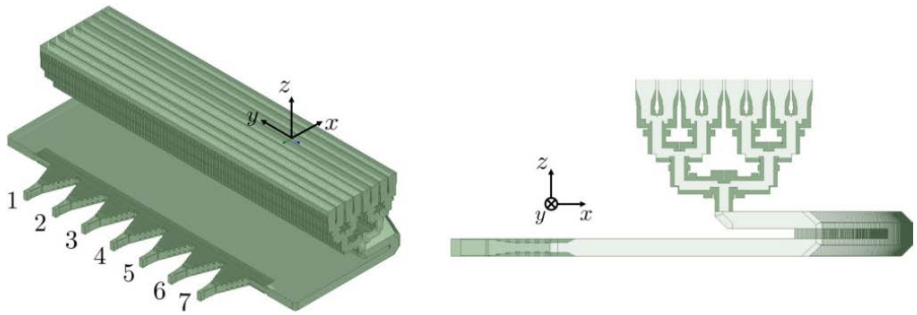

(b) Quasi-TE_1 pillbox beamformer.

FIGURE 4.20: 3-D and cross-sectional views of the designed dual-mode, dual-polarized CTS array. The radiating part of the antenna consists of that presented in Section 4.2, whereas two quasi-optical beamformers are used to excite the quasi- (a) TEM and (b) TE_1 modes, respectively.

performance is achieved by displacing the feeding horns (placed at the input section of the bottom-most PPW) along the y-axis. Each horn corresponds to a specific beam in the yz-plane. The two pillboxes have been specifically designed in order to have the same pointing direction at 30 GHz and make a fair comparison between the radiated H- and V-polarizations. In brief, the measurements prove that the antenna is well matched in the frequency band 29-32 GHz and exhibits good scanning performance up to $\pm 45°$ in the yz-plane. The cross-polarization discrimination (XPD) is higher than 24 dB within the same frequency band.

4.3.1 Pillbox systems for TEM and TE_1 excitation

The pillbox architecture recalls that used in [6, 19, 20, 48]. It consists of two stacked hollow PPWs. The feeding mode is launched into the bottom PPW, via a rectangular horn embedded in the same PPW. The input horn launches E-fields with cylindrical wave-fronts that are coupled to the upper PPW, after

being reflected by an embedded parabola. In the upper PPW, the field exhibits a quasi-plane wavefront. In particular, its amplitude is fairly constant all over a certain angular zone and tapered in the y-axis direction. The phase is linearly varied to achieve beam scanning in the yz-plane. The field in the lower PPW is coupled with the upper one through a 180° bend, contouring the embedded parabola for both TEM and TE_1 modes.

A dedicated pillbox is designed for each excitation (i.e., TEM and TE_1). The propagation constant is different for each mode and it can be approximated by

$$\begin{aligned} \beta_{TEM} &\sim k_0 \\ \beta_{TE_1} &\sim \sqrt{k_0^2 - \left(\frac{\pi}{h_{TE}}\right)^2} \end{aligned} \tag{4.14}$$

As result, the electrical paths traveled by the two modes are different. Consequently, the focal distance F of the two parabolas is non-identical for the two mode operations and the field impinging onto the parabola is reflected in different directions, as depicted in Fig. 4.21. The design of the two pillbox systems

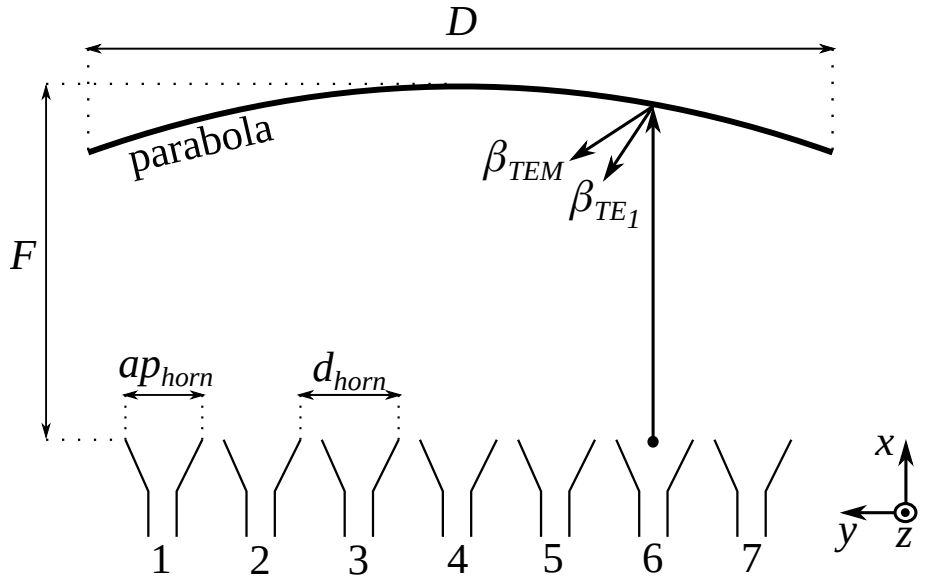

FIGURE 4.21: Schematic drawing of the pillbox system from a top view.

has thus been addressed considering two separate problems. Specifically, the horn positions have been selected in order to have same pointing angle for both systems. Seven horns were designed, whose pointing angles (0°, 7.5°, 15°, 22.5°) are equal for both modes in the yz-plane. The designed geometrical parameters

[refer to Fig. 4.21] are listed in Table 4.2. The choice of the parabola diameter

TABLE 4.2: MAIN PARAMETERS OF THE PILLBOX SYSTEMS.

	D	F	ap_{horn}	d_{horn}
TEM	300	180	25	25
TE_1	300	150	25	25

* Dimensions are in mm.

$D = 30\lambda_0 = 300$ mm derives from the antenna requirement of a directivity about 33 dBi at 30 GHz. All parameters have been retrieved by using an in-house tool based on geometrical optics (GO) [101]. Afterward, the structures have been optimized through full-wave simulations [81].

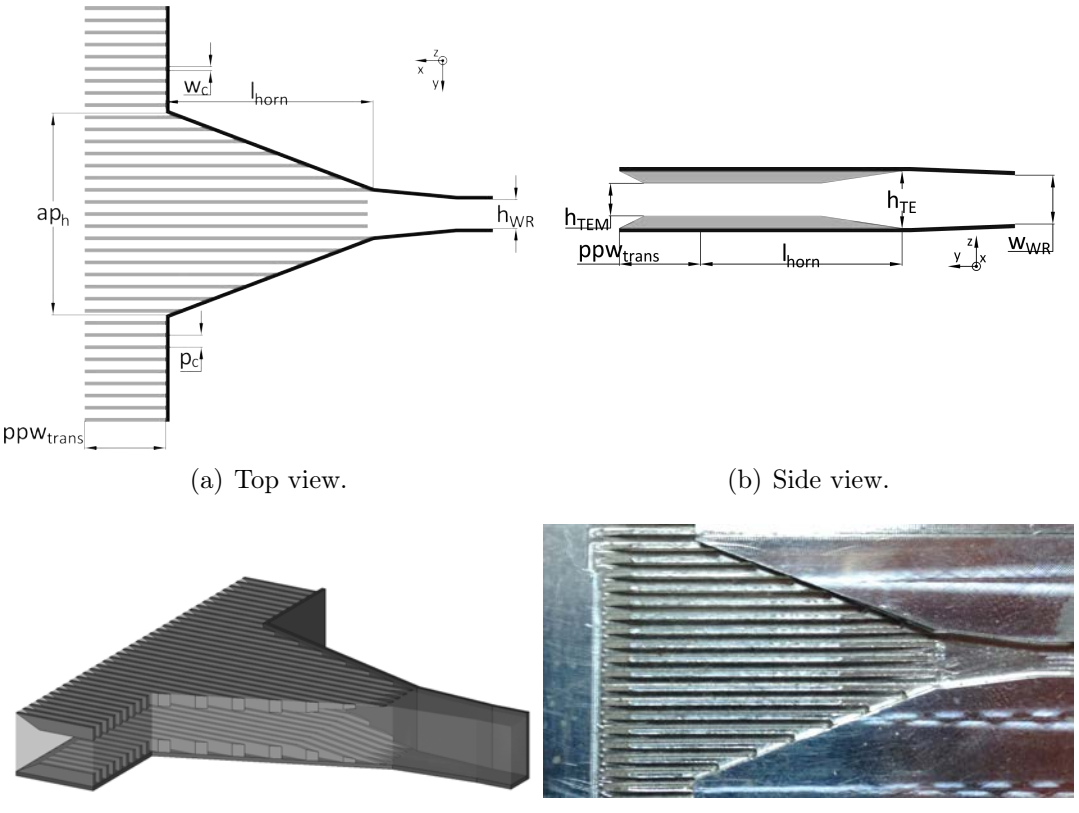

(a) Top view. (b) Side view.

(c) Perspective view. (d) Fabricated horn.

FIGURE 4.22: Schematic illustrating the input feeding horn embedded in the pillbox system under quasi-TE_1 mode operation. (a) Top, (b) side and (c) 3-D view of the horn. (d) Fabricated prototype.

The design for TEM operation is not discussed here as it recalls standard design procedures as in [6, 9, 20, 54]. On the contrary, several modifications have been applied to the design under the quasi-TE_1 mode operation. The main difference lies in having engineered the input section of the pillbox system by using a 90° rotated standard WR28 waveguide, in combination with a longitudinally-corrugated planar horn. The geometry of the designed input horn is illustrated in Fig. 4.22. The coaxial-to-rectangular waveguide connector launches y-polarized E-fields into the bottom-most PPW. The length of the tapered section of the horn is $l_{horn} = 25$ mm, whereas the aperture is 7×20 mm^2. Longitudinal corrugations are employed in the design to ensure the guidance of the desired mode. The corrugation parameters are: $w_c = 0.5$ mm, $hc = 1.5$ mm and $p_c = 1.5$ mm [refer to Figs. 4.22(a) and (b)]. The corrugations are

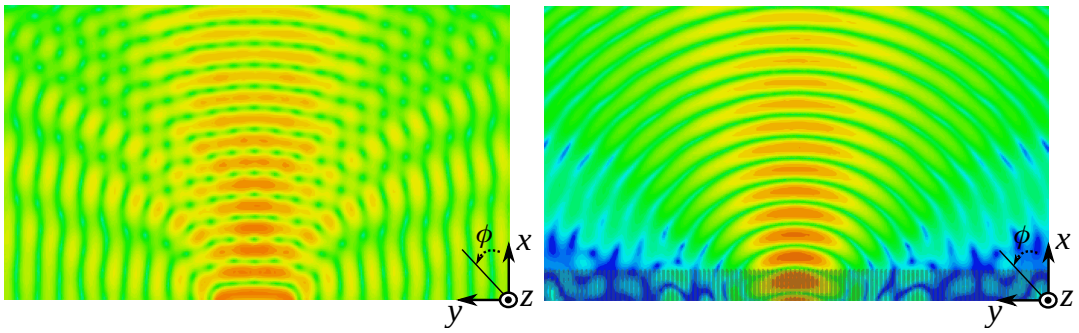

(a) Without corrugations. (b) With corrugations.

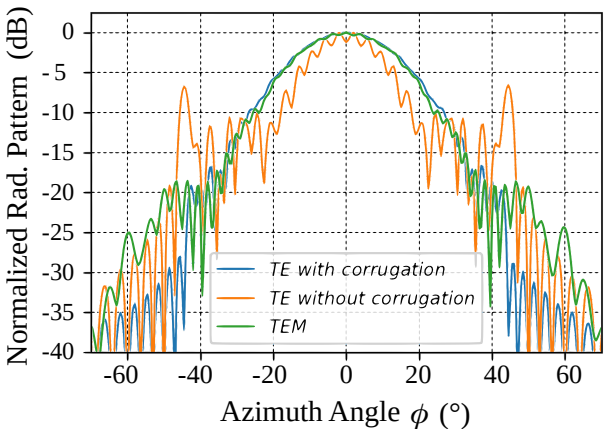

(c) Far field.

FIGURE 4.23: Amplitude of E-field in the bottom PPW of the pillbox beamformer for quasi-TE_1 mode. (a) Without and (b) with longitudinal corrugations. These plots refer to the xy-plane cut at $z = h_{TE}/2$. (c) Simulated far-field patterns of Horn 4 [see Fig. 4.21] at 30 GHz. The results are compared to those of quasi-TEM and non-corrugated quasi-TE_1 pillbox systems.

extended by ppw_{trans} = 10 mm beyond the aperture, to mild the transition horn-to-PPW. As mentioned earlier, the use of corrugations (x-axis directed) is needed to guarantee the desired field distribution within the structure. Specifically, Figs. 4.23(b) and (a) plot the E-field amplitude in the lower PPW in presence of corrugations and not, respectively. It can be noticed that the use of corrugations ensures having a cylindrical wave traveling along the PPW. When no corrugation is included, Fig. 4.23(a) shows that the field tends to propagate along y-axis too, thus spreading the energy in unwanted directions. For the sake of completeness, Fig. 4.23(c) plots the far-field radiated by the horn at 30 GHz. The radiated field is compared to that of a pillbox beamformer without corrugations. It can be observed that, in absence of corrugations, the E-field is distorted and high SLLs appear. On the other hand, the corrugated horn exhibits radiation patterns very much similar to those radiated by the pillbox system under TEM operation. In this case, the half-power beamwidth (HPBW) is about 35°.

In most cases of standard two-layer pillbox beamformers, multi-slots (contouring the parabola) are used to couple energy from the lower PPW to the upper one [19, 30]. These solutions are not easily implementable here, since they require thin metallic layers (not feasible with CNC milling technology). The cross-section of the proposed structure is depicted in Figs. 4.24(a) and (b) for TEM and TE_1 mode, respectively. A 180°-bend is employed to couple

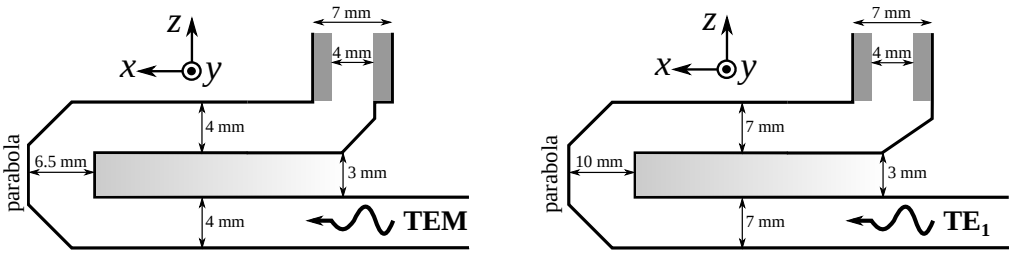

(a) Quasi-TEM mode. (b) Quasi-TE_1 mode.

FIGURE 4.24: Schematic with main geometrical parameters of the cross section of the two pillbox systems: (a) TEM and (b) TE_1 mode.

the energy between the two stacked PPWs. These configurations enhance the robustness of the overall structure, thus easing the fabrication process in CNC milling technology. As shown in Figs. 4.24(a) and (b), different pillbox-to-CTS

transitions have also been realized for TEM and TE_1 modes to improve the matching.

In conclusion, Figs. 4.25(a) and (b) plot the normalized radiation patterns in the xy-plane, when the pillbox beamformers are terminated to an open-ended PPW. Using HFSS [81], the pillbox structures are surrounded by PEC, and

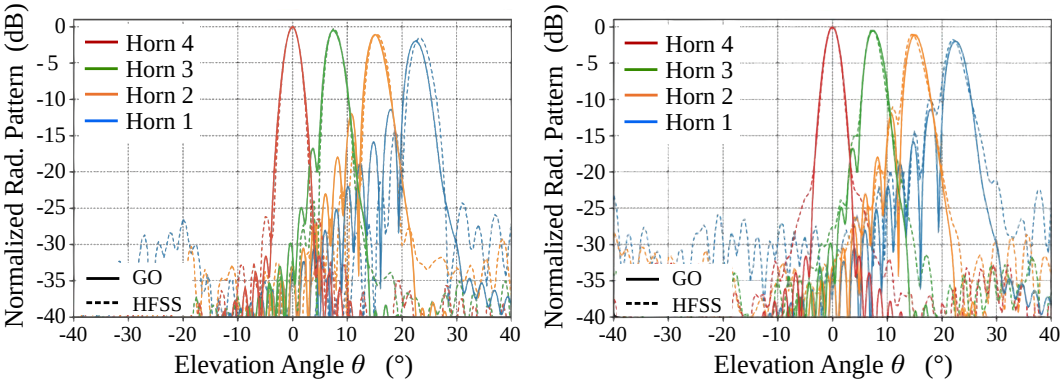

(a) Quasi-TEM mode. (b) Quasi-TE_1 mode.

FIGURE 4.25: Simulated radiation patterns of the open-ended pillbox systems at 30 GHz: (a) TEM and (b) TE_1 scenarios. The plots refer to the xy-plane.

the radiation boundary condition is enforced on the open end. The full-wave results are seen to be in good agreement with the GO prediction [101]. The two pillboxes slightly differ in HPBW. Specifically, the broadside beams show HPBW equal to 2.8° and 2.6° for TEM and TE_1 mode excitations, respectively. This difference is likely due to the E-field distribution of the two modes over the PPW's cross-section. As mentioned earlier, the amplitude profile of TEM mode is constant between the two plates, whereas that of TE_1 mode follows a cosine-like function [see Fig. 1.10]. Note that, due to the presence of metal walls, the E-field distribution exhibits the same tapering along the y-axis for both modes.

4.3.2 Fabricated prototype

The dual-polarized CTS array and the pillbox systems have been fabricated using both SLA and CNC milling technologies. The fabrication strategy consists of realizing several blocks and assembling them using screws and dowels. Eleven pieces were so built, as shown in Fig 4.26(a). The final antenna assembling is shown in Fig. 4.26(b).

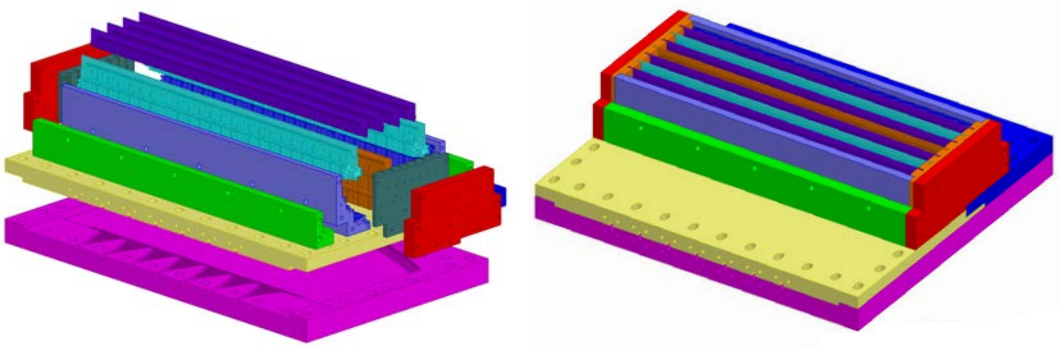

(a) Exploded view. (b) Assembled antenna.

FIGURE 4.26: (a) Exploded and (b) assembled view of the antenna architecture when fed by quasi-TE_1 pillbox beamformer. The various blocks are highlighted with different colors.

The SLA process shapes a photopolymer resin, thus defining layer-by-layer its transverse section. Afterward, an electroless copper plating ($10\mu m$ of thickness) is applied to realize the metallization. Figs. 4.27(a)-(c) show the details of one of the fabricated block before [see Fig. 4.27(a) and (b)] and after [see Fig. 4.27(c)] the copper plating. The measured tolerance of the corrugations is about 10 μm. For the sake of completeness, Fig. 4.27(d) and (e) show all fabricated antenna's building blocks before and after the copper plating, respectively. The fabrication process has turned out to be satisfactory, in terms of the accuracy of the fabricated pieces. On the contrary, the copper plating process is less reliable in terms of roughness and adhesive contact.

A picture of the overall antenna system is shown in Fig. 4.28. Specifically, the photograph of the pillbox system (for TEM operation) is reported in Fig. 4.28(a), whereas the radiating part in Fig. 4.28(b). The radiating open-ended stubs, made of LCPPWs, are filled with foam spacers (white part) in order to improve the mechanical stability of the system. The plastic blocks (fabricated using SLA) are, indeed, quite flexible (being very thin) and may bend and move with respect to their nominal position. This effect may result in creating a non-uniform power division provided by the CFN, which is undesired to our problem. The use of the full-metal 3-D printing technology would provide more robust components that might mitigate these issues. However, the roughness ensured by this technology has been deemed unsuitable to the fabrication of Ka-band components at the time. Finally, a picture of the prototype assembly

(a) Building block's zoomed-in detail.

(b) Before metal plating.

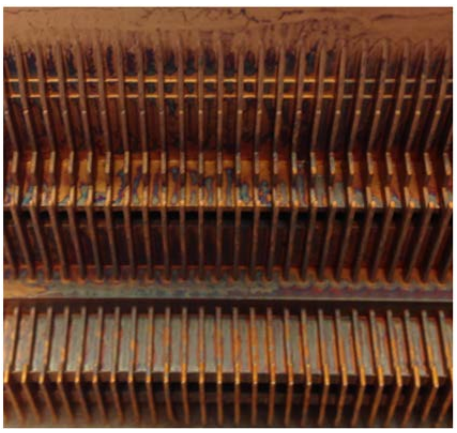

(c) After metal plating.

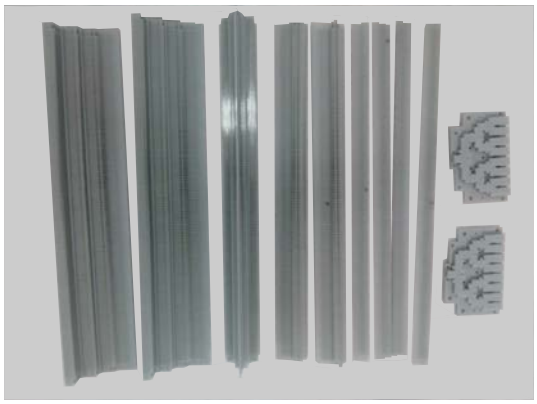

(d) Before metal plating.

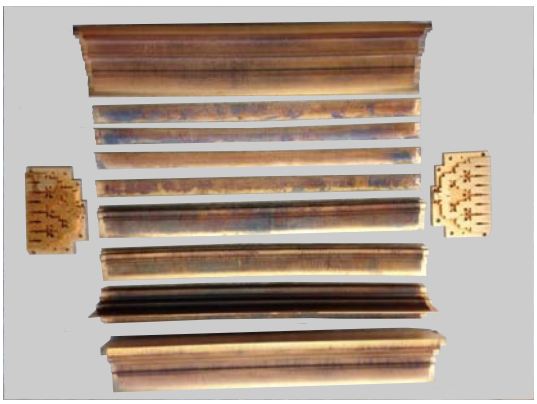

(e) After metal plating.

FIGURE 4.27: Detail of the LCPPW fabricated using SLA technology. (a) Building block's detail. (b) Before and (c) after copper plating. Also, photographs of all antenna building blocks of the over-moded CTS array: (a) before and (b) after the metal plating.

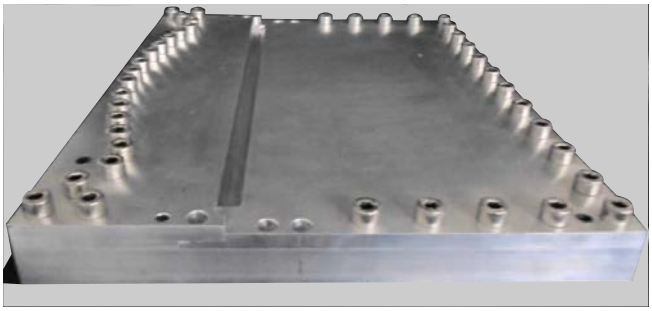

(a) Quasi-TEM pillbox.

(b) Radiating over-moded CTS array.

(c) Prototype assembly.

FIGURE 4.28: Photographs of the assembled prototype. (a) Qausi TEM pillbox beamformer. (b) Radiating long slot array, (c) Prototype assembly.

is shown in Fig. 4.28(c) when connected to the pillbox beamformer for quasi-TEM operation. The input focal array (seven feed horns) can be seen in the foreground.

4.4 Experimental results

The reflection coefficient of the prototype in Fig. 4.28(c) is measured by connecting each input horn to a vector network analyzer (VNA). A coaxial-to-WR28 transition was used to carry out the measurements reported in Figs. 4.29(a) and (b) for quasi-TEM and TE_1 mode operations, respectively. The worst results are obtained for the in-focus feed, i.e., Horn 4, whose aperture is centered in the focus of the parabola. From Fig. 4.29(a), we observe that

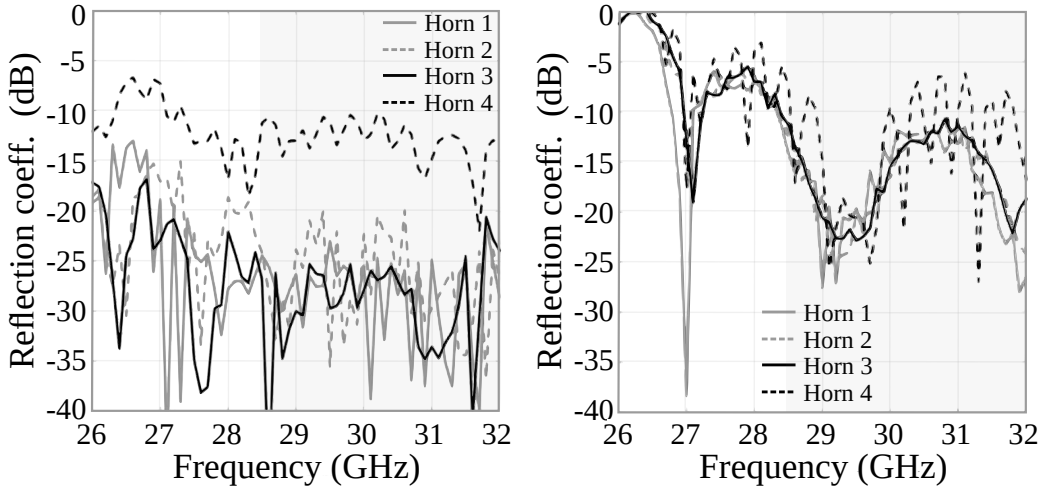

(a) Quasi-TEM operation.

(b) Quasi-TE_1 operation.

FIGURE 4.29: Measured reflection coefficient of the designed dual-polarized CTS array: (a) TEM and (b) TE_1 excitation. The reflection coefficient are measured at the input of the seven feeding horns for different beam steering.

the input reflection coefficient is lower than -10 dB over the band 27-32 GHz. On the other hand, the antenna exhibits -10-dB-impedance bandwidth in the frequency range 28.5-32 GHz for quasi-TE_1 mode excitation. Also in this case, the worst measured performance is found when Horn 4 is switched on. When the in-focus horn is operative, the reflection coefficient exhibits ripples around 31 GHz. Moreover, Fig. 4.29(b) shows that the cut-off frequency of the quasi-TE_1 mode is around 26.5 GHz. This value is higher with respect to its design value (24.5 GHz). As above discussed, this discrepancy is likely attributed to the bending effects of the plastic components in the antenna assembly.

The radiation patterns were measured using the anechoic chamber in IETR's facilities. The co-polar components of radiated fields along the yz-plane are plotted in Fig. 4.30 in comparison with the full-wave simulation at 30 GHz.

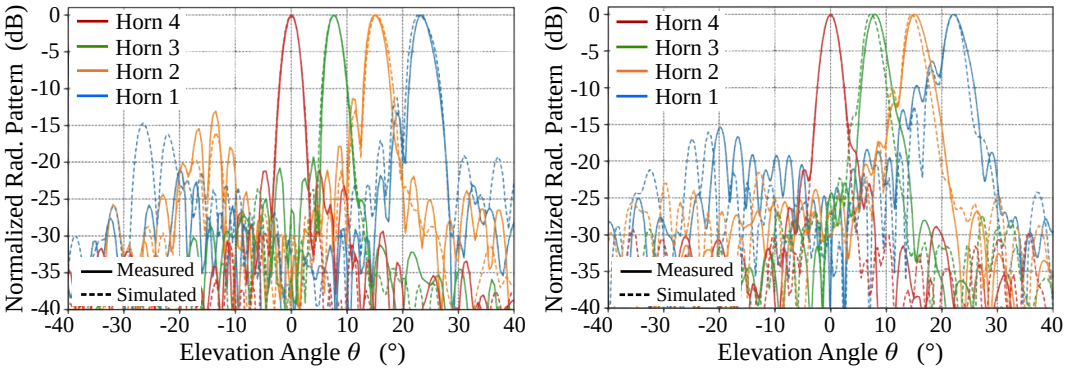

(a) H polarization. (b) V polarization.

FIGURE 4.30: Measured radiation patterns (yz-pane cut) of the designed dual-polarized CTS array at 30 GHz when fed by quasi-(a) TEM and (b) TE_1 beamformers. Each beam is normalized to its maximum.

Each beam is normalized to its maximum value. The measured beams deviate by less than 1° with respect to full-wave simulations. This deviation is more relevant for V-polarized fields. This trend is straightforward and derives from the shift of the quasi-TE_1 cut-off frequency, observed in the reflection coefficient measurements in Fig. 4.29(b). The first SLLs increase with scan angles, due to the off-focus illumination of the beamformers, and reach -11 dB and -8 dB for the H- and V-polarized outermost beams, respectively.

Fig. 4.31 shows the measured gain patterns in the yz-plane cut as function of frequency and elevation angle, when the antenna is fed by the pillbox beamformer for a proper excitation of the quasi-TEM mode. The measurements refer to non-negative pointing angles, i.e., Horns 1 to 4. The measured patterns are very stable for broadside radiation within the frequency range 27-32 GHz. The SLLs are in average below -20 dB. The gain level decreases around 30.6 GHz, owing to a phase imbalance along the radiating slots. This effect likely derives from the aforementioned misalignment of the plastic pieces assembled in the full antenna module. In general, the quasi-TEM antenna exhibits very low scan losses to all beams, as well as a stable frequency performance all over the Ka-band. Also, the measured gain patterns of V-polarized radiation are shown in Fig. 4.32. The measurements demonstrate that the quasi-TE_1 antenna exhibits a higher beam squint than the TEM one, deriving from the dispersive behavior of the mode in propagation. The scan angle varies from 21.1° to 23.6° between 29 and 32 GHz. The scan loss for the outermost beam is 2.8 dBi at 30.5 GHz.

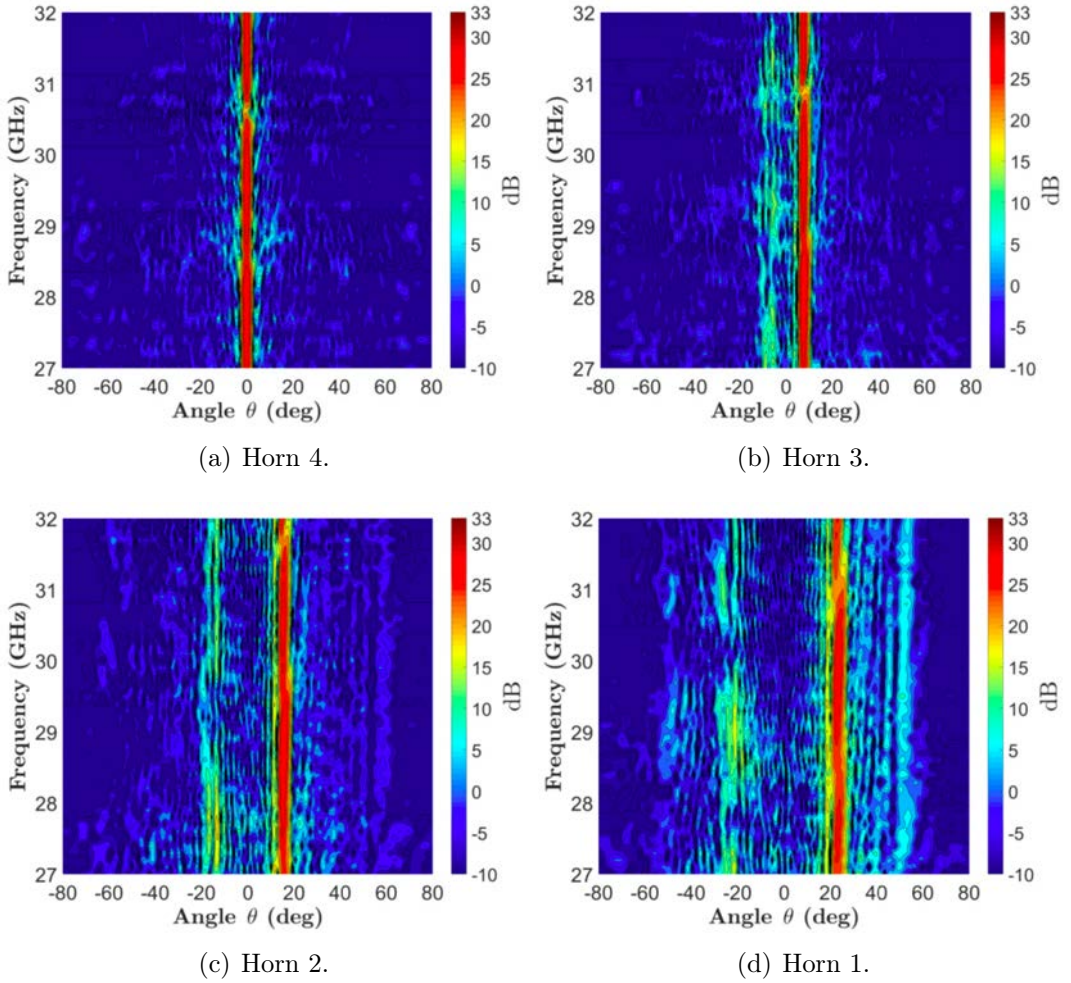

(a) Horn 4.

(b) Horn 3.

(c) Horn 2.

(d) Horn 1.

FIGURE 4.31: Measured gain patterns as function of frequency and elevation angle in yz-plane. The antenna is fed by the quasi-TEM pillbox beamformer.

It can be also observed that the cut-off frequency of the TE_1 mode varies in scanning. This effect is straightforwardly intuitive and can be mitigated by an optimal engineering of LCPPW's dispersion in scanning by following the approach proposed in Chapter 3. Although the LCPPWs have been optimized for broadside radiation, a good scanning performance is however observed for elevation angles up to $\pm 45°$ in the 28-32 GHz band.

The measured XPD in the band 29-32 GHz is reported in Table 4.3. The XPD is always higher than 11 dB, even for the outermost V-polarized beams. These results confirm that the proposed dual-mode antenna architecture achieves high polarization purity. Finally, the reliability of SLA as fabrication technology for Ka-band applications is also proved with the proposed prototype.

In conclusion, the measured realized gain is reported in Figs. 4.33(a) and (b)

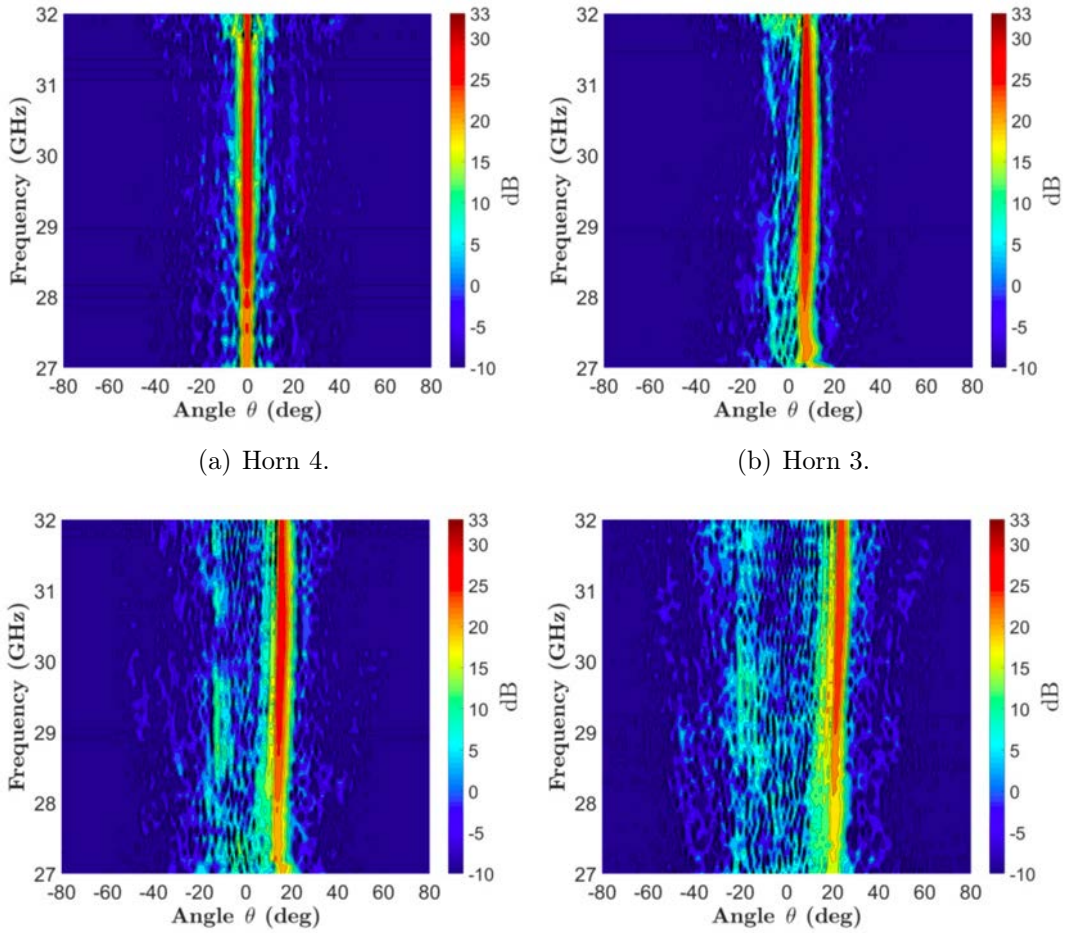

(a) Horn 4.

(b) Horn 3.

(c) Horn 2.

(d) Horn 1.

FIGURE 4.32: Measured gain patterns as function of frequency and elevation angle in yz-plane. The antenna is fed by the quasi-TE_1 pillbox beamformer.

TABLE 4.3: MEASURED XPD OF THE DUAL-POLARIZED CTS ARRAY IN THE BAND 29-32 GHZ.

HORN	**POL.**	**XPD (dB)**		
		29 GHz	30.5 GHz	32 GHz
1	H	19.2	12.6	14.1
	V	11.1	13.0	11.0
2	H	27.9	18.5	12.8
	V	14.4	19.5	12.7
3	H	29.6	21.7	17.6
	V	23.8	23.4	14.6
4	H	39.4	37.2	36.9
	V	24.2	24.9	28.1

for H- and V-polarized radiated fields, respectively. In general, the realized gain

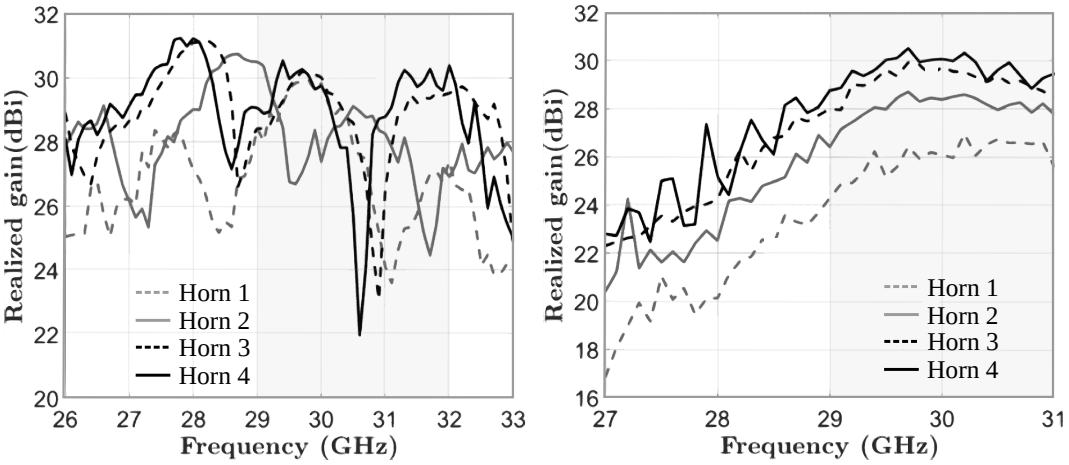

(a) H polarization. (b) V polarization.

FIGURE 4.33: Measured realized gain of the dual-polarized CTS array when alternately-fed by two pillbox beamformers for a proper excitation of quasi- (a) TEM and (b) TE_1 modes.

dips with respect to simulations [refer to Fig. 4.19]. This behavior has a two-fold explanation: fabrication limits and mismatch introduced by the pillbox-to-CTS transition, shown in Fig. 4.24. Firstly, the fabricated plastic pieces may easily result in bending, thus mismatching the radiating part of the antenna. Secondly, the pillbox-to-CTS transition may enable higher-order modes to propagate, thus resulting in undesired field perturbations. When the TM_1 mode propagates, it can occur in mutual coupling with the TEM one. Consequently, the antenna performance of the TEM mode is more sensitive, in terms of realized gain, than that of the TE_1 one. This effect can be observed by comparing Figs. 4.33(a) and (b). However, the measured realized gain is above 25 dBi in the frequency range 29-32 GHz for both modes. The measured peaks of the realized gain of the broadside beams are 31.3 dBi and 30.6 dBi for H- and V-polarizations, respectively.

4.5 State-of-the-art dual-polarized antennas

The key figures of merit of the proposed parallel-fed, over-moded CTS array are compared with the current state-of-the-art of dual-polarized antenna arrays. They are listed in Table 4.4. Different types of antenna systems are present in literature that achieve polarization agility. The most relevant works generally

TABLE 4.4: STATE-OF-THE-ART DUAL-POLARIZED ANTENNAS.

REF.	ARCHITECTURE	POLAR.	APERTURE SIZE	BANDWIDTH	PEAK GAIN	SCAN RANGE	RAD. EFF.
[102]	Microstrip array	Dual LP	n.a.	3.1%	26 dBi	±20°	40%
[103]	Quasi Yagi-Uda	Dual LP	$1.4\lambda_0 \times 1.32\lambda_0$ @ 36 GHz	22.2%	14 dBi	No scan	80%
[104]	Magneto-electric dipoles	Dual LP	n.a.	18%	16 dBi	No scan	82%
[105]	Reflector + Phased array	Dual LP	n.a.	15%	19 dBi	±30°	n.a.
[31]	Vivaldi array	Dual LP	$4\lambda_0 \times 4\lambda_0$ @ 10 GHz	102.5%	25.8 dBi	±30°	n.a.
[4]	Connected-dipole array	Dual LP	$5\lambda_0 \times 5\lambda_0$ @ 10 GHz	30%	35.4 dBi	±60°	n.a.
[60]	Cross-connected slots	Dual CP	$10.3\lambda_0 \times 10.3\lambda_0$ @ 94 GHz	1.1%	26 dBi	No scan	57.5%
[99]	Cross-connected slots	Dual LP	$5.1\lambda_0 \times 5.1\lambda_0$ @ 12.35 GHz	1.6%	17.8 dBi	±40°	n.a.
This work	Dual-mode CTS array	Dual LP	$30\lambda_0 \times 8\lambda_0$ @ 30 GHz	11.6%	31.3 dBi	±24°	80%

exhibit a trade-off in terms of encumbrance, bandwidth, and efficiency. For example, the antenna proposed in [105] combines a reflector with a phased array. The solution is broadband and has a relatively large field-of-view. On the other hand, the final system is very expensive, being bulky and complex. More compact solutions suffer either by bandwidth [102] or scanning capabilities [103, 104].

The ultra-wideband performance of Vivaldi arrays (about 102.5%) is confirmed for dual-polarized radiation [31]. This type of arrays exhibits also important scanning capabilities, as well as high-gain operation. Their main drawback lies in the feeding system, deemed too expensive for the modern SatCom applications. Each radiating element of the array in [31] is fed by a dedicated SMP connector, for a total of one hundred. For this reason mainly, Vivaldi arrays do not propose an affordable solution for the majority of the currently-used satellite services. Also, their encumbrance and weight do not suit well the SatCom requirements.

Connected-dipole arrays have also been proposed in [4] as a valid solution to the problem of polarization diversity. The antenna exhibits a large impedance bandwidth (30%) and achieves a very high-gain performance. The prototype presented in [4] accommodates the receive and transmit band in Ku-band within the same module. The main drawback of connected arrays lies in their bulky profile and, as for Vivaldi arrays, in the costs of the feeding network. Moreover, connected arrays suffer from inherent common-mode disturbs.

Cross-connected long-slot structures have been recently proposed in [60, 99] and achieve interesting performances. Both solutions rely on cross-connected slots, series-illuminated by dedicated quasi-optical systems. The antennas exploit the TEM mode propagation, thus mitigating issues due to dispersion in the structure. Circular polarization is attained in [60] and scanning performances

in [99]. Nonetheless, these solutions are series-fed, thus resulting in a narrow bandwidth operation, as typical of traveling-wave antennas. For the first time, our structure proposes a CTS array, having parallel-fed architecture, that attains polarization agility. All the advantages (e.g., broadband, wide scanning, etc.) offered by parallel-fed structures are then retained by the proposed array. The dual-mode CTS array, in fact, achieves an eight-fold enhanced -3-dB-gain bandwidth with respect to [99]. In conclusion, whilst the prototype in [60] does not enable beam scanning, the antenna in [99] performs a $\pm 40^{\circ}$ coverage in elevation (for all azimuth planes), by resorting to a mechanically rotated Riley prism that is placed over the array aperture. This device further narrows the bandwidth for off-boresight radiation.

4.6 Conclusions

In this Chapter, a novel dual-mode CTS array is designed and fabricated to demonstrate that polarization agility can be achieved by parallel-fed CTS arrays that support the propagation of orthogonally-polarized modes. The antenna array consists of eight over-moded long slots that are illuminated by two dedicated pillbox systems (one for each mode operation). A CFN, made of LCPPWs, is used to provide an equal field distribution over the radiating slots in amplitude and gradually phased to achieve beam scanning. Key advantages over existing dual-polarized CTS antennas include broadband operation and the use of a single radiating aperture instead of two orthogonally-oriented arrays, which are excited individually by a dedicated beamformer. Moreover, the proposed architecture allows for beam-scanning in one plane without any add-on motorized phase-shifting surface. The antenna has been fabricated using a low-cost SLA process. The measured broadside beams exhibit stable characteristics and comparable realized gain values in the band 29-32 GHz. Such a wide bandwidth ($\sim 11.6\%$) largely exceeds those attained by the state-of-the-art of dual-polarized CTS arrays, which are penalized by the traveling-wave radiation mechanism. In this band, the peaks of the realized gain are 31.3 dBi and 30.6 dBi, whereas the cross-polar components are less than -37 dB and -28 dB, under quasi-TEM and quasi-TE_1 excitations, respectively. The antenna achieves good performance for scanning angles as far as 22.5° in the yz-plane between 29 GHz

and 32 GHz. The antenna performance is partially limited by the fabrication technology, which has resulted in bending the plastic pieces within the antenna assembly. Alternative fabrication processes, such as SLM, may represent a more reliable solution. The experimental tests reveal that this concept of antenna is a valuable candidate, to be used as a next generation antenna for the SatCom ground segment.

Chapter 5

Dual-band, Orthogonally-Polarized LP-to-CP Converter

As discussed in Chapter 2, continuous transverse stub (CTS) arrays represent a good candidate to satisfy some of the modern SatCom requirements, owing to their wideband operation, large field-of-view and low-profile. However, the performance of standard CTS arrays is limited to a mono-modal operation that guarantees the radiation of linearly-polarized fields. Dual-mode CTS arrays propose a solution to radiate circular polarization (CP), but do not allow for the engineering of devices with CP diversity in non-adjacent bands. Modern K/Ka-band SatCom terminals, in fact, operate in two separate frequency bands, i.e., 17.7-21 GHz and 27.5-31 GHz, associated to the down-link and the up-link, respectively. Orthogonal polarizations are preferred in these two bands to further improve the isolation between transmitted and received signal. The design of highly-efficient CTS arrays, achieving a dual-band, orthogonally-polarized operation, is not straightforward. Combining linear-to-circular polarization (LP-to-CP) converters with linearly-polarized antennas (e.g., CTS arrays [6]) represents a simpler solution that meets the above-mentioned SatCom specifications. Typically, the up- and down-link are covered by combining two distinct radiating apertures with LP-to-CP converters [59]. This Chapter[1] is meant to propose a novel dual-band circular polarizer to attain orthogonal CPs in the K/Ka-band. This solution will be presented and characterized as stand-alone device. Once its performance will be established, it may be used in combination with a single aperture SatCom terminal covering both bands.

[1]This Chapter is an extended version of the article [J-3]. The list of the author's publications is included at the end of this Ph.D. dissertation.

Such a terminal may be a mono-modal CTS array [6, 9, 54], whose wideband capabilities have been largely outlined over the last decades.

Polarization converters usually consist of cascaded frequency selective surfaces (FSS) [106]. Multi-layer meander lines or more complex geometries have been designed to achieve broadband, single-band LP-to-CP converters [107–110]. The design method proposed in [107–110] is typically based on multi-parameter optimizations. A semi-analytic method to design single-band LP-to-CP converters has recently been proposed in [111]. The systematic procedure in [111] follows that of negative-refractive index (NRI) meta-materials [112, 113]. Basically, it is based on engineering the dispersion of a given unit cell's phase-shifter. In [111], the unit cell consists of three cascaded metasurfaces. By modeling each metasurface with a given circuit topology, the axial ratio (AR) bandwidth can be broadened, thus reducing insertion losses. However, the works to date [107–111] do not provide a systematic procedure to address the design of dual-band LP-to-CP converters with polarization conversion versatility (orthogonal polarizations in separate bands).

The design of dual-band, orthogonally-polarized LP-to-CP converters remains an open area of research. Only a few works can be found in literature. Most of them are based on equivalent circuit models (ECM), whose entries are usually obtained using multi-parameter optimizations. These procedures aim to search for the values of circuit elements for which the given ECM exhibits the desired dual-band frequency response. Specifically, the goal is to maximize the transmission at two frequencies and shape the AR response according to the project specifications. Multi-layer FSS-based structures have been proposed operating either in reflection [114–118] or transmission [119, 120]. In [120], the entries of ECMs are obtained by performing optimizations in Keysight Advanced Design System (ADS) [121]. The ECMs of [119] have been recently presented in [122], but they refer to a given unit cell's geometry. Generic ECMs, irrespective of unit cell's geometry, have not been presented yet. Alternatively, all-dielectric cascaded metasurfaces can achieve multi-band, multi-functional polarization controllers [123, 124]. Such low-loss topologies are very attractive but in general thicker than cascades of patterned metallic surfaces in the K/Ka-band. The solution proposed in [125] combines a four layer meander line

polarizer with a polarization rotator. This solution is very interesting from a systemic standpoint, but its overall profile is quite bulky. Moreover, the real-time re-configurable property, offered by time-modulated metasurfaces, has been recently receiving large attention. Among their multi-functional capabilities, it would represent a further way to realize dual-band, orthogonally-polarized LP-to-CP converters, as was done for polarization rotators in [126]. However, this is still an open field of research and we will not focus on this type of devices in the following.

The aim of this Chapter is is to introduce a fully analytic design procedure for dual-band, orthogonally-polarized LP-to-CP metasurface-based converters. A dual-band quarter-wave plate is realized by cascading three anisotropic electric sheet admittances, separated by two isotropic dielectric slabs. As shown in Fig. 5.1, 45°-slanted LP plane-waves are converted to left- (LHCP) and right-hand circularly-polarized (RHCP) waves in the down- and up-link channels of K/Ka-band SatCom link. The problem is studied by considering two equivalent shunt-loaded transmission line (TL) problems for each transverse field component, i.e., x- and y-polarized waves. The desired polarization conversion

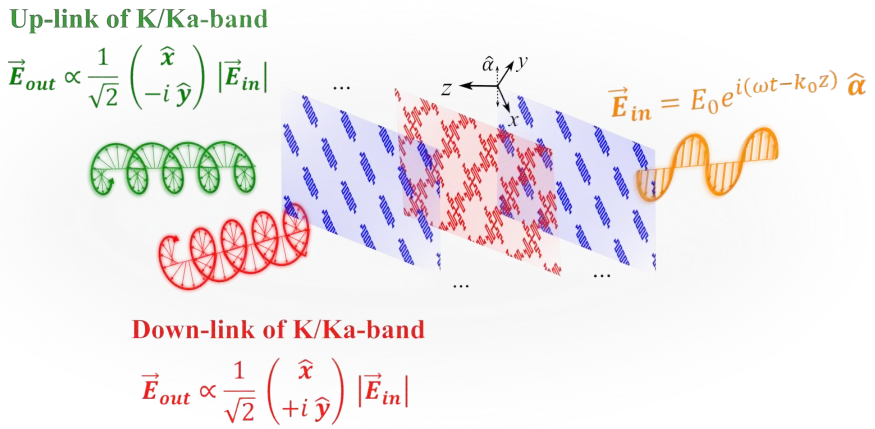

FIGURE 5.1: Exploded view of the dual-band, orthogonally-polarized LP-to-CP converter. The incident waves are linearly polarized at 45° with respect to the orientation of the metal patterns. They are converted into right- and left-hand circularly-polarized waves in two separate bands. The polarizer is a symmetric structure consisting of three patterned metallic claddings (metasurfaces).

is achieved by enforcing 100% transmission at two design frequencies in the two

considered bands. A ±90° phase delay is also enforced between the two transmitted transverse components to achieve orthogonal CPs to the two bands. The proposed ECMs are fully characterized using analytic formulae. This work has been carried out in the framework of a collaboration with the Radiation Laboratory and the group of Prof. Anthony Grbic at the University of Michigan, Ann Arbor, MI, USA.

5.1 Analytic model

A LP-to-CP converter is also referred to as a quarter-wave plate [127]. When the quarter-wave plate works in transmission mode, it conveys two orthogonal transverse field components phased ±90° with respect to each other while maintaining equal amplitudes. Fig. 5.2 shows the geometry of the considered unit cell's phase-shifter. Three sheet admittances are cascaded along z-axis.

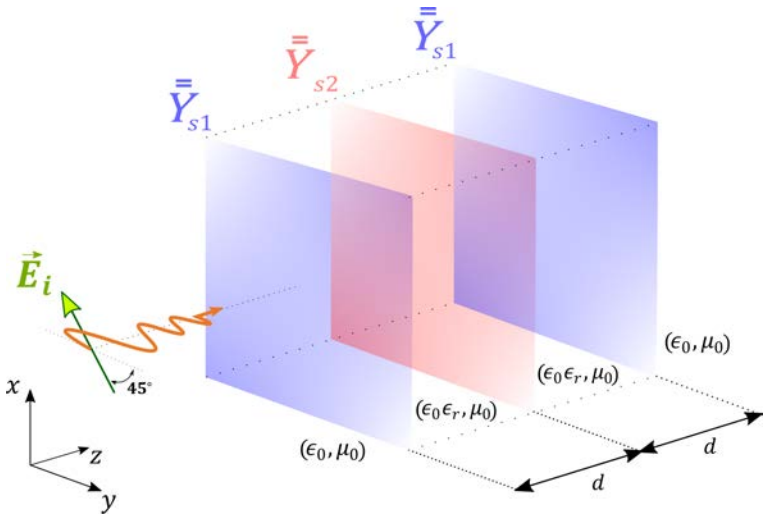

FIGURE 5.2: Geometry of the problem under analysis. Three anisotropic sheet admittances are cascaded along the z-axis. The external sheet admittances are equal.

Two dielectric slabs of thickness d and relative dielectric constant ϵ_r are used to separate each electric sheet. The transverse extent of the structure is assumed infinite. The outer sheets $\bar{\bar{Y}}_{s1}$ are diagonal and equal to each other. The inner admittance $\bar{\bar{Y}}_{s2}$ is also diagonal but distinct. The electric admittance of each sheet is given by

$$\bar{\bar{Y}}_{sn} = \begin{bmatrix} Y_{sn}^{xx} & 0 \\ 0 & Y_{sn}^{yy} \end{bmatrix}, \qquad n = \{1, 2\} \tag{5.1}$$

Given that the admittances are diagonal, the structure in Fig. 5.2 can be modeled as the combination of two separate phase shifters considering each orthogonal transverse component separately. To streamline the mathematical formulation, we will consider scalar admittances hereinafter.

The structure in Fig. 5.2 can be seen as the unit cell of periodic structure consisting of a transmission line (TL), loaded with reactive elements. Therefore, the theory of two-port microwave networks can be used in the analysis [74]. Let us assume that the admittance matrix of such a network is symmetric (reciprocal) and its entries are purely imaginary quantities (lossless). Each sheet admittance can be expressed in terms of the Bloch phase delay ϕ of the unit cell. To this end, the transmission matrix of the unit can be computed [74]

$$\begin{bmatrix} A & B \\ C & D \end{bmatrix} = \begin{bmatrix} A_1 & B_1 \\ C_1 & D_1 \end{bmatrix} \begin{bmatrix} 1 & 0 \\ Y_{s2} & 1 \end{bmatrix} \frac{1}{\xi} \begin{bmatrix} D_1 & B_1 \\ C_1 & A_1 \end{bmatrix} \tag{5.2}$$

where

$$\begin{bmatrix} A_1 & B_1 \\ C_1 & D_1 \end{bmatrix} = \begin{bmatrix} 1 & 0 \\ Y_{s1} & 1 \end{bmatrix} \begin{bmatrix} \cos\theta & i\eta_d \sin\theta \\ \frac{i\sin\theta}{\eta_d} & \cos\theta \end{bmatrix} \tag{5.3}$$

where θ is the electrical length of each dielectric slab and $\eta_d = \eta_0/\sqrt{\epsilon_r}$, where η_0 is the characteristic impedance of free-space. The quantity ξ can be re-written as

$$\xi = det\left\{ \begin{bmatrix} A_1 & B_1 \\ C_1 & D_1 \end{bmatrix} \right\} = A_1 D_1 - B_1 C_1 \tag{5.4}$$

where $det\{\cdot\}$ indicates the determinant of a matrix.

The inner and outer sheet admittances can both be expressed in closed formulae as function of Bloch impedance Z_B and Bloch phase delay ϕ of the unit cell in Fig. 5.2. After some algebraic manipulations and exploiting the symmetry of the network [128], we obtain

$$Y_{s1} = \frac{i}{\eta_d}\left(\cot\theta - \frac{\eta_d}{Z_B}\cot(\phi/2)\right) \tag{5.5}$$

$$Y_{s2} = \frac{i}{\eta_d}\left(2\cot\theta - \frac{Z_B}{\eta_d}\csc^2\theta\sin\phi\right) \tag{5.6}$$

Additional material to detail the derivation of equations (5.5) and (5.6) is reported in Appendix C.

The transmission coefficient S_{21} of the unit cell in Fig. 5.2 is given by

$$S_{21} = \left(\cos\phi + i\frac{\sin\phi}{2}\left(\frac{Z_B}{\eta_0} + \frac{\eta_0}{Z_B}\right) \right)^{-1} \tag{5.7}$$

Transmission is maximized by setting $|S_{21}| = 1$ in (5.7), thus yielding to

$$\frac{Z_B}{\eta_0} + \frac{\eta_0}{Z_B} = 2 \quad \Rightarrow \quad Z_B = \eta_0 \tag{5.8}$$

Equation (5.8) shows that the network exhibits maximum transmission when impedance is matched to free-space. This result is easy to understand being equivalent to the zero reflection condition in TL theory [56, 74]. It is important to note that equation (5.8) does not necessarily lead to maximum efficiency [56].

Finally, substituting (5.8) into (5.5) and (5.6) provides the sheet admittance values in 100% transmission regime

$$B_{s1}(\phi, f) = \Im\{Y_{s1}\} = \frac{1}{\eta_d}\left(\cot\theta - \frac{\cot(\phi/2)}{\sqrt{\epsilon_r}}\right) \tag{5.9}$$

$$B_{s2}(\phi, f) = \Im\{Y_{s2}\} = \frac{1}{\eta_d}\left(2\cot\theta - \sqrt{\epsilon_r}\csc^2\theta\sin\phi\right) \tag{5.10}$$

5.1.1 Design procedure

The design procedure for dual-band, orthogonally-polarized LP-to-CP converters starts specifying an appropriate frequency behavior for each electric sheet admittance. Once this is done, the design work-flow consists of enforcing the maximum transmission condition (5.8) at two distinct design frequencies: f_{01} and f_{02}. The systematic method depends on the variable ϕ_{01}^{xx}, i.e. the Bloch phase delay of the unit cell in Fig. 5.2 for x-polarized waves at frequency f_{01}. Note that this model establishes ϕ_{01}^{xx} as the only required input parameter to the design. After assuming a value for ϕ_{01}^{xx}, equations (5.9) and (5.10) are used to compute the sheet susceptances $B_{s1,01}^{xx} = B_{s1}^{xx}(\phi_{01}^{xx}, f_{01})$ and $B_{s2,01}^{xx} = B_{s2}^{xx}(\phi_{01}^{xx}, f_{01})$ at frequency f_{01}. According to the value calculated for $B_{s1,01}^{xx}$, two scenarios must be considered: the value of $B_{s1,01}^{xx}$ is positive or negative. The frequency response of Y_{s1}^{xx} is then calculated based on these two scenarios and thus assumed to be that of an inductor or a capacitor. A graphical representation of the two cases is depicted in Fig. 5.3. The outer sheet admittance for x-polarized waves Y_{s1}^{xx}

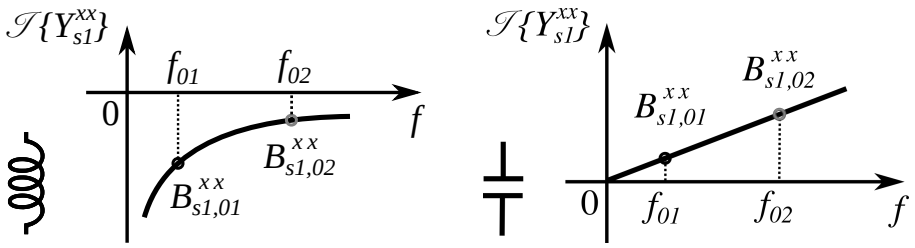

(a) $B_{s1,01}^{xx}$ is negative. (b) $B_{s1,01}^{xx}$ is positive.

FIGURE 5.3: Frequency response of Y_{s1}^{xx}. According to the sign of $B_{s1,01}^{xx}$, the frequency response of Y_{s1}^{xx} is assumed to be that of an inductor of a capacitor, refer to (5.11). (a) $B_{s1,01}^{xx} < 0$. (b) $B_{s1,01}^{xx} > 0$.

can be then expressed as a function of the frequency, as follows

$$Y_{s1}^{xx} = \begin{cases} i\omega C_{s1}^{xx}, & if \quad B_{s1,01}^{xx} > 0 \\ \\ (i\omega L_{s1}^{xx})^{-1}, & if \quad B_{s1,01}^{xx} < 0 \end{cases} \tag{5.11}$$

where

$$\begin{aligned} C_{s1}^{xx} &= B_{s1,01}^{xx}/\omega_{01} \\ L_{s1}^{xx} &= \left(\ \omega_{01}|B_{s1,01}^{xx}| \ \right)^{-1} \end{aligned} \tag{5.12}$$

where ω is the angular frequency and $\omega_{01} = \omega(f_{01})$. The fact that ϕ_{01}^{xx} is the only input parameter to the model is a direct consequence of having modeled Y_{s1}^{xx} as a single shunt inductor or capacitor. Note that different circuit topologies (e.g., LC-series) could be chosen for Y_{s1}^{xx} as well. This scenario would require a more complex approach (e.g., optimizations) to address the design of the polarizer. This point will be further clarified in the following of this Chapter.

Next, the phase delay for x-polarized fields ϕ_{02}^{xx} is obtained by inverting (5.9) at the frequency f_{02}, thus resulting in

$$\phi_{02}^{xx} = 2 \arctan\left(\frac{1}{\sqrt{\epsilon_r} \cot\theta_{02} - \eta_0 B_{s1,02}^{xx}} \right) \tag{5.13}$$

where $\theta_{02} = \theta(f_{02})$ and $B_{s1,02}^{xx} = B_{s1}^{xx}(\phi_{02}^{xx}, f_{02})$ is calculated by inverting (5.11) at the frequency f_{02}. Note this systematic procedure may be repeated assuming the frequency response of Y_{s2}^{xx} is that of a single lumped reactive element. This calculation is straightforward and do not lead to a more performing design method. Given the symmetry of the problem, it represents the dual case of

the considered design flow and, for this reason, is not reported for the sake of brevity.

Once ϕ_{01}^{xx} and ϕ_{02}^{xx} are known, we enforce the phase delay for y-polarized waves to be $\pm 90^{\circ}$ and $\mp 90^{\circ}$ shifted with respect to x-polarized fields at the two design frequencies f_{01} and f_{02}, respectively. The following conditions is thus enforced

$$\phi_{01}^{yy} = \phi_{01}^{xx} \pm 90^{\circ} \tag{5.14}$$

$$\phi_{02}^{yy} = \phi_{02}^{xx} \mp 90^{\circ} \tag{5.15}$$

Equations (5.14) and (5.15) guarantee orthogonal LP-to-CP conversions at the two design frequencies. At this point, equation (5.13) is inserted into (5.10) and $B_{s2}^{xx}\left(\phi_{02}^{xx}, f_{02}\right)$ is calculated at the frequency f_{02}. Likewise, B_{s1}^{yy} and B_{s2}^{yy} are computed at the two design frequencies, by substituting both (5.14) and (5.15) into (5.9) and (5.10), respectively. Thus, the frequency responses of Y_{s2}^{xx}, Y_{s1}^{yy}, and Y_{s2}^{yy} are assumed to be those of series-LC resonators, yielding

$$Y_{s1}^{yy} = \left(i\omega L_{s1}^{yy} + \frac{1}{i\omega C_{s1}^{yy}}\right)^{-1} \tag{5.16}$$

$$Y_{s2}^{xx} = \left(i\omega L_{s2}^{xx} + \frac{1}{i\omega C_{s2}^{xx}}\right)^{-1} \tag{5.17}$$

$$Y_{s2}^{yy} = \left(i\omega L_{s2}^{yy} + \frac{1}{i\omega C_{s2}^{yy}}\right)^{-1} \tag{5.18}$$

where

$$C_{sm}^{\psi\psi} = \begin{cases} \frac{|B_{sm,01}^{\psi\psi}|\left(1-\Delta f^2\right)}{\omega_{01}\left(1+\Delta f|\Delta B_{sm}^{\psi\psi}|\right)}, & if \quad \begin{matrix} B_{sm,01}^{\psi\psi} > 0 \\ B_{sm,02}^{\psi\psi} < 0 \end{matrix} \\ \frac{|B_{sm,01}^{\psi\psi}|\left(1-\Delta f^2\right)}{\omega_{01}\left(1-\Delta f|\Delta B_{sm}^{\psi\psi}|\right)}, & if \quad 0 < B_{sm,01}^{\psi\psi} < B_{sm,02}^{\psi\psi} \\ -\frac{|B_{sm,01}^{\psi\psi}|\left(1-\Delta f^2\right)}{\omega_{01}\left(1-\Delta f|\Delta B_{sm}^{\psi\psi}|\right)}, & if \quad B_{sm,01}^{\psi\psi} < B_{sm,02}^{\psi\psi} < 0 \end{cases} \tag{5.19}$$

$$L_{sm}^{\psi\psi} = \begin{cases} \frac{|B_{sm,01}^{\psi\psi}| - \omega_{01} C_{sm}^{\psi\psi}}{\omega_{01}^2 C_{sm}^{\psi\psi} |B_{sm,01}^{\psi\psi}|}, & if \quad \begin{array}{r} B_{sm,01}^{\psi\psi} > 0 \\ B_{sm,02}^{\psi\psi} < 0 \\ C_{sm}^{\psi\psi} < |B_{sm,01}^{\psi\psi}|/\omega_{01} \end{array} \\ \frac{|B_{sm,01}^{\psi\psi}| - \omega_{01} C_{sm}^{\psi\psi}}{\omega_{01}^2 C_{sm}^{\psi\psi} |B_{sm,01}^{\psi\psi}|}, & if \quad \begin{array}{r} 0 < B_{sm,01}^{\psi\psi} < B_{sm,02}^{\psi\psi} \\ C_{sm}^{\psi\psi} < |B_{sm,01}^{\psi\psi}|/\omega_{01} \end{array} \\ \frac{|B_{sm,01}^{\psi\psi}| + \omega_{01} C_{sm}^{\psi\psi}}{\omega_{01}^2 C_{sm}^{\psi\psi} |B_{sm,01}^{\psi\psi}|}, & if \quad B_{sm,01}^{\psi\psi} < B_{sm,02}^{\psi\psi} < 0 \end{cases} \tag{5.20}$$

where

$$m = \begin{cases} 2, & if \quad \psi = x \\ \{1, 2\}, & if \quad \psi = y \end{cases} \tag{5.21}$$

and $\Delta f = f_{01}/f_{02}$, $\Delta B_{sm}^{\psi\psi} = B_{sm,01}^{\psi\psi}/B_{sm,02}^{\psi\psi}$ where $B_{sm,01}^{\psi\psi} = B_{sm}^{\psi\psi}(\phi_{01}^{\psi\psi}, f_{01})$ and

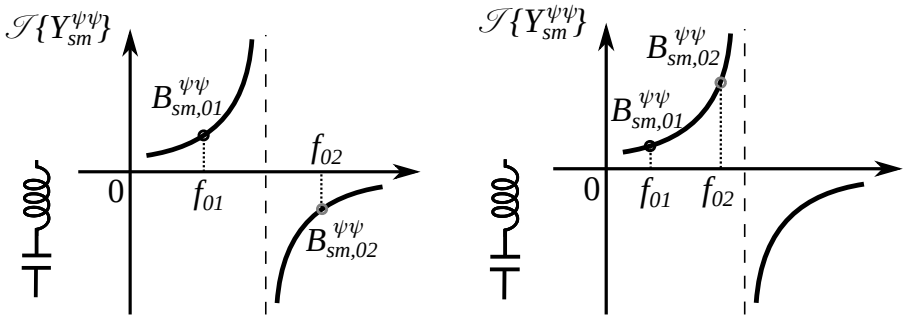

(a) $B_{sm,01}^{\psi\psi} > 0$ and $B_{sm,02}^{\psi\psi} < 0$.

(b) $0 < B_{sm,01}^{\psi\psi} < B_{sm,02}^{\psi\psi}$.

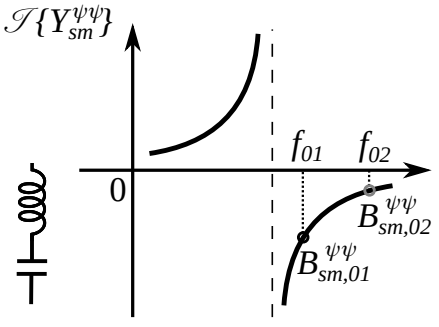

(c) $B_{sm,01}^{\psi\psi} < B_{sm,02}^{\psi\psi} < 0$.

FIGURE 5.4: Frequency response of $Y_{sm}^{\psi\psi}$. According to the sign of $B_{sm,01}^{\psi\psi}$ and $B_{sm,02}^{\psi\psi}$, the frequency response of $Y_{sm}^{\psi\psi}$ is assumed to be that of a LC-series, refer to (5.16), (5.17) and (5.18). (a) $B_{sm,01}^{\psi\psi} > 0$ and $B_{sm,02}^{\psi\psi} < 0$. (b) $0 < B_{sm,01}^{\psi\psi} < B_{sm,02}^{\psi\psi}$. (c) $B_{sm,01}^{\psi\psi} < B_{sm,02}^{\psi\psi} < 0$.

$B^{\psi\psi}_{sm,02} = B^{\psi\psi}_{sm}(\phi^{\psi\psi}_{02}, f_{02})$. As difference with respect to Y^{xx}_{s1}, the rest admittance sheets are subject to three cases-of-study, according to the sign of $B^{\psi\psi}_{sm,01}$ and $B^{\psi\psi}_{sm,02}$. Fig. 5.4 shows a graphical representation of these scenarios.

As mentioned earlier, ϕ^{xx}_{01} is the only parameter fully controlled by the designer. This is a direct consequence of having modeled Y^{xx}_{s1} as a single reactive lumped circuit element (inductor or capacitor). Other circuit typologies (e.g., LC-series) could be selected for Y^{xx}_{s1}. The latter would provide two design parameters, namely ϕ^{xx}_{01} and ϕ^{xx}_{02}. The desired dual-band frequency response of ECMs can be then obtained by employing a more complex approach (e.g., optimization) to search for the best values of ϕ^{xx}_{01} and ϕ^{xx}_{02}. Besides, inductors and capacitors are easier to design than resonators using patterned metallic claddings, i.e., metasurfaces.

5.1.2 Numerical results

The goal of this Section is to propose the design of a dual-band, orthogonally-polarized LP-to-CP converter at K/Ka-band for the next generation of SatCom applications. Such device is required to attain polarization diversity between the down-link (17.7-21.2 GHz) and the up-link (27.5-31 GHz) communication channels in the K/Ka-band. We enforce a LP-to-LHCP conversion in the lower frequency band, as well as a LP-to-RHCP conversion in the upper band. In the following, the bandwidth of the polarizer will be referred to as the frequency range over which the AR $<$ 3 dB and the transmission is higher than -1 dB.

The model proposed in Section 5.1 is used to retrieve all the design parameters, i.e., the entries of ECMs. Once the ECMs are fully characterized, each electric sheet is realized as a sub-wavelength textured metallic cladding: a metasurface [129, 130]. As shown in Fig. 5.2, this class of polarization converters consists of three electric sheets, interleaved by two dielectric slabs. Two Rogers RO3003$^{\text{TM}}$ panels ($\epsilon_r = 3.00$, $\tan\delta = 0.0010$ @ 10 GHz) of thickness $d = 1.524$ mm are used as dielectric substrates. They are bonded together using Taconic FastRise$^{\text{TM}}$ FR-27-0030-25 (F) ($\epsilon_r = 2.72$, $\tan\delta = 0.0014$ @ 10 GHz) of $\sim 80\mu m$ pressed thickness. The overall thickness of the polarizer is approximately 3.145 mm. The design frequencies are $f_{01} = 19.5$ GHz and $f_{02} = 29$ GHz. The design flow starts by sweeping the value of ϕ^{xx}_{01} over the range $[0°, 360°]$ and observing the impact of its values on AR and transmission bandwidths. By enforcing

LHCP in (5.14) and RHCP in (5.15), contour plots of the AR and the transmission are shown in Fig. 5.5. Values of ϕ_{01}^{xx} within the range $[75°, 90.5°]$ lead

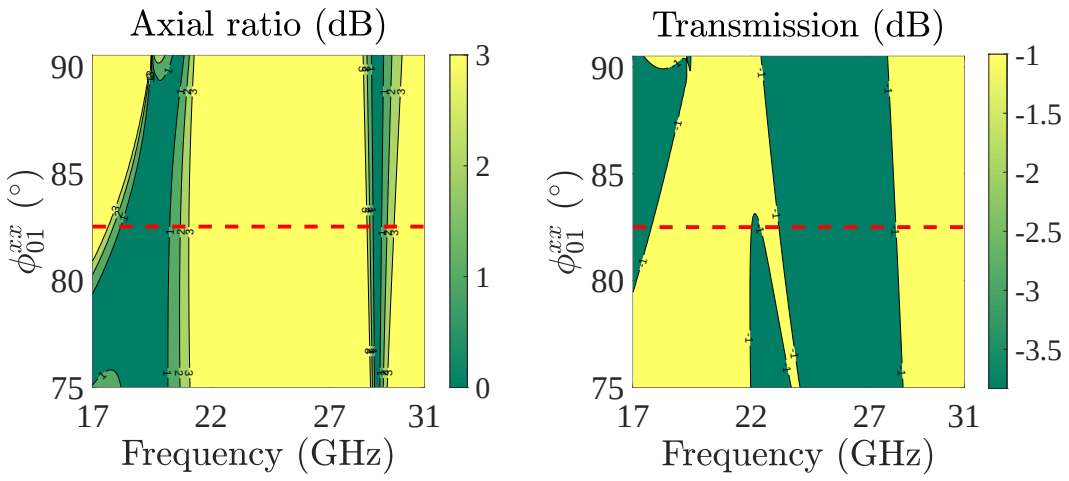

(a) (b)

FIGURE 5.5: Contour plots of the absolute value of (a) axial ratio and (b) transmission coefficient as a function of frequency and ϕ_{01}^{xx}. The dashed red line indicates the chosen operating point for the design.

to dual-band LP-to-CP conversions with orthogonal CP functionality. Unlike in [129], a 360°-phase coverage is not achieved while designing multi-band polarization converters. Furthermore, different bandwidths result from distinct

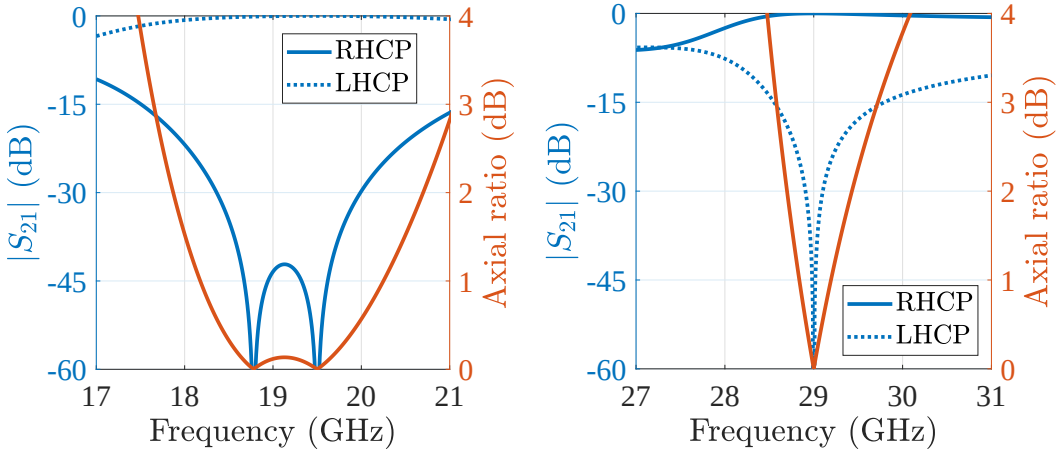

(a) Down-link of K/Ka-band. (b) Up-link of K/Ka-band.

FIGURE 5.6: Numerical results for the dual-band, orthogonally-polarized LP-to-CP converter with $\phi_{01}^{xx} = 82.5°$. Axial ratio and transmission coefficients for both RHCP and LHCP are plotted in two bands: (a) 17-21 GHz and (b) 27-31 GHz.

values of ϕ_{01}^{xx}. Considering the trade-off, a phase delay of $\phi_{01}^{xx} = 82.5°$ is chosen. The choice of this operating point is not casual. It represents the average value of the range $[75°, 90.5°]$, as graphically depicted by a dashed red line in Fig. 5.5. This choice pertains operating with large bandwidths and ensuring robustness of the system to tolerances.

The corresponding AR and transmission coefficients are plotted in Fig. 5.6. Specifically, the polarizer conveys LHCP and RHCP fields in the frequency bands 17.6-21 GHz and 28.5-29.7 GHz, respectively. The model of Section 5.1 has been used to predict the frequency behavior of each sheet admittance. All sheet admittances can thus be studied by means of ECMs, as depicted in Fig. 5.7 for x- and y-polarized waves. Y_{s1}^{xx} is modeled as a shunt inductor, whereas

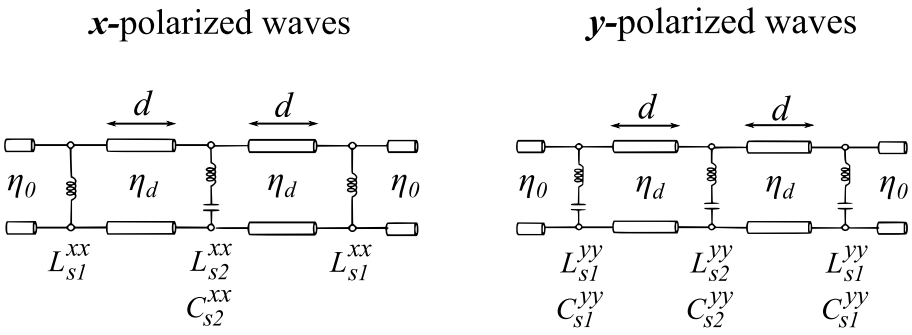

FIGURE 5.7: Equivalent circuit models of the structure. Networks for x- and y-polarized waves are analyzed separately.

LC-series resonators model the remaining sheet admittances. For the sake of completeness, the values of the lumped circuit elements are listed in Table 5.1.

TABLE 5.1: CIRCUIT ELEMENTS OBTAINED BY USING THE ANALYTIC METHOD PROPOSED IN CHAPTER 5.1

	Outer sheets $(n = 1)$	**Inner sheet** $(n = 2)$	
C_{sn}^{xx}	n.a.	20.5	(fF)
C_{sn}^{yy}	6.97	12.3	
L_{sn}^{xx}	14.5	4.80	(nH)
L_{sn}^{yy}	5.98	3.10	

5.1.3 Physical design and full-wave results

Periodic sub-wavelength patterned metallic cladding are used to physically design each admittance sheet [106]. The unit cell's shape and geometrical sizes have been carried out by means of full-wave simulations in ANSYS HFSS 2018.2 [81]. The simulation setup can be found in [130]. The first two fundamental Floquet modes excite the unit cell, whose sides are surrounded by periodic boundary conditions. The frequency responses are then extracted from the reflection coefficient [130] for both x- and y-polarized fields and matched to those of the ECMs in Fig. 5.7. The choice of the unit cell's geometry is inspired by standard Jerusalem cross shapes, whose simplified ECM consists of LC-series resonators [131, 132]. The designed unit cells are shown in Figs. 5.8(a) and 5.8(b). The dimensions of the metasurface's unit cell are $0.28\lambda_{min} \times 0.28\lambda_{min}$, where λ_{min} is the free-space wavelength at 31 GHz. Gap capacitors are designed in combination with meandered lines, to attain the circuit elements in Table 5.1. Their susceptances are plotted in Figs. 5.8(c) to 5.8(f) for normal incidence in the frequency band 17-31 GHz. The desired susceptance values [refer to (5.9) and (5.10)] are also plotted using black and grey dot markers at the frequencies f_{01} and f_{02}, respectively. Very good agreement between ECMs and full-wave simulations is observed. No optimization process has been performed in the design. Note that in Fig. 5.8(c) the large inductance L_{s1}^{xx} is realized as a very small capacitor. In terms of physical design, there is no metal pattern along x-axis for the outer sheets [refer to Fig. 5.8(a)]. This is only possible when the sheet admittance approaches the open condition, as follows

$$Y_{s1}^{xx} \xrightarrow{C_{s1}^{xx}\to 0 \;\; or \;\; L_{s1}^{xx}\to +\infty} 0 \tag{5.22}$$

Full-wave simulation have been carried out to observe the performance of the polarizer's unit cell. The simulation setup is illustrated in Fig. 5.9(a). The stack-up of the polarizer is simulated as a structure that is transversely periodic. The illumination consists of a LP plane-wave with the E-field polarized in the direction $\hat{\alpha} = (\hat{x} \pm \hat{y})/\sqrt{2}$. The simulated results pertain to a normal incidence. The LP-to-CP converter performs a LP-to-LHCP conversion in the lower band and LP-to-RHCP in the upper band, as shown in Fig. 5.9(b). The

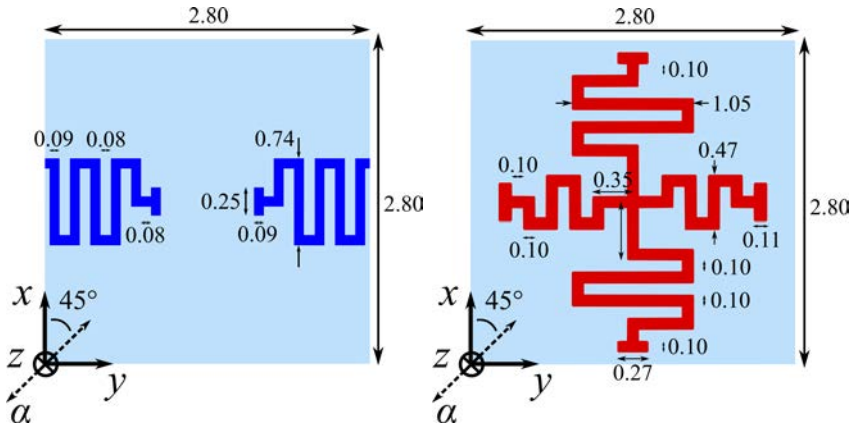

(a) Outer sheets' unit cell. (b) Inner sheet's unit cell.

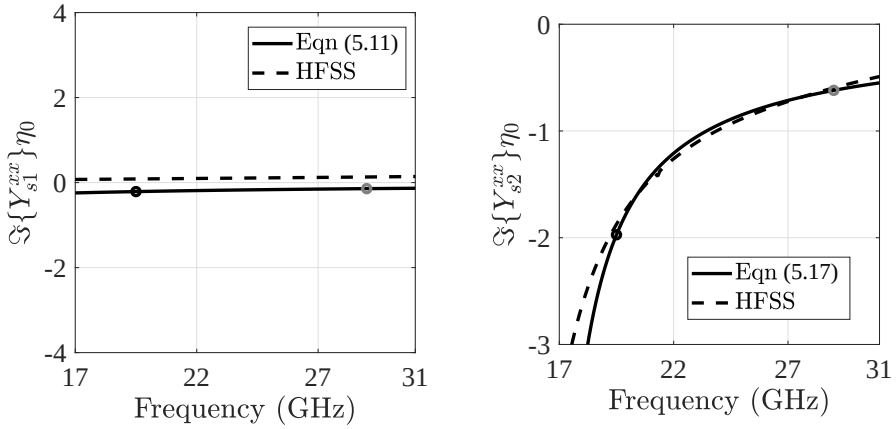

(c) Outer sheets: x-pol fields. (d) Inner sheet: x-pol fields.

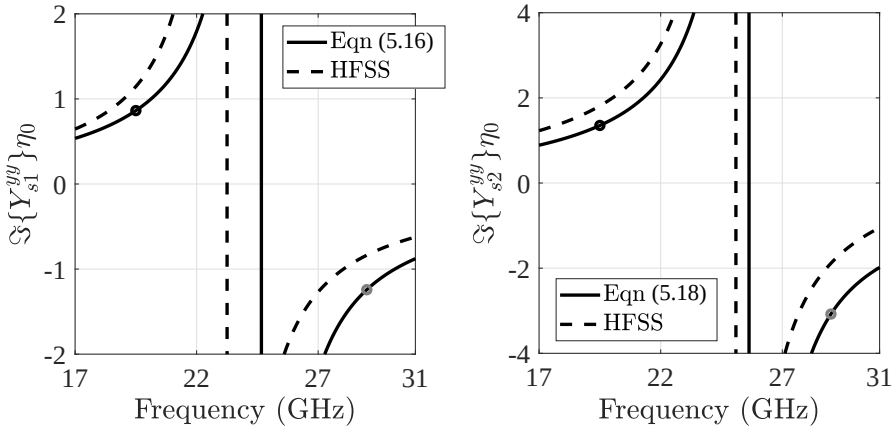

(e) Outer sheets: y-pol fields. (f) Inner sheet: y-pol fields.

FIGURE 5.8: Patterned metallic geometries of the metasurfaces' unit cell: (a) outer and (b) inner sheets. All dimensions are given in millimeters. The simulated susceptances for the patterned metallic geometries are shown in (c)-(e) for x- and (d)-(f) for y-polarized fields. The black and grey dot markers indicate the desired design values at the frequency f_{01} and f_{02}, respectively.

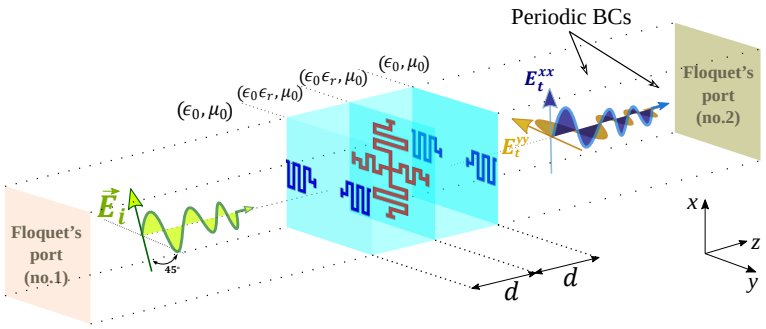

(a) Simulation setup.

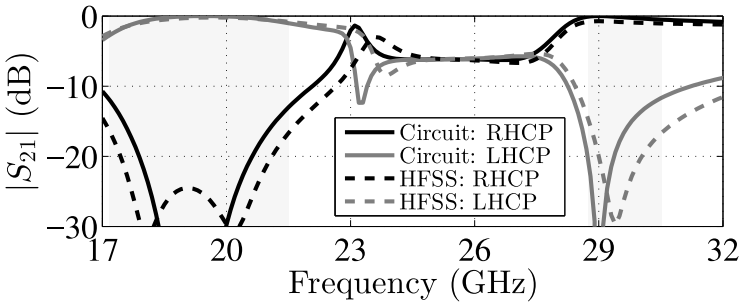

(b) Transmitted coefficients.

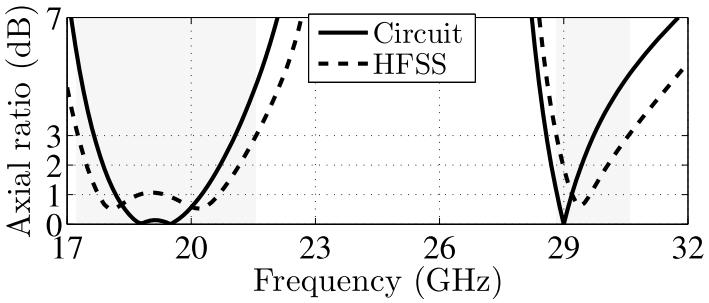

(c) Axial ratio.

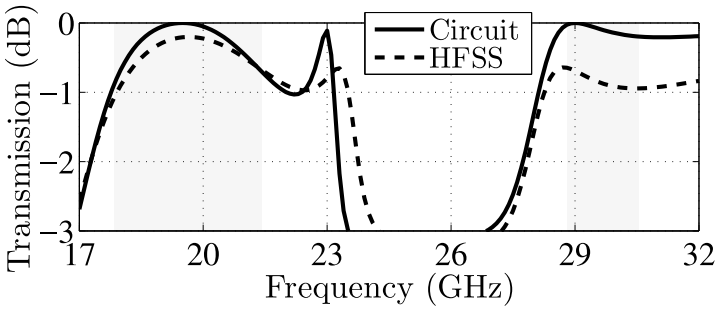

(d) Total transmission.

FIGURE 5.9: (a) Simulation setup of the polarizer's unit cell. A comparison between the circuit network and full-wave simulations [81] is reported. (b) Transmitted LHCP and RHCP. (c) Axial ratio. (d) Total transmission. The full-wave simulations considers a normal incidence onto the polarizer. Besides, the incident E-field is linearly-polarized in the direction $\hat{\alpha} = (\hat{x} \pm \hat{y})/\sqrt{2}$.

CP purity is estimated in terms of AR, whose plot is shown in Fig. 5.9(d). The designed polarizer exhibits larger 3-dB-AR bandwidths than its ECM. The total transmission is 0.7 dB lower than the ECM results in the upper band [refer to Fig. 5.9(d)]. This is likely due to a difference between ECMs and physical design. In fact, the outer metasurface's unit cell present a capacitive response for x-polarized waves with respect to the inductive one given by ECMs. As detailed earlier, no metal pattern has been introduced for Y_{s1}^{xx} along x-axis (i.e., capacitive behavior), as shown in Fig. 5.8(c), thus resulting in a different frequency response of the overall structure. Nonetheless, given Y_{s1}^{xx} approaches the open condition, this effect is negligible and acceptable for the requirements we aim to reach out, i.e., total transmission above -1 dB everywhere in the bands of interest.

5.2 Prototype and experimental results

The design introduced in Section 5.1.3 has been validated with a prototype. Several modules were fabricated using standard printed circuit board (PCB) technology. A schematic representation of the polarizer cross-section is depicted in Fig. 5.10(a). The patterned metallic surfaces are etched on the faces of the substrates, with a 45°-rotated orientation with respect to the circuit board edges. A photograph of the fabricated board is shown in Fig. 5.10(b). The transverse size of the board is $\sim 7\lambda_{max}$, where λ_{max} is the free-space wavelength at 17 GHz, whereas the overall dimension of the board is $123.74 \times 123.74 \times 3.14$ mm^3. As shown in Fig. 5.10(b), the inner textured metal cladding is not visible.

The dual-band, orthogonally-polarized LP-to-CP converter was experimentally characterized using a quasi-optical measurement system (Thomas Keating Ltd) [133]. A schematic illustration of the experimental setup is shown in Fig. 5.11. The fabricated boards are illuminated by a collimated Gaussian beam, under normal and oblique incidence. Specifically, two corrugated circular-horn antennas are employed for illumination and reception. The first horn [refer to TX in Fig. 5.11] feeds a pair of reflectors, whose purpose is to focus the incident Gaussian beam on the device under test (DUT). A second pair of reflectors focuses the field, conveyed by the sample, to a receiving corrugated circular-horn antenna [refer to RX in Fig. 5.11]. The horns are connected to a PNA network

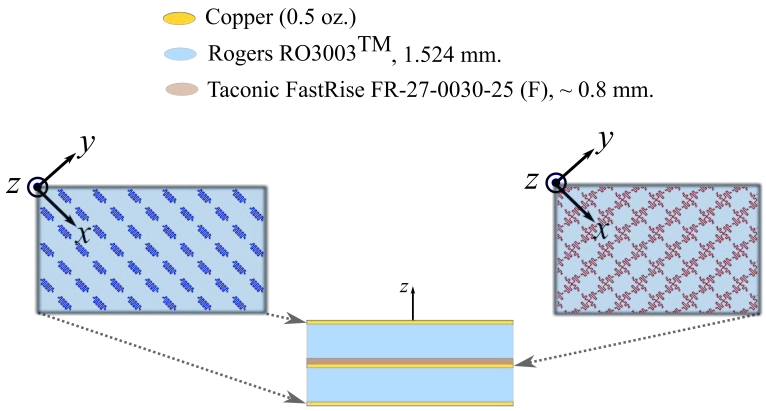

(a) Cross section of the polarizer.

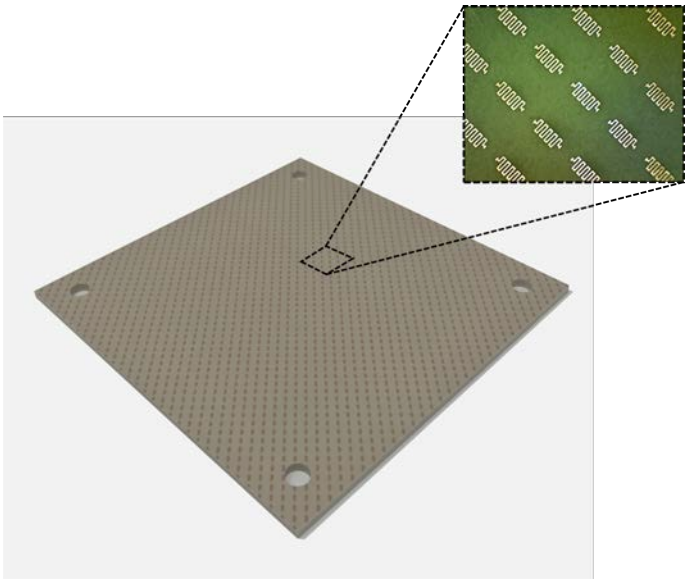

(b) Fabricated prototype.

FIGURE 5.10: (a) PCB stack-up of the polarizer. (b) Fabricated prototype. The overall size of the board is $123.74 \times 123.74 \times 3.14$ mm^3. The outer metal pattern is highlighted by a zoomed-in photograph's detail.

analyzer (Keysight N5227A) with coaxial cables. The experiments in the band 17-31 GHz were carried out considering two separate measurement setups to cover the two bands 18-26 GHz and 26-40 GHz, respectively.

A free-space thru, reflect, line (TRL) calibration procedure is performed to calibrate the input ports located at the interfaces of the coaxial cables. The effects of waveguide transitions and horn-antennas are not calibrated out, but a time-gating procedure is applied to isolate the DUT. The transmission coefficients are measured by rotating the receiving horn in the direction of the x-

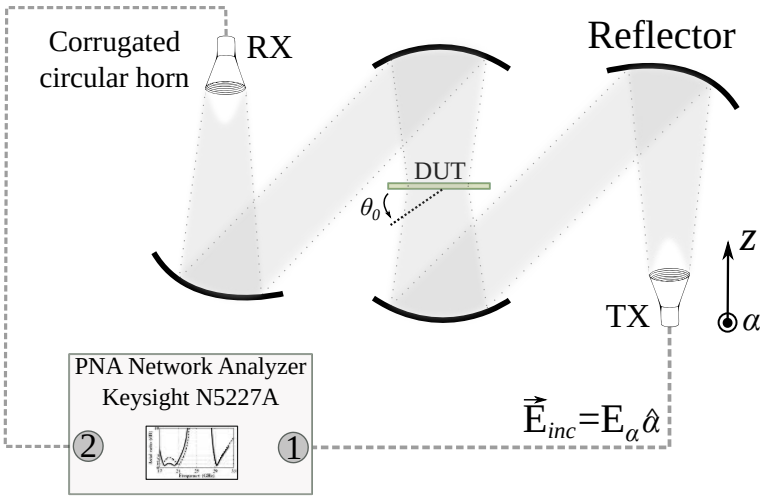

FIGURE 5.11: Schematic drawing of the experimental setup used to measure the polarizer: quasi-optical test-bench [133].

and y-axis [see Fig. 5.10(a)]. The DUT is characterized in terms of its scattering matrix. Finally, the AR and the transmitted power are calculated by post-processing the measured data.

5.2.1 Measured results for normal incidence

The measured results are plotted in Fig. 5.12, when the DUT is illuminated under normal incidence. As shown in Fig. 5.12(a), the dual-band and the orthogonally-polarized transmission of the polarizer have been demonstrated. A 45°-slanted LP plane-wave is transformed into LHCP and RHCP plane-waves in two separate bands. The CP's purity is characterized in terms of AR, whose plot is shown in Fig. 5.12(b). Also, the total efficiency of the polarizer is plotted in Fig. 5.12(c). Several experiments were performed on four fabricated boards. The measured results were in excellent agreement with full-wave simulations, thus demonstrating the reliability of fabrication and measurement processes. A slight frequency shift exists between the measured and simulated results at lower frequencies. This is likely due to a phase variation, resulting from fabrication tolerances. In Fig. 5.12(c), it is evident that the measured transmitted power matches very well in amplitude with simulations. This points to the fact that there is a phase mismatch at lower frequencies between measurement and simulation. Fig. 5.13(a) compares the phase difference $\Delta\phi = \phi^{yy} - \phi^{xx}$ in measurement and simulation. A percentage variation of more than 10% occurs between the measured and simulated phase difference $\Delta\phi$ at lower frequencies,

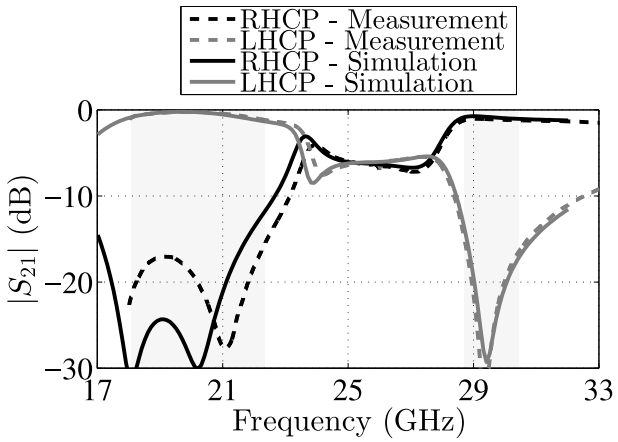

(a) Transmitted LHCP and RHCP.

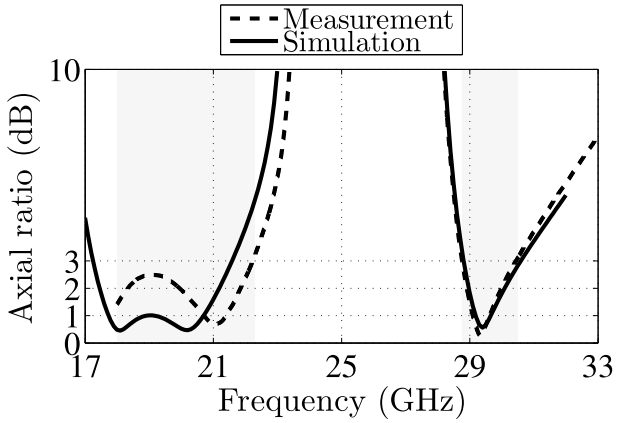

(b) Axial ratio.

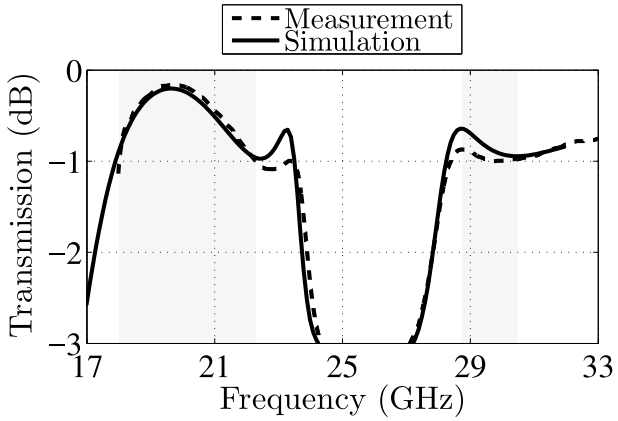

(c) Total transmission.

FIGURE 5.12: Comparison between measured and full-wave performance of the polarizer. (a) Transmitted LHCP and RHCP. (b) Axial ratio. (c) Total transmission of the polarization converter. The measurements refer to a normal illumination of the DUT.

whereas such a difference is lower than 5% in the upper band, as shown in Figs. 5.13(b) and (c). This difference is likely due to fabrication tolerances.

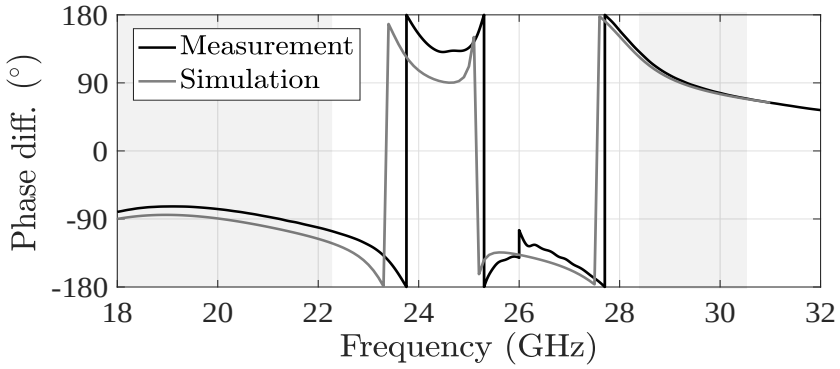

(a) Phase difference $\Delta\phi = \phi^{yy} - \phi^{xx}$.

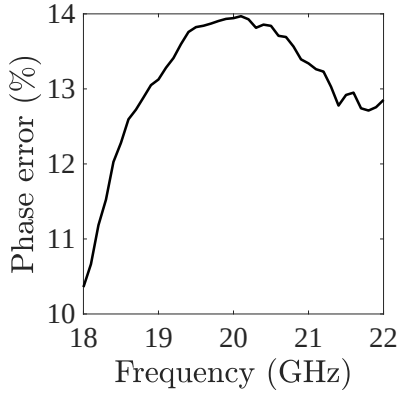

(b) Downlink of K/Ka-band.

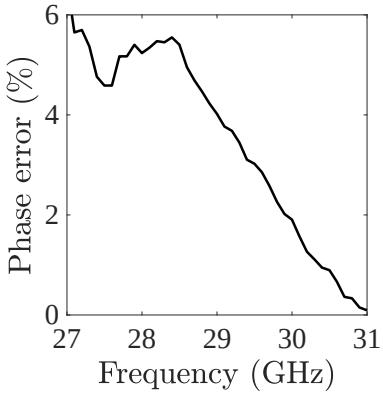

(c) Uplink of K/Ka-band.

FIGURE 5.13: (a) Phase difference $\Delta\phi = \phi^{yy} - \phi^{xx}$ comparison between measurements and simulations. Percentage error of measured data in the (a) downlink and (b) uplink of the K/Ka-band.

Indeed, tolerances in the substrate's thickness d impact the electrical paths of the propagating waves. Likewise, variations in the dielectric constant ϵ_r result in different refraction behaviors. In both cases, the phase delay ϕ may vary with respect to the design value. These effects can be observed using the ECMs introduced in Section 5.1. Figs. 5.14(a) and (b) show the AR variation when fabrication tolerances are considered for d and ϵ_r, respectively. The tolerances $\delta_{toll} = 0.0762$ mm and $\delta_{r,toll} = 0.04$ are provided by Rogers Corporation [134]. It is clear from Fig. 5.14 that tolerances in d and ϵ_r cause a frequency shift at lower frequencies. The AR response remains nearly unvaried in the upper band. Therefore, the AR response exhibits a more robust stability to tolerances at higher frequencies than at lower. This behavior at lower frequencies is attributed to the presence of two resonances near in frequency in the transmission coefficient response, as shown in Fig. 5.12(a). Small variations of the

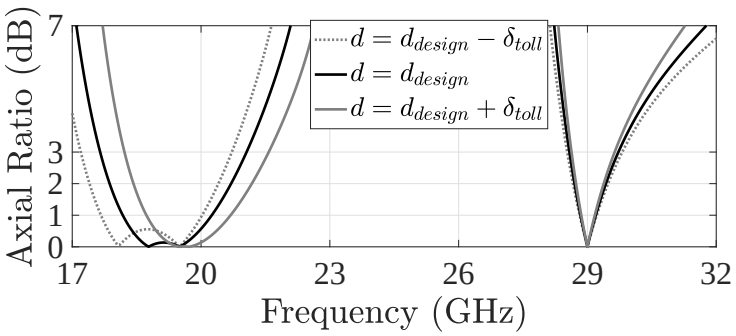

(a) Tolerances of the substrate's thickness.

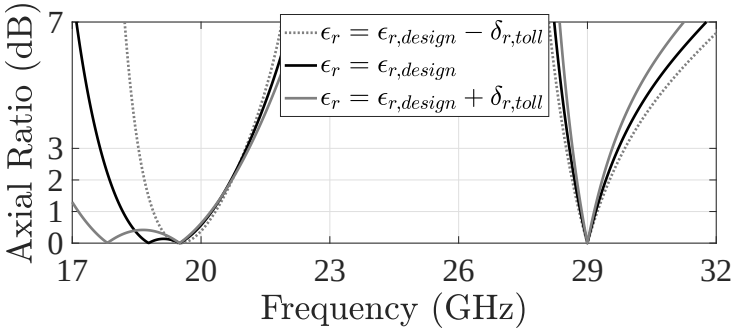

(b) Tolerances of the substrate's dielectric constant.

FIGURE 5.14: Tolerances effects of (a) d and (b) ϵ_r on AR using ECMs. The nominal values of d and ϵ_r are varied by fabrication tolerances provided by Rogers Corporation [134].

phase delay in the structure in Fig. 5.2 have a stronger impact on shifting the two resonances. Along the design procedure the only selected resonance (by enforcing maximum transmission) results indeed at the frequency $f_{01} = 29$ GHz. The other resonance emerges from an inherent response of the ECM, thus it is not controllable by the designer. The result ends up not having a solid stability at that frequency. On the other hand, only one resonance appears in the upper band, as shown in Fig. 5.12(a). A more robust frequency behavior is then expected in this case. This effect is confirmed by the measurements shown in Fig. 5.12(b).

To conclude, the performance of the converter is summarized in Table 5.2. The polarizer performs a LP-to-LHCP conversion over a 21% fractional bandwidth. Furthermore, a LP-to-RHCP conversion is performed over a 6% fractional bandwidth. These bandwidths are calculated considering a transmission higher than -1 dB.

TABLE 5.2: MEASURED FRACTIONAL BANDWIDTHS OF THE PROPOSED DUAL-BAND, ORTHOGONALLY-POLARIZED LP-TO-CP CONVERTER UNDER NORMAL PLANE-WAVE INCIDENCE

	LHCP	**RHCP**	
Axial ratio (< 3 dB)	[17, 22.2]	[28.7, 30.4]	(GHz)
Transmission (> -1 dB)	[18, 22.3]	[28.4, 31]	
Total relative bandwidth	~ 21	~ 6	(%)

* Total bandwidth: AR < 3 dB and transmission above -1 dB.

5.2.2 Measured results for oblique incidence

The fabricated boards were also tested under oblique incidence. The DUT is mechanically-rotated on the quasi-optical test-bench. The impinging waves illuminate the DUT at different angles θ_0, as shown in Fig. 5.11. Specifically, two types of illuminations were considered. In the first scenario, the impinging plane-wave presents the E-field polarized along the $\hat{\alpha}$ direction (TE illumination). Secondly, a plane-wave with the H-field along the $\hat{\alpha}$ direction (TM illumination) is considered. A graphical illustration of these two types of illumination is depicted in Fig. 5.15.

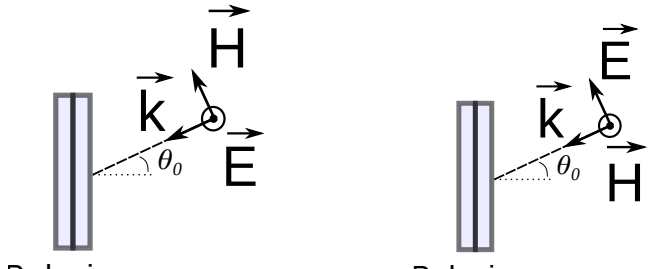

(a) TE illumination. (b) TM illumination.

FIGURE 5.15: Field orientation of the two scenarios considered in the measurements: (a) TE and (b) TM illumination.

The measured results are shown in Figs. 5.16(a)-(b) for the TE illumination and in Figs. 5.16(c)-(d) for the TM. In general, the measured results slightly differ for TE and TM illuminations, respectively. In particular, the TM case is more sensitive to oblique incidences. This is likely due to the asymmetry of the polarizer's unit cell, as seen in Figs. 5.8(a) and (b). The 3-dB-AR bandwidth is very stable for angles of incidence up to $\pm 45°$, within the upper frequency

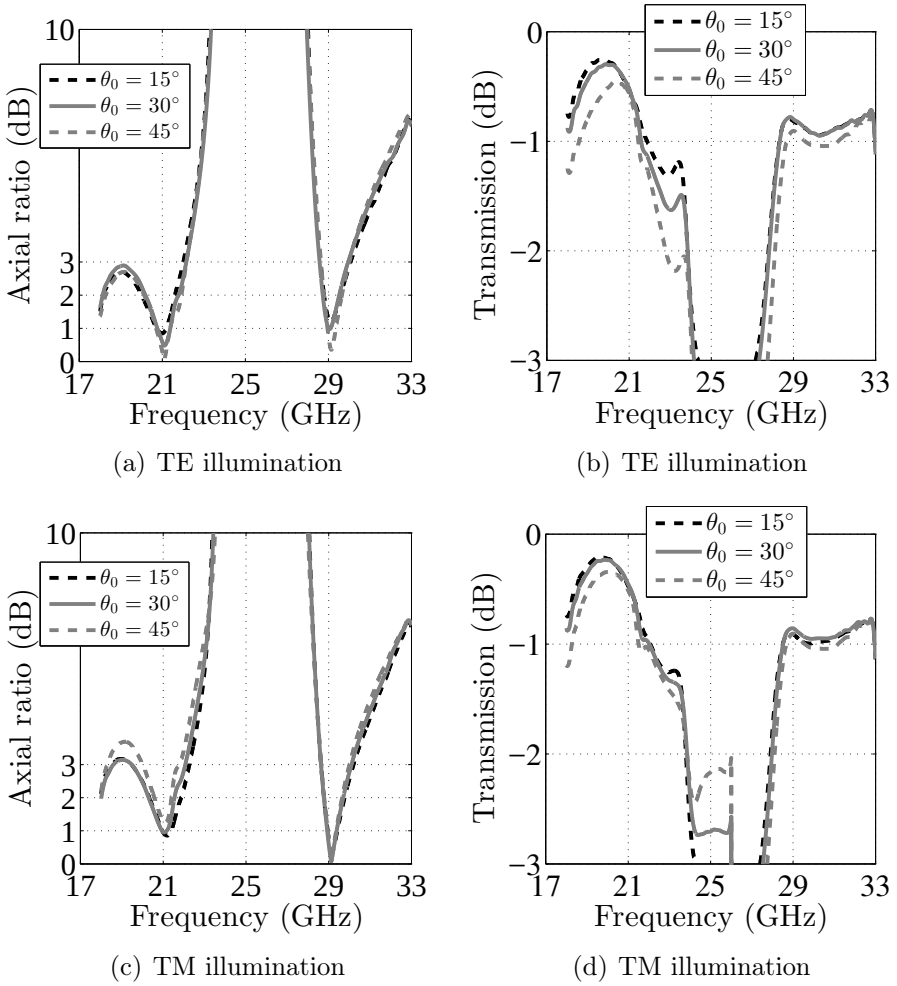

(a) TE illumination (b) TE illumination

(c) TM illumination (d) TM illumination

FIGURE 5.16: Measured performance of the polarization converter under different incident angles in the βz-plane where $\hat{\beta} = \hat{\alpha} \times \hat{z}$, see Fig. 5.11. (a)-(c) Axial ratio. (b)-(d) Total transmission. Both vertical (TE) and horizontal (TM) E-field illuminations are considered.

band. On the contrary, the lower bandwidth is slightly reduced, as shown in Fig. 5.16(c). The total efficiency of the polarization converter remains nearly unvaried for all incident angles, as plotted in Figs. 5.16(d). A detailed and complete summary of the polarizer's performance is reported in Table 5.3 for both TE and TM illuminations. The total bandwidth in Table 5.3 is calculated as the frequency range where AR < 3 dB and the total transmission is higher than -1 dB. The TM illumination results in narrower bandwidths at lower frequencies, whereas the opposite behavior is observed at higher frequencies. Moreover, the difference between TE and TM illuminations is mitigated at upper frequencies. The coupling effect between the polarizer sheets is, indeed, reduced at those frequencies and a quasi-plane-wave field propagation can be assumed through

the metasurfaces.

TABLE 5.3: MEASURED FRACTIONAL BANDWIDTHS OF THE PROPOSED DUAL-BAND, ORTHOGONALLY-POLARIZED LP-TO-CP CONVERTER UNDER OBLIQUE PLANE-WAVE INCIDENCE.

TE illumination	$\theta_0 = 15°$		$\theta_0 = 30°$		$\theta_0 = 45°$		
	LHCP	**RHCP**	**LHCP**	**RHCP**	**LHCP**	**RHCP**	
Axial ratio (< 3 dB)	[17, 22]	[28.6, 30]	[17, 22]	[28.6, 30]	[17, 22]	[28.6, 30]	(GHz)
Transmission (> -1 dB)	[18, 21.9]	[28.3, 31]	[18, 21.6]	[28.3, 31]	[18.6, 21.4]	[28.6, 31]	
Total relative bandwidth	19.5	4.8	18.2	4.8	14.0	4.8	(%)

* The total bandwidth refers to the frequency range for which AR < 3 dB and the total transmission is better than -1 dB.

TM illumination	$\theta_0 = 15°$		$\theta_0 = 30°$		$\theta_0 = 45°$		
	LHCP	**RHCP**	**LHCP**	**RHCP**	**LHCP**	**RHCP**	
Axial ratio (< 3 dB)	[19.4, 22.3]	[28.6, 30.2]	[19.4, 22]	[28.6, 30.1]	[20, 21.8]	[28.6, 30.1]	(GHz)
Transmission (> -1 dB)	[18, 22]	[28.5, 31]	[18, 22.04]	[28.5, 31]	[18.3, 21.5]	[28.7, 31]	
Total relative bandwidth	12.5	5.4	12.5	5.1	7.2	4.7	(%)

* The total bandwidth refers to the frequency range for which AR < 3 dB and the total transmission is better than -1 dB.

5.3 State-of-the-art comparison

The aim of this Section is to introduce a comparison with the state-of-the-art dual-band, orthogonally-polarized LP-to-CP converters for SatCom applications. Table 5.4 lists some prior articles that have proposed a solution to this problem. Our converter represents a good trade-off between performance

TABLE 5.4: COMPARISON WITH STATE-OF-THE-ART DUAL-BAND, ORTHOGONALLY-POLARIZED LP-TO-CP CONVERTERS.

Ref.	**Total bandwidths** (%)	**Thickness** (λ)	**Unit cell size** (λ)	**Analytic design**	**Angular stability** (°)
[119], [122]	2.5 and 1.7	0.08	0.37	Quasi	±30 ***
[120]	14.1 and 8.1	0.13	0.33	No	±20
[135]	n.a.	0.06	0.41	No	n.a.
[125]	8 and 2.3	1.05	n.a.	No	n.a.
[136]	3.5 and 2.6	1.3 ****	0.57 ****	No	±5 ***
This work	21.3 and 6	0.26	0.23	Yes	±45

* The total bandwidths refer to the frequency ranges for which AR < 3 dB and the total transmission is better than -1 dB.
** λ is the free-space wavelength at 25 GHz.
*** This result refers to full-wave simulations only.
**** This result is reported in terms of the free-space wavelength at 15.2 GHz.

and size. Polarization conversion is efficiently performed over larger frequency bands with respect to the state-of-the-art. The bandwidths in Table 5.4 refer to frequency bands for which AR < 3 dB and transmission is above -1 dB.

As detailed in Section 5.2.2, the angular stability is also highly improved. Angular stability is dependent on the choice of the geometrical shapes for the metasurfaces' unit cells. In fact, the geometries in Fig. 5.8(a)-(b) mitigate the mutual coupling between the transmitted orthogonal transverse components. Jerusalem's cross-like FSSs are indeed well-known for ensuring low sensitivity to oblique incidences [137, 138].

5.4 Advantages and limitations of the model

In this Section, we present a brief discussion about advantages and limitations of the model outlined in Section 5.1. The underlying idea of the model is to provide closed formulae to give insights for the design and avoid more complex approaches, such as optimizations. As mentioned above, the only parameter the designer can fully manipulate is ϕ_{01}^{xx}. It follows that sweeping the value of ϕ_{01}^{xx} is sufficient to enable one having an overall view of the maximum achievable performance of the polarizer. Basically, this is the approach used to carry out the design presented in Section 5.1.3. However, the values of further parameters, e.g., d and ϵ_r, are assumed and do not represent a degree of freedom in the systematic procedure. In other words, the simplicity of the model of Section 5.1 may exclude potential solutions given by enhancing the number of degree of freedoms in the design method. In the following, we will thus present a discussion about the impact of the parameters d and ϵ_r on the polarizer performance.

In Figs. 5.17 and 5.18, the impact of a 20% variation in d and ϵ_r with respect to their design values ($d_{nom} = 1.524$ mm and $\epsilon_{r,nom} = 3.00$) is plotted in terms of AR, respectively. These parameters clearly represent key assets in engineering the 3-dB-AR bandwidths. For instance, Fig. 5.17(a) shows that larger bandwidths are achieved at higher frequencies when $d = 1.2d_{nom}$. This operating point resembles performance achieved in previous contributions [119, 120]. Likewise, broader 3-dB-AR bandwidths are obtained at lower frequencies, when $\epsilon_r = 0.8\epsilon_{r,nom}$ or $\epsilon_r = 1.2\epsilon_{r,nom}$ [see Fig. 5.18(a)].

Using d and ϵ_r as design parameters may impact the overall design of the structure. One issue is the physical implementation of the ECM's elements. The range of values of the ECM's entries is dependent on the geometry of the metasurfaces' unit cells. Assuming a given unit cell geometry, only a limited

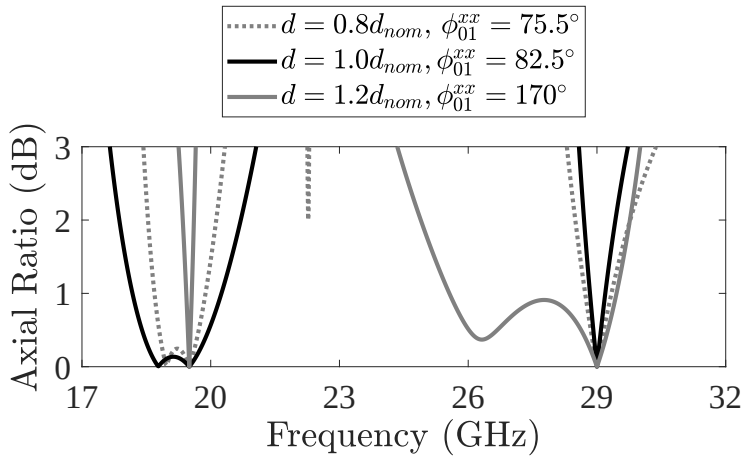

(a) AR for different d.

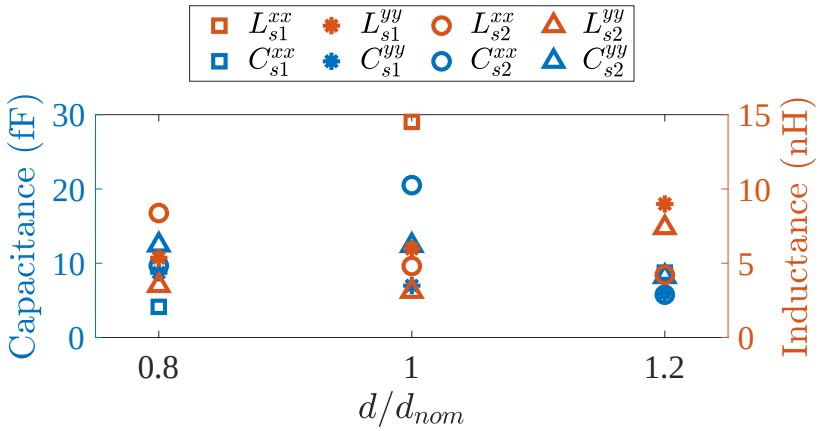

(b) ECMs elements.

FIGURE 5.17: (a) AR versus frequency for different substrate's thicknesses d. (b) Related circuit parameters.

range of circuit element values can be realized. To give an example, the geometries shown in Figs. 5.8(a) and (b) can realize capacitances and inductances in the range of [6.5, 25] (fF) and [2.5,15] (nH), respectively. As shown in Figs. 5.17(b) and 5.18(b), the design complexity fairly increases for $d = 0.8d_{nom}$ and $\epsilon_r = 0.8\epsilon_{r,nom}$, since the capacitance C_{s1}^{xx} reaches very low values. In this scenario, the geometries in Figs. 5.8(a) and (b) cannot be employed in the physical design. Different geometries can obviously help in overcoming this issue. Nonetheless, the set of usable geometries is limited, given the electrically-small unit cell's size at K/Ka-band. Finally, fabrication constraints represent a further limitation in the implementation of the circuit elements.

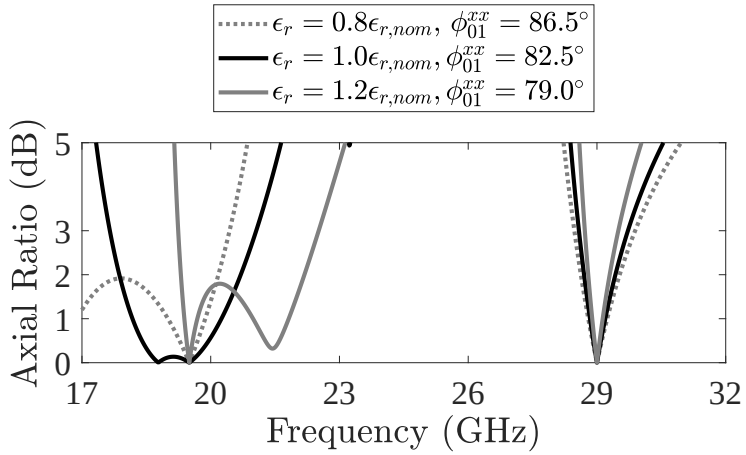

(a) AR for different ϵ_r.

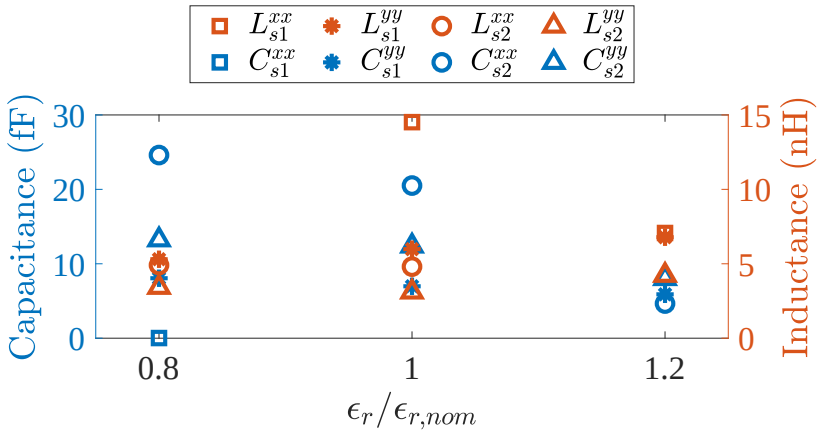

(b) ECMs elements.

FIGURE 5.18: (a) AR versus frequency for different substrate's dielectric constants ϵ_r. (b) Related circuit parameters.

5.5 Conclusions

In this Chapter, a novel methodology has been presented for the design of dual-band LP-to-CP polarizers attaining polarization versatility between two non-adjacent frequency bands. In the framework of modern SatCom applications, the demand of ground antennas achieving orthogonal CPs in the down- and up-link channels of K/Ka-band has shifted the attention to developing polarizing screens that fulfill such requirements. To this aim, this work has proposed a systematic design procedure based on ECMs. Closed-form analytic expressions are provided to fully characterize the ECMs, avoiding the use of optimizations to search for their entries. This approach leads in having one only input parameter. An overall view of the maximum achievable performance can be thus extracted

by sweeping it over a given range of values and observing its impact on AR bandwidth and total transmission. The design of a dual-band polarizer has been addressed and validated by means of experimental results conducted on a physical prototype. Under normal incidence, the polarizer performs LP-to-LHCP conversion over about 21% (18-22.2 GHz). A LP-to-RHCP performance is observed in the band 28.7-30.4 GHz ($\sim$ 6 %). A transmission higher than -1 dB is measured in the same two bands. An excellent angular stability ($\pm 45°$) is also found, due to the geometry of the proposed metasurfaces' unit cells.

Such a device is intended to be employed in combination with a single LP antenna aperture that covers the K/Ka-band. Standard CTS arrays [6] surely represent a good candidate to this purpose, due to their wideband and wide-angle scanning performance deriving from the parallel-fed architecture and working principle. The polarizing screen is thus meant to be placed in proximity of the radiating long slots. The final antenna module can offer the best trade-off between antenna performance, size and design complexity. To this purpose, the polarizer must exhibit low insertion losses (total transmission above -1 dB) and robust behavior to incident angles. A low profile is needed as well. The proposed dual-band, orthogonally-polarized LP-to-CP converter complies with these specifications and may be considered for the next generation of K/Ka-band SatCom ground applications.

Chapter 6

Ultra-low-profile CTS array at K/Ka-band

The antenna integration with the transceivers represents an essential feature to modern SatCom requirements. Reduced weight and encumbrance have, indeed, become key assets to ease the integration into different vehicles, such as trains and aircrafts. This device generation requests to greater endeavors for ultimate antenna miniaturization. The downside is paid for the highly increased complexity of the antenna system. Indeed, the design of all-in-package antennas is not straightforward and arouses growing interest in the scientific community.

Owing to their attractive features for millimeter-wave applications, continuous transverse stub (CTS) arrays offer a valid solution to these requirements. A low-profile CTS array was realized using multi-layer modules in low-temperature co-fired ceramic (LTCC) technology at V-band for broadside [7] and electronically controlled multibeam [8] radiation. Although the works [7, 8] have experimentally demonstrated that an ultra-low-profile is achievable with parallel-fed CTS antennas, their operative bandwidth is not as broad as required to modern wireless communications (about 50% of relative bandwidth). In [10], the proposed long-slot array exhibits a very contained encumbrance and a low-factor at E-band, being fabricated in printed circuit board (PCB) technology. The prototype demonstrates that the PCB technology is a very reliable solution to compact the antenna size, but the module suffers from narrowband capabilities.

The reliability of PCB technology has been selected in the frame of a collaboration with Thales Communication and Security (TCS), within the working collaboration of the Agence Nationale de la Recherche (ANR) project RAFQO [64], to design a CTS array achieving broadband performance. The main goal

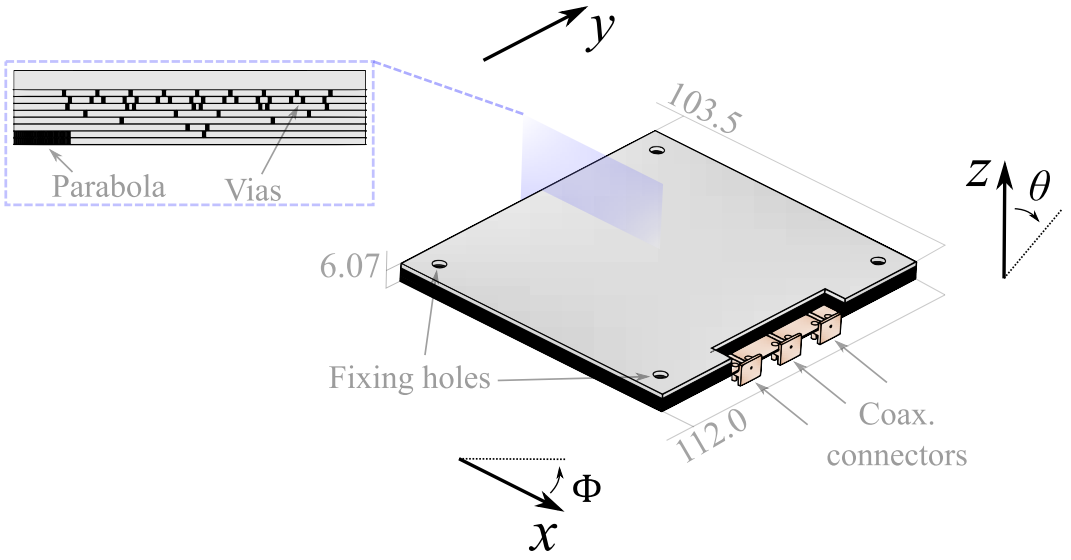

(a) Lateral view.

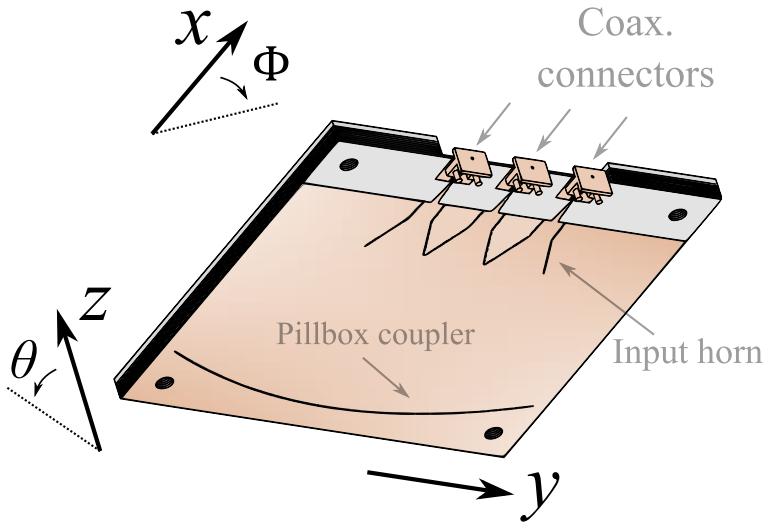

(b) Bottom view.

FIGURE 6.1: Perspective view of the antenna architecture from the (a) lateral and bottom (b) views. The orange and grey colors indicate the copper and the substrates, respectively. Dimensions are given in millimeters.

of the R&D activity is to develop a disruptive, modular, and ultra-low-profile antenna architecture for the next generation of high-data-rate SatCom systems for moving platforms. The system is required to operate in the K/Ka-band to benefit from the high-speed communications offered by the future satellite constellations. Two frequency bands are dedicated to the receive (19.2-21.2 GHz) and transmit (29-31 GHz) channels. The required field-of-view of the antenna is about $\pm 20°$. The antenna is demanded to work in circular polarization, to be realized by placing a wideband polarization converter in the proximity of the

radiating slots. A perspective view of the designed antenna module is graphically depicted in Fig. 6.1. In the following of this Chapter, the antenna design will be described. Afterward, the polarizer, introduced in Chapter 5, will be integrated into the antenna design, in order to achieve circular polarization (CP) for dual-band operation and polarization agility between the two non-adjacent bands.

6.1 Design procedure and antenna performance

In this Section, the design procedure of the CTS array in PCB technology is exhaustively discussed. Firstly, the waveguide technology will be studied. The radiating unit cell of the array will be then introduced and its performance investigated. Afterward, the feeding network design will be discussed. Finally, the overall antenna performance is predicted with full-wave simulations of the whole structure.

6.1.1 Quasi substrate integrated PPW

A parallel-fed CTS array can be designed in PCB technology by replacing the continuous metallic walls of the open-ended PPWs with vias-fences. A three-dimensional (3-D) view of this type of PPWs is shown in Fig. 6.2. The modes

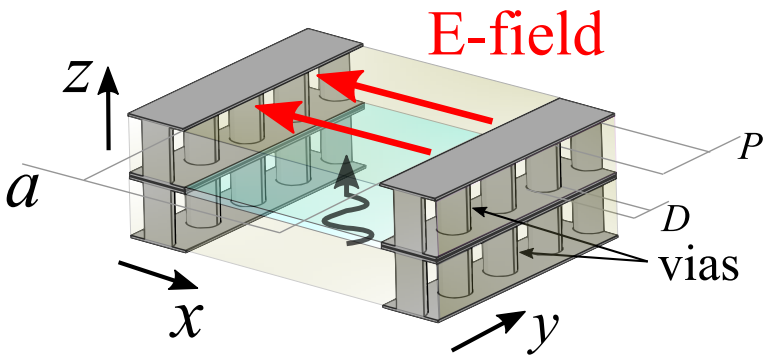

FIGURE 6.2: Perspective view of a quasi substrate integrated parallel-plate waveguide. Geometrical parameters: $D = 0.3$ mm and $P = 0.6$ mm.

propagate in the positive direction of the z-axis. The structure resembles the substrate integrated waveguide (SIW) technology with a different propagation direction of modes, i.e., along the z- instead of the y-axis [see Fig. 6.2]. For this reason, we will refer to this type of waveguide as quasi-SI PPW. The SIW

technology is well-established and exhaustively documented in literature. The main design guidelines are extracted from the articles [139–143] and can be summarized as follows

$$\begin{aligned} D &< \lambda_{g,max}/5 \\ P &\leq 2D \end{aligned} \tag{6.1}$$

where $\lambda_{g,max}$ is the largest operating wavelength in the substrate, and D and P are the vias' diameter and periodicity along y-axis [refer to Fig. 6.2], respectively. Considering the Rogers RT/duroid 5880® ($\epsilon_r = 2.2$ and $\tan\delta = 0.0009$ @ 10 GHz) [134], the quasi-SI PPW is designed having $D = 3$ mm and $P = 2D$. The laminated layers are glued one another with the adhesive film Rogers Cu-Clad 6250 ($\epsilon_r = 2.43$ and $\tan\delta = 0.0014$ @ 10 GHz) [144], whose pressed thickness is about $100\mu m$.

The dispersion diagram of the structure [see Fig. 6.2] is plotted in Fig. 6.3. The geometric parameters of the structure are listed in the caption of Fig. 6.3. By studying the dispersion diagram, it is possible to understand which modes are in propagation within the structure. As for standard PPW, the quasi-SI PPW supports a quasi transverse electromagnetic (TEM) mode. The dispersion curve of the quasi-TEM mode does not match perfectly with the non-dispersive line, i.e., $\beta = k_0\sqrt{\epsilon_r}$ where k_0 is the free-space wavenumber. As a consequence, the mode in propagation inside the quasi-SI PPW is not a pure TEM wave, as the E-field's lines are slightly perturbed near the walls made of via-fences. However, the structure exhibits a mono-modal propagation in the

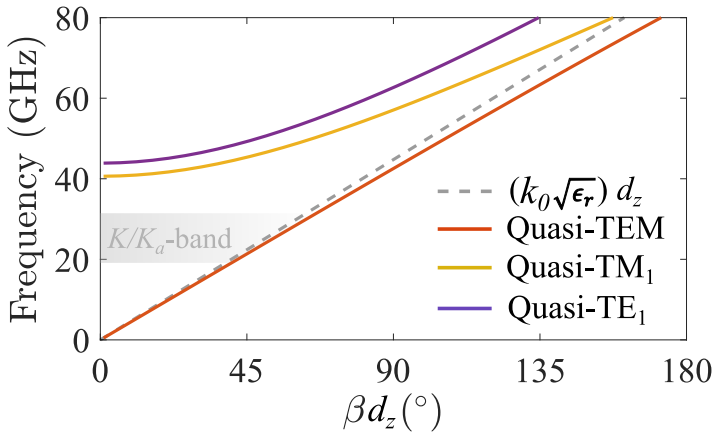

FIGURE 6.3: Dispersion diagram of the quasi-SI PPW shown in Fig. 6.2. The structure's geometrical parameters are: $D = 0.3$ mm, $P = 0.6$ mm, $a = 2.13$ mm, $\epsilon_r = 2.2$, and $d_z = 1.1$ mm.

band of interest [refer to the gray area in Fig. 6.3]. The supported mode can be seen as a standard TEM wave propagating inside a PPW filled with a dielectric of effective dielectric constant $\epsilon_{r,eff} = 2.5$ (instead of $\epsilon_r = 2.2$). As shown in Fig. 6.3, the first transverse electric (TE_1) and magnatic (TM_1) modes are also supported but they are in cut-off within the band of interest.

Fig. 6.4(a) shows a cross-sectional view of the quasi-SI PPW and the simulated insertion losses (IL) are reported in Fig. 6.4(b). As it is shown in

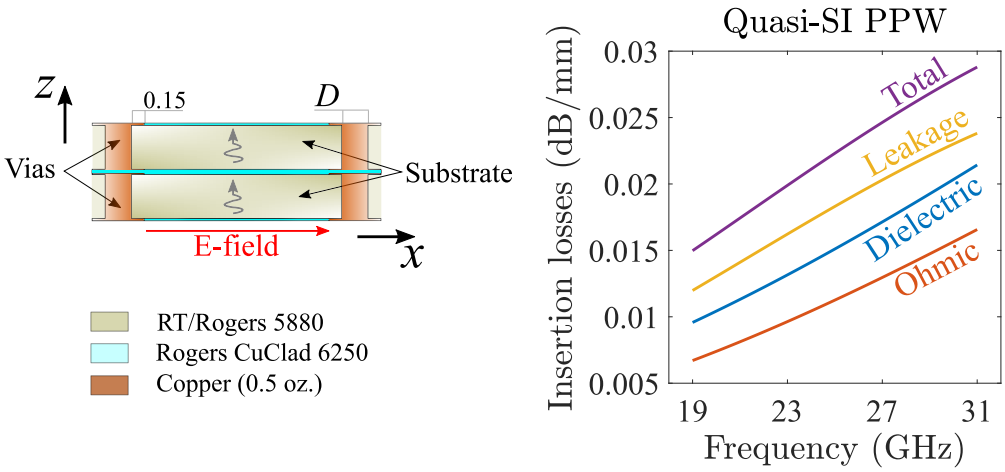

(a) Cross-section. (b) Insertion losses.

FIGURE 6.4: (a) Cross-section of the quasi-SI PPW in the xz-plane cut. (b) Simulated insertion losses of the quasi-SI PPW. The vias' diameter is $D = 3$ mm. All other dimensions are given in millimeters.

Fig. 6.4(b), the ILs are of three kinds: ohmic, dielectric, and due to leakages. The ohmic losses derive from the copper used to model the metallic parts of the antenna. The dielectric losses are associated with the substrate's dielectric properties. Finally, there are leakages due to the bonding layer, placed between two consecutive substrates [refer to the light-blue color in Fig. 6.4(a)], and to the blank distance occurring from a via to the next one [see Fig. 6.2]. The leakages are reduced by tuning the copper plates, placed in a mushroom-like configuration on the top of each via [see Fig. 6.4(a)]. This analysis is carried out by performing full-wave simulations in CST Microwave Studio [72] and is reported in Fig. 6.4(b). The most critical ILs derive from the leakages that the structure exhibits. In addition, the dielectric ILs are more severe than the ohmic ones. In general, the total ILs range from 0.015 to 0.028 dB/mm in the

frequency range 19-31 GHz. Note that the ILs behaves as an increasing function with frequency. It is indeed well-known that dielectric and ohmic losses are more severe at higher frequencies as they are associated with the hysteresis loop and the skin effect, respectively. In addition, the leakages also worsen at higher frequencies because the operating wavelength becomes smaller at those frequencies and, hence, the blank distances between the vias can be seen as electrically larger.

6.1.2 Radiating cell and corporate feed network

The design of the CTS array in PCB technology starts from studying the performance of its radiating cell. The unit cell's simulation setup is shown in Fig. 6.5. The open-ended quasi-SI PPW is arranged in a periodic environment. The

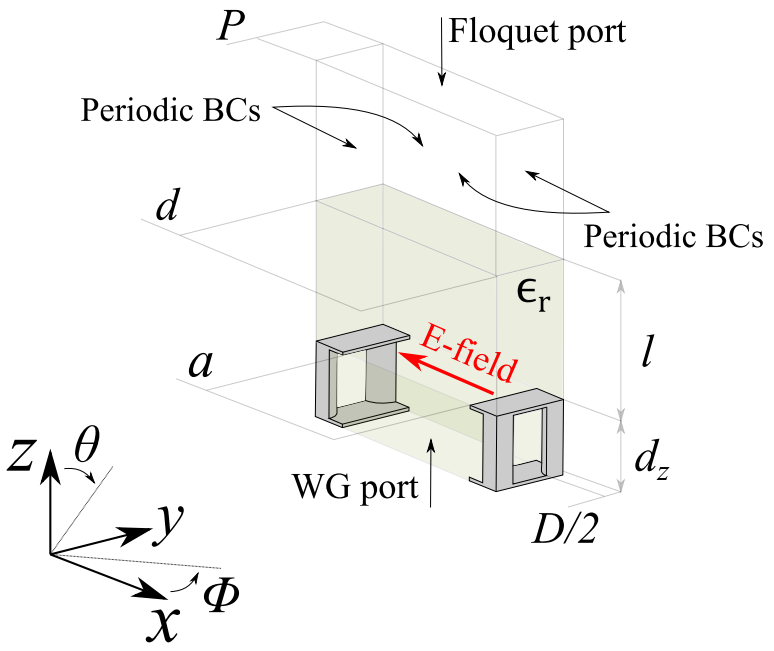

FIGURE 6.5: Simulation setup of the radiating cell of the CTS array in PCB technology. The unit cell's performance has been studied using a full-wave simulator [72] in a periodic configuration. Geometrical parameters: $a = 2.13$ mm, $d = 2.73$ mm, $l = 1.544$ mm, $d_z = 0.558$ mm, $D = 0.3$ mm, $P = 0.6$ mm, and $\epsilon_r = 2.2$.

long slots are etched on the top of a ground plane and fed by a quasi-PPW of width $a = 2.13$ mm. They occur periodically by $d = 2.73$ in the direction of x-axis and they are infinite along y-axis. Each slot is embedded in a substrate of relative permittivity $\epsilon_r = 2.2$ and thickness 0.508 mm. A wide-angle

impedance matching (WAIM) [78] is also realized by placing a dielectric layer of thickness $l = 1.544$ mm on the top of the radiating slots. The cell is studied by means of full-wave simulations [72]. As it is shown in Fig. 6.5, periodic boundary conditions (BC) are enforced on the lateral faces of the array's radiating cell. A Floquet's port is placed on the top of the radiating air box, whereas a waveguide port is considered on the bottom-most face of the structure. The waveguide port is used to launch a TEM mode into the unit cell that radiates a x-polarized E-fields with a plane wavefront. Note that the TEM wave is the only field distribution supported by the structure [refer to Fig. 6.3]. The simulated active reflection coefficient is plotted in Fig. 6.6 for different scan angles along the yz-plane. The active reflection coefficient is lower than -15 dB, everywhere

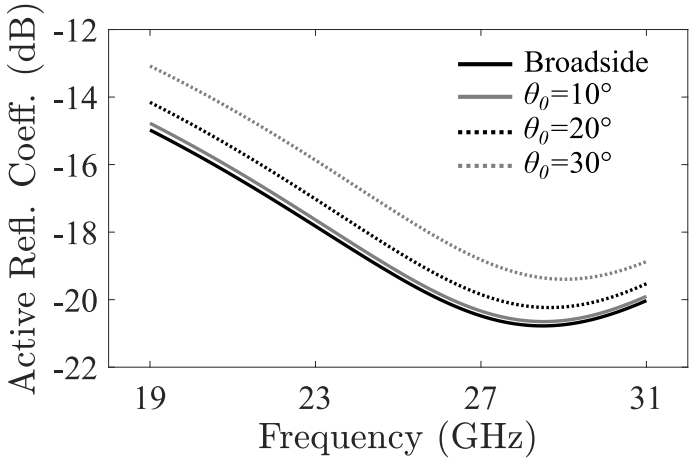

FIGURE 6.6: Simulated active reflection coefficient of the array's unit cell. The results are proposed for four beam directions along the yx-plane (H-plane). The simulation setup is depicted in Fig. 6.5.

in the frequency band 19-31 GHz for broadside radiation. When scanning along the yz-plane (H-plane), the impedance bandwidth remains roughly unvaried. The simulations show that the reflection coefficient is below -13 dB all over the band of interest, when the array is steering the beam at $\theta_0 = 30°$ along the H-plane. These results remark the broadband capabilities of parallel-fed CTS arrays even using the multilayer PCB technology. Specifically, the achieved impedance bandwidth is larger than 48%.

The long radiating slots are parallel-fed by means of a corporate feed network (CFN) made of 1-to-2 way power dividers in quasi-SI PPW technology. The design of the power dividers, realized using only two PCB panels, results in

a very compact structure that, in addition to further reducing the antenna bulkiness, also enhances the fabrication reliability reducing the misalignment between two consecutive stacked-up layers. A schematic drawing of the CFN is shown in Fig. 6.7, as seen in the cross-section along the xz-plane. The antenna

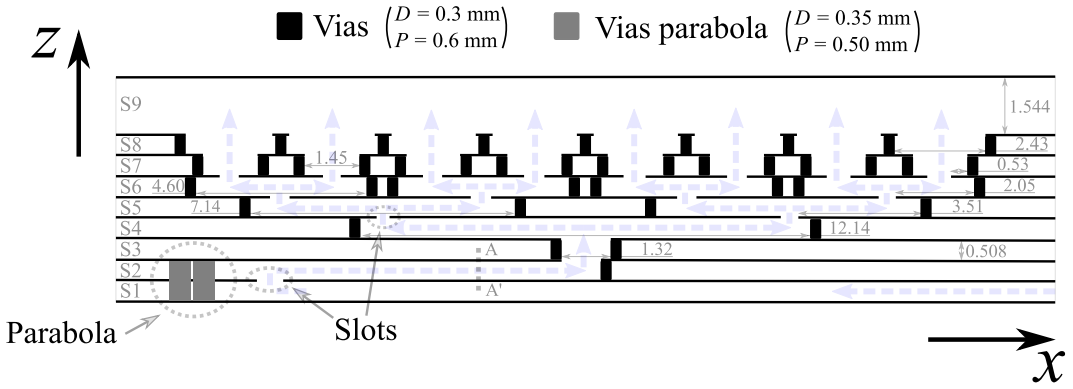

FIGURE 6.7: Schematic drawing of the CFN made of 1-to-2 way power splitter network using quasi-SI PPW technology, as seen in the cross-section along the xz-axis. The dashed blue arrows depict the Poynting's vector of propagating waves in the structure. All dimensions are given in millimeters.

array consists of eight radiating long slots parallel-fed through the CFN. As it is depicted in Fig. 6.7, the CFN is organized in seven substrates (S2 to S8) of thickness 0.508 mm and one substrate (S9) of thickness 1.544 mm placed on the top of the slots as matching layer. Each power divider is realized using two substrates, connected to each other through coupling slots. All the details about the antenna's geometry are reported in Fig. 6.7. The Poynting vector is depicted all across the structure to ease the comprehension of the electric paths traveled by the propagating waves. A pillbox coupler is integrated within the substrates S1 and S2, to realize a continuous line source along the y-axis for feeding the long slots. The parabola is designed using metallic vias of diameter 0.35 mm and periodicity 0.5 mm. The pillbox system will be discussed later in this Chapter.

The CFN was designed by means of an optimization procedure, performed in [72], with the aim to minimize the reflection coefficient at section AA' [see Fig. 6.7]. The simulated reflection coefficient at section AA' is reported in Fig. 6.8. The -10 dB impedance matched band is from 18 to 32.2 GHz (about 62% of relative bandwidth). For broadside radiation, the reflection coefficient is below -20 dB almost everywhere in the band of interest, i.e., 19-31 GHz.

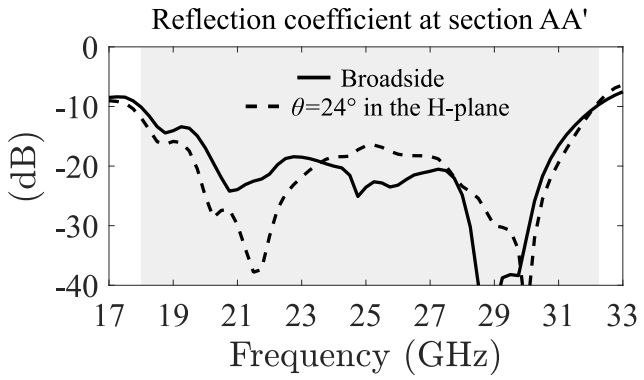

FIGURE 6.8: Simulated reflection coefficient of the CFN at section AA'. The array steers its main beam in the broadside direction.

6.1.3 Pillbox beam-former in PCB technology

This section aims at presenting the quasi-optical beam-forming system, employed to feed the CTS array in PCB technology. As for typical parallel-fed CTS array configurations [6], a good candidate is the pillbox coupler [19, 20, 48]. The top view of the pillbox system is depicted using a schematic drawing in Fig. 6.9. Two substrates, i.e., S1 and S2, are dedicated to the design [refer to

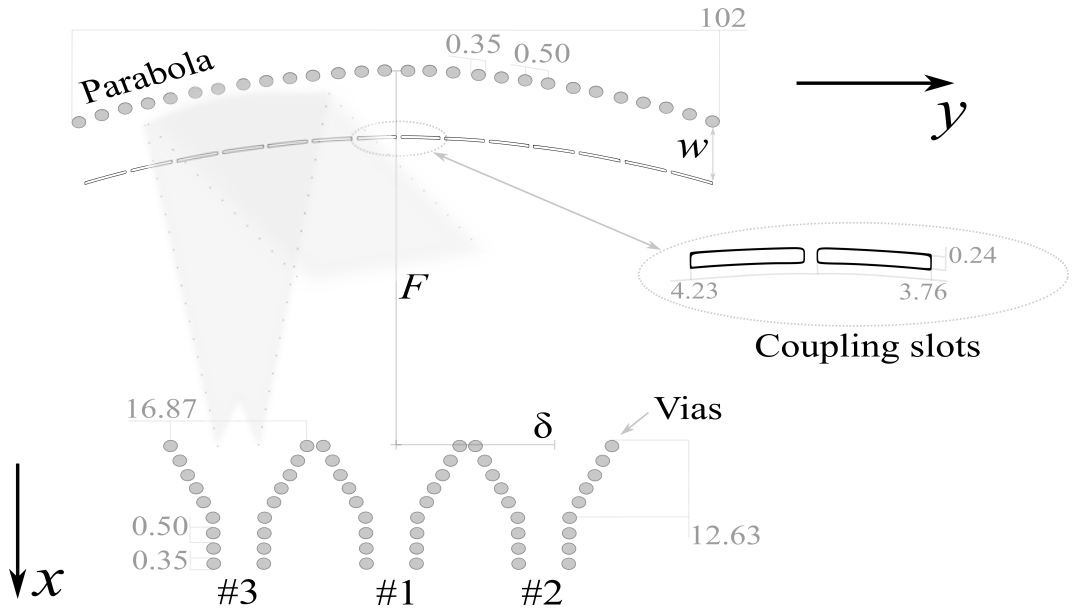

FIGURE 6.9: Schematic of the quasi-optical system as seen from a top view. All the dimensions are given in millimeters.

Fig. 6.7]. As it is shown in Fig. 6.9, the parabola is realized with periodic vias (diameter 0.35 mm and period 0.50 mm) drilled trough the substrates S1 and S2 [see Fig. 6.7]. The focal length of the parabola is $F = 60$ mm. Embedded

in the substrate S1, three input horns in SIW technology are employed for the parabola illumination. The horns displacement δ is linked to the scanning angle of the array θ_0, as follows [30]

$$\theta_0 \sim \frac{\delta}{F\sqrt{\epsilon_r}} \tag{6.2}$$

By setting the extreme scanning angle to be $\theta_0 = 20°$, one obtains $\delta = 17.5$ mm.

The simulated magnitudes of the E-field, in the substrates S1 and S2, are

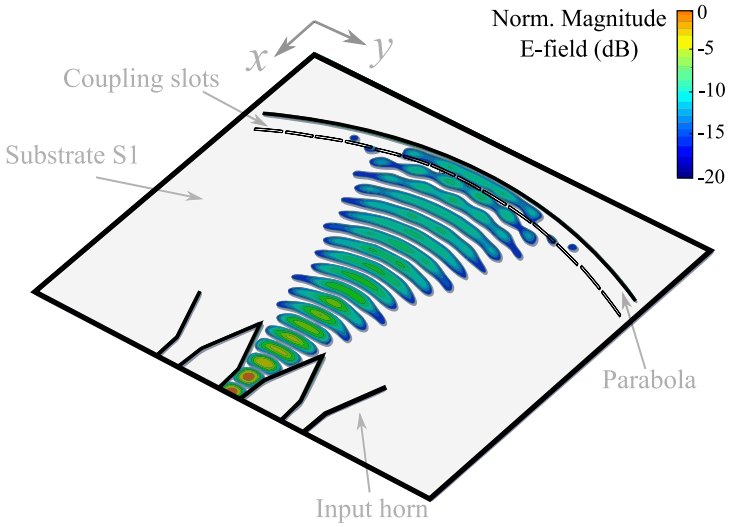

(a) Substrate S1.

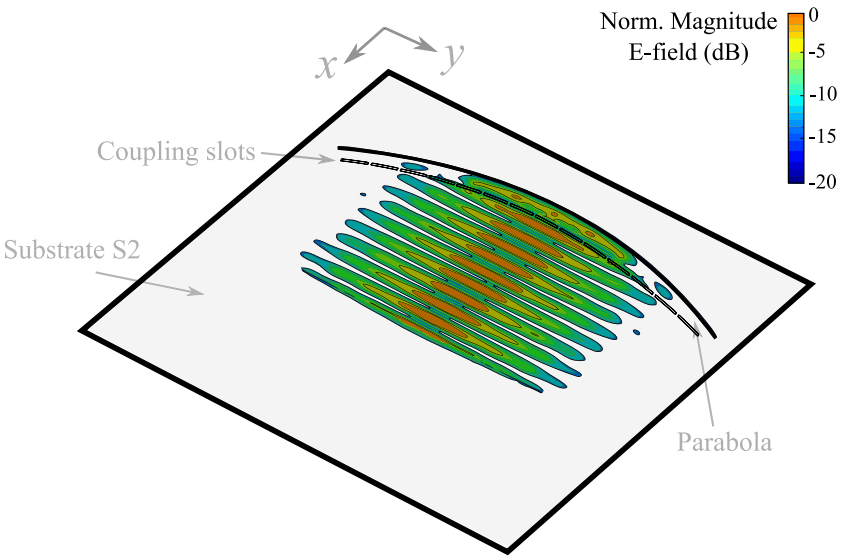

(b) Substrate S2.

FIGURE 6.10: Simulated magnitude of the field in the substrates (a) S1 and (b) S2. The parabola is illuminated by the Horn #1. The field is normalized to its maximum.

shown in Figs. 6.10(a) and (b), respectively. In the substrate S1, the waves have a cylindrical wavefront and are launched onto the parabola using the SIW horn [see Fig. 6.10(a)]. After being reflected by the parabola, the wavefront is transformed into a planar one and the field is coupled to the substrate S2 through rectangular slots [see Fig. 6.10(b)]. The latter are etched on the metallic layers between the substrates S1 and S2 and are placed at a distance $w = 3.4$ mm from the parabola. Inside the substrate S2, the field has a planar wavefront and propagates along the x-axis.

The radiating apertures of the input horns are arranged along a y-oriented line at the focal distance of the parabola [see Fig. 6.9]. The three horns are so displaced along the focal length, in order to provide a gradually-phased field

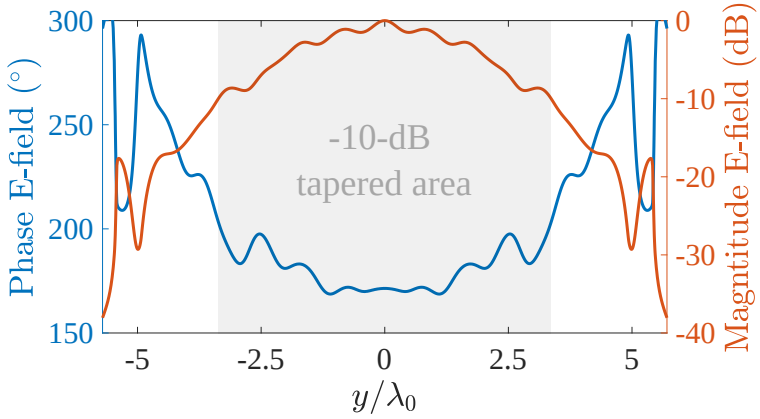

(a) Horn #1.

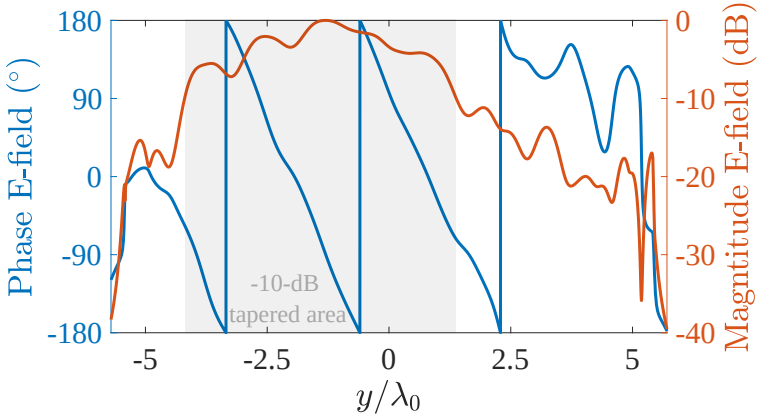

(b) Horn #2.

FIGURE 6.11: Simulated E-field in the substrates S2 as function of the variable y, when the parabola is illuminated by the horns (a) #1 and (b) #2. The radiating slots are centered at $y = 0$. λ_0 is the wavelength at 29 GHz.

distribution along y-axis and, hence, enabling the array to attain beam-scanning along the H-plane. The simulated E-field distributions in the substrate S2 are reported in Figs. 6.11(a) and (b) as a function of the variable y, when the parabola is illuminated by the horns #1 and #2, respectively. As shown in Fig. 6.11(a), the magnitude of the E-field is tapered at the edges of the parabola and the slots are illuminated by a field distribution having a flat phase profile. This ensures the array to point its main beam in the boresight direction. Note that the illumination of the slots is mainly provided by the field distribution occurring within the -10 dB tapered area [see the grey area in Fig. 6.11(a)]. On the contrary, the horn #2 provides a field distribution still having a tapered amplitude, but with a sawtooth-like phase behavior [see Fig. 6.11(b)]. The latter provides a linear phasing of the long slots, thus enabling the beam steering along the H-plane.

6.1.4 Coaxial-to-GCPW-to-SIW transition

The input section of the antenna consists of a 50 Ω female coaxial connector, i.e., Southwest 1092-01A-9 [145]. Three connectors are used to feed the horns in the focal plane of the pillbox system. They are solderless and mounted using fixing screws. For each connector, the pin has a standard diameter of 2.92 mm and is adjusted on a grounded co-planar waveguide (GCPW), thus creating an electric contact to feed the SIW horns via a GCPW-to-SIW transition. A perspective view of the antenna input section is shown in Fig. 6.12. The GCPW-to-SIW transition consists of a stepped impedance matching circuit in microstrip technology. It was designed by means of a full-wave optimization in [72] aiming at minimizing the reflection coefficients at port 1 and 2, as well as to maximizing the transmission between the same two ports [see Fig. 6.12]. The top view of the GCPW-to-SIW transition is reported in Fig. 6.13. The pin is connected to a GCPW surrounded by vias that enhance the field confinement around the central RF trace. A stepped transition conveys the energy from the coaxial to the input horn in SIW technology. The simulated S-parameters of the transition are reported in Fig. 6.14. Both the reflection coefficients at port 1 and 2 are below -15 dB all over the band 19-31 GHz. The insertion losses are lower than 0.5 dB in the same frequency band with an average value around 0.3 dB.

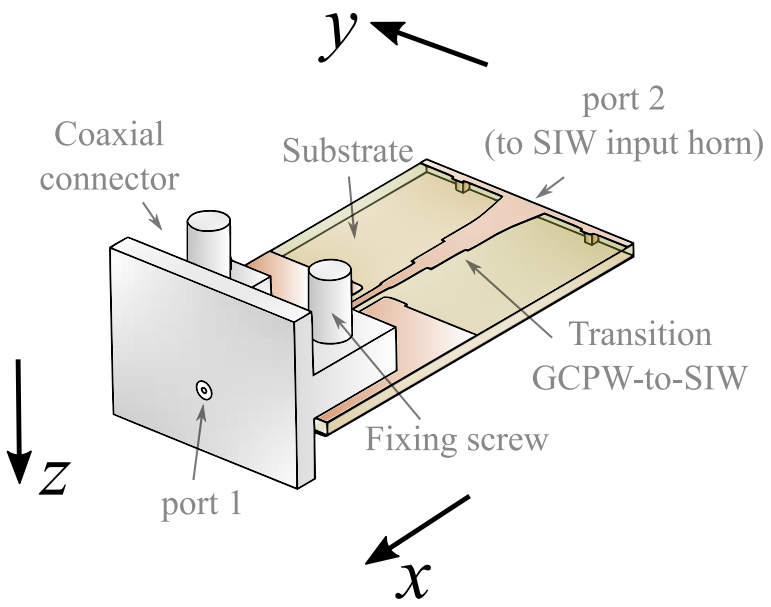

FIGURE 6.12: Schematic drawing of the 3-D view of the coaxial-to-GCPW-to-SIW transition. The orange color is used to indicate the copper and the grey one stands for the connector's metal. Finally, the substrate is illustrated in green.

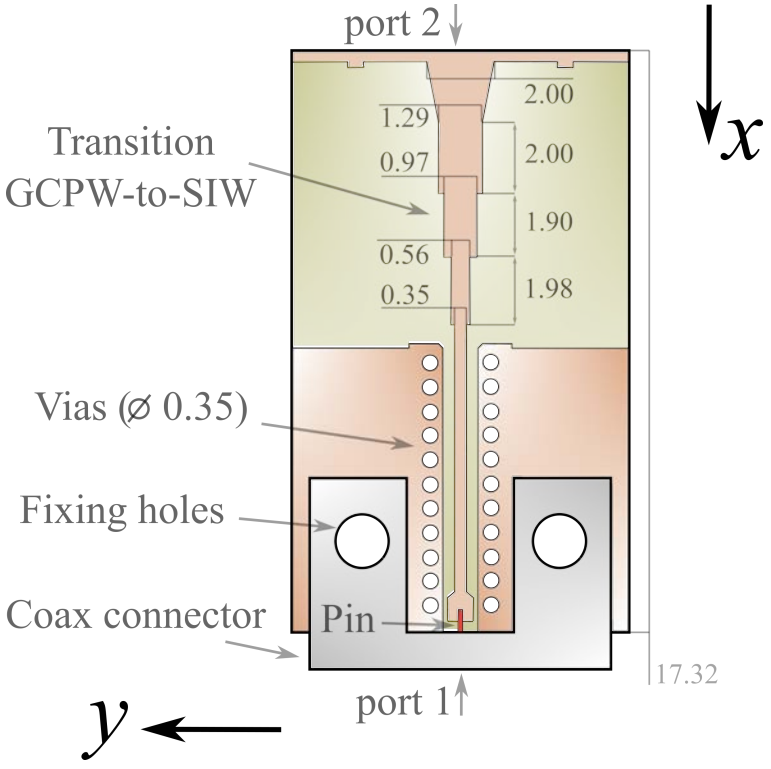

FIGURE 6.13: Schematic drawing of the top view of the coaxial-to-GCPW-to-SIW transition. The grey color is used to indicate the connector's metal. The orange and green colors illustrate the copper and the substrate, respectively. All dimensions are given in millimeters.

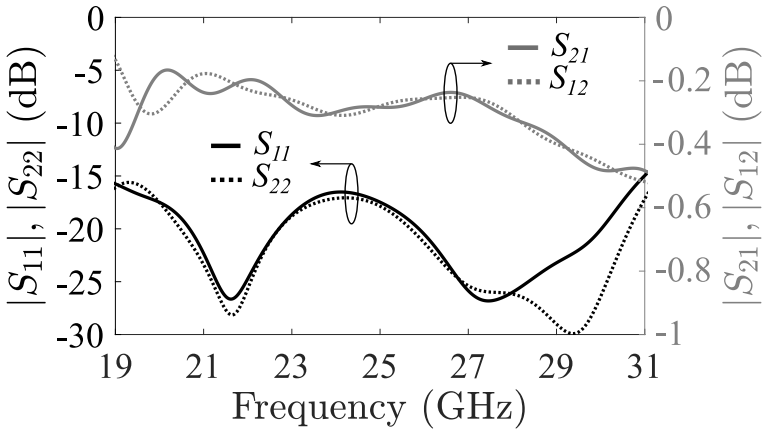

FIGURE 6.14: Simulated S-parameters of the coaxial-to-GCPW-to-SIW transition.

6.1.5 Performance of the antenna module

A 3-D view of the overall antenna architecture is depicted in Fig. 6.1. The radiating long slots are not visible because they are covered by a matching layer. However, the cross-sectional view of the antenna's inner part is illustrated in a zoomed-in detail in Fig. 6.1(a). As it is shown in Fig. 6.1(b), the coaxial connector is used to feed the SIW horns, through the GCPW-to-SIW transition described in Section 6.1.4. According to the selected connector, the antenna pointing directions (ϕ_0, θ_0) are $(90°, 0°)$ or about $(90°, \pm 24°)$. Furthermore, the coaxial-to-GCPW-to-SIW transition is designed on the reverse side with respect to the main beam direction of the antenna. This is to avoid field perturbations deriving from the radiated leakages of the microstrip line present in the GCPW-to-SIW transition. The final antenna module shows an ultra-low-profile which makes it a very appealing solution for modern SatCom applications.

The simulated input reflection coefficient of the antenna is plotted in Fig. 6.15 when the horns #1 and #2 are operating, respectively. The simulations take into account the ohmic and dielectric losses, as well as the radiated leakages. A -10 dB impedance bandwidth is observed in the band 19-31.7 GHz (50%) for horn #1 excitation. When the antenna is excited by horn #2, the impedance bandwidth is furthermost larger. This effect is typical in antennas using quasi-optical systems as a feeding network [6]. The in-focus position, in fact, gathers the biggest amount of reflected power from the parabola. In summary, the input reflection coefficient is below -10 dB everywhere in the band 19-31 GHz and confirms the broadband capability of this type of antennas.

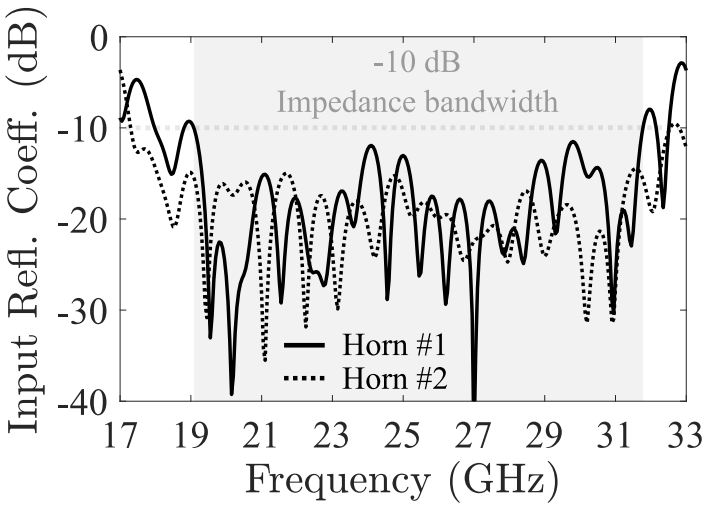

FIGURE 6.15: Simulated input reflection coefficient of the antenna for horn #1 and #2 excitation.

The radiating performance can be predicted by the numerical model presented in Chapter 2.3.1, by using the field distribution in Figs. 6.11(a) and (b) as windowing functions. The calculated patterns are also validated by full-wave simulations, as shown in Fig. 6.16. The normalized patterns are computed at 25

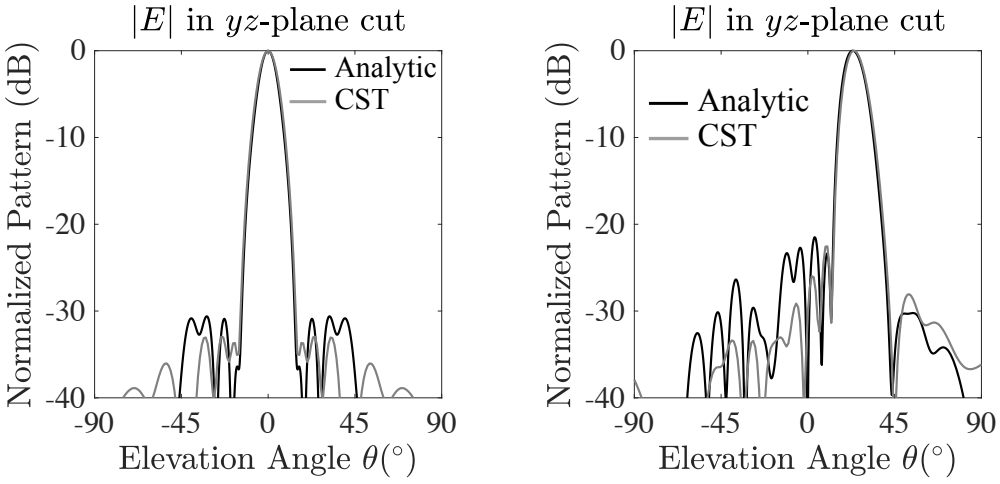

(a) Horn #1.

(b) Horn #2.

FIGURE 6.16: Simulated radiation patterns using the numerical model presented in chapter 2.3.1 and the full-wave software [72] at 25 GHz. Each pattern is normalized to its maximum. (a) Horn #1. (b) Horn #2.

GHz and an excellent agreement is observed between computed and simulated radiation patterns. In particular, the first sidelobe levels (SLL) appear to be lower than -30 dB for broadside radiation and -22 dB when the antenna points

at $\theta_0 = 20°$ in the yz-plane. The plots of the array directivity, as a function of the frequency and the scan angle, are shown in Figs. 6.17 (a) and (b) for horn #1 and #2 excitation, respectively. For broadside radiation, the pointing direc-

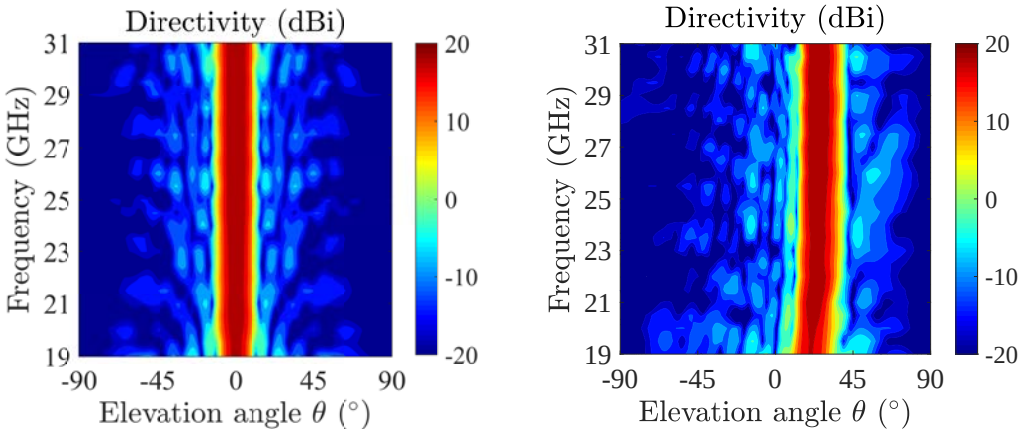

(a) Horn #1. (b) Horn #2.

FIGURE 6.17: Simulated array directivity as function of the frequency and scan angle for horn (a) #1 and (b) #2 excitation. The patterns are simulated along the yz-plane.

tion of the array is very stable all over the frequency band of interest. On the contrary, the beamwidth narrows at lower frequencies for horn #2 excitation. The focal distance of the parabola may, in fact, be slightly different at those frequencies. On the other hand, the directivity peak is around 20 dBi and is roughly constant all over the band 19-31 GHz.

Finally, the radiation efficiency and the realized gain of the antenna system are plotted in Fig. 6.18. The radiation efficiency is on average higher than 70%

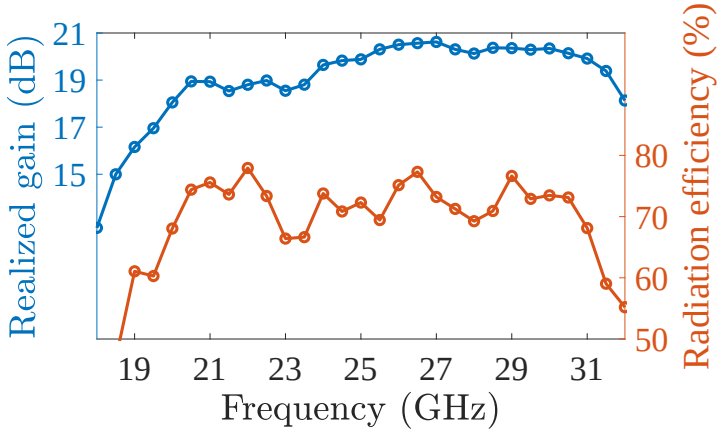

FIGURE 6.18: Simulated radiation efficiency and realized gain of the antenna system.

over the band 19-31 GHz. In particular, it decreases at the extreme frequencies of the same band due to a deterioration of the antenna matching. The peak of radiation efficiency is 80%, which is interesting, given the compactness and the broadband performance of the antenna. Consequently, the peak of the realized gain is about 21 dB at the same frequencies, where the antenna performs with maximum efficiency. In general, the simulated realized gain ranges from 16 to 21 dB all over the K/Ka-band.

6.2 Prototype and experimental results

Some photographs of the fabricated prototype are shown in Fig. 6.19. The

(a) Perspective view.

(b) Bottom view.

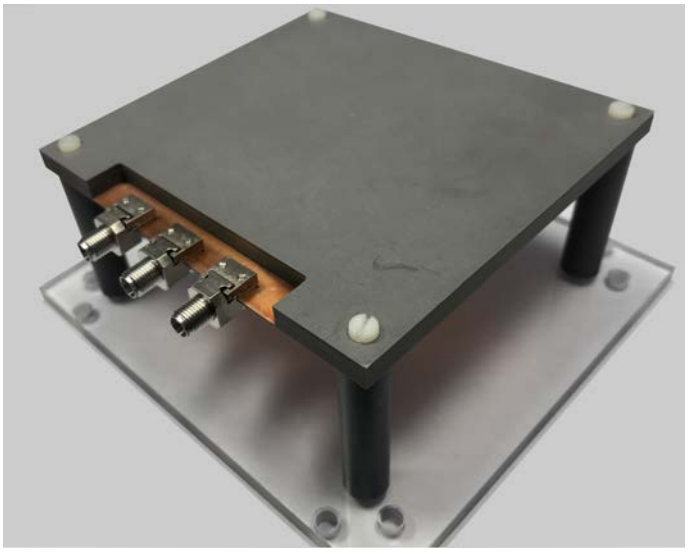

(c) Perspective view with plastic support.

FIGURE 6.19: Photographs of the fabricated prototype. (a) Perspective and (b) bottom views. (c) Antenna adjusted on a plastic support.

antenna was fabricated using standard PCB technology. The coaxial connectors were mounted using a microscope. The vias are visible from the antenna bottom-side [see Fig. 6.19(b)], thus describing the parabolic profile as well as the input SIW horns. A plastic support was also built as mechanical support to ease in performing the experimental tests in the anechoic chamber. The latter is connected to the antenna through fixing plastic screws, as shown in Fig. 6.19(c).

The reflection coefficient of the antenna has been measured with a PNA network analyzer (Keysight N5227A). A thru, reflect, line (TRL) calibration was performed to calibrate the coaxial cables. The measured results are shown in Fig. 6.20 for horn #1, #2 and #3 operation. As it was predicted by the

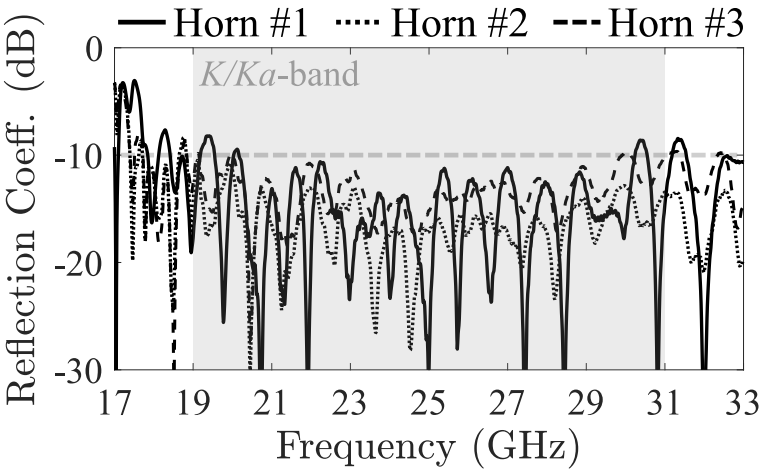

FIGURE 6.20: Measured reflection coefficients of the CTS array in PCB technology.

full-wave simulations, the reflection coefficient is lower than -10 dB almost everywhere in the band of interest, i.e., 19-31 GHz. The measured results remark a broadband performance. Moreover, the PCB technology suits well to the fabrication of miniaturized CTS antenna arrays. The reliability of the fabrication process is, indeed, outstanding as no misalignment issue between the stacked layers has occurred during the antenna construction.

At the time of this manuscript's redaction, the radiation properties of the self-standing antenna have been tested over the 26-31 GHz band only. The measured radiation patterns along the H-plane [yz-plane in Fig. 6.1] are reported in Fig. 6.21. The measured patterns are in good agreement with the full-wave simulations and confirm the antenna performs highly-directive pencil-beam radiation. Specifically, the results shown in Figs. 6.21(a)-(f) refer to broadside

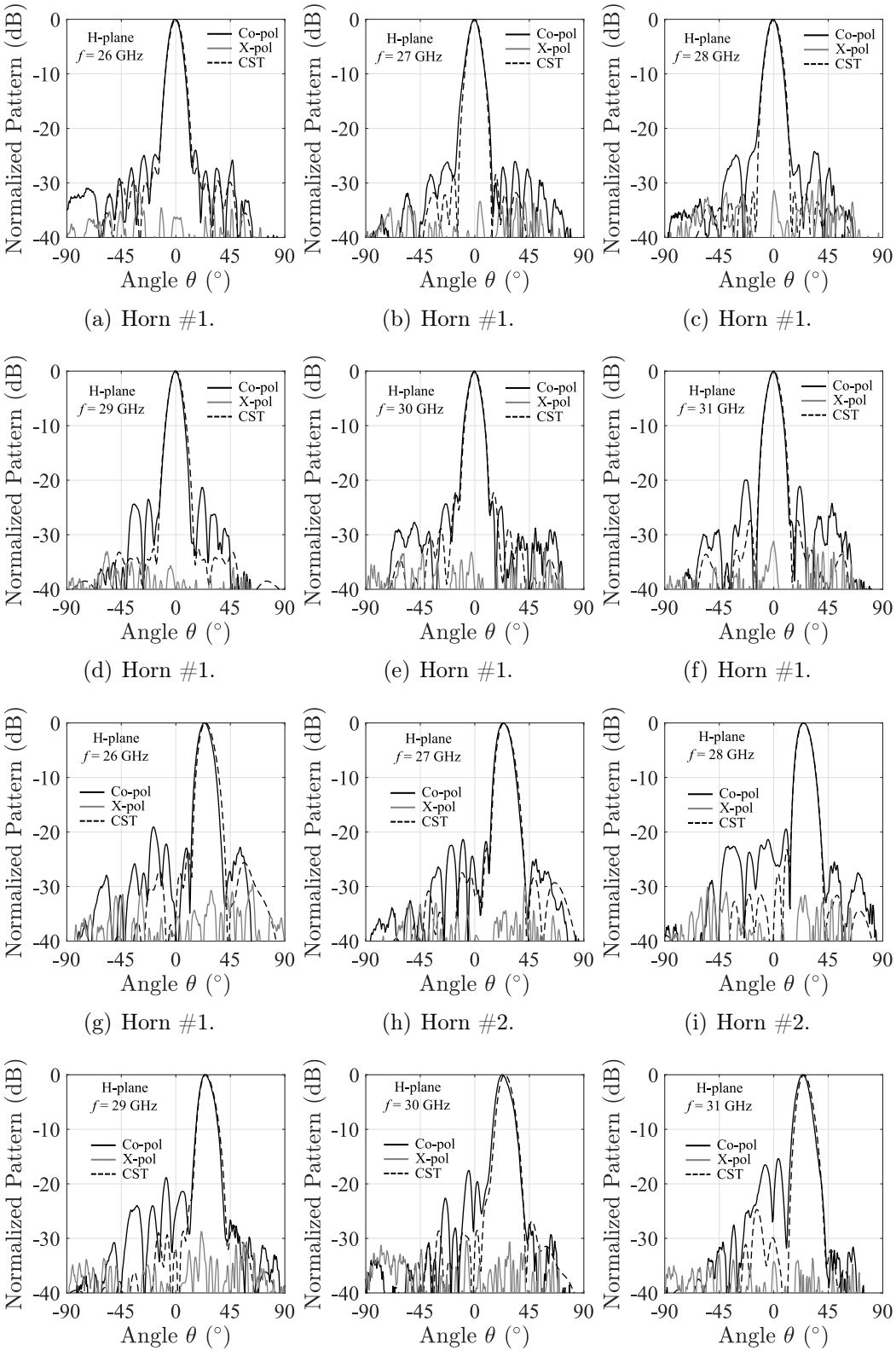

(a) Horn #1. (b) Horn #1. (c) Horn #1.

(d) Horn #1. (e) Horn #1. (f) Horn #1.

(g) Horn #1. (h) Horn #2. (i) Horn #2.

(j) Horn #2. (k) Horn #2. (l) Horn #2.

FIGURE 6.21: Measured normalized patterns at different frequencies. (a)-(f) Horn #1 excitation. (g)-(l) Horn #2 excitation.

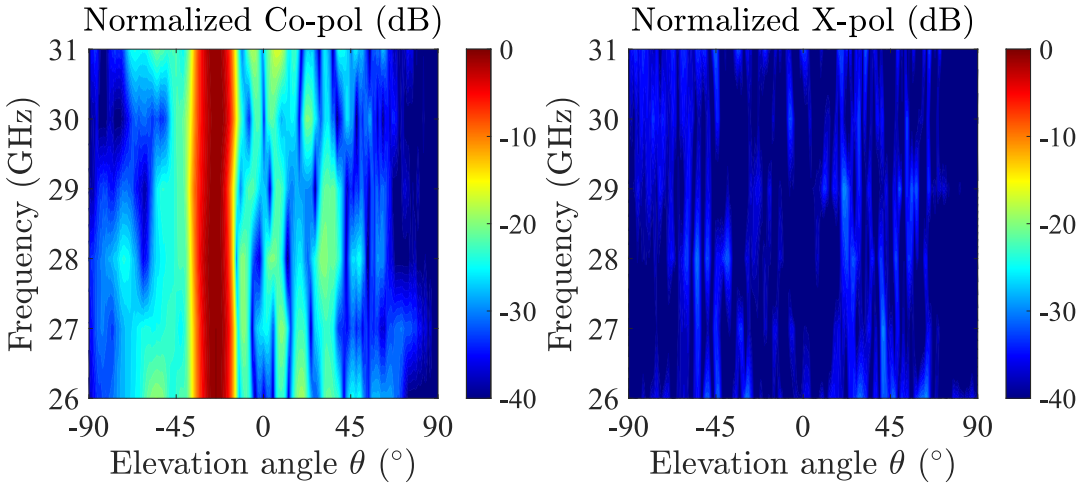

(a) Horn #3.

(b) Horn #3.

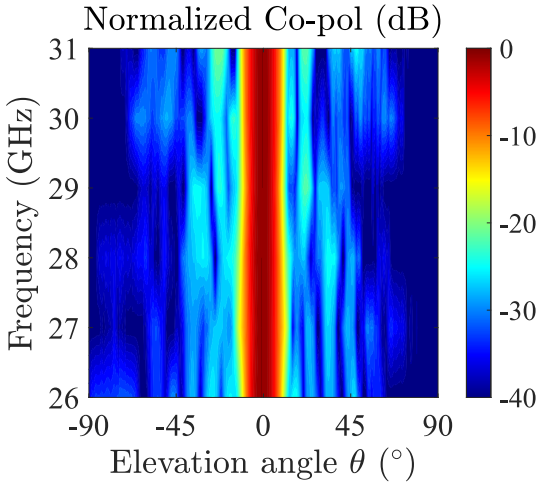

(c) Horn #1.

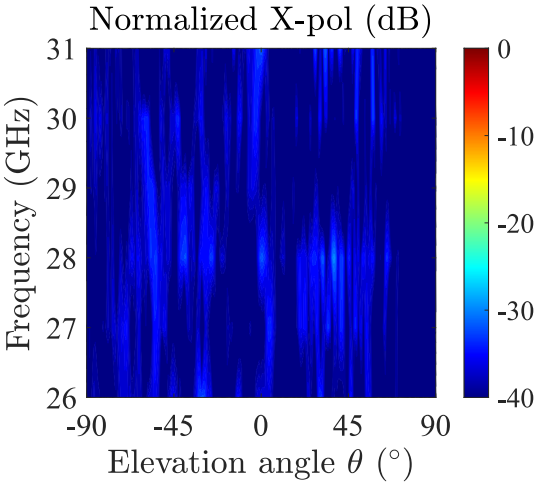

(d) Horn #1

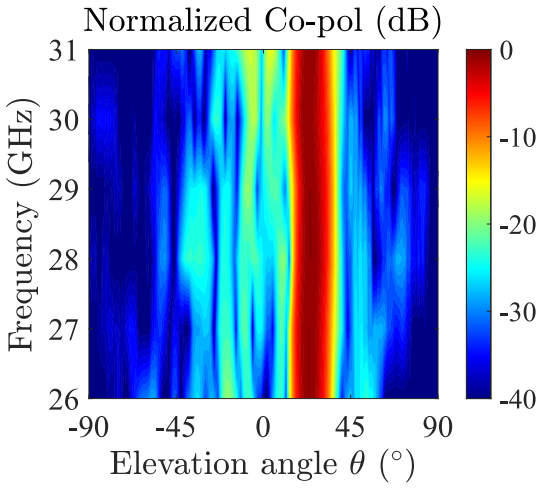

(e) Horn #2.

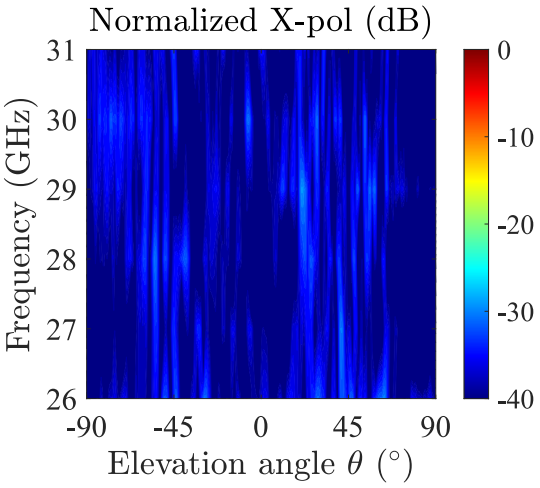

(f) Horn #2.

FIGURE 6.22: Measured (a,c,e) co- and (b,d,f) cross-polarization patterns versus the frequency and the angle θ along the H-plane.

radiation, whereas those in Figs. 6.21(g)-(l) to the performance while scanning. The SLLs are below -20 dB along the H-plane for broadside radiation [see Figs. 6.21(a)-(f)], everywhere in the band 26-31 GHz. Also, the cross-polarization component is lower than -30 dB along with the same azimuth plane and frequency range. Similarly, the radiation performance in scanning shows SLLs below -18 dB, as well as a cross-polarization lower than -30 dB with respect to the peak value of the main beam [see Figs. 6.21(g)-(l)]. The frequency stability of the beam direction can be observed from Fig. 6.22, where the normalized co- and cross-polarization are reported as a function of the angle θ (along the H-plane) and the frequency. Specifically, the broadside beam [see Fig. 6.22(c)] is found to be very stable in terms of pointing angle and beamwidth all over the 26-31 GHz band. When the antenna performs in scanning [refer to Figs. 6.22(a) and (e)], the pointing direction of the array slightly varies with frequency. Nonetheless, this variation is acceptable (maximum 2°) and might be due to fabrication tolerances. Furthermore, the cross-polarization, normalized to the peak value of the co-polarization, is plotted in Figs. 6.22(b),(d) and (f) for Horn #3, #1, and #2, respectively. The measured results are very satisfactory, considering that the cross-polarization is observed to be below -25 dB everywhere in the 26-31 GHz frequency range along the H-plane.

For the sake of completeness, the measured radiation patterns along the E-plane [xz-plane in Fig. 6.1] as a function of the frequency and the angle θ

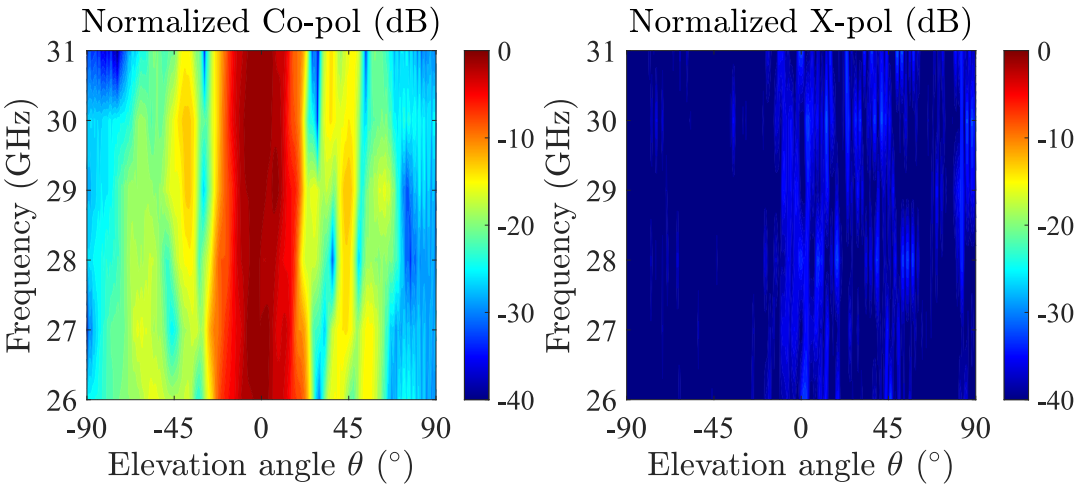

(a) Horn #1.

(b) Horn #1

FIGURE 6.23: Measured (a) co- and (b) cross-polarization patterns versus the frequency and the angle θ along the E-plane.

are also reported in Fig. 6.23. The measurements along the E-plane have been carried out for broadside radiation only. Fig. 6.23(a) reports the measured co-polarization and shows that the antenna's pointing angle is stable in frequency. Also, the SLLs are lower than -15 dB everywhere in the frequency range 26-31 GHz. On the other hand, the measurements of the cross-polarization are reported in Fig. 6.23(b), showing values below -25 dB everywhere in the 26-31 GHz band.

At the moment of this manuscript's redaction, the antenna is under test over the band 19-26 GHz using the IETR's facilities. The realized gain, as well as the antenna radiation efficiency, will be also measured.

6.3 CTS array with the dual-band polarizer

The aim of this Section is to present the performance of the CTS array, when combined with the dual-band polarizer introduced in Chapter 5. The linear-to-circular polarization (LP-to-CP) converter is used as add-on component and

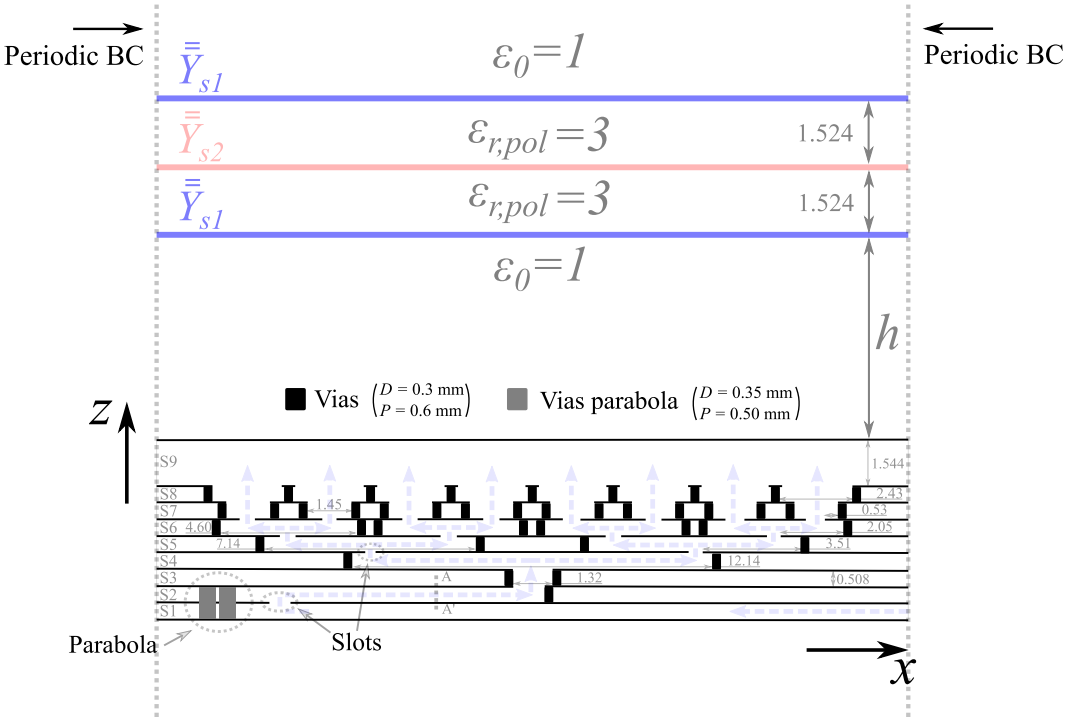

FIGURE 6.24: Schematic of the simulation setup. The CFN of the array is simulated in a periodic environment and three electric sheet admittances are placed on the top of the radiating aperture, at a distance h. All the dimensions are given in millimeters.

placed on the top of the radiating aperture. The overall system is expected to perform dual-band radiation with versatile circular polarization (CP). Being the overall structure (CTS array plus polarizer) electrically large, its full-wave simulation would be excessively time-consuming. For this reason, the performances are estimated by means of equivalent sheet admittances that replace the LP-to-CP converter, as done in Chapter 5. The simulation setup is illustrated in Fig. 6.24 from a cross-sectional view. The CFN of the array is simulated in a periodic environment using [81] and three sheet admittances are placed on the top of the radiating aperture, at a distance h. Two consecutive sheets are interleaved by a dielectric slab of dielectric constant $\epsilon_{r,pol} = 3$ and thickness 1.524 mm. The structure is excited from the section AA' with a TEM wave, launched into the substrate S1 [refer to Fig. 6.24]. The polarizer is simulated by means of admittance sheets, as discussed in Section 5.1. The electric sheet admittances are anisotropic and their mathematical expression is given by

$$\bar{\bar{Y}}_{s1} = \begin{bmatrix} \left(i\omega L_{s1}^{x'x'}\right)^{-1} & 0 \\ 0 & \left(i\omega L_{s1}^{y'y'} + \frac{1}{i\omega C_{s1}^{y'y'}}\right)^{-1} \end{bmatrix} \tag{6.3}$$

$$\bar{\bar{Y}}_{s2} = \begin{bmatrix} \left(i\omega L_{s2}^{x'x'} + \frac{1}{i\omega C_{s2}^{x'x'}}\right)^{-1} & 0 \\ 0 & \left(i\omega L_{s2}^{y'y'} + \frac{1}{i\omega C_{s2}^{y'y'}}\right)^{-1} \end{bmatrix} \tag{6.4}$$

where ω is the angular frequency and the lumped elements $L_{s1}^{x'x'}$, $L_{s1}^{y'y'}$, $C_{s1}^{y'y'}$, $L_{s2}^{x'x'}$, $C_{s2}^{x'x'}$, $L_{s2}^{y'y'}$, and $C_{s2}^{y'y'}$ can be found in Table 5.1. The entries of $\bar{\bar{Y}}_{s1}$ and $\bar{\bar{Y}}_{s2}$ correspond to a Cartesian reference system (x', y') as rotated by 45° with respect to the x-axis indicated in Fig. 6.24. The distance h is optimized by means of a parametric study. The optimum is found for $h = 70$ mm. The simulated axial ratio (AR) and reflection coefficient (at section AA') are reported in Fig. 6.25. The grey areas in Fig. 6.25 indicate the bands of operation. They are defined as the frequency ranges for which AR$<$ 3 dB and the reflection coefficient is below -10 dB. As it is shown in Fig. 6.25, the antenna system radiates agile circular polarization within the frequency bands 18.7-20.7 GHz and 28.2-30 GHz. These simulated results are only indicative, as they do not refer to a real structure. Anyway, they can provide an estimation of the attainable performance of the structure. Note that the simulations in Fig. 6.25 refer to broadside radiation.

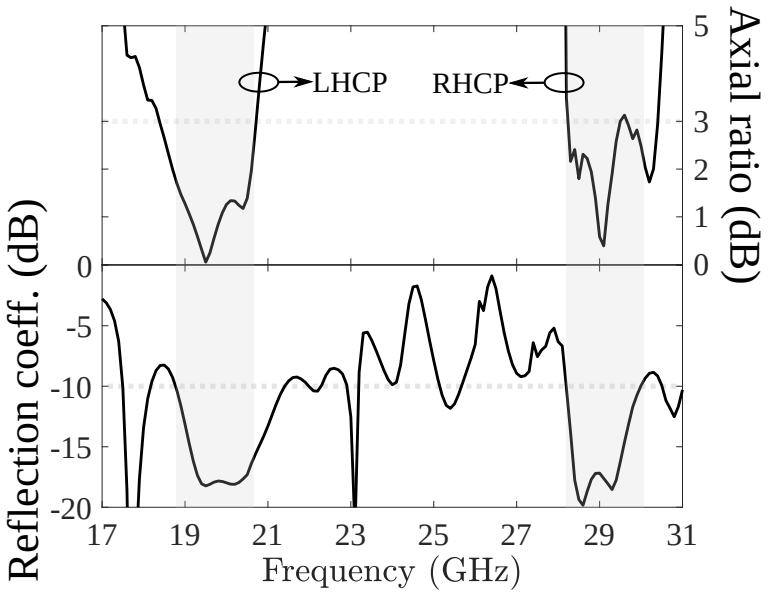

FIGURE 6.25: Simulated axial ratio (AR) and reflection coefficient (at section AA') of the structure in Fig. 6.24. The gray areas indicate the achieved bands of operation. The latter are defined as the frequency ranges for which AR$<$ 3 dB and the reflection coefficient is below -10 dB. The array is pointing the main beam at broadside.

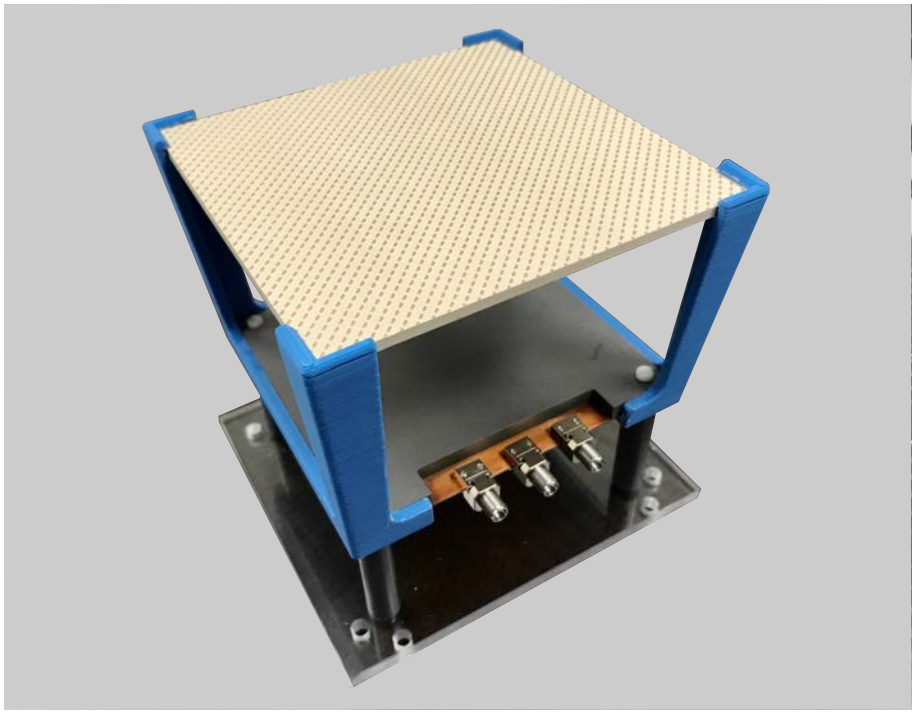

FIGURE 6.26: Photograph of the prototyped CTS array in PCB technology, used in combination with the dual-band polarizer shown in Fig. 5.10(b).

A plastic support was fabricated to hold the polarizer over the radiating aperture at a distance of 70 mm, as can be seen in Fig. 6.26. The radiation performance of the antenna module was estimated by performing measurements in the anechoic chamber. To the date of this manuscript's redaction, the structure in Fig. 6.26 has been characterized in the band 26-31 GHz and the measured results are reported in Figs. 6.27(a), (b) and (c). By virtue of the dual-band

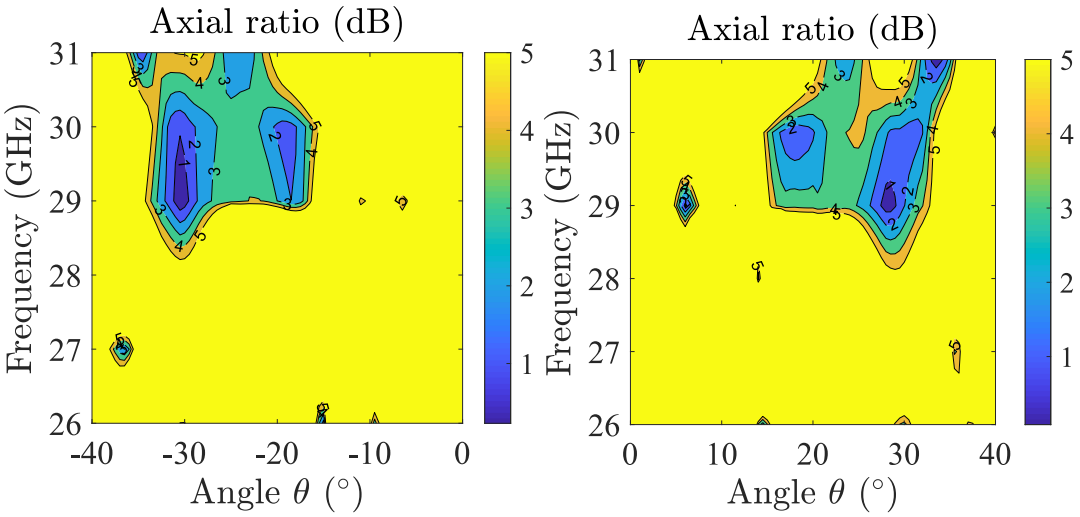

(a) Horn #3.

(b) Horn #2.

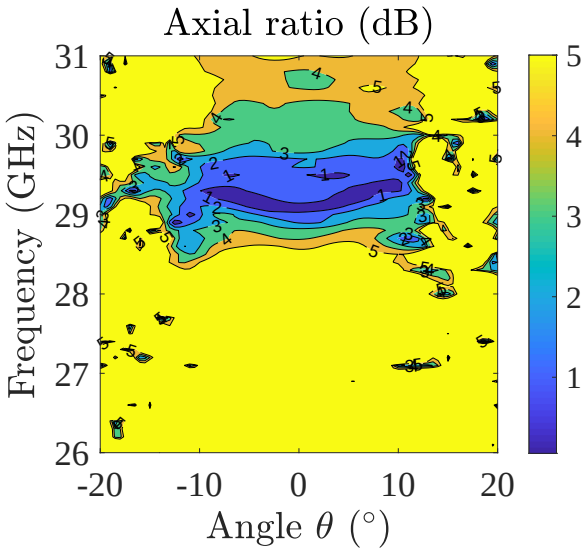

(c) Horn #1.

FIGURE 6.27: Measured axial ratio of the prototype shown in Fig. 6.26. The axial ratio is reported as function of the angle θ in the yz-plane and the frequency. Horn (a) #3, (b) #2 and (c) #1 excitation.

polarizer, the antenna radiates circularly-polarized fields in the band of interest.

Fig. 6.27(b) shows that an AR below 3 dB is measured around the frequency range 29-30.1 GHz for scanning around 20°. A further 3-dB-AR bandwidth is observed around $\theta = 30°$. The latter effect might be due to a shift of the pointing angle of the array, as a result of having placed the polarizing screen in front of the aperture. Similar comments can be done for Horn #3 excitation, whose measurements are shown in Fig.6.27(a). Finally, the measured AR for broadside radiation is reported in Fig. 6.27(c). The AR pattern is very stable in frequency around the pointing direction of the antenna (broadside). The metasurface-based polarizing screen behave as a transparent component in the operating band and transform linearly-polarized wave into right hand circularly-polarized radiation.

The purity of the radiation patterns can be observed from the measured results shown in Fig. 6.28. The radiation patterns are plotted in the space (ξ, ζ). These two angles correspond to the elevation and azimuth angles typically used in the antenna measurements. Their formal definition can found in the third Ludwig's definition outlined in the article [79]. Basically, the angle ξ is the polar angle in the xz-plane for a given direction in the yz-plane. As a matter of example, the scanning plane (yz-plane) is associated with the portion of the (ξ, ζ) space corresponding to $\xi = 0°$. The radiation patters are measured at 29 GHz. Figs. 6.28(d), (e) and (f) refer to broadside radiation (horn #1 excitation). As predicted by the simulations, the co-polar component of the E-field is given by the right-hand circular polarization (RHCP) [see Fig. 6.28(e)]. On the other hand, the cross-polarization is below -14.6 dB with respect to the maximum value of the co-polarization [refer to Fig. 6.28(d)]. A very good cross-polar discrimination (XPD) is so observed and the corresponding measured AR is lower than 3 dB within the half-power beamwidth area of the RHCP pattern. Very similar comments can be done when the array performs scanning. Specifically, Figs. 6.28(a), (b) and (c) show the radiation patterns when the array is steering its main beam at $(\theta_0, \phi_0) = (0°, -24.2°)$, i.e., horn #3 excitation, whereas Figs. 6.28(g), (h) and (i) are associated with the array when scanning at $(\theta_0, \phi_0) = (0°, 24.2°)$, i.e., horn #2 excitation. In these scenarios, a very high CP purity (AR below 3 dB) is observed around the pointing angles of the array. The XPD is around 14.4 dB.

In conclusion, the AR measured in the pointing direction of the array is

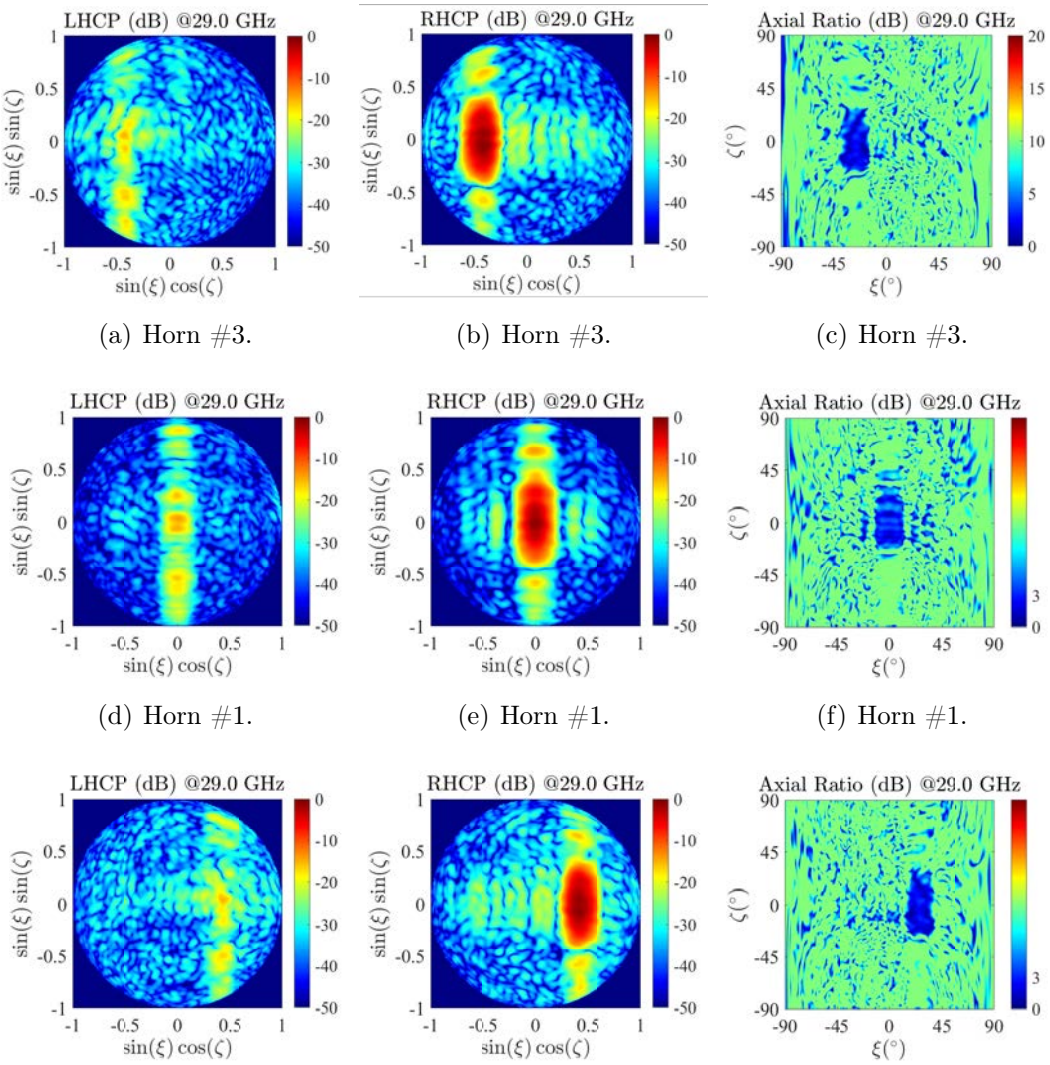

(a) Horn #3. (b) Horn #3. (c) Horn #3.

(d) Horn #1. (e) Horn #1. (f) Horn #1.

(g) Horn #2. (h) Horn #2. (i) Horn #2.

FIGURE 6.28: Measured radiation patterns of the structure in Fig. 6.26. The radiation patterns are reported in the (ξ, ζ) space. Horn (a-b-c) #3, (d-e-f) #1 and (g-h-i) #2 excitation. The patterns are measured at 29 GHz.

plotted in Fig. 6.29 as a function of the frequency. The measured results are compared with the measurements of the polarizer as self-standing device for normal incidence, as reported in Section 5.2.1. The measurements show a very good agreement in the up-link band (28.8-30.1 GHz). The integration of the CTS array with the dual-band LP-to-CP converter is well characterized in the upper band and the measured results are very much in line with the expected performance.

At the time of the redaction of this manuscript, the measurements for the rest of the operating band are still ongoing.

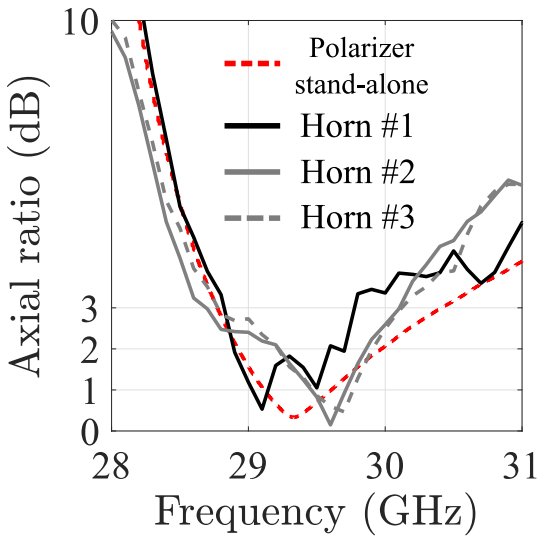

FIGURE 6.29: Measured axial ratio as a function of the frequency. The axial ratio is computed in the pointing direction of the array and it is associated with the RHCP pattern.

6.4 Conclusions

In this Chapter, the design of an ultra-low profile CTS array has been proposed and discussed. The antenna system has been developed in the frame of a collaboration between IETR and TCS. The proposed design is intended as an advanced miniaturized antenna, able to fulfill modern satellite communication on-the-move (SOTM) requirements. The antenna is entirely designed in PCB technology, which has turned out to be a very reliable fabrication process at K/Ka-band. The module is entirely fabricated using 9 PCB layers and comprises a quasi-optical beamformer as feeding system, fully integrated into only two PCB layers. The vertical propagation of TEM waves is achieved through a layer-to-layer capacitive coupling by exploiting a quasi-SI PPW technology. Even though leakages and ohmic/dielectric losses are unavoidable using such a technology, their effect has been mitigated by performing a dedicated optimization procedure. As result, the overall antenna system exhibits a radiation efficiency higher than 70% everywhere in the band of interest. The designed CTS array, indeed, exhibits an impedance-matched bandwidth that exceeds the 19-31 GHz band. Also, the beam steering is enabled along the H-plane. The antenna system has been prototyped and tested in terms of reflection coefficient and radiation patterns (in the range 26-31 GHz), showing excellent results. In

the future, the antenna radiating properties will be also characterized in the frequency range 19-26 GHz, using the IETR's facilities. Finally, such an interesting device is integrated with a dual-band LP-to-CP converter to attain a dual-band versatile CP radiation. The performance of the system has been evaluated by means of equivalent circuit models and shows a good impedance matching within the two bands of interest, as well as interesting 3-dB-AR bandwidths. A plastic support has been constructed to integrate the LP-to-CP screen and preliminary measurements have been carried out in terms of AR. The measured results have been carried out in the frequency range 26-31 GHz. By exciting from the out-of-focus horns, a 3-dB-AR bandwidth is observed in the frequency range 29-30.1 GHz around the pointing angle $\theta = \pm 20°$.

Chapter 7

Conclusions

This Chapter presents an overall outlook of the thesis. Firstly, a summary and the novel contributions will be outlined. Afterward, a brief discussion about perspectives and possible future developments will be proposed.

7.1 Summary and achievements

This thesis has dealt with the study and the development of novel antenna solutions for the next generation of satellite communications (SatCom). The main focus has been dedicated to a promising antenna architecture, namely the continuous transverse stub (CTS) array. This class of arrays makes use of a quasi-optical beamformer as feeding system, which enables the beam steering with a reduced number of active elements with respect to classical phased arrays. The CTS arrays are also well-known to exhibit wideband operation, large field-of-views, and low-profile. The main drawback of these structures lies in their scarce ability in achieving polarization diversity. In fact, classical CTS arrays are inherently linearly-polarized. To overcome this issue, the concept of dual-mode CTS arrays has been proposed and exhaustively investigated in this manuscript. Firstly, a numerical modeling has been developed and implemented to explore the maximum achievable performances of this class of arrays [refer to Chapter 2]. The model has been validated by a full-wave commercial software [72] and used to retrieve important design guidelines. Afterward, an original feeding system has been engineered to provide the desired mode excitation and a possible design carried out at Ka-band. Up to the date of this manuscript's redaction, the antenna is still under fabrication. The results of this research activity have been the object of a journal paper [J-1], published in

an international magazine, as well as two international conference papers [IC-5, IC-6].

Later on, an exact analytic study has been carried out to survey the antenna's dispersion. The dual-mode CTS arrays, indeed, suffer from two inherent problems: inter-modal dispersion between the transverse electromagnetic (TEM) and first transverse electric (TE_1) modes; the second one is about a strong coupling occurring between the TEM and first transverse magnetic (TM_1) modes. By means of the theoretical study reported in Chapter 3, these issues have been contained and deleted. This work has resulted in an international journal paper [J-2].

In Chapter 4, the physical design of a dual-mode CTS array, attaining dual-linear polarization, is proposed and detailed. The analytic study, outlined in Chapter 3, has turned out to be a fast and accurate method to design longitudinally-corrugated parallel-plate waveguides (PPW). In particular, the antenna module has been deprived of the mutual coupling, occurring between TEM and TM_1 modes by means of guiding structures, engineered *ad-hoc*. The antenna array has been prototyped and tested. The concept of dual-mode CTS arrays and its application, to attain dual-polarized radiation, have been experimentally proved. This work has received the Best Innovation Award at the 39^{th} ESA Antenna Workshop, held in Noordwijk, The Netherlands, in 2018. Furthermore, it has resulted in two international journal papers [J-4, J-5], as well as two conference papers [IC-7, IC-9].

During a six-months project in collaboration with the University of Michigan, a dual-band linear-to-circular polarization (LP-to-CP) converter has been designed. The work, presented in Chapter 5, has concerned the development of an analytic method, based on equivalent circuit models, whose originality and accuracy enable to approach the design without the use of optimization processes. A prototype has been fabricated and measured, showing excellent performances. The polarizer stands out as the state-of-the-art of dual-band LP-to-CP converters, in terms of insertion losses and polarization purity. The work has been published as a journal paper [J-3] in an international magazine. Two more conference papers [IC-1, IC-3] have been published on the same subject to share these achievements with the scientific community.

Finally, a single-mode CTS array has been designed to operate in the unified

K/Ka-band. The antenna is fully built in printed-circuit board (PCB) technology to lower its overall profile. Specifically, 9 PCB panels have been employed to realize the antenna architecture [refer to Chapter 6 for more details]. Such a low-profile is intended to miniaturize the bulkiness, in such a way to enable the integration within a huge variety of moving platforms, e.g., aircrafts, trains, naval vehicles, etc. The antenna efficiently performs a highly-directive multi-beam radiation with a discrete aperture efficiency. The module has also been tested in combination with the dual-band polarizer, presented in Chapter 5. The latter constitutes a compact way to achieve the diversity of the circular polarization over non-adjacent frequency bands. This work has resulted in two conference papers [IC-2, IC-4] and a journal paper is currently in preparation for submission to an international magazine.

7.2 Future perspectives

The aim of this Section pertains to stress out aspects that could be of interest to future related developments.

As it is trivial, the prototype proposed in Chapter 2 has to be tested in the anechoic chamber. The latter would provide a proof-of-concept of the usability of dual-mode CTS arrays as circularly-polarized terminal devices in practical applications. Also, the scanning capabilities of this antenna are drastically reduced by the inter-modal dispersion that occurs between the TEM and TE_1 modes. A possible solution could be, hence, offered by equi-dispersive structures, as argued in Chapter 3. Thus, a physical design must be carried out for these guiding parallel-plate domains. Further analytic studies are also to be performed when the propagation direction of the modes is tilted with respect to the normal wavefront incidence.

The prototype presented in Chapter 4 makes use of two separate pillbox systems for a selected mode operation, respectively. The design of a single and compact pillbox beamformer, performing a dual-linear multi-beam radiation, should be investigated. A possible idea is to engineer a double-parabola system that can deal with the TEM and TE_1 modes separately. This point is the main subject of ongoing research activities at the Institut d'Électronique et Technologies du numéRique (IETR). Furthermore, new technologies must be

investigated to attend a more reliable fabrication process for the dual-mode CTS array. As a matter of example, the laser selective melting technology would be a good candidate for this purpose.

Furthermore, an in-house tool could be developed to efficiently design the corporate feed network (CFN) of the corrugated CTS array. For instance, all the discontinuities, occurring along the CFN, can be analyzed by merging a method of moments (MoM) and a mode-matching technique (MMT) by means of the equivalence theorem. The numerical model would provide a fast and accurate tool to synthesize the CFN of the antenna.

The model employed for the dual-band polarizer in Chapter 5 could be extended to the design of N-band polarization converters. The underlying idea is to model the equivalent circuits with resonators, made of N lumped reactive components. By enforcing the maximum transmission at N different frequencies, a linear system of N unknowns and an equal number of equations can be obtained. Thus, the obtained linear system can be solved analytically and closed-form expressions retrieved for a complete characterization of the circuit models.

Furthermore, the dual-band polarizer could be designed to achieve not only a polarization diversity between the two bands, but also a switching capability of the two orthogonal circular polarization within the same bands. This can be done by inserting active components between adjacent cells of the polarizer's metasurfaces. By focusing on a user-controlled biasing, each cell is theoretically able to switch its reactive behavior, in such a way to enable the desired polarization conversion. This research activity is currently a subject of study at the University of Michigan and relies on an edge-cutting technology, namely time-modulated metasurfaces. Hence, it could represent a possible solution and certainly be a future perspective of research activity in this field-of-study.

The characterization of the self-standing CTS array, proposed in Chapter 6, should be completed in the band 19-26 GHz, as well as its integration with the dual-band polarizing screen. Also, an accurate analytic study might be conducted on the antenna radiation in the near-field zone. This study would enable one to engineer the electrical sheet admittances for achieving a polarization conversion with a single device, placed in the very proximity of the radiating aperture. The latter would enhance the compactness of the overall

structure, as well as its dual-band performance. This study could be also carried out by using circuit models. In fact, the active impedance of the open-ended stubs is accurately predicted by the model in Chapter 2. A study could be pursued, whose aim is to reach out a conjugate matching between the polarizer's equivalent circuits and the CTS array's active impedance to attain agile CP radiation.

Appendix A

Additional Material on Chapter 2

In this Appendix, we present supplemental details about the mathematical derivation of the spectral mode-matching introduced in Chapter 2.1.

A.1 Entries of the matrices in (2.22)

The entries of the block matrices in (2.22) are reported in this Appendix.

- Matrix $\underline{\underline{Y}}^{TE,TE}$:

$$\begin{aligned} Y_{pq}^{TE,TE} = &-\frac{b_q^{TE}}{Y_q^{TE} d} \sum_{n=-N_f}^{N_f} \Lambda_q(k_{xn}) \Lambda_p(-k_{xn}) \tilde{G}_{yy}^{HM}(k_{xn}, k_{y0}) \\ &- \frac{c_q^{TE}}{Y_q^{TE} d} \sum_{n=-N_f}^{N_f} \Gamma_q(k_{xn}) \Lambda_p(-k_{xn}) \tilde{G}_{yx}^{HM}(k_{xn}, k_{y0}) + \frac{a}{\nu_q} b_q^{TE} \delta_{pq} \end{aligned} \tag{A.1}$$

  where $p = \{0, 1, \ldots, M-1\}$ and $q = \{0, 1, \ldots, M-1\}$.

- Matrix $\underline{\underline{Y}}^{TE,TM}$:

$$\begin{aligned} Y_{pq}^{TE,TM} = &\frac{b_q^{TM}}{Y_q^{TM} d} \sum_{n=-N_f}^{N_f} \Lambda_q(k_{xn}) \Lambda_p(-k_{xn}) \tilde{G}_{yy}^{HM}(k_{xn}, k_{y0}) \\ &- \frac{c_q^{TM}}{Y_q^{TM} d} \sum_{n=-N_f}^{N_f} \Gamma_q(k_{xn}) \Lambda_p(-k_{xn}) \tilde{G}_{yx}^{HM}(k_{xn}, k_{y0}) - \frac{a}{2} b_q^{TM} \delta_{pq} \end{aligned} \tag{A.2}$$

  where $p = \{0, 1, \ldots, M-1\}$ and $q = \{1, \ldots, M-1\}$.

- Matrix $\underline{\underline{Y}}^{TM,TE}$:

$$\begin{aligned} Y_{pq}^{TM,TE} = &-\frac{c_q^{TE}}{Y_q^{TE} d} \sum_{n=-N_f}^{N_f} \Gamma_q(k_{xn}) \Gamma_p(-k_{xn}) \tilde{G}_{xx}^{HM}(k_{xn}, k_{y0}) \\ &- \frac{b_q^{TE}}{Y_q^{TE} d} \sum_{n=-N_f}^{N_f} \Lambda_q(k_{xn}) \Gamma_p(-k_{xn}) \tilde{G}_{xy}^{HM}(k_{xn}, k_{y0}) + \frac{a}{2} c_q^{TE} \delta_{pq} \end{aligned} \tag{A.3}$$

  where $p = \{1, \ldots, M-1\}$ and $q = \{0, 1, \ldots, M-1\}$.

- Matrix $\underline{\underline{Y}}^{TM,TM}$:

$$\begin{aligned} Y_{pq}^{TM,TM} = &\frac{b_q^{TM}}{Y_q^{TM} d} \sum_{n=-N_f}^{N_f} \Lambda_q(k_{xn}) \Gamma_p(-k_{xn}) \tilde{G}_{xy}^{HM}(k_{xn}, k_{y0}) \\ &+ \frac{c_q^{TM}}{Y_q^{TM} d} \sum_{n=-N_f}^{N_f} \Gamma_q(k_{xn}) \Gamma_p(-k_{xn}) \tilde{G}_{xx}^{HM}(k_{xn}, k_{y0}) - \frac{a}{2} c_p^{TM} \delta_{pq} \end{aligned} \tag{A.4}$$

  where $p = \{1, \ldots, M-1\}$ and $q = \{1, \ldots, M-1\}$.

A.2 Spectral Green's function of multi-layer medium

In this Section, we will provide further details about the mathematical derivation of the Green's function (GF) in presence of plane-stratified media used in Sections 2.1 and 2.3. The proposed formalism follows that described in [38, 70, 146].

A.2.1 Vector potentials for electric and magnetic sources

The electromagnetic field can be written in terms of auxiliary vector potentials $\mathbf{A}$ and $\mathbf{F}$ related to the electric ($\mathbf{J}$) and magnetic ($\mathbf{M}$) current sources, respectively. Their mathematical relation is expressed as follows [24]

$$\begin{aligned} \mathbf{E} &= -ik\eta \left(\mathbf{A} + \frac{1}{k^2} \nabla (\nabla \cdot \mathbf{A}) \right) - \nabla \times \mathbf{F} \\ \mathbf{H} &= -i\frac{k}{\eta} \left(\mathbf{F} + \frac{1}{k^2} \nabla (\nabla \cdot \mathbf{F}) \right) - \nabla \times \mathbf{A} \end{aligned} \tag{A.5}$$

where $k = \omega\sqrt{\epsilon\mu}$, $\eta = \sqrt{\mu/\epsilon}$ and ω is the angular frequency. The auxiliary vector potentials $\mathbf{A}$ and $\mathbf{F}$ satisfy the following condition

$$\begin{aligned} \nabla^2\mathbf{A} + k^2\mathbf{A} &= -\mathbf{J} \\ \nabla^2\mathbf{F} + k^2\mathbf{F} &= -\mathbf{M} \end{aligned} \tag{A.6}$$

Assuming a cylindrical symmetry, a convenient choice for the vector potentials $\mathbf{A}$ and $\mathbf{F}$ is given by

$$\begin{aligned} \mathbf{A} &= A_z\hat{z} \\ \mathbf{F} &= F_z\hat{z} \end{aligned} \tag{A.7}$$

By inserting (A.7) into (A.5), the electromagnetic field can be arranged in the following form

$$\begin{aligned} \mathbf{E} &= \mathbf{E_{TM}} + \mathbf{E_{TE}} \\ \mathbf{H} &= \mathbf{H_{TM}} + \mathbf{H_{TE}} \end{aligned} \tag{A.8}$$

where

$$\begin{aligned} \mathbf{E_{TM}} &= -ik\eta\left[\left(1 + \frac{1}{k^2}\frac{\partial^2}{\partial z^2}\right)A_z\hat{z} + \frac{1}{k^2}\nabla_t\left(\frac{\partial A_z}{\partial z}\right)\right] \\ \mathbf{E_{TE}} &= -\nabla_t \times F_z\hat{z} \\ \mathbf{H_{TM}} &= \nabla_t \times A_z\hat{z} \\ \mathbf{H_{TE}} &= -i\frac{k}{\eta}\left[\left(1 + \frac{1}{k^2}\frac{\partial^2}{\partial z^2}\right)F_z\hat{z} + \frac{1}{k^2}\nabla_t\left(\frac{\partial F_z}{\partial z}\right)\right] \end{aligned} \tag{A.9}$$

The boundary conditions (BC) to be satisfied by the equations (A.9) depend on the problem. In case of multi-layer media, we will enforce the continuity of tangential fields at discontinuities. Further details to obtain equations (A.9) can be found in [38].

A.2.2 Equivalence with transmission line theory

The calculation of the GF of a plane-stratified medium is eased using the equivalence with transmission line (TL) theory [70]. To this aim, it is convenient to refer to the unknown potentials in the Fourier domain, as follows

$$\begin{aligned} I_{TM}(k_x, k_y, z) &= \mathfrak{F}^{-1}\left\{A_z(x, y, z)\right\} \\ V_{TE}(k_x, k_y, z) &= \mathfrak{F}^{-1}\left\{F_z(x, y, z)\right\} \end{aligned} \tag{A.10}$$

where $\mathfrak{F}^{-1}\{\cdot\}$ stands for the 2-D inverse Fourier's transform and is defined as

$$g(x,y,z) = \mathfrak{F}^{-1}\{f(k_x,k_y,z)\} = \frac{1}{4\pi^2}\iint_{\mathbb{R}^2} f(k_x,k_y,z)e^{-i\mathbf{k}_\rho\cdot\boldsymbol{\rho}}dk_x dk_y \tag{A.11}$$

where $\mathbf{k}_\rho = k_x\hat{x} + k_y\hat{y}$ and $\boldsymbol{\rho} = x\hat{x} + y\hat{y}$. For the sake of completeness, we define also the 2-D Fourier's transform $\mathfrak{F}\{\cdot\}$ as follows

$$f(k_x,k_y,z) = \mathfrak{F}\{g(x,y,z)\} = \iint_{\mathbb{R}^2} g(x,y,z)e^{i\mathbf{k}_\rho\cdot\boldsymbol{\rho}}dxdy \tag{A.12}$$

After some algebraic manipulations, the 2-D Fourier's transform of (A.8) can be arranged in the form [38]

$$\begin{aligned}\tilde{\mathbf{E}} &= \mathfrak{F}\{\mathbf{E}\} = \tilde{\mathbf{E}}_{\mathbf{TM}} + \tilde{\mathbf{E}}_{\mathbf{TE}}\\ \tilde{\mathbf{H}} &= \mathfrak{F}\{\mathbf{H}\} = \tilde{\mathbf{H}}_{\mathbf{TM}} + \tilde{\mathbf{H}}_{\mathbf{TE}}\end{aligned} \tag{A.13}$$

where

$$\begin{aligned}\tilde{\mathbf{E}}_{\mathbf{TM}} &= i|\mathbf{k}_\rho|V_{TM}\hat{\mathbf{k}}_\rho - i\eta\frac{|\mathbf{k}_\rho|^2}{k}I_{TM}\hat{z}\\ \tilde{\mathbf{E}}_{\mathbf{TE}} &= -i|\mathbf{k}_\rho|V_{TE}\hat{\boldsymbol{\alpha}}\\ \tilde{\mathbf{H}}_{\mathbf{TM}} &= i|\mathbf{k}_\rho|I_{TM}\hat{\boldsymbol{\alpha}}\\ \tilde{\mathbf{H}}_{\mathbf{TE}} &= i|\mathbf{k}_\rho|I_{TE}\hat{\mathbf{k}}_\rho - i\frac{|\mathbf{k}_\rho|^2}{k\eta}V_{TE}\hat{z}\end{aligned} \tag{A.14}$$

where

$$\begin{aligned}\hat{\mathbf{k}}_\rho &= \frac{\mathbf{k}_\rho}{|\mathbf{k}_\rho|}\\ \hat{\boldsymbol{\alpha}} &= \hat{z}\times\hat{\mathbf{k}}_\rho\\ V_{TM} &= \eta\frac{k_z}{k}I_{TM}\\ I_{TE} &= \frac{k_z}{k\eta}V_{TE}\\ k_z &= \sqrt{k^2 - |\mathbf{k}_\rho|^2}\end{aligned} \tag{A.15}$$

A.2.3 Spectral Green's function for magnetic source

Here, we provide the extended mathematical expressions of the dyadic spectral GFs in the spectral domain, $\underline{\underline{\tilde{G}}}^{HM}$ and $\underline{\underline{\tilde{G}}}^{EM}$, used in the Sections 2.1 and 2.3, respectively. The geometry shown in Fig. 2.1 exhibits a discontinuity at $z = 0$. The spectral GFs can be thus calculated by enforcing the continuity of the electric and magnetic fields at $z = 0$. A magnetic current $\mathbf{M_t}(x,y)$ is

considered at the discontinuity, resulting from the field distribution provided by the feeding PPWs:

$$\mathbf{M_t}(x,y) = \boldsymbol{m}(x,y)\delta(x,y) \tag{A.16}$$

where $\boldsymbol{m}(x,y) = M_x(x,y)\hat{x} + M_y(x,y)\hat{y}$. The condition of continuity for the fields is given by [24]

$$\begin{aligned} \hat{z} \times \big(\mathbf{H}(x,y,0^+) - \mathbf{H}(x,y,0^-)\big) &= 0 \\ \hat{z} \times \big(\mathbf{E}(x,y,0^+) - \mathbf{E}(x,y,0^-)\big) &= -\boldsymbol{m}(x,y)\delta(x,y) \end{aligned} \tag{A.17}$$

In the spectral domain equation (A.17) can be written as [38]

$$\begin{aligned} \hat{z} \times \Big(\tilde{\mathbf{E}}_{\mathbf{TE}}(k_x,k_y,0^+) - \tilde{\mathbf{E}}_{\mathbf{TE}}(k_x,k_y,0^-)\Big) \cdot \hat{\mathbf{k}}_\rho &= -\boldsymbol{m} \cdot \hat{\mathbf{k}}_\rho \\ \hat{z} \times \Big(\tilde{\mathbf{E}}_{\mathbf{TM}}(k_x,k_y,0^+) - \tilde{\mathbf{E}}_{\mathbf{TM}}(k_x,k_y,0^-)\Big) \cdot \hat{\boldsymbol{\alpha}} &= -\boldsymbol{m} \cdot \hat{\boldsymbol{\alpha}} \end{aligned} \tag{A.18}$$

By substituting (A.14) into (A.18), it emerges that a discontinuity is present at $z = 0$ and can be modeled as a generator placed in series to TLs [38]. In formulae:

$$\begin{aligned} V_{TE}^{z=0} &= -\frac{\boldsymbol{m} \cdot \hat{\mathbf{k}}_\rho}{i|\mathbf{k}_\rho|} \\ V_{TM}^{z=0} &= -\frac{\boldsymbol{m} \cdot \hat{\boldsymbol{\alpha}}}{i|\mathbf{k}_\rho|} \end{aligned} \tag{A.19}$$

To take into account the generator placed at the discontinuity, the equivalent voltages and currents can be obtained downstream from a normalization to $V_{TE}^{z=0}$ and $V_{TM}^{z=0}$, as follows

$$\begin{aligned} v_{TM} &= V_{TM}/V_{TM}^{z=0} \\ v_{TE} &= V_{TM}/V_{TE}^{z=0} \\ i_{TM} &= I_{TM}/V_{TM}^{z=0} \\ i_{TE} &= i_{TE}/V_{TE}^{z=0} \end{aligned} \tag{A.20}$$

A circuital schematic of the TL problem is shown in Fig. A.1. Note that the voltage amplitude of the series generator is unitary. The wave impedance Z_0^{TM} and Z_0^{TE} are given by

$$\begin{aligned} Z_0^{TM} &= \eta\frac{k_z}{k} \\ Z_0^{TE} &= \eta\frac{k}{k_z} \end{aligned} \tag{A.21}$$

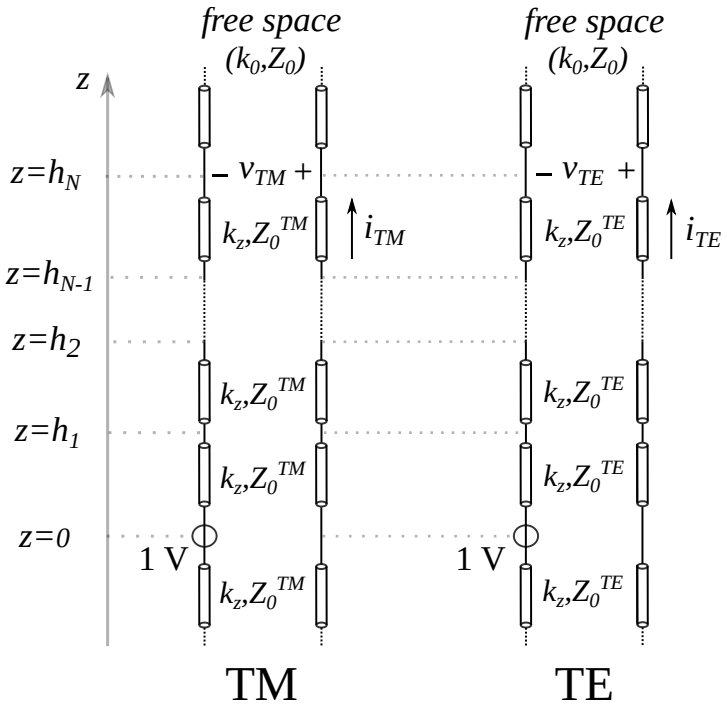

FIGURE A.1: Equivalent transmission line problem to obtain the normalized voltages (i.e., v_{TM} and v_{TE}) and currents (i.e., i_{TM} and i_{TE}). The unitary voltage generator is placed at the discontinuity $z = 0$. The height of each dielectric layer is indicated with h_n where $n \in \mathbb{N}^+$.

Finally, the extended form of the dyadic GFs in the spectral domain, $\underline{\underline{\tilde{G}}}^{HM}$ and $\underline{\underline{\tilde{G}}}^{EM}$, can be found by substituting (A.20) into (A.14), yielding

$$\begin{aligned}
\underline{\underline{\tilde{G}}}^{HM} &= \begin{bmatrix} \tilde{G}^{HM}_{xx} & \tilde{G}^{HM}_{xy} & \tilde{G}^{HM}_{xz} \\ \tilde{G}^{HM}_{yx} & \tilde{G}^{HM}_{yy} & \tilde{G}^{HM}_{yz} \\ \tilde{G}^{HM}_{zx} & \tilde{G}^{HM}_{zy} & \tilde{G}^{HM}_{zz} \end{bmatrix} = \begin{bmatrix} -\frac{i_{TE}k_x^2 + i_{TM}k_y^2}{|\mathbf{k}_\rho|^2} & \frac{(i_{TM}-i_{TE})k_xk_y}{|\mathbf{k}_\rho|^2} & 0 \\ \frac{(i_{TM}-i_{TE})k_xk_y}{|\mathbf{k}_\rho|^2} & -\frac{i_{TM}k_x^2 + i_{TE}k_y^2}{|\mathbf{k}_\rho|^2} & 0 \\ \frac{k_x}{\eta k} v_{TE} & \frac{k_y}{\eta k} v_{TE} & 0 \end{bmatrix} \\
\underline{\underline{\tilde{G}}}^{EM} &= \begin{bmatrix} \tilde{G}^{EM}_{xx} & \tilde{G}^{EM}_{xy} & \tilde{G}^{EM}_{xz} \\ \tilde{G}^{EM}_{yx} & \tilde{G}^{EM}_{yy} & \tilde{G}^{EM}_{yz} \\ \tilde{G}^{EM}_{zx} & \tilde{G}^{EM}_{zy} & \tilde{G}^{EM}_{zz} \end{bmatrix} = \begin{bmatrix} \frac{(v_{TM}-v_{TE})k_xk_y}{|\mathbf{k}_\rho|^2} & -\frac{v_{TM}k_x^2 + v_{TE}k_y^2}{|\mathbf{k}_\rho|^2} & 0 \\ \frac{v_{TE}k_x^2 + v_{TM}k_y^2}{|\mathbf{k}_\rho|^2} & -\frac{(v_{TM}-v_{TE})k_xk_y}{|\mathbf{k}_\rho|^2} & 0 \\ -\eta\frac{k_y}{k} i_{TM} & \eta\frac{k_x}{k} i_{TM} & 0 \end{bmatrix}
\end{aligned} \tag{A.22}$$

Appendix B

Complements on the study outlined in Chapter 3

This appendix includes additional details on the modal analysis of equi-dispersive (ED) dual-mode parallel-plate waveguides (PPW). Firstly, an exhaustive derivation of the characteristic equations (CE) for TE (i.e., (3.8)) and TM (i.e., (3.14)) modes is outlined. Afterward, a rigorous mathematical demonstration is provided to highlight the main properties of eigenvalue problems that respond to impedance boundary conditions (IBC) enforced on the contour of the domain under analysis. In particular, we will focus on eigenvalue problems associated with the Helmholtz operator.

B.1 Characteristic equation of TE modes

In a compact form, the CE for TE modes can be written as (3.8). The analytic derivation of (3.8) is here reported and discussed. Waveguide TE modes can be derived by solving the Helmholtz equation (3.1). The boundary conditions enforced on the waveguide contour are given by the extended formulation (3.7). The field components can be written as a function of the arbitrary potential ϕ_m^{TE} as given by (3.5). Considering that TE modes in a parallel plate domain take the form as (3.6), the E-field can be written as follows [56]:

$$\begin{aligned} E_x^{TE} &= 0 \\ E_y^{TE} &= \sum_m V_m^{TE} e_{ym}^{TE} \\ E_z^{TE} &= 0 \end{aligned} \tag{B.1}$$

where V_m^{TE} are the modal voltages and e_{ym}^{TE} is the modal vector of TE modes and can be expressed as a function of the scalar potential ϕ_m^{TE} using (2.4). Also, m is an integer number. On the other hand, the H-field is given by

$$\begin{aligned} H_x^{TE} &= \sum_m I_m^{TE} h_{xm}^{TE} \\ H_y^{TE} &= 0 \\ H_z^{TE} &= \sum_m V_m^{TE} \frac{(k_{xm}^{TE})^2}{i\omega\mu_0\mu_r} \phi_m^{TE} \end{aligned} \tag{B.2}$$

where $h_{xm}^{TE} = -e_{ym}^{TE}$. In the following, we will not use the subscript m to streamline the mathematical treatment. In light of expressions (B.1) and (B.2), the IBCs (3.7) can be written as

$$\begin{aligned} Z_{surf}^{TE} &= -\frac{i\omega\mu_0\mu_r}{(k_x^{TE})^2} \frac{\left(\nabla_t \phi^{TE} \times \hat{z}\right) \cdot \hat{y}}{\phi^{TE}} \Big|_{x=+h/2} \\ Z_{surf}^{TE} &= +\frac{i\omega\mu_0\mu_r}{(k_x^{TE})^2} \frac{\left(\nabla_t \phi^{TE} \times \hat{z}\right) \cdot \hat{y}}{\phi^{TE}} \Big|_{x=-h/2} \end{aligned} \tag{B.3}$$

where

$$\nabla_t \phi^{TE} \times \hat{z} = -\partial_x \phi^{TE} \hat{y} = i k_x^{TE} A^{TE} \left[\xi^{TE+} - B^{TE} \xi^{TE-}\right] \hat{y} \tag{B.4}$$

and $\xi^{TE\pm} = e^{\pm i k_x^{TE}(x+h/2)}$. By inserting (3.5) and (B.4) into (B.3) and after some algebraic manipulations, the surface impedance for TE modes Z_{surf}^{TE} can be written as

$$Z_{surf}^{TE} = -\frac{\omega\mu_0\mu_r}{k_x^{TE}} \frac{e^{ik_x^{TE}h} - B^{TE} e^{-ik_x^{TE}h}}{e^{ik_x^{TE}h} + B^{TE} e^{-ik_x^{TE}h}} \tag{B.5}$$

$$Z_{surf}^{TE} = +\frac{\omega\mu_0\mu_r}{k_x^{TE}} \frac{1 - B^{TE}}{1 + B^{TE}} \tag{B.6}$$

By equaling (B.5) and (B.6), we obtain

$$\frac{1 - B^{TE}}{1 + B^{TE}} = -\frac{e^{ik_x^{TE}h} - B^{TE} e^{-ik_x^{TE}h}}{e^{ik_x^{TE}h} + B^{TE} e^{-ik_x^{TE}h}} \tag{B.7}$$

that can be solved for B^{TE}, thus yielding to the two-form expression

$$B^{TE\pm} = \pm e^{ik_x^{TE\pm}h} \tag{B.8}$$

Finally, (3.8) is obtained by substituting (B.8) into (B.6).

B.2 Characteristic equation of TM modes

The analytic derivation of the CE of TM modes follows the same procedure used for TE modes. The E-field for TM modes is given by (3.12) and takes the following form

$$\begin{aligned} E_x^{TM} &= \sum_m V_m^{TM} e_{xm}^{TM} \\ E_y^{TM} &= 0 \\ E_z^{TM} &= \sum_m I_m^{TM} \frac{(k_{xm}^{TM})^2}{i\omega\epsilon_0\epsilon_r} \phi_m^{TM} \end{aligned} \tag{B.9}$$

where V_m^{TM} and I_m^{TM} are the modal voltages and currents, respectively. Moreover, the H-field is given by

$$\begin{aligned} H_x^{TM} &= 0 \\ H_y^{TM} &= \sum_m I_m^{TM} h_{ym}^{TM} \\ H_z^{TM} &= 0 \end{aligned} \tag{B.10}$$

where $h_{ym}^{TM} = e_{xm}^{TM} = -\nabla_t \phi_m^{TM} \cdot \hat{x}$. As done for TE modes, let us avoid using the subscript m to ease the reading. By inserting (B.9) and (B.10) into (3.13), the IBCs for TM modes are written in terms of the scalar potential ϕ^{TM}. For each mode, it follows:

$$\begin{aligned} Z_{surf}^{TM} &= +\frac{(k_x^{TM})^2}{i\omega\epsilon_0\epsilon_r} \frac{\phi^{TM}}{\nabla_t \phi^{TM} \cdot \hat{x}} \Bigg|_{x=+h/2} \\ Z_{surf}^{TM} &= -\frac{(k_x^{TM})^2}{i\omega\epsilon_0\epsilon_r} \frac{\phi^{TM}}{\nabla_t \phi^{TM} \cdot \hat{x}} \Bigg|_{x=-h/2} \end{aligned} \tag{B.11}$$

where ϕ^{TM} is given by (3.11) and

$$\nabla_t \phi^{TE} = -ik_x^{TM} A^{TM} \left[\xi^{TM+} - B^{TM} \xi^{TM-} \right] \hat{x} \tag{B.12}$$

with $\xi^{TM\pm} = e^{\pm ik_x^{TM}(x+h/2)}$. The IBCs can be simplified by inserting (3.11) and (B.12) into (B.11), yielding

$$Z_{surf}^{TM} = -\frac{k_x^{TM}}{\omega\epsilon_0\epsilon_r} \frac{e^{ik_x^{TM}h} + B^{TM} e^{-ik_x^{TM}h}}{e^{ik_x^{TM}h} - B^{TM} e^{-ik_x^{TM}h}} \tag{B.13}$$

$$Z_{surf}^{TM} = +\frac{k_x^{TM}}{\omega\epsilon_0\epsilon_r}\frac{1+B^{TM}}{1-B^{TM}} \tag{B.14}$$

By equaling (B.13) to (B.14), the obtained equation is solved for B^{TM}, yielding

$$B^{TM\pm} = \pm e^{ik_x^{TM\pm}h} \tag{B.15}$$

The CE in (3.14) is, thus, obtained by substituting (B.15) into (B.14).

B.3 Properties of Helmholtz operator with IBCs

The aim of this section is to investigate the properties of the eigenvalues associated with the Helmholtz operator when enforcing IBCs. In this scenario, we will focus on demonstrating that the Helmholtz operator is no longer Hermitian (or self-adjoint), thus some associated eigenvalues might be purely imaginary. Specifically, the modes supported by a waveguide with IBCs can be classified into two categories: standard guided modes (purely real eigenvalues) and surface-wave modes (purely imaginary eigenvalues) [147–149]. The latter are confined around the waveguide walls and exhibit an exponential decay. Deepening the study of these modes is crucial, as they may be supported by the structure studied in Chapter 3. For instance, inductive surface impedances for TM modes, as well as capacitive ones for TE modes, can trigger the propagation of surface-wave modes.

To demonstrate that surface-wave modes can be supported, we have to rely on *Lemma 1*, which states that real eigenvalues are supported by a generic Hermitian (or self-adjoint) operator. Its mathematical demonstration is reported in the following.

Lemma 1 *Hermitian operators have only real eigenvalues. The null eigenvalue can exist too.*

Proof 1 *Let us consider functions that belong to the functional space $L^2\{\cdot\}$, associated with the field of complex numbers $\mathbb{C}$. Those functions are thus square summable. The functional space $L^2\{\cdot\}$ is a Hilbert space, i.e., a complete metric space. It also possesses an inner real/complete product, defined as follows*

$$\langle f, g\rangle_\Omega = \iint_\Omega f g^* d\Omega \tag{B.16}$$

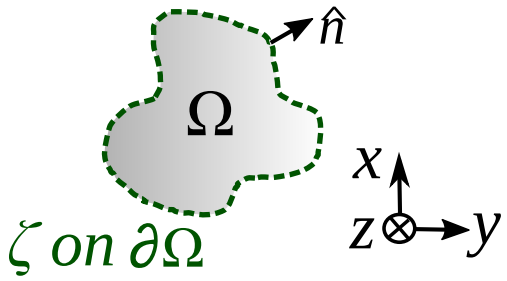

FIGURE B.1: Generic waveguide cross-section. The waveguide contour is $\partial\Omega$. The structure has a cylindrical symmetry, i.e., the waveguide cross-section Ω is invariant along z-axis. Finally, $\hat{n}$ is the unitary vector normal to $\partial\Omega$, outwardly directed with respect to Ω.

where $f, g \in L^2\{\Omega\}$ *and the superscript* * *denotes the complex conjugate of a function. Moreover,* Ω *is the cross-section of a generic waveguide, as shown in Fig. B.1. The structure exhibits a cylindrical symmetry, i.e., the waveguide contour* $\partial\Omega$ *is invariant along* z*-axis.*
A generic operator $\mathfrak{L}\{\cdot\}$ *is Hermitian (self-adjoint) if*

$$\langle \mathfrak{L}\{f\}, g\rangle_\Omega = \langle f, \mathfrak{L}^\dagger\{g\}\rangle_\Omega \in \mathbb{R} \tag{B.17}$$

where the superscript $\dagger$ *denotes the adjoint of an operator. Let us consider now the following eigenvalue problem*

$$\mathfrak{L}\{\phi\} = \lambda^2\phi \tag{B.18}$$

where $\phi \in L^2\{\Omega\}$ *and* λ *are the eigenvalues of the operator* $\mathfrak{L}\{\cdot\}$*. Taking the inner product of (B.18) with* ϕ*, it follows*

$$\langle \mathfrak{L}\{\phi\}, \phi\rangle_\Omega = \lambda^2\langle \phi, \phi\rangle_\Omega \tag{B.19}$$

that can be re-written as

$$\lambda^2 = \frac{\langle \mathfrak{L}\{\phi\}, \phi\rangle_\Omega}{\langle \phi, \phi\rangle_\Omega} = \frac{\langle \mathfrak{L}\{\phi\}, \phi\rangle_\Omega}{\|\phi\|^2} = \underbrace{\frac{\langle \phi, \mathfrak{L}^\dagger\{\phi\}\rangle_\Omega}{\|\phi\|^2}}_{\mathfrak{L}\{\cdot\}\ is\ self-adjoint} \tag{B.20}$$

where $\|\cdot\|$ *denotes the* L^2*-norm. Equation (B.20) shows that the square of the eigenvalues* λ *are real because the denominator is the square of a norm and the nominator presents a quantity that equals its adjoint, thus it is real [refer to*

(B.17)]. It follows that $\lambda \in \mathbb{R}$ since the square root of a real number remains a real number. Note that if the operator $\mathfrak{L}\{\cdot\}$ is positive definite, its eigenvalues are real and positive. The null eigenvalue can also exist and it corresponds to the condition $\langle \phi, \mathfrak{L}^{\dagger}\{\phi\}\rangle_{\Omega} = 0$.

Being proved the *Lemma* 1, we can focus on eigenvalue problems associated to Helmholtz operator. Let us consider the following eigenvalue problem fulfilling the below-reported IBCs

$$\begin{cases} \mathcal{H}\{\phi\} = 0 \quad on \;\; \Omega \\ BC\{\phi\} = 0 \quad on \;\; \partial\Omega \end{cases} \tag{B.21}$$

where

$$\mathcal{H}\{\cdot\} = \nabla_t^2 - \lambda^2 \tag{B.22}$$

with $\nabla_t = \partial_x \hat{x} + \partial_y \hat{y}$ and λ being the associated eigenvalues. Moreover:

$$BC\{\cdot\} = \nabla_t \cdot \hat{n} - \zeta = \frac{\partial}{\partial n} - \zeta \tag{B.23}$$

that denotes the IBCs enforced on the waveguide contour $\partial\Omega$. The surface impedance/admittance is indicated by ζ. Also, ϕ stands for the eigenvectors of the problem. Finally, we can define the adjoint problem to (B.21), as follows

$$\begin{cases} \mathcal{H}^{\dagger}\{\psi\} = 0 \quad on \;\; \Omega \\ BC^{\dagger}\{\psi\} = 0 \quad on \;\; \partial\Omega \end{cases} \tag{B.24}$$

where

$$\begin{aligned} \mathcal{H}^{\dagger}\{\cdot\} &= \nabla_t^2 - \left(\lambda^2\right)^* \\ BC^{\dagger}\{\cdot\} &= \frac{\partial}{\partial n} - \zeta^* \end{aligned} \tag{B.25}$$

and ψ denotes the eigenvectors associated to the adjoint problem.

To demonstrate that the Helmholtz operator is no longer Hermitian while enforcing IBCs, we need to introduce the Green's second identity. Given the functions $f, g \in L^2\{\Omega\}$, it follows

$$\iint_{\Omega} \left(f\nabla_t^2 g - g\nabla_t^2 f\right) d\Omega = \oint_{\partial\Omega} \left(f\frac{\partial g}{\partial n} - g\frac{\partial f}{\partial n}\right) dS \tag{B.26}$$

By substituting $f = \psi$ and $g = \phi$, the Green's second identity can be re-written as follows

$$\iint_{\Omega} \psi \nabla_t^2 \phi \, d\Omega = \iint_{\Omega} \phi \nabla_t^2 \psi \, d\Omega + \oint_{\partial\Omega} \left(\psi \frac{\partial \phi}{\partial n} - \phi \frac{\partial \psi}{\partial n} \right) dS \tag{B.27}$$

Let us now add the quantity $-\iint_{\Omega} \psi \lambda^2 \phi \, d\Omega$ to the right and the left hand sides of (B.27). It follows

$$\iint_{\Omega} \underbrace{\left(\psi \nabla_t^2 \phi - \psi \lambda^2 \phi \right)}_{=\psi \mathcal{H}\{\phi\}} d\Omega = \iint_{\Omega} \underbrace{\left(\phi \nabla_t^2 \psi - \psi \lambda^2 \phi \right)}_{=\phi \mathcal{H}\{\psi\} = \phi \left(\mathcal{H}^{\dagger}\{\psi^*\} \right)^*} d\Omega + \oint_{\partial\Omega} \left(\psi \frac{\partial \phi}{\partial n} - \phi \frac{\partial \psi}{\partial n} \right) dS \tag{B.28}$$

Let us focus on the closed-line integral in (B.28). The boundary condition of the problem (B.21) can be re-written as $\partial_n \phi|_{\partial\Omega} = \zeta \phi|_{\partial\Omega}$. By using some algebraic manipulations, the closed-line integral in (B.28) can be arranged in the following form

$$\begin{aligned} \oint_{\partial\Omega} \left(\psi \frac{\partial \phi}{\partial n} - \phi \frac{\partial \psi}{\partial n} \right) dS = - \oint_{\partial\Omega} & \underbrace{\left(\phi \frac{\partial \psi}{\partial n} - \psi \frac{\partial \phi}{\partial n} \right)}_{= \phi \frac{\partial \psi}{\partial n} - \psi \zeta \phi = \phi \left(\partial_n - \zeta \right) \psi = \\ & = \phi BC\{\psi\}} dS = \\ = - \oint_{\partial\Omega} \phi BC\{\psi\} dS & \end{aligned} \tag{B.29}$$

By substituting (B.29) into (B.28), we obtain

$$\underbrace{\iint_{\Omega} \psi \mathcal{H}\{\phi\} \, d\Omega}_{=\langle \mathcal{H}\{\phi\}, \psi^* \rangle_{\Omega}} = \underbrace{\iint_{\Omega} \phi \left(\mathcal{H}^{\dagger}\{\psi^*\} \right)^* d\Omega}_{=\langle \phi, \mathcal{H}^{\dagger}\{\psi^*\} \rangle_{\Omega}} - \oint_{\partial\Omega} \phi BC\{\psi\} dS \tag{B.30}$$

that can be written in a more compact form as follows

$$\langle \mathcal{H}\{\phi\}, \psi^* \rangle_{\Omega} = \langle \phi, \mathcal{H}^{\dagger}\{\psi^*\} \rangle_{\Omega} - \oint_{\partial\Omega} \phi BC\{\psi\} dS \tag{B.31}$$

Equation (B.31) shows that, if the close-line integral on the right hand side is null, the Helmholtz operator is then Hermitian [see (B.17)]. In this scenario, the eigenvalues λ associated to the problem (B.21) will be real as demonstrated

by the *Lemma* 1. From the IBCs of the adjoint problem (B.24), we know

$$BC^{\dagger}\{\psi\} = \left(\frac{\partial}{\partial n} - \zeta^{*}\right)\psi = 0 \quad on\ \partial\Omega \tag{B.32}$$

On the other hand, the argument of the closed-line integral in (B.31) can be written as

$$BC\{\psi\} = \left(\frac{\partial}{\partial n} - \zeta\right)\psi \quad on\ \partial\Omega \tag{B.33}$$

Using (B.32), it is straightforward to see that (B.33) is null if and only if $\zeta = \zeta^{*}$, i.e., $\zeta \in \mathbb{R}$. In this scenario, the closed-line integral in (B.31) will be null and the Helmholtz operator will be Hermitian (self-adjoint). We can thus state:

"*Given a Helmholtz eigenvalue problem fulfilling IBCs, the associated eigenvalues are real if and only if the impedance enforced on the contour is a finite real number (Ohmic losses) or null/infinite (perfect electric/magnetic conductor). For more general problems, if the IBCs are complex, the eigenvalues may be complex too. In both cases, the eigenvalues are infinitely countable, as the domain is closed.*"

B.3.1 Surface-wave modes in PPWs with IBCs

In this Section, we propose a representative example of PPWs with IBCs that supports surface-wave modes. The IBCs are engineered such that purely imaginary eigenvalues $k_x^{TE/TM}$ appear. Specifically, inductive surface impedance is considered for TM modes and capacitive for TE ones.

TM modes

For TM modes, the PPW having impedance walls exhibits surface-wave modes when the surface impedance is inductive. Considering a PPW of height $h = \lambda_{min}/2$ (λ_{min} is the wavelength associated to the highest frequency $f_{max} = 40$ GHz) and a surface impedance $Z_{surf}^{TM} = i\frac{2}{3}\eta_0$, the characteristic impedance (3.14) is plotted in Fig. B.2 at the highest frequency f_{max}. As shown in Fig. B.2, two poles are present in the visible range. They are associated with modal branches, whose behavior resembles hyperbolic trigonometric non-basic functions (dashed lines in Fig. B.2). On the other hand, standard waveguide modes (solid lines in Fig. B.2) are present as well and their behavior is periodic, e.g., trigonometric

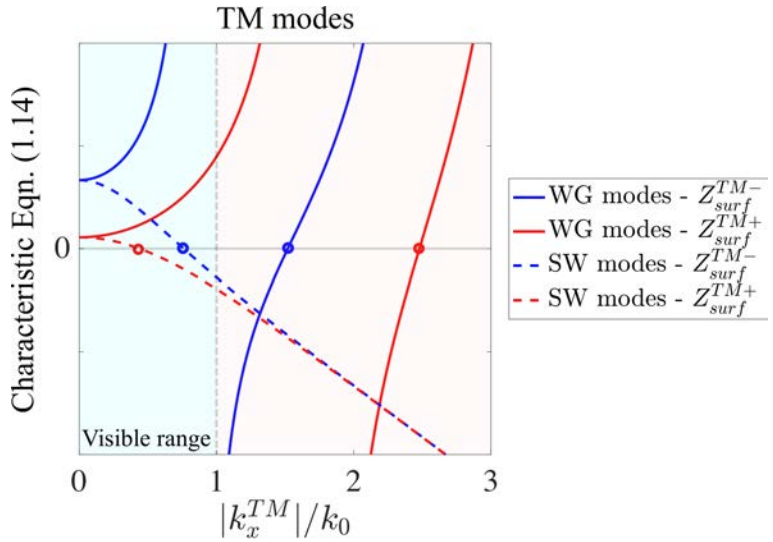

FIGURE B.2: Impedance loci of TM modes when the PPW's height is $h = \lambda_{min}/2$, where λ_{min} is the wavelength at the highest frequency. The characteristic equations are plotted at the maximum frequency of $f_{max} = 40$ GHz. The PPW is air-filled (i.e., $\epsilon_r = \mu_r = 1$). The dot markers indicate the calculated eigenvalues using [87].

non-basic functions. For the sake of completeness, we can see that the poles in the visible range are purely imaginary. To this purpose, Fig. B.3 plots in dB the characteristic equation (3.14). The eigenvalues are then illustrated as blue

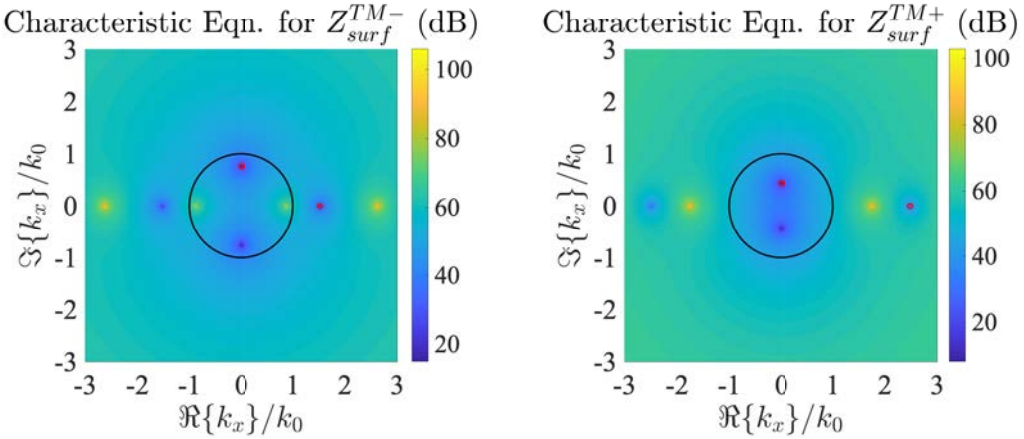

FIGURE B.3: Characteristic equation for TM modes at the frequency f_{max}. The plot is shown in dB, thus the poles are illustrated with dark blue spots. The black circle indicates the visible range ($|k_x| = k$) and red dot markers represent the calculated poles using [87]. The PPW is air-filled and its height is $h = \lambda_{min}/2$.

spots. It is worth noticing that two eigenvalues appear [see Fig. B.3(a) and (b)]

in the visible range (black circle in Fig. B.3) and they are purely imaginary (i.e., $k_x^{TM\pm} = i\Im\{k_x^{TM\pm}\}$). Since it is been demonstrated that surface-wave modes can be supported by these structures, the surface impedance for TM modes must be capacitive in order to have the desired purely ortho-guided-mode propagation.

TE modes

Following the procedure shown for TM modes, it can be shown that PPWs with IBCs may support surface-wave TE modes as well. In this case, the surface impedance must be capacitive. For instance, the characteristic equation (3.8) is plotted in Fig. B.4 at the highest frequency $f_{max} = 40$ GHz, when the $Z_{surf}^{TE} = -i\frac{3}{2}\eta_0$. The PPW's height is $h = \lambda_{min}/2$. As for TM modes, purely

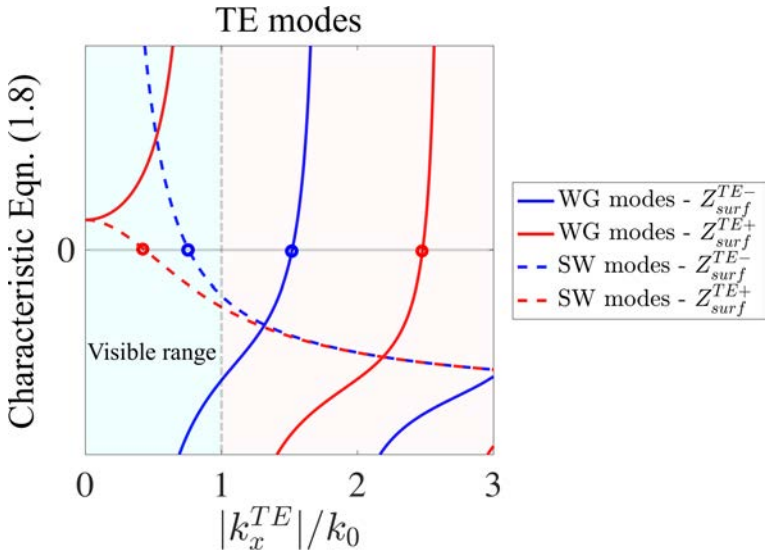

FIGURE B.4: Impedance loci of TE modes when the PPW's height is $h = \lambda_{min}/2$, where λ_{min} is the wavelength at the highest frequency. The characteristic equations are plotted at the maximum frequency of $f_{max} = 40$ GHz. The PPW is air-filled (i.e., $\epsilon_r = \mu_r = 1$). The dot markers indicate the calculated eigenvalues using [87].

imaginary eigenvalues appear on modal branches that have a hyperbolic behavior. Standard waveguide modes are present too, even though they do not appear within the visible range. The latter belong to periodic modal branches as for TM modes. Figs. B.5(a) and (b) show that the eigenvalues within the visible range are purely imaginary. This analysis proves that an inductive surface impedance is required to the structure for optimal dual-ortho-mode operation.

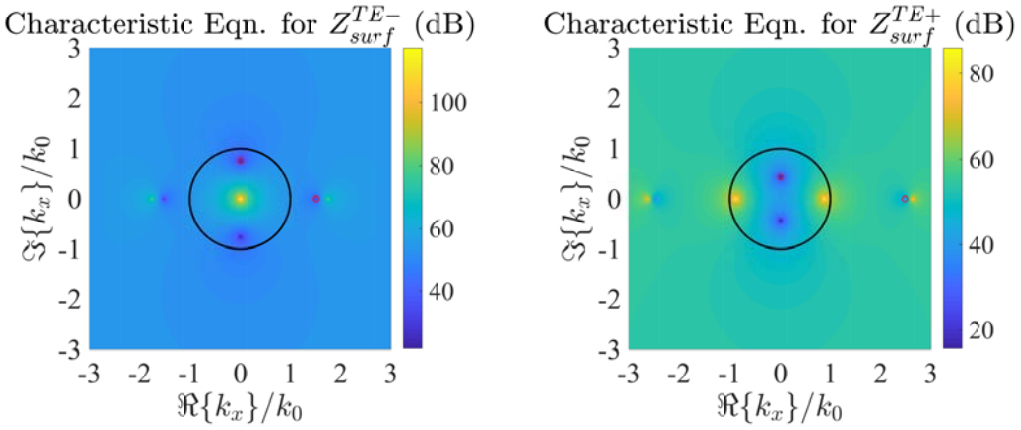

(a) (b)

FIGURE B.5: Characteristic equation for TE modes at the frequency f_{max}. The plot is shown in dB, thus the poles are illustrated with dark blue spots. The black circle indicate the visible range ($|k_x| = k$) and red dot markers represent the calculated poles using [87]. The PPW is air-filled and its height is $h = \lambda_{min}/2$.

Inductive surface impedance, indeed, guarantees that one only waveguide mode will appear in the visible range, as it can be noticed from Fig. B.4.

Appendix C

Additional Details about Chapter 5

In this Appendix, we provide additional details about the mathematical derivation equations (5.5) and (5.6). A scalar formulation will be used in the following to streamline the mathematical content. Furthermore, we will assume the network to be symmetric, reciprocal and lossless. Under these assumptions, the following relation holds [74]

$$\xi = det\left\{\begin{bmatrix} A_1 & B_1 \\ C_1 & D_1 \end{bmatrix}\right\} = A_1 D_1 - B_1 C_1 = 1 \tag{C.1}$$

where A_1, B_1, C_1 and D_1 are defined in (5.3). Their extended form is given by [74]

$$A_1 = \cos\theta \tag{C.2}$$

$$B_1 = i\eta_d \sin\theta \tag{C.3}$$

$$C_1 = Y_{s1}\cos\theta + \frac{i\sin\theta}{\eta_d} \tag{C.4}$$

$$D_1 = iY_{s1}\eta_d \sin\theta + \cos\theta \tag{C.5}$$

C.0.1 Closed form of Y_{s1}

The unit cell in Fig. 5.2 is assumed infinitely periodic along z-axis. This allows a Bloch phase delay ϕ and the Bloch impedance Z_B to be defined. The Bloch impedance Z_B can be expressed in terms of an $ABCD$ matrix formulation [74], yielding

$$Z_B = -\frac{iB}{D\tan(\phi)} \tag{C.6}$$

where A, B, C and D are defined in (5.2). Using the matrix multiplication, they can be written as

$$A = \frac{1}{\xi}(A_1D_1 + B_1C_1 + B_1D_1Y_{s2}) = A_1D_1 + B_1C_1 + B_1D_1Y_{s2} \tag{C.7}$$

$$B = \frac{1}{\xi}(2A_1B_1 + B_1^2Y_{s2}) = 2A_1B_1 + B_1^2Y_{s2} \tag{C.8}$$

$$C = \frac{1}{\xi}(2C_1D_1 + D_1^2Y_{s2}) = 2C_1D_1 + D_1^2Y_{s2} \tag{C.9}$$

$$D = A \tag{C.10}$$

From [74], the Bloch phase delay can be found, yielding

$$\cos\phi = A = A_1D_1 + B_1C_1 + B_1D_1Y_{s2} \tag{C.11}$$

Exploiting (C.1), the relation (C.11) reduces to

$$\cos\phi = 2A_1D_1 + B_1D_1Y_{s2} - 1 \tag{C.12}$$

At this point, we can focus on finding the expression of the Bloch impedance Z_B as function of the Bloch phase delay ϕ, the $ABCD$ matrix and Y_{s2}, by substituting (C.8) and (C.10) into (C.6). In formulae [74, 128]

$$Z_B = \frac{-iB}{D\tan\phi} = \frac{-iB_1(2A_1 + B_1Y_{s2})}{(A_1D_1 + B_1C_1 + B_1D_1Y_{S2})\tan\phi} \tag{C.13}$$

Using equation (C.12), one can obtain

$$\frac{1+\cos\phi}{D_1} = 2A_1 + B_1Y_{S2} \tag{C.14}$$

By substituting (C.11) and (C.14) into (C.13), it follows

$$Z_B = \frac{-iB_1(1+\cos\phi)}{D_1\cos\phi\tan\phi} \tag{C.15}$$

By employing the following trigonometric identity:

$$\frac{1+\cos\phi}{\cos\phi\tan\phi} = \frac{1}{\tan(\phi/2)} \tag{C.16}$$

equation (C.15) becomes

$$Z_B = -\frac{iB_1}{D_1 \tan(\phi/2)} \tag{C.17}$$

By inserting (C.3) and (C.5) into (C.17), the following relation is found

$$Z_B = \frac{\eta_d \sin\theta}{(iY_{s1}\eta_d \sin\theta + \cos\theta)\tan(\phi/2)} \tag{C.18}$$

Finally, (5.5) is obtained by inverting (C.18) and applying some algebraic manipulations.

C.0.2 Closed form of Y_{s2}

By inserting (C.1) into (5.2), the second entry B of the overall $ABCD$ matrix takes the following form

$$B = i\eta_d \sin(2\theta) - Y_{s2}\eta_d^2 \sin^2\theta \tag{C.19}$$

Furthermore, it can be expressed in terms of the Bloch unit cell's phase delay ϕ and Bloch impedance Z_B, yielding

$$B = iZ_B \sin\phi \tag{C.20}$$

Y_{s2} is found by equating (C.19) and (C.20), yielding

$$Y_{s2} = \frac{i}{\eta_d}\left(\frac{\sin(2\theta)}{\sin^2\theta} - \frac{Z_B}{\eta_d}\csc^2\theta \sin\phi\right) \tag{C.21}$$

Finally, equation (5.6) is obtained using the following trigonometric identity: $\frac{\sin(2\theta)}{\sin^2\theta} = 2\cot\theta$.

Bibliography

[1] R. A. Pearson, J. Vazquez, M. W. Shelley, A. Payne, V. Stoiljkovic, and M. Steel. "Next generation mobile SATCOM terminal antennas for a transformed world". In: *Proceedings of the 5th European Conference on Antennas and Propagation (EUCAP)*. 2011, pp. 2341–2345.

[2] S. Otto, I. Nistal, S. Holzwarth, O. Litschke, and R. Baggen IMST. "Planar satcom antenna systems in Ka-band". In: *ESA Antenna workshop, Noorwijk, The Netherlands*. Oct. 3-5, 2012.

[3] *ThinKom*. `http://www.thinkom.com/antenna-products/thinsat/commander/`.

[4] R. J. Bolt, D. Cavallo, G. Gerini, D. Deurloo, R. Grooters, A. Neto, and G. Toso. "Characterization of a Dual-Polarized Connected-Dipole Array for Ku-Band Mobile Terminals". In: *IEEE Transactions on Antennas and Propagation* 64.2 (2016), pp. 591–598.

[5] F. Foglia Manzillo, M. Ettorre, M. Casaletti, N. Capet, and R. Sauleau. "Active impedance of infinite parallel-fed continuous transverse stub arrays". In: *IEEE Transactions on Antennas and Propagation* 63.7 (2015), pp. 3291–3297.

[6] M. Ettorre, F. F. Manzillo, M. Casaletti, R. Sauleau, L. Le Coq, and N. Capet. "Continuous transverse stub array for Ka-band applications". In: *IEEE Transactions on Antennas and Propagation* 63.11 (2015), pp. 4792–4800.

[7] F. Foglia Manzillo, M. Ettorre, M. S. Lahti, K. T. Kautio, D. Lelaidier, E. Seguenot, and R. Sauleau. "A multilayer LTCC solution for integrating 5G access point antenna modules". In: *IEEE Transactions on Microwave Theory and Techniques* 64.7 (2016), pp. 2272–2283.

[8] F. Foglia Manzillo, M. Śmierzchalski, L. Le Coq, M. Ettorre, J. Aurinsalo, K. T. Kautio, M. S. Lahti, A. E. I. Lamminen, J. Säily, and R. Sauleau. "A wide-angle scanning switched-beam antenna system in LTCC technology with high beam crossing levels for V-band communications". In: *IEEE Transactions on Antennas and Propagation* 67.1 (2019), pp. 541–553.

[9] T. Potelon, M. Ettorre, L. Le Coq, T. Bateman, J. Francey, D. Lelaidier, E. Seguenot, F. Devillers, and R. Sauleau. "A low-profile broadband 32-slot continuous transverse stub array for backhaul applications in E-Band". In: *IEEE Transactions on Antennas and Propagation* 65.12 (2017), pp. 6307–6316.

[10] T. Potelon, M. Ettorre, L. Le Coq, T. Bateman, J. Francey, and R. Sauleau. "Reconfigurable CTS Antenna Fully Integrated in PCB Technology for 5G Backhaul Applications". In: *IEEE Transactions on Antennas and Propagation* 67.6 (2019), pp. 3609–3618.

[11] *SpaceX's Starlink satellite megaconstellation*. `https://www.starlink.com/`.

[12] European commission. "Low-Earth Orbit satellites: Spectrum access". In: *Digital Transformation Monitor* (Jul. 2017).

[13] B.R. Rao, K. McDonald, and W. Kunysz. *GPS/GNSS Antennas*. Artech House telecommunications library. Artech House, 2013. ISBN: 9781596931503.

[14] Jonathan C. McDowell. "The Low Earth Orbit Satellite Population and Impacts of the SpaceX Starlink Constellation". In: *The Astrophysical Journal* 892.2 (2020), p. L36. ISSN: 2041-8213. DOI: 10.3847/2041-8213/ab8016. URL: http://dx.doi.org/10.3847/2041-8213/ab8016.

[15] *European Space Agency: Galileo Constellation*. `http://www.esa.int/Applications/Navigation/Galileo/Galileo_a_constellation_of_navigation_satellites`.

[16] Robert Dybdal. *Communication satellite antennas: system architecture, technology, and evaluation*. New York: McGraw-Hill Education, 2009.

[17] F. Doucet, N. J. G. Fonseca, E. Girard, H. Legay, and R. Sauleau. "Analytical Model and Study of Continuous Parallel Plate Waveguide Lens-like Multiple-Beam Antennas". In: *IEEE Transactions on Antennas and Propagation* 66.9 (2018), pp. 4426–4436.

[18] N. J. G. Fonseca, Q. Liao, and O. Quevedo-Teruel. "Equivalent Planar Lens Ray-Tracing Model to Design Modulated Geodesic Lenses Using Non-Euclidean Transformation Optics". In: *IEEE Transactions on Antennas and Propagation* 68.5 (2020), pp. 3410–3422.

[19] V. Mazzola and J. E. Becker. "Coupler-type bend for pillbox antennas". In: *IEEE Transactions on Microwave Theory and Techniques* 15.8 (1967), pp. 462–468.

[20] Ronan Sauleau and Mauro Ettorre. *Multilayer pillbox type parallel-plate waveguide antenna and corresponding antenna system*. U.S. Patent 9 246 232 B2. 2016.

[21] T. Rossi, M. De Sanctis, M. Ruggieri, C. Riva, L. Luini, G. Codispoti, E. Russo, and G. Parca. "Satellite communication and propagation experiments through the alphasat Q/V band Aldo Paraboni technology demonstration payload". In: *IEEE Aerospace and Electronic Systems Magazine* 31.3 (2016), pp. 18–27.

[22] *European Space Agency*. `https://www.esa.int/Applications/Telecommunications_Integrated_Applications/Satellite_frequency_bands`.

[23] Ali Al-Saegh, Aduwati Sali, J. Mandeep, Alyani Ismail, Abdulmajeed Al-Jumaily, and Chandima Gomes. "Atmospheric Propagation Model for Satellite Communications". In: Sept. 2014, p. 28. ISBN: 978-953-51-1719-3. DOI: `10.5772/58238`.

[24] Constantine A. Balanis. *Antenna theory: analysis and design*. USA: Wiley-Interscience, 2005. ISBN: 0471714623.

[25] International Telecommunication Union. *Choice of polarization for the broadcasting-satellite service*. BO.791. 1992.

[26] H. Bayer, A. Krauss, T. Zaiczek, R. Stephan, O. Enge-Rosenblatt, and M. A. Hein. "Ka-Band User Terminal Antennas for Satellite Communications [Antenna Applications Corner]". In: *IEEE Antennas and Propagation Magazine* 58.1 (2016), pp. 76–88.

[27] H. Bayer, A. Krauss, R. Stephan, and M. A. Hein. "Compact Ka-band Cassegrain antenna with multimode monopulse tracking feed for satcom-on-the-move applications". In: *2016 10th European Conference on Antennas and Propagation (EuCAP)*. 2016, pp. 1–5.

[28] R. M. Davis, C. . Cha, S. G. Kamak, and A. Sadigh. "A scanning reflector using an off-axis space-fed phased-array feed". In: *IEEE Transactions on Antennas and Propagation* 39.3 (1991), pp. 391–400.

[29] M. Letizia, B. Fuchs, A. Skrivervik, and J. R. Mosig. "Circularly polarized homogeneous lens antenna system providing multibeam radiation pattern for haps". In: *URSI Radio Science Bulletin* 2010.333 (2010), pp. 18–28.

[30] M. Ettorre, R. Sauleau, and L. Le Coq. "Multi-beam multi-layer leaky-wave SIW pillbox antenna for millimeter-wave applications". In: *IEEE Transactions on Antennas and Propagation* 59.4 (2011), pp. 1093–1100.

[31] J. Yan, S. Gogineni, B. Camps-Raga, and J. Brozena. "A Dual-Polarized 2–18-GHz Vivaldi Array for Airborne Radar Measurements of Snow". In: *IEEE Transactions on Antennas and Propagation* 64.2 (2016), pp. 781–785.

[32] J. D. S. Langley, P. S. Hall, and P. Newham. "Balanced antipodal Vivaldi antenna for wide bandwidth phased arrays". In: *IEE Proceedings - Microwaves, Antennas and Propagation* 143.2 (1996), pp. 97–102.

[33] H. Wheeler. "Simple relations derived fom a phased-array antenna made of an infinite current sheet". In: *IEEE Transactions on Antennas and Propagation* 13.4 (1965), pp. 506–514.

[34] S. S. Holland and M. N. Vouvakis. "The Planar Ultrawideband Modular Antenna (PUMA) Array". In: *IEEE Transactions on Antennas and Propagation* 60.1 (2012), pp. 130–140.

[35] S. S. Holland, D. H. Schaubert, and M. N. Vouvakis. "A 7–21 GHz Dual-Polarized Planar Ultrawideband Modular Antenna (PUMA) Array". In: *IEEE Transactions on Antennas and Propagation* 60.10 (2012), pp. 4589–4600.

[36] M. Y. Lee, R. W. Kindt, and M. N. Vouvakis. "Planar ultrawideband modular antenna (PUMA) wavelength-scaled array". In: *2016 IEEE International Symposium on Antennas and Propagation (APSURSI)*. 2016, pp. 435–436.

[37] J. T. Logan, R. W. Kindt, M. Y. Lee, and M. N. Vouvakis. "A New Class of Planar Ultrawideband Modular Antenna Arrays With Improved Bandwidth". In: *IEEE Transactions on Antennas and Propagation* 66.2 (2018), pp. 692–701.

[38] D. Cavallo. "Connected array antennas : analysis and design". In: Ph.D. dissertation. 2011.

[39] D. Cavallo, A. Neto, and G. Gerini. "Green's Function Based Equivalent Circuits for Connected Arrays in Transmission and in Reception". In: *IEEE Transactions on Antennas and Propagation* 59.5 (2011), pp. 1535–1545.

[40] W. H. Syed, D. Cavallo, H. Thippur Shivamurthy, and A. Neto. "Wideband, Wide-Scan Planar Array of Connected Slots Loaded With Artificial Dielectric Superstrates". In: *IEEE Transactions on Antennas and Propagation* 64.2 (2016), pp. 543–553.

[41] D. Cavallo, W. H. Syed, and A. Neto. "Connected-Slot Array With Artificial Dielectrics: A 6 to 15 GHz Dual-Pol Wide-Scan Prototype". In: *IEEE Transactions on Antennas and Propagation* 66.6 (2018), pp. 3201–3206.

[42] B. A. Munk. *Finite Antenna Arrays and FSS*. New York, NY, USA: Wiley, 2003.

[43] J. P. Doane, K. Sertel, and J. L. Volakis. "A Wideband, Wide Scanning Tightly Coupled Dipole Array With Integrated Balun (TCDA-IB)". In: *IEEE Transactions on Antennas and Propagation* 61.9 (2013), pp. 4538–4548.

[44] M. H. Novak and J. L. Volakis. "Ultrawideband Antennas for Multiband Satellite Communications at UHF–Ku Frequencies". In: *IEEE Transactions on Antennas and Propagation* 63.4 (2015), pp. 1334–1341.

[45] H. Moody. "The systematic design of the Butler matrix". In: *IEEE Transactions on Antennas and Propagation* 12.6 (1964), pp. 786–788.

[46] N. J. G. Fonseca. "Printed S-Band 4 × 4 Nolen Matrix for Multiple Beam Antenna Applications". In: *IEEE Transactions on Antennas and Propagation* 57.6 (2009), pp. 1673–1678.

[47] W. Rotman. "Wide-angle scanning with microwave double-layer pillboxes". In: *IRE Transactions on Antennas and Propagation* 6.1 (1958), pp. 96–105.

[48] E. L. Holzman. "Pillbox antenna design for millimeter-wave base-station applications". In: *IEEE Antennas and Propagation Magazine* 45.1 (2003), pp. 27–37.

[49] N. E. Lindenblad. *Multiple slot antenna.* U.S. Patent 2 628 311 A. 1948.

[50] W. W. Milroy. *Continuous transverse stub element devices and methods of making same.* U.S. Patent 5 266 961 A. 1993.

[51] W. W. Milroy. "The continuous transverse stub (CTS) array: basic theory, experiment, and application". In: *Proc. Antenna Appl. Symp.* 2 (1991), 253–283.

[52] W. H. Henderson and W. W. Milroy. "Wireless communication applications of the continuous transverse stub (CTS) array at microwave and millimeter wave frequencies". In: *IEEE/ACES International Conference on Wireless Communications and Applied Computational Electromagnetics, 2005.* 2005, pp. 253–256.

[53] A. Lemons, R. Lewis, W. Milroy, R. Robertson, S. Coppedge, and T. Kastle. "W-band CTS planar array". In: *1999 IEEE MTT-S International Microwave Symposium Digest.* Vol. 2. 1999, 651–654 vol.2.

[54] T. Potelon, M. Ettorre, T. Bateman, J. Francey, and R. Sauleau. "Broadband passive two-feed-per-beam pillbox architecture for high beam crossover level". In: *IEEE Transactions on Antennas and Propagation* 68.1 (2020), pp. 575–580.

[55] T. Potelon, M. Ettorre, and R. Sauleau. "Long slot array fed by a nonuniform corporate feed network in PPW technology". In: *IEEE Transactions on Antennas and Propagation* 67.8 (2019), pp. 5436–5445.

[56] N. Marcuvitz. *Waveguide Handbook. Edited by N. Marcuvitz.* Massachusetts Institute of Technology. Radiation Laboratory Series. vol. 10. McGraw-Hill Book Company, 1951.

[57] A. Neto and J. J. Lee. "Ultrawide-band properties of long slot arrays". In: *IEEE Transactions on Antennas and Propagation* 54.2 (2006), pp. 534–543.

[58] A. Neto and J. J. Lee. ""Infinite bandwidth" long slot array antenna". In: *IEEE Antennas and Wireless Propagation Letters* 4 (2005), pp. 75–78.

[59] A. V. Stankovsky, Y. A. Litinskaya, A. M. Alexandrin, S. V. Polenga, and Y. P. Salomatov. "Spatial polarizers for CTS structure-based antenna arrays". In: *2019 IEEE Conference of Russian Young Researchers in Electrical and Electronic Engineering (EIConRus)*. 2019, pp. 885–889.

[60] Y. J. Cheng, J. Wang, and X. L. Liu. "94 GHz substrate integrated waveguide dual-circular-polarization shared-aperture parallel-plate long-slot array antenna with low sidelobe level". In: *IEEE Transactions on Antennas and Propagation* 65.11 (2017), pp. 5855–5861.

[61] S. K. Sharma, L. Shafai, and M. Barakat. "Ka-band dual circularly polarized feed horn polarizer for reflector antennas for satellite communications". In: *11th International Symposium on Antenna Technology and Applied Electromagnetics [ANTEM 2005]*. 2005, pp. 1–4.

[62] L. Diamond. "Ka-Band user terminal antennas". In: *ESA Antenna workshop*. 2012.

[63] N. Bartolomei, M. Garcia-Vigueras, F. Doucet, D. Blanco, E. Girard, R. Sauleau, and M. Ettorre. "Circularly Polarized Parallel Plate Waveguide Multiple-Beam Lens-like Antenna for Satcom Applications". In: *2019 13th European Conference on Antennas and Propagation (EuCAP)*. 2019, pp. 1–3.

[64] *Agence Nationale de la Recherche*. `https://anr.fr/Project-ANR-16-ASMA-0006`. Accessed: 2029-08-28.

[65] Mailloux Robert J. *Phased array antenna handbook*. 3rd. USA: Artech House, Inc., 2017. ISBN: 1630810290.

[66] G. Floquet. "Sur les équations différentielles linéaires à coefficients périodiques". fr. In: *Annales scientifiques de l'École Normale Supérieure* 2e série, 12 (1883), pp. 47–88. DOI: 10.24033/asens.220. URL: http://www.numdam.org/item/ASENS_1883_2_12__47_0.

[67] R.E. Collin, IEEE Antennas, and Propagation Society. *Field theory of guided waves*. IEEE/OUP series on electromagnetic wave theory. IEEE Press, 1990. ISBN: 9780198592136.

[68] R.F. Harrington. *Time-harmonic electromagnetic fields*. IEEE Press Series on Electromagnetic Wave Theory. Wiley, 2001. ISBN: 9780471208068.

[69] K. Kurokawa. *An introduction to the theory of microwave circuits*. Electrical science series. Academic Press, 1969.

[70] L.B. Felsen and N. Marcuvitz. *Radiation and scattering of waves*. IEEE Press Series on Electromagnetic Wave Theory. Wiley, 1994. ISBN: 9780780310889.

[71] Roberto Sorrentino and Giovanni Bianchi. *Microwave and RF engineering*. John Wiley & Sons, Ltd., 2010. ISBN: 978-0-470-75862-5.

[72] CST STUDIO SUITE® Computer simulation technology. 2017.

[73] D. M. Pozar. "The active element pattern". In: *IEEE Transactions on Antennas and Propagation* 42.8 (1994), pp. 1176–1178.

[74] D.M. Pozar. *Microwave Engineering*. Wiley, 2004. ISBN: 9780471448785.

[75] A. Ishimaru, R. Coe, G. Miller, and W. Geren. "Finite periodic structure approach to large scanning array problems". In: *IEEE Transactions on Antennas and Propagation* 33.11 (1985), pp. 1213–1220.

[76] W. P. M. N. Keizer. "Planar phased-array antennas: mutual coupling and ultralow peak sidelobes". In: *IEEE Antennas and Propagation Magazine* 61.1 (2019), pp. 14–28.

[77] J. A. Kasemodel, C. Chen, and J. L. Volakis. "Wideband planar array with integrated feed and matching network for wide-angle scanning". In: *IEEE Transactions on Antennas and Propagation* 61.9 (2013), pp. 4528–4537.

[78] E. Magill and H. Wheeler. "Wide-angle impedance matching of a planar array antenna by a dielectric sheet". In: *IEEE Transactions on Antennas and Propagation* 14.1 (1966), pp. 49–53.

[79] A. Ludwig. "The definition of cross polarization". In: *IEEE Transactions on Antennas and Propagation* 21.1 (1973), pp. 116–119.

[80] J. E. Roy and L. Shafai. "Generalization of the Ludwig-3 definition for linear copolarization and cross polarization". In: *IEEE Transactions on Antennas and Propagation* 49.6 (2001), pp. 1006–1010.

[81] ANSYS Electronics Desktop 2018.2 – High-frequency structure simulation. 2018.

[82] DMG MORI: *en.dmgmori.com*.

[83] Ming Chen and G. Tsandoulas. "A wide-band square-waveguide array polarizer". In: *IEEE Transactions on Antennas and Propagation* 21.3 (1973), pp. 389–391.

[84] J. Bornemann and V. A. Labay. "Ridge waveguide polarizer with finite and stepped-thickness septum". In: *IEEE Transactions on Microwave Theory and Techniques* 43.8 (1995), pp. 1782–1787.

[85] G. Tsandoulas and G. Knittel. "The analysis and design of dual-polarization square-waveguide phased arrays". In: *IEEE Transactions on Antennas and Propagation* 21.6 (1973), pp. 796–808.

[86] J. R. Wait. "On the theory of shielded surface waves". In: *IEEE Transactions on Microwave Theory and Techniques* 15.7 (1967), pp. 410–414.

[87] Vincenzo Galdi and Innocenzo Pinto. "Simple algorithm for accurate location of leaky-wave poles for grounded inhomogeneous dielectric slabs". In: *Microwave and Optical Technology Letters* 24 (Jan. 2000), pp. 135 –140.

[88] R. B. Dybdal, L. Peters, and W. H. Peake. "Rectangular waveguides with impedance walls". In: *IEEE Transactions on Microwave Theory and Techniques* 19.1 (1971), pp. 2–8.

[89] M. N. M. Kehn, M. Nannetti, A. Cucini, S. Maci, and P. . Kildal. "Analysis of dispersion in dipole-FSS loaded hard rectangular waveguide". In: *IEEE Transactions on Antennas and Propagation* 54.8 (2006), pp. 2275–2282.

[90] O. Luukkonen, C. Simovski, G. Granet, G. Goussetis, D. Lioubtchenko, A. V. Raisanen, and S. A. Tretyakov. "Simple and Accurate Analytical Model of Planar Grids and High-Impedance Surfaces Comprising Metal Strips or Patches". In: *IEEE Transactions on Antennas and Propagation* 56.6 (2008), pp. 1624–1632.

[91] M. Ettorre, S. M. Rudolph, and A. Grbic. "Generation of Propagating Bessel Beams Using Leaky-Wave Modes: Experimental Validation". In: *IEEE Transactions on Antennas and Propagation* 60.6 (2012), pp. 2645–2653.

[92] A. E. Karbowiak. "Theory of imperfect waveguides: the effect of wall impedance". In: *Proceedings of the IEE - Part B: Radio and Electronic Engineering* 102.5 (1955), pp. 698–708.

[93] P. S. Kildal. "Artificially soft and hard surfaces in electromagnetics". In: *IEEE Transactions on Antennas and Propagation* 38.10 (1990), pp. 1537–1544.

[94] P. S. Kildal, Ahmed A. Kishk, and Zvonimir Sipus. "Asymptotic boundary conditions for strip-loaded and corrugated surfaces". In: 1996.

[95] M. Bosiljevac, Z. Sipus, and P.-S. Kildal. "Construction of Green's functions of parallel plates with periodic texture with application to gap waveguides – a plane-wave spectral-domain approach". In: *IET Microwaves, Antennas and Propagation* 4 (11 2010), 1799–1810(11).

[96] M. Ng Mou Kehn. "Modal analysis of all-walls longitudinally corrugated rectangular waveguides using asymptotic corrugations boundary conditions". In: *IEEE Transactions on Microwave Theory and Techniques* 61.11 (2013), pp. 3821–3837.

[97] M. Ng Mou Kehn. "Rapid surface-wave dispersion and plane-wave reflection analyses of planar corrugated surfaces by asymptotic corrugations

boundary conditions even for oblique azimuth planes". In: *IEEE Transactions on Antennas and Propagation* 61.5 (2013), pp. 2695–2707.

[98] J. A. Aas. "Plane-wave reflection properties of two artificially hard surfaces". In: *IEEE Transactions on Antennas and Propagation* 39.5 (1991), pp. 651–656.

[99] T. Lou, X. Yang, H. Qiu, Z. Yin, and S. Gao. "Compact dual-polarized continuous transverse stub array with 2-D beam scanning". In: *IEEE Transactions on Antennas and Propagation* 67.5 (2019), pp. 3000–3010.

[100] T. Lou, X. Yang, L. Li, and E. Abubaker. "A flat dual-polarized continuous transverse stub antenna array based on substrate integrated waveguide". In: *12th European Conference on Antennas and Propagation (EuCAP 2018)*. 2018, pp. 1–3.

[101] Francesco Foglia Manzillo. "Wideband and flat multibeam antenna solutions for ultrafast communications in millimeter band". Theses. Université Rennes 1, Mar. 2017.

[102] D. M. Pozar and S. D. Targonski. "A shared-aperture dual-band dual-polarized microstrip array". In: *IEEE Transactions on Antennas and Propagation* 49.2 (2001), pp. 150–157.

[103] Y. Hsu, T. Huang, H. Lin, and Y. Lin. "Dual-polarized quasi Yagi–Uda antennas with endfire radiation for millimeter-wave MIMO terminals". In: *IEEE Transactions on Antennas and Propagation* 65.12 (2017), pp. 6282–6289.

[104] A. Li, K. Luk, and Y. Li. "A dual linearly polarized end-fire antenna array for the 5G applications". In: *IEEE Access* 6 (2018), pp. 78276–78285.

[105] G. Mishra, S. K. Sharma, J. S. Chieh, and R. B. Olsen. "Ku-Band Dual Linear-Polarized 1-D Beam Steering Antenna Using Parabolic-Cylindrical Reflector Fed by a Phased Array Antenna". In: *IEEE Open Journal of Antennas and Propagation* 1 (2020), pp. 57–70.

[106] B. K. Munk. *Frequency selective surfaces : theory and design*. John Wiley & Sons, Ltd, 2005.

[107] M. . Joyal and J. . Laurin. "Analysis and design of thin circular polarizers based on meander lines". In: *IEEE Transactions on Antennas and Propagation* 60.6 (2012), pp. 3007–3011.

[108] S. M. A. Momeni Hasan Abadi and N. Behdad. "Wideband linear-to-circular polarization converters based on miniaturized-element frequency selective surfaces". In: *IEEE Transactions on Antennas and Propagation* 64.2 (2016), pp. 525–534.

[109] L. Martinez-Lopez, J. Rodriguez-Cuevas, J. I. Martinez-Lopez, and A. E. Martynyuk. "A multilayer circular polarizer based on bisected split-ring frequency selective surfaces". In: *IEEE Antennas and Wireless Propagation Letters* 13 (2014), pp. 153–156.

[110] M. Hosseini and S. V. Hum. "A circuit-driven design methodology for a circular polarizer based on modified Jerusalem cross grids". In: *IEEE Transactions on Antennas and Propagation* 65.10 (2017), pp. 5322–5331.

[111] F. F. Manzillo, M. Ettorre, R. Sauleau, and A. Grbic. "Systematic design of a class of wideband circular polarizers using dispersion engineering". In: *2017 11th European Conference on Antennas and Propagation (EUCAP)*. 2017, pp. 1279–1281.

[112] M. A. Antoniades and G. V. Eleftheriades. "Compact linear lead/lag metamaterial phase shifters for broadband applications". In: *IEEE Antennas and Wireless Propagation Letters* 2 (2003), pp. 103–106.

[113] M. A. Antoniades and G. V. Eleftheriades. "A broadband Wilkinson balun using microstrip metamaterial lines". In: *IEEE Antennas and Wireless Propagation Letters* 4 (2005), pp. 209–212.

[114] P. Naseri and S. V. Hum. "A dual-band dual-circularly polarized reflectarray for K/Ka-band space applications". In: *2019 13th European Conference on Antennas and Propagation (EuCAP)*. 2019, pp. 1–5.

[115] P. Naseri, M. Riel, Y. Demers, and S. V. Hum. "A dual-band dual-circularly polarized reflectarray for K/Ka-band space applications". In: *IEEE Transactions on Antennas and Propagation* (2020), pp. 1–1.

[116] N. J. G. Fonseca and C. Mangenot. "Low-profile polarizing surface with dual-band operation in orthogonal polarizations for broadband satellite applications". In: *The 8th European Conference on Antennas and Propagation (EuCAP 2014)*. 2014, pp. 471–475.

[117] N. J. G. Fonseca and C. Mangenot. "High-performance electrically thin dual-band polarizing reflective surface for broadband satellite applications". In: *IEEE Transactions on Antennas and Propagation* 64.2 (2016), pp. 640–649.

[118] W. Tang, S. Mercader-Pellicer, G. Goussetis, H. Legay, and N. J. G. Fonseca. "Low-profile compact dual-band unit cell for polarizing surfaces operating in orthogonal polarizations". In: *IEEE Transactions on Antennas and Propagation* 65.3 (2017), pp. 1472–1477.

[119] P. Naseri, S. A. Matos, J. R. Costa, C. A. Fernandes, and N. J. G. Fonseca. "Dual-band dual-linear-to-circular polarization converter in transmission mode application to K/Ka-band satellite communications". In: *IEEE Transactions on Antennas and Propagation* 66.12 (2018), pp. 7128–7137.

[120] H. B. Wang and Y. J. Cheng. "Single-layer dual-band linear-to-circular polarization converter with wide axial ratio bandwidth and different polarization modes". In: *IEEE Transactions on Antennas and Propagation* 67.6 (2019), pp. 4296–4301.

[121] Advanced Design System (ADS). *www.keysight.com*.

[122] P. Naseri, J. R. Costa, S. A. Matos, C. A. Fernandes, and S. V. Hum. "Equivalent circuit modeling to design a dual-band dual linear-to-circular polarizer surface". In: *IEEE Transactions on Antennas and Propagation* (2020), pp. 1–1.

[123] Amin Ranjbar and Anthony Grbic. "Analysis and synthesis of cascaded metasurfaces using wave matrices". In: *Phys. Rev. B* 95 (20 2017), p. 205114. DOI: 10.1103/PhysRevB.95.205114. URL: https://link.aps.org/doi/10.1103/PhysRevB.95.205114.

[124] Amin Ranjbar and Anthony Grbic. "Broadband, Multiband, and Multifunctional All-Dielectric Metasurfaces". In: *Phys. Rev. Applied* 11 (5 2019), p. 054066. DOI: 10.1103/PhysRevApplied.11.054066. URL: https://link.aps.org/doi/10.1103/PhysRevApplied.11.054066.

[125] E. Arnieri, F. Greco, L. Boccia, and G. Amendola. "A SIW-based polarization rotator with an application to linear-to-circular dual band polarizers at K/Ka band". In: *IEEE Transactions on Antennas and Propagation* (2020), pp. 1–1.

[126] Zhanni Wu, Younes Ra'di, and Anthony Grbic. "Tunable Metasurfaces: A Polarization Rotator Design". In: *Phys. Rev. X* 9 (1 2019), p. 011036. DOI: 10.1103/PhysRevX.9.011036. URL: https://link.aps.org/doi/10.1103/PhysRevX.9.011036.

[127] Max Born and Emil Wolf. *Principles of Optics: Electromagnetic Theory of Propagation, Interference and Diffraction of Light (7th Edition)*. 1999.

[128] A. Grbic. "Super-resolving negative-refractive-index transmission-line lenses". In: Ph.D. dissertation, University of Toronto, Toronto, Canada. 2006.

[129] C. Pfeiffer and A. Grbic. "Millimeter-wave transmitarrays for wavefront and polarization control". In: *IEEE Transactions on Microwave Theory and Techniques* 61.12 (2013), pp. 4407–4417.

[130] Carl Pfeiffer and Anthony Grbic. "Bianisotropic metasurfaces for optimal polarization control: analysis and synthesis". In: *Phys. Rev. Applied* 2 (4 2014), p. 044011. DOI: 10.1103/PhysRevApplied.2.044011.

[131] R.J. Langley. "Improved empirical model for the Jerusalem cross". In: *IEE Proceedings H (Microwaves, Optics and Antennas)* 129 (1 1982), 1–6(5). ISSN: 0143-7097.

[132] F. Costa, A. Monorchio, and G. Manara. "Efficient analysis of frequency-selective surfaces by a simple equivalent-circuit model". In: *IEEE Antennas and Propagation Magazine* 54.4 (2012), pp. 35–48.

[133] Thomas Keating Ltd: www.terahertz.co.uk.

[134] Rogers Corporation: https://www.rogerscorp.com/.

[135] H. Cao, X. Wu, Y. Pi, J. Liu, H. Xu, Z. Meng, Y. Yu, and J. Fan. "A novel chiral metamaterial circular polarizer based on e-shape structure". In: *2016 IEEE International Symposium on Antennas and Propagation (APSURSI)*. 2016, pp. 489–490.

[136] C. Molero, E. Menargues, and M. García-Vigueras. "All-metal 3-D frequency selective surface with versatile dual-band polarization conversion". In: *IEEE Transactions on Antennas and Propagation* (2020), pp. 1–1.

[137] Tian-Wu Li, Da Li, and Er-Ping Li. "A novel FSS structure with high selectivity and excellent angular stability for 5G communication radome". In: *2017 10th Global Symposium on Millimeter-Waves*. 2017, pp. 50–52.

[138] Mehdi Hosseini, Abbas Pirhadi, and Mohammad Hakkak. "A novel AMC with little sensitivity to the angle of incidence using 2-layer Jerusalem Cross FSS". In: *Progress in Electromagnetics Research-pier* 64 (Jan. 2006), pp. 43–51.

[139] J. E. Rayas-Sanchez and V. Gutierrez-Ayala. "A general EM-based design procedure for single-layer substrate integrated waveguide interconnects with microstrip transitions". In: *2008 IEEE MTT-S International Microwave Symposium Digest*. 2008, pp. 983–986.

[140] D. Deslandes and K. Wu. "Design Consideration and Performance Analysis of Substrate Integrated Waveguide Components". In: *2002 32nd European Microwave Conference*. 2002, pp. 1–4.

[141] Y. Cassivi, L. Perregrini, P. Arcioni, M. Bressan, K. Wu, and G. Conciauro. "Dispersion characteristics of substrate integrated rectangular waveguide". In: *IEEE Microwave and Wireless Components Letters* 12.9 (2002), pp. 333–335.

[142] Feng Xu and Ke Wu. "Guided-wave and leakage characteristics of substrate integrated waveguide". In: *IEEE Transactions on Microwave Theory and Techniques* 53.1 (2005), pp. 66–73.

[143] Ke Wu, D. Deslandes, and Y. Cassivi. "The substrate integrated circuits - a new concept for high-frequency electronics and optoelectronics". In: *6th International Conference on Telecommunications in Modern Satellite,*

Cable and Broadcasting Service, 2003. TELSIKS 2003. Vol. 1. 2003, P–III.

[144] Taconic® Advanced Dielectric Division: https://www.4taconic.com/.

[145] Southwest Microwave Inc.: *mpd.southwestmicrowave.com.*

[146] S. Maci, Z. Sipus, A. Freni, A. Mazzinghi, and S. Skokic. "Advanced mathematics for antenna analysis". In: Class notes for European School of Antennas Course. Dubrovnik, Croatia, May 10-18, 2010.

[147] W. Bi and V. Pagneux. "New insights into mode behaviours in waveguides with impedance boundary conditions". In: *arXiv:1511.05508* (Nov. 2015).

[148] F. P. Mechel. "Modal solutions in rectangular ducts lined with locally reacting absorbers". In: *Acustica* 73 (1991), pp. 223–239.

[149] S. W. Rienstra. "A classification of duct modes based on surface waves". In: *Wave Motion* 37 (2003), pp. 119–135.

List of publications

Journal papers

[J-1] M. Del Mastro, F. Foglia Manzillo, D. González-Ovejero, M. Śmierzchalski, P. Pouliguen, P. Potier, R. Sauleau, and M. Ettorre, "Analysis of circularly polarized CTS arrays," in *IEEE Trans. Antennas Propag.*, vol. 68, no. 6, pp. 4571-4582, Jun. 2020, doi: 10.1109/TAP.2020.2972438.

[J-2] M. Del Mastro, S. Lenzini, R. Sauleau, and M. Ettorre, "Equi-dispersive dual-mode long slot arrays," accepted for publication in *IEEE Antennas Wireless Propag. Lett.*, Sep. 2020.

[J-3] M. Del Mastro, M. Ettorre, and A. Grbic, "Dual-band, orthogonally-polarized LP-to-CP converter for SatCom applications," in *IEEE Trans. Antennas Propag.*, Apr. 2020, doi: 10.1109/TAP.2020.2989868.

[J-4] M. Śmierzchalski, F. Foglia Manzillo, M. Del Mastro, N. Capet, B. Palacin, R. Sauleau, and M. Ettorre, "A Novel dual-polarized continuous transverse stub antenna based on corrugated waveguides - part I: principle of operation and design," accepted for publication in *IEEE Trans. Antennas Propag.*, Sep. 2020.

[J-5] M. Śmierzchalski, F. Foglia Manzillo, M. Del Mastro, N. Capet, B. Palacin, R. Sauleau, and M. Ettorre, "A Novel dual-polarized continuous transverse stub antenna based on corrugated waveguides - part II: experimental demonstration," accepted for publication in *IEEE Trans. Antennas Propag.*, Sep. 2020.

[J-] M. Del Mastro, A. Mahmoud, T. Potelon, R. Sauleau, A. Grbic, L. Le Coq, and M. Ettorre, "Ultra-low-profile CTS array with versatile dual-band, circular polarization for SatCom applications," in preparation for submission to *IEEE Trans. Antennas Propag.*, 2020.

[J-] M. Del Mastro, S. Lenzini, L. Vincetti, and M. Ettorre, "Circularly-polarized dual-mode continuous transverse stub array in Ka-band," in preparation for submission to *IEEE Trans. Antennas Propag.*, 2020.

[J-] S. Lenzini, M. Del Mastro, L. Vincetti, and M. Ettorre, "Dual-mode pillbox beamformer for polarization agile planar antennas," in preparation for submission to *IEEE Trans. Antennas Propag.*, 2020.

International conference papers

[IC-1] M. Del Mastro, M. Ettorre, and A. Grbic, "Dual-band LP-to-CP converter with orthogonal polarization transmission," accepted for presentation at *IEEE Antennas Propag. Symp. (APS)*, Montréal, Québec, Canada, 5-10 Jul., 2020.

[IC-2] A. Mahmoud, M. Del Mastro, T. Potelon, M. Ettorre, and R. Sauleau, "High gain low profile array for SatCom applications," accepted for presentation at *IEEE Antennas Propag. Symp. (APS)*, Montréal, Québec, Canada, 5-10 Jul., 2020.

[IC-3] M. Del Mastro, M. Ettorre, and A. Grbic, "Analytic design of dual-band, dual-polarized LP-to-CP polarization converters," *Proc. 14^{t}h Eur. Conf. Antennas Propag. (EuCAP)*, Copenhagen, Denmark, 15-20 Mar., 2020, pp. 1-3, doi: 10.23919/EuCAP48036.2020.9135304 (*Convened session*).

[IC-4] M. Del Mastro, A. Mahmoud, T. Potelon, R. Sauleau, and M. Ettorre, "Broadband CTS array in PCB technology," accepted for presentation at *14^{t}h Eur. Conf. Antennas Propag. (EuCAP)*, Copenhagen, Denmark, 15-20 Mar., 2020 (*Convened session*).

[IC-5] M. Del Mastro, F. Foglia Manzillo, D. González-Ovejero, M. Śmierzchalski, P. Pouliguen, P. Potier, R. Sauleau, and M. Ettorre, "Modeling of circularly-polarized CTS arrays," *Proc. IEEE Antennas Propag. Symp. (APS)*, Atlanta, GA, USA, 7-12 Jul., 2019, pp. 1227-1228, doi: 10.1109/APUSNCURSINRSM.2019.8889314.

[IC-6] M. Del Mastro, F. Foglia Manzillo, D. González-Ovejero, M. Śmierzchalski, P. Pouliguen, P. Potier, R. Sauleau, and M. Ettorre, "Circularly-polarized CTS arrays," *Proc. 13th Eur. Conf. Antennas Propag. (EuCAP)*, Krakow, Poland, 31 Mar. – 5 Apr., 2019, pp. 1-3.

[IC-7] M. Śmierzchalski, F. Foglia Manzillo, M. Del Mastro, N. Capet, B. Palacin, R. Sauleau, and M. Ettorre, "A dual-mode CTS architecture for dual-polarized and circularly-polarized antenna systems," *Proc. 13th Eur. Conf. Antennas Propag. (EuCAP)*, Krakow, Poland, 31 Mar. – 5 Apr., 2019 (*Convened session*).

[IC-8] M. Del Mastro, M. A. Del Pino and M. Spirito, "A 3-D printed TE_{10} rectangular to TE_{01} circular waveguide transition for polymer waveguide characterization," *Proc. 92nd ARFTG Microwave Measurement Conference (ARFTG)*, Orlando, FL, USA, 2019, pp. 1-3, doi: 10.1109/ARFTG.2019.8637235.

[IC-9] M. Smierzchalski, F. Foglia Manzillo, M. Del Mastro, N. Capet, B. Palacin, M. Del Mastro, R. Sauleau, and M. Ettorre, "Innovative multibeam dual-polarized CTS antennas for space applications", *39th European Space Agency Antenna Workshop*, Noordwijk, The Netherlands, 2018.

About the author

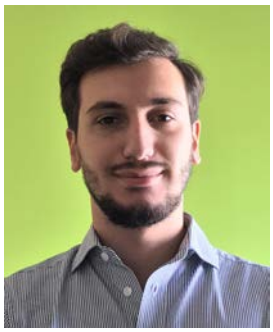

Michele Del Mastro was born in Avellino, Italy, on July 25^{th}, 1992.

He received the M. Mus. degree in clarinet from the Conservatorio di Musica 'D. Cimarosa', Avellino, Italy, in 2011, and the M.Sc. degree (summa cum laude) in electronics engineering from the Università degli Studi di Napoli 'Federico II', Naples, Italy, in 2017. Since October 2017, he started working toward his Ph.D. degree in electrical engineering at the Institut d'Électronique et des Technologies du numéRique (IETR), Université de Rennes 1, Rennes, France.

His Ph.D. degree was funded by Direction Générale de l'Armement (DGA) and concerned the analysis and design of innovative antenna solutions for SatCom applications. He was also involved in R&D projects of Thales SIX GTS, Paris, France, and Centre National d'Études Spatiales (CNES), Toulouse, France.

In 2016, he joined the Electronic Research Laboratory, Delft University of Technology, Delft, The Netherlands, where he held a position as intern. In the frame of a collaboration with NXP Semiconductor, he worked toward his master's thesis pertaining automotive applications.

From May to October 2019, he was Visiting Ph.D. Scholar with the Radiation Laboratory at the University of Michigan, Ann Arbor, MI, USA.

His research interests include the analysis and synthesis of wideband antenna arrays, numerical modeling, frequency-selective surfaces for polarization converters, and periodic structures.

Mr. Michele Del Mastro received the TICRA Foundation Travel Grant at the 13^{th} European Conference on Antennas and Propagation (EuCAP), Krakow, Poland, in 2019, and was a co-recipient of the Best Innovation Award at the 39^{th} European Space Agency Antenna Workshop, Noordwijk, The Netherlands, in 2018.

UNIVERSITÉ DE RENNES 1

Titre : Antenne CTS à double polarisation pour applications SatCom

Mots clés : Antenne CTS, large bande, guide d'ondes à plans parallèles, formateur de faisceaux.

Résumé : La demande croissante en systèmes de communication par satellite à large bande a conduit au déploiement de constellations de satellites en bande K/Ka et au développement de nouveaux terminaux pour les utilisateurs fixes et mobiles. Des exigences strictes sont imposées à l'antenne. L'antenne doit présenter un gain élevé (> 30 dB) et fonctionner en polarisation circulaire ou double polarisation sur un secteur angulaire couvrant tout le plan azimutal et un grand angle en élévation (jusqu'à 60°). L'objectif principal de la thèse est d'étudier l'analyse et la conception des réseaux « Continuous Transverse Stub » (CTS) à double polarisation. Les réseaux CTS se composent de longues fentes rayonnantes, de hauteur finie, reliés à un système d'alimentation en guide de plaques parallèles, en anglais parallel-plate waveguide (PPW), et rayonnant dans l'espace libre. Un réseau alimenté en parallèle sera considéré pour un fonctionnement large bande. L'idée à la base de la thèse est d'utiliser des réseaux CTS multimodale. Les réseaux CTS classiques adoptent le mode principal TEM (« Transerve Electromagnetic ») du guide PPW d'alimentation. Ici, nous proposons d'utiliser le mode TEM et le mode TE (« Transverse Electric »). Ces deux modes sont orthogonaux et, si correctement alimentés, peuvent générer une double polarisation.

Title : Circular and Dual-Linear Polarized Continuous Transverse Stub Arrays for SatCom Applications

Keywords : CTS antennas, wideband, parallel-plate waveguide, quasi-optical beamformer

Abstract : The ever-increasing demand of wideband systems for satellite communication (SatCom) links calls for satellite spacecrafts deployed in constellations. An advanced generation of ground antenna modules is thus requested to operate in K/Ka-band. The antenna requirements are consequently challenging. Specifically, the antenna must perform a high-gain (> 30 dB) and provide a circularly or dual-linearly polarized radiation. A large field-of-view is also demanded: a scan range up to 60° in elevation must be ensured along a fixed azimuthal plane. The aim of this thesis is to analyse and design a promising candidate as terminal antenna: the continuous transverse stub (CTS) array in circular or dual-linear polarization. The CTS arrays consist of open-ended radiating stubs, parallel-fed by a corporate feed network in parallel-plate waveguide (PPW) technology. The underlying idea of the thesis is to enlarge the radiating stubs, in such a way to enable the propagation of the transverse electromagnetic (TEM) and the first transverse electric (TE1) modes. These modes exhibit orthogonally-polarized E-fields over the waveguide cross section. If properly excited, they are thus able to generate a circularly-polarized radiation. Several numerical models have been developed throughout the manuscript and employed as in-house tools to address the design of four prototypes. Three fabricated prototypes have been also tested in the IETR's facilities, showing results of great interest to the scientific community.